Universidade do Minho
Escola de Engenharia

Sharlane Maria da Costa

Development of manufacturing technology for abrasive grinding wheels with internal cooling channels produced with 3D structures obtained by additive manufacturing

Janeiro 2026

Development of manufacturing technology for abrasive grinding wheels with internal cooling channels produced with 3D structures obtained by additive manufacturing

Sharlane Maria da Costa

UMinho | 2026

Universidade do Minho
Escola de Engenharia

Sharlane Maria da Costa

Development of manufacturing technology for abrasive grinding wheels with internal cooling channels produced with 3D structures obtained by additive manufacturing

Tese de Doutoramento
Programa Doutoral em Engenharia Mecânica

Trabalho efetuado sob a orientação de
Professor Doutor Delfim Fernandes Soares
Professor Doutor João Eduardo Pinto Castro Ribeiro
Professor Doutor Mário António Caixeiro Castro Pereira

Janeiro 2026

DIREITOS DE AUTOR E CONDIÇÕES DE UTILIZAÇÃO DO TRABALHO POR TERCEIROS

Este é um trabalho académico que pode ser utilizado por terceiros desde que respeitadas as regras e boas práticas internacionalmente aceites, no que concerne aos direitos de autor e direitos conexos.

Assim, o presente trabalho pode ser utilizado nos termos previstos na licença abaixo indicada.

Caso o utilizador necessite de permissão para poder fazer um uso do trabalho em condições não previstas no licenciamento indicado, deverá contactar o autor, através do RepositóriUM da Universidade do Minho.

Licença concedida aos utilizadores deste trabalho



Atribuição-NãoComercial
CC BY-NC

https://creativecommons.org/licenses/by-nc/4.0/

ACKNOWLEDGMENTS

This work reflects not only a prolonged scientific effort, but also a personal journey marked by geographical distance from those who have always been present, balanced by the warmth, generosity and relationships built throughout this stage.

I would like to thank my supervisor, Professor Delfim Soares, for his daily support in the laboratory and for closely following all stages of this work. His constant guidance and humane approach made him not only a scientific reference, but also an example as both a mentor and a person. I also express my sincere gratitude to Professor João Ribeiro, my master's supervisor and co supervisor in this doctoral program, for the trust placed in me since 2018, when I arrived in Portugal, and for the relationship of respect and friendship built over the years. I am also grateful to my co supervisor, Professor Mário Pereira, for his continuous availability, careful analysis of results and the rigor with which he reviewed each paper contributing decisively to the scientific quality of this work.

I would like to express my gratitude to the Department of Mechanical Engineering for providing the academic environment and institutional support that made this work possible. I also thank the technical workers for their constant assistance, professionalism and availability, which were essential to the development of the experimental and research activities.

I gratefully acknowledge the Fundação para a Ciência e a Tecnologia (FCT) for funding this work through the PhD grant 2021.07352.BD.

My thanks to Dragão Abrasivos, and in particular to Engineer Luís Carvalho, for the supply of materials and for the valuable technical support provided throughout this work.

I also thank my laboratory colleagues, Miguel, Leonor and Paulina, for making the working days lighter and more enjoyable, and for helping me see challenges from a different, often more balanced and positive perspective.

To all my friends, both those I met in Portugal throughout this journey, especially Andrews and Sabrina, who became family, and those who remained in Brazil, yet always stayed present and supportive.

My deepest gratitude goes to João, my life partner, who teaches me every day to be more patient and to trust myself more. His support was essential throughout this journey, sharing every difficulty with me, helping me find solutions, and celebrating each achievement as if it were his own.

To my family, I offer a special word of thanks. To my sister Mylena and to my godmothers, for their constant care and unconditional support. To my grandparents, who, although no longer with us, I know would be proud of the path I have taken. And, most especially, to my parents, to whom I owe far more than I can express in words. Thank you for being my foundation throughout my life, for the values you instilled in me, for your constant encouragement toward education, and for your unwavering confidence in my choices. Thank you for all your support, for a love that transcends physical distance, and for never questioning my dreams, even when they required absence and longing. This achievement is also yours.

Muito obrigada!

STATEMENT OF INTEGRITY

I hereby declare having conducted this academic work with integrity. I confirm that I have not used plagiarism or any form of undue use of information or falsification of results along the process leading to its elaboration.

I further declare that I have fully acknowledged the Code of Ethical Conduct of the University of Minho.

RESUMO

A retificação é um dos processos de fabrico mais relevantes na atualidade, mas é, também, um dos mais exigentes em termos consumo de fluidos de corte. A utilização excessiva destes fluidos representa, não apenas, um encargo económico significativo, mas também um problema ambiental grave, associado à sua utilização e ao seu descarte. Neste sentido, o desenvolvimento de estratégias alternativas de arrefecimento tem sido apontado como uma via essencial para aumentar a eficiência e a sustentabilidade do processo.

Neste contexto, a presente tese propõe um novo método de fabrico de mós abrasivas estruturadas com canais internos de refrigeração, para transporte do fluido de arrefecimento diretamente para a zona de contacto. O processo desenvolvido combina fabrico aditivo com prensagem a quente, permitindo a criação de geometrias complexas no interior da mó de forma económica, adaptável e flexível. Assim, entre as suas vantagens destacam-se a possibilidade de integrar canais ao longo de todo o corpo da ferramenta, eliminando a necessidade de recondicionamento, e a simplicidade de implementação quando comparado com métodos mais dispendiosos ou de difícil escalonamento. Esta abordagem confere maior liberdade de projeto à ferramenta abrasiva, permitindo a otimização do sistema de refrigeração em função das condições de retificação.

Ensaios experimentais e simulações numéricas mostraram que os parâmetros geométricos dos canais, como diâmetro e inclinação, assim como o número de camadas de canais, influenciam de modo decisivo a distribuição do fluido na zona metal/mó, e o desempenho térmico da retificação. Esta análise combinada permitiu compreender os mecanismos de escoamento do fluido e a sua relação direta com as forças de corte, a energia específica e a resposta térmica do processo. As mós desenvolvidas apresentaram, em testes de retificação, reduções de até 49 % na força tangencial e até 50 % na energia específica, bem como, até 59 % na variação de temperatura, face à refrigeração externa convencional, validando a eficácia do método proposto.

Este trabalho contribui, assim, para consolidar o conceito de refrigeração interna em mós abrasivas, demonstrando que a integração de canais internos por meio de um processo de fabrico inovador pode representar um passo significativo em direção a um processo de retificação mais eficiente e sustentável.

Palavras-chave: Manufatura aditiva; Mós estruturadas; Refrigeração interna; Retificação; Sustentabilidade.

ABSTRACT

Grinding is one of the most relevant manufacturing processes today, yet it remains one of the most demanding in terms of cutting fluid consumption. The excessive use of these fluids represents not only a significant economic burden but also a serious environmental concern associated with their use and disposal. In this context, the development of alternative cooling strategies has been identified as an essential pathway to improve the efficiency and sustainability of the process.

In this context, the present thesis proposes a new manufacturing method for structured grinding wheels with internal cooling channels, designed to deliver the coolant directly to the contact zone. The developed process combines additive manufacturing with hot pressing, enabling the creation of complex internal geometries in a cost-effective, adaptable and flexible manner. Among its advantages are the ability to integrate channels throughout the entire wheel body, eliminating the need for reconditioning, and the simplicity of implementation when compared with more expensive or less scalable methods. This approach provides greater design freedom for the abrasive tool, allowing the cooling system to be optimized according to the grinding conditions.

Experimental tests and numerical simulations showed that the geometric parameters of the channels, such as diameter and inclination, as well as the number of channel layers, strongly influence the fluid distribution in the wheel–workpiece interface and the thermal performance of the grinding process. This combined analysis enabled the understanding of fluid flow mechanisms and their direct relationship with cutting forces, specific energy and the thermal response of the process. The wheels developed in this work achieved reductions of up to 49 % in tangential force and up to 50 % in specific grinding energy, as well as up to 59 % in temperature variation, when compared with conventional external cooling, validating the effectiveness of the proposed method.

This work therefore contributes to consolidating the concept of internal cooling in grinding wheels, demonstrating that the integration of internal channels through an innovative manufacturing process can represent a significant step toward a more efficient and sustainable grinding process.

Keywords: Additive manufacturing; Grinding; Internal cooling; Structured wheels; Sustainability.

TABLE OF CONTENTS

ACKNOWLEDGMENTS ..... **iii**

RESUMO ..... **v**

ABSTRACT ..... **vi**

TABLE OF CONTENTS ..... **vii**

LIST OF FIGURES ..... **xii**

LIST OF TABLES ..... **xx**

LIST OF ABBREVIATIONS ..... **xxii**

LIST OF SYMBOLS ..... **xxiii**

1. INTRODUCTION **1**

1.1 Motivation 1

1.2 Objectives 5

1.3 Organization of the Document 6

1.4 Contributions of the Investigation 8

2. LITERATURE REVIEW **9**

2.1 Grinding Basics 9

2.1.1 Grinding Wheel 9

2.1.2 Grinding Process 11

2.2 Textured Grinding Wheels 13

2.2.1 Texturing Methods of Abrasive Grinding Wheels 14

2.2.2 Recent Advances in Texturing Methods (2022–2025) 37

2.2.3 General Assessment of Texturing Methods 39

2.3 Coolant Application in Surface Grinding 39

2.4 Fluid Flow Modeling in Grinding Wheels 47

2.5 Summary and Discussions 50

3. MATERIALS AND METHODS 52

3.1 Thermal and Thermomechanical Characterization 52

3.2 Wear Tests 54

3.3 Scanning Electron Microscopy (SEM) 55

3.4 Internal Lubrication System 56

3.5 Grinding Experimental Setup 57

4. MANUFACTURING OF STRUCTURED GRINDING WHEELS 61

4.1 New Grinding Wheel Design Methodology Concept 61

4.2 Printing Conditions 63

4.3 Optimization of Processing Conditions 67

4.3.1 Formulation of the green composite 68

4.3.2 Pressing Strategies 71

4.3.3 Drying Stage 74

4.3.4 Sintering Stage 74

4.4 Final Characterization of Produced Wheels 75

4.4.1 Dimensional Control 75

4.4.2 Microstructural Analysis 77

4.4.3 Wear Tests 77

4.5 Summary and Conclusions 78

5. NUMERICAL MODELING OF COOLANT FLOW IN STRUCTURED GRINDING WHEELS 80

5.1 Modeling Strategy 80

5.2 Preliminary Modeling Choices 81

5.2.1 Velocity Formulation 82

5.2.2 Turbulence Modeling 83
5.3 Setup A: Multiphase Model with Control Volume 85
5.3.1 Geometric Model and Computational Domain 85
5.3.2 Mesh Generation and Independence Study 87
5.3.3 Physical Models 88
5.3.4 Post-processing Indicators 90
5.4 Setup B: Relative Velocity Model (Single-phase) 93
5.4.1 Geometric Model and Computational Domain 93
5.4.2 Mesh Generation and Independence Study 94
5.4.3 Physical Models 96
5.4.4 Post-processing Indicators 97
5.5 Experimental Validation by High-speed Imaging 100
5.5.1 Fabrication of Transparent Resin Wheel 100
5.5.2 High-speed Imaging Setup 102
5.5.3 Particle Tracking Methodology 103
5.5.4 Experimental Validation of CFD via Particle Velocity 105
5.6 Summary and Conclusions 107
6. PARAMETRIC STUDIES ON CHANNEL GEOMETRY 109
6.1 Screening by Taguchi-Grey Analysis 109
6.1.1 Factor Selection 110
6.1.2 Post-processing and Grey Relational Analysis 113
6.1.3 Results and Discussion 113
6.2 Effect of Number of Layers 117
6.2.1 Grinding Wheel Geometries 118

6.2.2 Numerical Analysis 118
6.2.3 Grinding Performance 122
6.2.4 Concluding Remarks on Number of Layers 124
6.3 Effect of Channel Diameter 125
6.3.1 Grinding Wheel Geometries 126
6.3.2 Numerical Analysis 127
6.3.3 Grinding Performance 130
6.3.4 Correlation Between CFD and Experimental Results 133
6.3.5 Concluding Remarks on Channel Diameter 135
6.4 Effect of Channel Inclination 136
6.4.1 Grinding Wheel Geometries 137
6.4.2 Numerical Analysis 137
6.4.3 Flow Visualization Using High-Speed Camera 140
6.4.4 Grinding Performance 143
6.4.5 Concluding Remarks on Channel Inclination 145
6.5 General Discussion and Design Guidelines 146
7. GRINDING BEHAVIOR OF STRUCTURED GRINDING WHEELS 148
7.1 Wheel Configurations 148
7.2 Grinding Stages and Thermal Segmentation 149
7.3 Grinding Performance 154
7.3.1 Cutting Forces 154
7.3.2 Specific Grinding Energy 155
7.3.3 Temperature Variation (ΔT) 156
7.4 Integrated Analysis 156

7.5 Summary and Conclusions 157

8. CONCLUSIONS 159

8.1 Summary of the Main Contributions 159

8.2 Future Work 161

8.3 Publications 162

References 166

LIST OF FIGURES

CHAPTER 1

Figure 1.1 – Air barrier effect during conventional flood in grinding [15,16]. 2

Figure 1.2 – Entry pathways of cutting fluids into the human body and related diseases [21]. 3

CHAPTER 2

Figure 2.1 – Schematic representation of the grinding process: (a) interaction between abrasive grains and the workpiece, highlighting pores, bond and the main force components (Ft, Fn); (b) successive mechanisms of material removal: i) rubbing, ii) ploughing and iii) cutting stages [61,63]. 12

Figure 2.2 – PRISMA flow diagram of the study selection process. 15

Figure 2.3 – Distribution of works by the processing method of the grooves. 15

Figure 2.4 – Distributions of works by groove processing method. 16

Figure 2.5 – Principle of machined grooves and groove geometry [84]. 16

Figure 2.6 – Machined grooves in (a) slit form [101], (b) helical form, (c) zigzag form and (d) cross linear form [92]. 20

Figure 2.7 – Schematic of structuring the grinding wheel (a) flattening of the grinding wheel by common dressing which is followed by special conditioning to produce macro structures on the wheel surface (b) [107]. 21

Figure 2.8 – Topography of a monolayer abrasive grinding wheel with an arrangement pattern [111]. 22

Figure 2.9 – Typical examples of phyllotactic pattern (a) keteleeria davidiana, (b) anthurium, (c) pinecone [120]. 26

Figure 2.10 – (a) Structure of the internal-cooling grooved grinding wheel and (b) the abrasive ring with the phyllotaxy pattern of the abrasive [134]. 26

Figure 2.11 – Experimental setup for laser structuring [139]. 27

Figure 2.12 – Groove geometries produced by laser method with the shape of (a) hemispheres and (b) waves [138,144]. 27

Figure 2.13 – Different laser groove patterns discussed by Zhang *et al.* [145]. 30

Figure 2.14 – Texture appearance obtained using (a) appropriate and (b) inappropriate parameters [150]. 31

Figure 2.15 – Principle of the SLM process [158]. 33
Figure 2.16 – Abrasive wheels structured by the SLM method by (a) Tian *et al.* [158] and (b) Li *et al.* [161]. 33
Figure 2.17 – Abrasive grinding wheel with internal cooling holes produced by SLS method [159]. 34
Figure 2.18 – Fabrication of the diamond grinding wheel by DIW [157]. 34
Figure 2.19 – A segmented grinding wheel [162]. 35
Figure 2.20 – Texturing procedure by Micro-abrasive water jet [166]. 36
Figure 2.21 – Grooves produced by AWJ method [167]. 37
Figure 2.22 – (a) Segmented grinding wheel with controlled radial coolant supply [183]. (b) Sandwich grinding wheel with centrifugal coolant provision [184]. 42
Figure 2.23 – (a) Grinding wheel with radial internal channels. (b) Movable limiter for zonal coolant delivery. (c) One-layer wheel. (d) Three-layer wheel [31]. 43
Figure 2.24 – Grinding wheels with internal cooling channels fabricated by additive manufacturing: (a) coolant supply through tool holder, (b) holes for internal flow and c-d) wheel designs (SS, CP, CP+S, VCP+S) [33]. 44
Figure 2.25 – Directional coolant supply system proposed by Peng *et al.* [182]: (a) tested wheel slot patterns, (b) schematic of the internal supply system and (c) detail of the coolant distribution through the manifold and micro-channels. 44
Figure 2.26 – Timeline of representative studies on grinding wheels with internal coolant supply [31–33,182–184]. 46

CHAPTER 3

Figure 3.1 – (a) Y-shaped PLA insert used to generate internal features in the abrasive composite. (b) Vitrified composite specimen (Ø6 × 6 mm) containing the embedded PLA insert. 53
Figure 3.2 – Schematic representation of the pin-on-disc wear test configuration used for the abrasive grinding wheels. 55
Figure 3.3 – Internal lubrication system: (a) Grinding machine (b) CAD model of the rotating shaft and wheel holder; (c) photograph of coolant exiting through the radial channels of the grinding wheel (wheel not rotating). 56

Figure 3.4 – Schematic representation of the lubrication systems: (a) external flood cooling, (b) internal cooling via radial channels. Directions of wheel rotation (Vs), workpiece feed (Vw), thermocouple location and load cell placement are indicated (schematic only, not to scale). 58

Figure 3.5 – Grinding experimental setup: (a) grinding wheel, (b) workpiece, (c) load cell, (d) thermocouple embedded below the workpiece surface. 60

CHAPTER 4

Figure 4.1 – Schematic representation of the new grinding wheel design methodology for the integration of internal cooling channels. 63

Figure 4.2 – Fabrication strategy of the PLA sacrificial inserts: (a) printed components comprising the base of the structure (Part 1), the single-layer channel array (Part 2) and the top section (Part 3); (b) final assembly forming the complete insert responsible for defining the internal channel geometry of the GW. 64

Figure 4.3 – DSC/TGA of the PLA precursor (10 °C/min, air atmosphere). 66

Figure 4.4 – Thermomechanical analysis (TMA) of abrasive composites with and without PLA structure (air atmosphere, heating rate 4 °C/min). 68

Figure 4.5 – Thermomechanical analysis (TMA) of polysaccharide solution samples with varying water contents (7, 20, 26 and 30, in wt %) under air atmosphere and heating rate of 4 °C/min. 69

Figure 4.6 – Thermomechanical Analysis (TMA) of abrasive composites with included PLA structure, manufactured with W30 organic binder contents of 4.5 wt. %, 7.5 wt. % and 10.5 wt. % (4 °C/min, air atmosphere). 70

Figure 4.7 – Schematic representation of tested abrasive composite samples, featuring a PLA structure at the center (a). Temperature and stress profiles for the two hot-pressing strategies: HP1 (load maintained during cooling) and HP2 (load released before cooling) (b–c). 71

Figure 4.8 – (a) Dimensional variation of the abrasive composite with a PLA structure under HP1 and HP2 conditions, starting from the beginning of the thermal cycle and (b) dimensional variations of the composite and the PLA components, and the total deformation, before and after unloading and recovering. 72

Figure 4.9 – Comparison between structured abrasive wheels after pressing: (a) cracks formed near the channels when conventional pressing was applied; (b) defect-free wheel produced using the optimized pressing strategy (HP2 with B7.5 composition). 73

Figure 4.10 – Dimensional analysis (TMA) of B7.5 abrasive composite with incorporated PLA structure in green, as a function of heating rates (0.1, 1.0 and 4.0 °C/min): (a) temperature-dependent; (b) time-dependent. 74

Figure 4.11 – (a) Unstructured reference disc. (b) Perspective view of the PLA structure designed to incorporate the channel network in abrasive grinding wheels. (c) Surface view of the hexagonal structured abrasive grinding wheel prototype. (d) Internal view of the grinding wheel, with the 3D internal cooling system, in the region of the cross-sectional cut. 76

Figure 4.12 – SEM images of the structured grinding wheel after sintering: (a) cross-section of the channel region, showing a continuous vitrified bond around the cavity and absence of residues; (b) detail of the abrasive grains embedded in the vitrified matrix, with homogeneous porosity distribution. 77

Figure 4.13 – Results of the wear tests: wear rate of the grinding discs (a) and the alumina pins (b); G-ratio for the reference and structured wheels (c). 78

CHAPTER 5

Figure 5.1 – Velocity profiles at the channel outlet with different formulations: (a) absolute velocity, dominated by wheel rotation; (b) relative velocity, showing a physically consistent jet with zero velocity at the walls. Simulation conditions: 5000 rpm, 800 mL/min. 83

Figure 5.2 – Grinding wheel and fluid domain model. 86

Figure 5.3 – Dimensional drawing of the structured grinding wheel used in simulations. 87

Figure 5.4 – Mesh convergence test results: relationship between the number of elements and the mass flow rate of water at the contact surface between the grinding wheel and the workpiece. 88

Figure 5.5 – Water volume fraction obtained for a grinding wheel with 30 radial channels of 1.5 mm diameter distributed in three layers (10 channels per layer): (a) contour on a plane crossing one of the channel layers; (b) contour on the workpiece surface; (c) water volume fraction profile extracted along the contact line on the workpiece surface. 91

Figure 5.6 – Velocity field around the grinding wheel obtained from Setup A: (a) contour of velocity magnitude, (b) velocity vectors illustrating jet trajectories and recirculation. Both representations share the same velocity scale (0–8 m/s). 93

Figure 5.7 – Computational domain used in Setup B. The inlet was defined at the shaft and the channel outlets were set as outlet boundaries. 94

Figure 5.8 – Setup B: (a) computational mesh of the wheel; (b) convergence of maximum outlet velocity with increasing number of elements. 95

Figure 5.9 – Velocity contour at the outlet of a representative channel (diameter 1.7 mm, single-layer configuration with 30 channels). 98

Figure 5.10 – Velocity contours across channel cross-sections of a structured wheel with 30 channels of 1.5 mm diameter in a single-layer configuration (1000 rpm; 800 mL/min). 99

Figure 5.11 – Streamlines inside the channels of a structured wheel with 30 inclined channels of 1.5 mm diameter in a single-layer configuration (250 rpm; 800 mL/min). 100

Figure 5.12 – Fabrication of the transparent resin grinding wheel: (a) printing on the Anycubic Photon D2 using DLP technology; (b) wheel immediately after printing; (c) post-curing under UV light; (d) prototype after curing; (e) final wheel after surface polishing, showing the positive inclination channels ($\theta = 12°$). 101

Figure 5.13 – Experimental setup for high-speed imaging: (a) coolant reservoir (supplied mass control), (b) magnetic stirrer, (c) coolant pump (flow control), (d) supply pipe, (e) surface grinding machine, (f) resin grinding wheel, (g) reservoir for water collection, (h) optical lenses, (i) high-speed camera, (j) triaxial translation stage, (k) illumination system and (l) computer for image acquisition and processing. 103

Figure 5.14 – Manual particle tracking method: (a) initial position of the reference particle (p_1) at time t_1; (b) final position (p_1') at time t_2; (c) rotation-corrected overlay of the two frames showing the measured displacement (Δp) used for velocity calculation. 104

Figure 5.15 – (a) Fluid velocity field obtained by CFD simulation (positive inclination geometry, 250 rpm, 800 mL/min). (b) Particle trajectories tracked from high-speed videos using *TrackMate*. Colors represent local particle speed. 106

Figure 5.16 – Average particle speed obtained through automatic tracking (*TrackMate*), manual measurement and CFD simulation. Error bars represent the standard deviation. 107

CHAPTER 6

Figure 6.1 – Front view of a single-layer grinding wheel with channels inclined at an angle θ relative to the radial direction (a), structured grinding wheels with two layers of channels (b), side view showing the interlayer distance (ID) (c) and three-layer configurations in two scenarios: one channel in contact with the workpiece (d) and two channels in contact with the workpiece (e). 110

Figure 6.2 – Main effects plot for Mean Grey Relation Grade. 115

Figure 6.3 – Structured grinding wheels with internal channels inclined at 12°: (a) single-layer configuration, (b) two-layer configuration and (c) three-layer configuration. 118
Figure 6.4 – Water volume fraction for the single-layer configuration over time: (a) along the contact line, (b) in each layer and (c) on the workpiece surface. 119
Figure 6.5 – Water volume fraction for the two-layer configuration over time: (a) along the contact line, (b) in each layer and (c) on the workpiece surface. 120
Figure 6.6 – Water volume fraction for the three-layer configuration over time: (a) along the contact line. (b) in each layer and (c) on the workpiece surface. 122
Figure 6.7 – Grinding forces as a function of depth of cut for wheels with one, two and three channel layers: (a) tangential force and (b) normal force. 123
Figure 6.8 – Temperature variation (ΔT) as a function of depth of cut for grinding wheels with one, two and three channel layers. 124
Figure 6.9 – Internal 3D structures, in PLA (a–c) and corresponding sintered grinding wheels (d–f) with different channel configurations: (a, d) 190 channels of ø 0.6 mm; (b, e) 69 channels of ø 1.0 mm; (c, f) 30 channels of ø 1.5 mm. 126
Figure 6.10 – Velocity vectors on the external surface of the grinding wheels and in the contact zone: (a) GW_190_0.6, (b) GW_69_1.0 and (c) GW_30_1.5. 127
Figure 6.11 – Velocity contour maps at the outlet surface of the grinding wheels: (a) GW_190_0.6, (b) GW_69_1.0 and (c) GW_30_1.5. 128
Figure 6.12 – Relationship between Geometric Flow Index (GFI), average outlet velocity and percentage of low-velocity area (V < 0.1 m/s) for the three grinding wheel configurations. 129
Figure 6.13 – Tangential (a) and normal (b) grinding forces as a function of depth of cut. 130
Figure 6.14 – Specific energy as a function of depth of cut. 131
Figure 6.15 – Maximum temperature variation (ΔT) measured in the workpiece for different cutting depths. 132
Figure 6.16 – Correlation between the outlet area with velocity below 0.1 m/s and experimental results: (a) tangential force; (b) maximum temperature variation (ΔT), for three cutting depths (10, 50 and 120 μm). 134

Figure 6.17 – Velocity distribution at the channel outlets obtained by CFD (a–c) and fluid ejection observed on the grinding wheel surface during operation (d–f): (a, d) GW_190_0.6; (b, e) GW_69_1.0; (c, f) GW_30_1.5. 135

Figure 6.18 – Transparent resin prototypes of structured grinding wheels used for flow visualization and particle tracking: (a) positive inclination (θ = 12° in the rotation direction); (b) straight (θ = 0°); and (c) negative inclination (θ = 12° opposite to the rotation direction). 137

Figure 6.19 – Average outlet velocity as a function of wheel speed for three internal channel inclination geometries: negative, straight and positive. 138

Figure 6.20 – Velocity contour maps at the channel outlets for grinding wheels with internal channels of negative inclination (left), straight (center) and positive inclination (right), at (a) 2000 rpm, (b) 3000 rpm and (c) 5000 rpm..... 139

Figure 6.21 – Zoomed view of the streamline distribution at the transition between the wheel center and the channels, for three internal cooling channel geometries: (a) negative inclination, (b) straight and (c) positive inclination (5000 rpm). 140

Figure 6.22 – High-speed images of fluid jets emerging from GW with three internal-channel geometries: negative (left column), straight (center) and positive inclination (right), at (a) 2000 rpm, (b) 3000 rpm and (c) 5000 rpm. Insets in (c) magnify the contact zone to highlight jet continuity at high rotation. 141

Figure 6.23 – (a) Average jet inclination angles at 5000 rpm for negative, straight and positive channels. (b) Schematics and high-speed images showing mean jet angles of 41.2°, 30.0° and 6.7°, respectively. ... 142

Figure 6.24 – Effect of channel inclination on grinding forces: (a) tangential force (Ft) and (b) normal force (Fn) as a function of depth of cut. 144

Figure 6.25 – Maximum temperature variation (ΔT) as a function of depth of cut for grinding wheels with positive, straight and negative channel inclination..... 144

CHAPTER 7

Figure 7.1 – Development of the structured grinding wheel with internal cooling channels: (a) CAD model, (b) sacrificial PLA insert produced by additive manufacturing and (c) vitrified wheel after sintering. 149

Figure 7.2 – Dimensional characteristics of the structured grinding wheel with internal cooling channels: (a) geometric parameters of the channel network and (b) dimensional references in the grinding wheel. 149

Figure 7.3 – Schematic representation of the three grinding stages (cut in, steady state and cut out) for a conventional flood lubrication system – Reference; (a) and a structured grinding wheel with internal cooling – Structured (b). Adapted from Malkin and Guo [61]. 150

Figure 7.4 – Tangential force profile during the grinding operation for Reference and Structured wheels, with the three stages identified from the force signal..... 151

Figure 7.5 – Temperature profiles measured by thermocouple for cutting depths of 10 μm (a) and 120 μm (c) and corresponding heating rates (b, d), for both lubrication systems. The thermocouple was positioned 7.5 mm from the start of the grinding path, as shown in (a) and (c) and 1 mm below the surface. 152

Figure 7.6 – Tangential (a) and normal (b) grinding forces as a function of depth of cut for grinding wheels operating with an External Cooling System and with an Internal Cooling System. 154

Figure 7.7 – Specific grinding energy as a function of depth of cut for wheels operating with an External Cooling System (Reference) and with an Internal Cooling System (Structured). 155

Figure 7.8 – Maximum temperature variation (ΔT) measured by thermocouple as a function of depth of cut for wheels operating with an External Cooling System (Reference) and with an Internal Cooling System (Structured). 156

LIST OF TABLES

CHAPTER 2

Table 2.1 – Summary of publications with machined grooves. 16

Table 2.2 – Grooving tool and machined grooves geometries and dimensions. 19

Table 2.3 – Summary of publications with engineered grooves. 23

Table 2.4 – Engineered grooves geometries and dimensions. 25

Table 2.5 – Summary of publications with laser grooves. 28

Table 2.6 – Laser grooves geometries and dimensions. 29

Table 2.7 – Summary of publications with 3D-printed grooves. 32

Table 2.8 – 3D-printed method and geometry. 32

Table 2.9 – Summary of work with segmented grooves. 35

Table 2.10 – Summary of publications with grooves produced by AWJ. 36

Table 2.11 – Geometries and dimensions of the grooves produced by AWJ. 36

Table 2.12 – Examples of grinding fluid supply methods in surface grinding processes [31,43,179–184]. 41

Table 2.13 – Representative studies on internally cooled grinding wheels in surface grinding, including main process parameters, channel designs and performance outcomes. 45

Table 2.14 – Summary of simulation setups, varied parameters and analyzed outputs in studies of internally cooled grinding wheels. 48

Table 2.15 – Summary of CFD simulations applied to internally cooled cup-type grinding wheels. 49

CHAPTER 3

Table 3.1 – Experimental conditions applied in the thermal and thermomechanical analyses. 54

Table 3.2 – Experimental conditions of the wear tests of the abrasive grinding wheels. 55

Table 3.3 – Technical specifications of the custom grinding machine developed for testing structured wheels with internal channels. 57

Table 3.4 – Grinding parameters used in the tests for evaluating external and internal cooling systems. ... 59

CHAPTER 4

Table 4.1 – Printing parameters and dimensional results for the PLA channel inserts produced with the Ultimaker 3 and Bambu A1. 65

Table 4.2 – Tested compositions for the study of plasticity in Ø 6 x 6 mm test specimens of organic binder (polysaccharide + water. 69

Table 4.3 – Study of plasticity in the cylindrical test specimen of green abrasive composite by varying the W30 organic binder content. 70

Table 4.4 – Dimensional characteristics of the PLA structure, the reference disc and the structured disc. 76

Table 4.5 – Optimal processing conditions established for the fabrication of structured abrasive composites with PLA inserts, including binder formulation, pressing, drying and sintering parameters. 79

CHAPTER 5

Table 5.1 – Reynolds numbers for selected cases under a maximum flow rate of 800 mL/min (water at 20 °C, Setup B conditions, 0 rpm). 84

Table 5.2 – Summary of simulation parameters used in Setup A. 89

Table 5.3 – Summary of simulation parameters used in Setup B. 96

Table 5.4 – Manual measurements of particle displacement and speed obtained from the high-speed recordings. 105

CHAPTER 6

Table 6.1 – Factors and their levels, used in the Taguchi experimental design. 111

Table 6.2 – Geometry factor combinations used in the simulations according to the Taguchi experimental design (L18 array). 112

Table 6.3 – Grey relational coefficient and Grey grade values. 114

Table 6.4 – Main effects on Grey relation grades. 115

Table 6.5 – Results of ANOVA on Grey relational grade 116

Table 6.6 – Geometric specifications of the structured grinding wheels evaluated in this study. 126

Table 6.7 – Average outlet velocity and fraction of low-velocity regions ($V < 0.1$ m/s) for the three structured wheel configurations. 128

LIST OF ABBREVIATIONS

AWJ – Abrasive Waterjet

CAD – Computer-Aided Design

CAM – Computer-Aided Manufacturing

CBN – Cubic Boron Nitride

CFD – Computational Fluid Dynamics

CVD-D – Chemical Vapor Deposition Diamond

DIW – Direct Ink Writing

DMA – Dynamic Mechanical Analysis

DLP – Digital Light Processing

DSC/TGA – Differential Scanning Calorimetry and Thermogravimetric Analysis

FDM – Fused Deposition Modelling

FEM – Finite Element Method

G-ratio – Grinding Ratio

GFI – Geometric Flow Index

GW – Grinding Wheel

ID – Interlayer Distance

MQL – Minimum Quantity Lubrication

MRF – Multiple Reference Frame

PLA – Polylactic Acid

SEM – Scanning Electron Microscopy

SiC – Silicon Carbide

SLM – Selective Laser Melting

SLS – Selective Laser Sintering

TMA – Thermomechanical Analysis

TPMS – Triply Periodic Minimal Surface

VOF – Volume of Fluid

LIST OF SYMBOLS

Latin Symbols

Symbol	Unit (SI)	Description
a_e	µm	Depth of cut
a_{ed}	µm	Dressing depth of cut
a_g	µm	Groove depth
b_g	µm	Groove width
D	mm	Hydraulic diameter
Ec	J/mm³	Specific grinding energy
F_n	N	Normal grinding force
F_t	N	Tangential grinding force
F-value	[-]	F statistic (ratio of variances)
f_{ad}	mm/min	Dressing feed
k	m²/s²	Turbulent kinetic energy
mean_sq	[-]	Mean square
P-value	[-]	Significance probability (P-value)
p_1	mm	Initial position of the tracked particle
p_1'	mm	Final position of the tracked particle
Q_w	mm³/s	Material removal rate
$\vec{r}$	m	Position vector
Re	[-]	Reynolds number
sum_sq	[-]	Sum of squares
T	°C	Temperature
Tc	°C	Crystallization temperature
Tg	°C	Glass transition temperature
Tm	°C	Melting temperature (melting point)

Symbol	Unit (SI)	Description
t_1	s	Initial time instant
t_2	s	Final time instant
U	m/s	Mean velocity inside the channel
V	m/s	Fluid velocity
$\vec{V}_{abs}$	m/s	Absolute velocity vector
$\vec{V}_{rel}$	m/s	Relative velocity vector
V_s	m/s	Wheel peripheral speed
V_w	mm/min	Workpiece feed speed
v_{p1}	m/s	Particle velocity measured from displacement and time
x_i	[-]	Original value of the response i
x_i'	[-]	Normalized value of response i (larger-is-better)
Ø	mm	Diameter symbol

Greek Symbols

Symbol	Unit (SI)	Description
$\Delta_i(k)$	[-]	Absolute deviation from ideal normalized value
Δt	ms	Time interval between successive frames
ΔT	°C	Temperature variation
Δ_p	mm	Linear displacement of the tracked particle
ε	m^2/s^3	Turbulent dissipation rate
γ_i	[-]	Grey relational grade for experiment i
λ	nm	Wavelength of the ultraviolet light
μ	Pa·s	Dynamic viscosity
ρ	kg/m^3	Density
σ	px	Standard deviation used in the Gaussian blur filter

Symbol	Unit (SI)	Description
θ	°	Channel inclination angle
$\xi_i(k)$	[-]	Grey relational coefficient for experiment i, response k
ζ	[-]	Distinguishing coefficient
ω	$1/s$	Specific dissipation rate
$\vec{\Omega}$	rad/s	Angular velocity vector

1. INTRODUCTION

Grinding is a fundamental manufacturing process to achieve high dimensional accuracy and surface quality, yet it is characterized by intense heat generation and significant challenges in coolant delivery to the grinding zone. Conventional external lubrication often proves ineffective due to the air barrier formed around the wheel at high speed, resulting in low effective cooling and excessive fluid consumption. In this context, the integration of internal cooling channels into the grinding wheel (GW) has emerged as a promising approach to improve fluid distribution, reduce thermal damage and enhance process efficiency. Despite these advantages, several challenges remain concerning wheel manufacturing, prediction of coolant transport and experimental validation under realistic grinding conditions. This thesis addresses these issues by combining experimental investigations with Computational Fluid Dynamics (CFD) simulations to evaluate the performance of structured wheels with internal channels. This introductory chapter presents the motivation, the scope and the objectives of the research, the organization of the thesis and the main results achieved.

1.1 Motivation

Grinding is one of the most indispensable processes in modern manufacturing, widely applied whenever high surface quality and dimensional accuracy are required [1,2]. Unlike conventional machining, it relies on the collective action of thousands of randomly distributed abrasive grains that simultaneously rub, plough and cut the material [3]. This unique cutting mechanism allows grinding wheels to process a wide range of metallic and ceramic components as well as polymers, wood and cork, from automotive and aerospace parts to biomedical implants, often achieving tolerances in the micron range and surface finishes unattainable by other methods [4–8]. For this reason, grinding wheels remain critical tools in industries where performance, safety and reliability strongly depend on surface integrity and geometric precision and surface roughness.

Yet, the very characteristics that make grinding indispensable also impose severe thermal challenges. Approximately 70–80 % of the input energy is converted into heat, which is concentrated in the thin contact zone between the wheel and the workpiece [9]. Localized temperatures can exceed 1000 °C under extreme conditions, leading to thermal damage, surface burns and microstructural alterations if cooling is not properly managed [10–12]. Although flood cooling is traditionally applied to mitigate these effects, the high-speed

rotation of the wheel generates a boundary layer of air that acts as an aerodynamic shield (Figure 1.1). This barrier deflects much of the coolant jet away from the cutting zone, meaning that large fluid volumes are supplied while only a small fraction effectively penetrates the region where heat is generated [13–15].

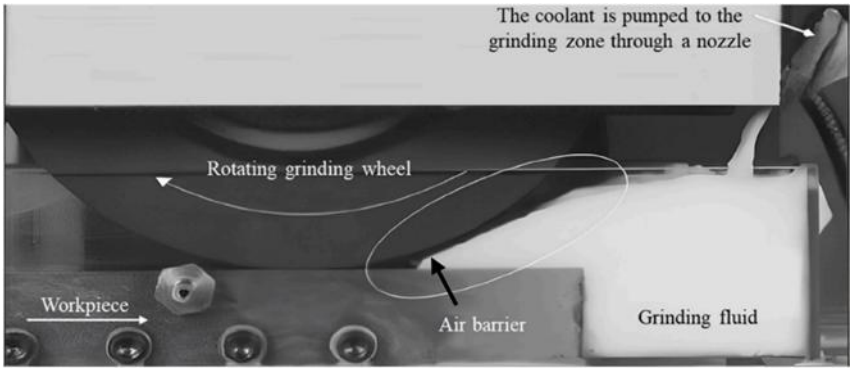


Figure 1.1 – Air barrier effect during conventional flood in grinding [15,16].

This inefficiency is aggravated by the fact that flood cooling requires very high fluid flow rates, typically between 10 to 100 L/min [15,17]. Such volumes not only waste resources but also generate environmental burdens and health risks for operators [18].

The use of cutting fluids in machining and grinding processes is today one of the main barriers to sustainable manufacturing. It is estimated that more than 4 million tons of cutting fluids are consumed annually worldwide, most of them based on petroleum-derived mineral oils [19]. This massive consumption implies not only high costs, which can account for up to 15–20 % of the total production cost and be three to five times higher than the cost of the tools themselves, but also serious environmental risks. Just one liter of mineral oil can contaminate up to one million liters of water, compromising aquatic ecosystems and soil quality [20].

In addition to the environmental impact, cutting fluids poses significant occupational health risks. Their exposure can occur through inhalation of mists, dermal contact or accidental ingestion of contaminated particles and it has been associated with chronic respiratory problems, dermatological disorders and potential carcinogenic effects. These risks directly affect workers' quality of life and generate additional costs for the industry related to absenteeism, staff turnover and protective measures. Figure 1.2 summarizes the main exposure pathways and adverse effects reported in the literature [21].

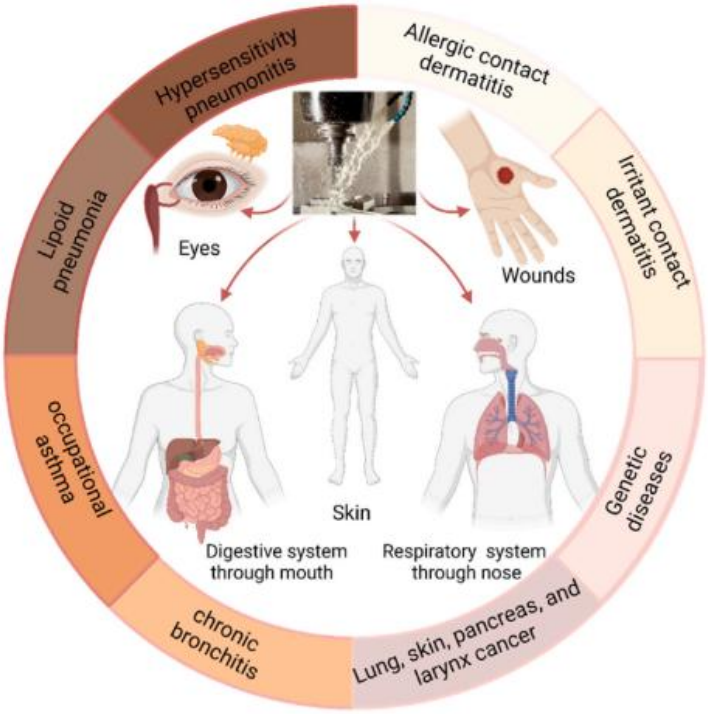


Figure 1.2 – Entry pathways of cutting fluids into the human body and related diseases [21].

From a broader sustainability perspective, both the life cycle of grinding wheels and the excessive use of coolants are increasingly critical. To address these concerns, several alternative strategies have been proposed, such as Minimum Quantity Lubrication (MQL), cryogenic cooling and textured grinding wheels [15,18]. Although these strategies have shown partial improvements, they present inherent limitations. MQL provides limited cooling capacity in high-energy grinding, which restricts its applicability [22,23]. Cryogenic cooling offers effective heat dissipation but lacks adequate lubrication and requires costly infrastructure, which reduces its industrial feasibility [24,25].

Among these, surface texturing of grinding wheels has been widely investigated to improve coolant accessibility and facilitate chip evacuation. Zhang *et al.* [26] developed shark-fin structured grinding wheels with different groove widths, which, when grinding MgF_2 ceramics, achieved a 22.2 % reduction in surface roughness, improved surface quality and increased wheel wear resistance compared with conventional unstructured wheels. Wen *et al.* [27] designed a bionic bronze-bonded diamond grinding wheel with a feather-like surface structure, which, when grinding SiC (Silicon Carbide) ceramics, reduced grinding forces, enhanced wheel wear resistance and achieved up to a 32.8 % reduction in surface roughness compared with a traditional textured wheel. Surendran and Sooraj [28] proposed a hybrid sweating-type wheel combining surface textures with self-adaptive internal reservoirs, which, when grinding Ti6Al4V, achieved a 58 %

reduction in temperature, 37–42 % reduction in grinding forces and 16–45 % improvement in surface roughness.

However, since all these surface-based solutions eventually lose their effectiveness as the wheel wears, a more robust alternative is the integration of internal cooling channels, capable of delivering fluid directly from the wheel center to the contact zone, thereby overcoming the air barrier generated by rotation and maintaining efficiency throughout the entire wheel life [29]. Among the earliest and most systematic investigations of this concept were those of Sieniawski and co-workers, based on the manufacturing method described in patent PL203295B1 [30]. In their study, vitrified alumina wheels with 1, 2 or 3 rows of radial channels demonstrated that even with a 90 % reduction in fluid flow (0.5 vs. 5.0 L/min), the process remained thermally stable and surface quality comparable to flood was maintained [31], while grinding forces were 20–25 % lower and exhibited a slower force increase over time, suggesting longer wheel life [32].

The main limitation, however, lies in the manufacturing method. The Patent PL203295B1 [30] describes the formation of channels by means of tensioned metallic wires inserted through the mold during pressing, which are later removed mechanically to leave continuous channels. Any geometric modification requires a new mold, making the process inflexible. Moreover, the resulting channels are always linear, therefore preventing the creation of curved, interconnected, organic, or special-section structures, such as the hexagonal geometries explored in the present work. This rigidity explains why Sieniawski's approach has remained confined to laboratory-scale studies and, to date, has not been extensively replicated by other authors.

More recently, other authors have explored internal cooling channels using additive manufacturing, such as Barmouz *et al.* [33] who produced resin-bonded wheels with cylindrical and venturi-shaped channels. Unlike the approach of Sieniawski, the fluid was supplied externally through customized holders and guided into internal channels, with results showing substantial reductions in grinding forces, improved tool life and higher G-ratio, especially for venturi configurations, which increased coolant velocity and cooling efficiency. Nevertheless, despite the promising results, the Digital Light Processing (DLP) approach remains more suited for prototyping and resin-bonded wheels of limited size, since the long curing times per layer make the process challenging to apply at industrial scale. In addition, because the coolant is still supplied externally, a large amount of fluid is wasted and only a small fraction actually enters the slots, as evidenced by the high flow rates required in their tests (45 L/min).

In this context, the present work proposes an innovative solution based on the use of sacrificial polymeric structures, produced by additive manufacturing and inserted directly into the mold during wheel pressing.

These structures are eliminated during the sintering stage, generating continuous internal channels without the need for additional removal operations or special molds. The method stands out for its simplicity and low cost, since it can be integrated into the conventional manufacturing process of vitrified wheels without significant equipment modifications. Beyond enabling internal lubrication, the technique also allows the creation of texturizations distributed throughout the wheel body, which, unlike conventional approaches (laser, abrasive water jet, etc.), do not require periodic reconditioning during the tool's lifetime. Another decisive aspect is its high geometric flexibility, enabling the design of straight, inclined, or multi-layer channels, as well as curvilinear, interconnected, or non-conventional cross-section structures, thereby expanding the range of feasible solutions. From an industrial perspective, this approach is technically viable, economically attractive and aligned with increasing sustainability demands, as it effectively reduces coolant consumption, extends tool life and can improve the productivity of grinding operations.

1.2 Objectives

The development of grinding wheels with internal cooling channels represents a relevant opportunity to overcome the limitations associated with conventional external lubrication, particularly regarding the air barrier generated by tool rotation and the consequent waste of fluid. However, the practical implementation of this concept still involves significant challenges, mainly related to establishing a reliable manufacturing method and demonstrating its effectiveness under realistic grinding conditions. This thesis was designed to address these challenges by integrating complementary approaches of manufacturing, numerical simulation and experimental validation.

The central goal was the development, manufacturing and performance evaluation of internally cooled structured grinding wheels, aiming to improve the thermal and tribological efficiency of the grinding process while simultaneously reducing fluid consumption. To achieve this purpose, the following specific objectives were defined:

- To develop and validate a manufacturing process for structured grinding wheels with internal channels, using polymeric inserts produced by additive manufacturing, ensuring channel formation after sintering and the dimensional and microstructural integrity of the wheels.
- To develop and apply CFD methodologies to describe fluid flow under rotating conditions, using complementary models to evaluate both the external jet dispersion and the outlet velocity at the channels.

- To validate the numerical results through the application of high-speed imaging and particle tracking techniques, integrating experimental and numerical analysis to consolidate the understanding of the flow.
- To perform comparative grinding tests between conventional and structured wheels, quantifying cutting forces, specific energy and temperature variation, under controlled conditions.
- To investigate the influence of channel geometric parameters, namely the number of layers, channel diameter and inclination on the fluid transport and the grinding performance, in order to establish design guidelines with practical relevance for industrial applications.

By addressing the objectives defined in this work, the thesis establishes a comprehensive framework that integrates manufacturing, CFD simulations and experimental validation, thus paving the way for the broader adoption of internally cooled grinding wheels in advanced machining processes.

1.3 Organization of the Document

The present thesis addresses the development and evaluation of internally cooled grinding wheels, combining the design and manufacture of innovative abrasive tools with the use of advanced experimental and numerical methodologies. The multidisciplinary character of the work results from the integration of additive manufacturing techniques, experimental grinding tests and Computational Fluid Dynamics modeling, allowing a comprehensive understanding of how internal cooling channels affect the fluid transport and the grinding performance. To ensure coherence, the document is divided into eight chapters that follow a logical progression from motivation and background to conclusions and future perspectives.

Chapter 1 introduces the context and motivation of the study. The limitations of conventional cooling methods are outlined and the potential of internal channels is presented as a promising alternative. The objectives of the thesis are defined and an overview of the document's structure is provided.

Chapter 2 presents an extensive literature review on grinding processes, cooling methods and surface texturing strategies. The discussion begins with the fundamentals of grinding and the main thermal and tribological challenges of the process. Different coolant application approaches are then presented, including traditional nozzles, texturization of abrasive wheels by different methods and the introduction of internal channel lubrication. Special attention is given to additive manufacturing as an enabling technology for the

fabrication of complex internal structures, as well as to the application of Computational Fluid Dynamics in this field. The chapter concludes by identifying research gaps that frame the contribution of the present work.

Chapter 3 describes the materials and methodologies used in the thesis. The composition and characteristics of the grinding wheels are presented together with the selected workpiece material. The experimental setups are explained in detail, including the configurations employed for fluid flow visualization and grinding tests, as well as the measurement techniques used for monitoring forces and temperatures.

Chapter 4 is dedicated to the manufacturing method developed for structured grinding wheels with internal channels. The process based on sacrificial polymeric inserts produced by additive manufacturing is described step by step. Its validation through dimensional and microstructural analyses is also reported, confirming the method's viability and reproducibility.

Chapter 5 focuses on the numerical modeling of coolant flow in internally cooled wheels. The procedures for domain definition, mesh generation and boundary condition assignment are described, together with the solver strategies employed. The chapter also addresses the validation of the CFD model using high-speed imaging and particle tracking techniques, ensuring the consistency of the numerical and experimental approaches.

Chapter 6 integrates the different investigations carried out in the thesis. It begins with a screening study using the Taguchi method, followed by statistical analysis to identify the most influential factors on coolant distribution. Based on these findings, a systematic evaluation of channel geometry is performed, including the number of layers, channel diameter and inclination. The combination of CFD simulations and experimental results provides insights into how these design parameters affect coolant transport and grinding performance.

Chapter 7 presents the grinding experiments conducted to compare the behavior of conventional and internally cooled wheels. The performance of the wheels is analyzed in terms of tangential and normal forces, specific grinding energy and temperature variation under controlled conditions.

Chapter 8 concludes the thesis by summarizing the main contributions of the work, highlighting their scientific relevance and outlining recommendations for future research, particularly concerning the optimization and potential industrial application of internally cooled structured grinding wheels. In addition, the publications resulting from this research are presented.

1.4 Contributions of the Investigation

The work developed in this doctoral thesis has contributed to the advancement of knowledge in the field of structured grinding wheels with internal cooling channels, bridging the gap between tool design, manufacturing feasibility and performance evaluation, under grinding conditions. The thesis combines methodologies from additive manufacturing, materials processing, Computational Fluid Dynamics (CFD) and experimental tribology, resulting in a comprehensive framework for assessing coolant transport and its impact on grinding performance.

At the manufacturing level, the thesis proposes and validates a novel method for the production of vitrified alumina wheels with three-dimensional internal channels, using sacrificial polymeric inserts produced by additive manufacturing. The process ensures channel formation after sintering while preserving the microstructural integrity of the abrasive matrix, confirming its feasibility for structured wheel production.

From the numerical perspective, advanced CFD methodologies were implemented to simulate coolant transport in rotating wheels. Different geometrical configurations were analyzed, including the effect of the number of channel layers, channel diameter and inclination, supported by systematic mesh refinement and convergence studies. Validation was achieved through a direct comparison between CFD predictions and experimental results obtained via high-speed imaging and particle tracking, ensuring the reliability of the numerical analysis.

Experimentally, the thesis presents a comparative assessment between conventional and internally cooled grinding wheels, covering grinding forces, specific grinding energy and temperature variation. These results provide direct evidence of the benefits and current limitations of structured wheels in grinding conditions.

A key contribution of this thesis lies in the integration of numerical simulations with experimental validation, providing a comprehensive understanding of coolant transport in structured grinding wheels. The application of the Taguchi method enabled the identification of the most influential parameters, which guided the systematic investigation of channel geometries. The resulting insights converge into clear design guidelines that enhance cooling efficiency and grinding performance, thereby strengthening the basis for future optimization and potential industrial adoption of internally cooled wheels.

Finally, the research has contributed to scientific dissemination through publications in peer-reviewed international journals and conference proceedings, consolidating the relevance of internally cooled grinding wheels in the broader context of sustainable and efficient manufacturing technologies.

2. LITERATURE REVIEW

This chapter presents a comprehensive review of the state of the art in grinding processes, with particular emphasis on the design and manufacturing methods of textured grinding wheels. It begins with a general overview of grinding fundamentals, including wheel compositions, cutting mechanisms, thermal challenges and then, progresses to advanced strategies aimed at improving performance, such as the incorporation of superficial grooves and internal cooling channels. In addition, the chapter includes an overview of Computational Fluid Dynamics applications in the study of fluid flow within grinding wheels, highlighting its relevance as a complementary tool to experimental investigations and as a design-oriented methodology for developing innovative wheel geometries. Part of the content, especially the systematic mapping of texturing methods and their advantages and limitations, is based on the paper "Texturing Methods of Abrasive Grinding Wheels: A Systematic Review", published in Materials [34], which provided a structured foundation for the critical discussion developed here.

2.1 Grinding Basics

Grinding is a precision machining process distinguished by its ability to achieve tight dimensional tolerances and superior surface quality, which makes it indispensable in the production of high-value components. Unlike conventional cutting, it relies on the collective action of numerous abrasive grains, whose behavior is determined not only by their intrinsic properties but also by the characteristics of the bond and the wheel structure and the grinding conditions [35]. A clear understanding of these fundamentals is crucial for analyzing grinding performance, as they directly influence material removal efficiency, thermal effects and tool wear. The following sections, therefore, address the composition and the role of the main constituents of grinding wheels, followed by a discussion of the grinding process and its underlying mechanisms.

2.1.1 Grinding Wheel

Grinding wheels are composite tools designed for precision material removal. They are typically composed of three essential elements: abrasive grains, bonding material and pores. The proportion and interaction among these elements define the wheel's cutting performance, its thermal behavior and its durability [36,37].

Abrasive grains are the active cutting elements of the wheel and must be significantly harder than the workpiece to ensure effective material removal without excessive wear [38]. They are generally classified into conventional abrasives (alumina and SiC) and superabrasives (CBN – Cubic Boron Nitride and diamond). From softest to hardest, they can be arranged as alumina, SiC, CBN and diamond. The first two are widely used in conventional applications, while the latter two are reserved for demanding processes, despite their higher cost [39,40]. Grain performance is not determined only by the base material: friability, grain size and morphology also play decisive roles. Friable grains tend to fracture and self-sharpen, extending the wheel's efficiency, whereas tougher grains provide longer retention but may blunt over time [41,42].

The bonding material is responsible for retaining abrasive grains until they become dull, at which point it should release them, exposing new sharp edges. The balance between retention and release is critical: overly hard bonds may cause worn grains to remain on the surface, leading to thermal damage and dimensional errors, while overly soft bonds accelerate wheel wear. The most common bonds are [43,44]:

- Vitrified bonds: ceramic matrices offering rigidity, thermal stability and chemical resistance; suitable for both conventional and superabrasives.
- Resin bonds: provide flexibility and shock absorption; commonly used with alumina and SiC and, in some cases, with diamond.
- Metallic and galvanic bonds: used exclusively with superabrasives, offering very high retention forces. In electroplated wheels, only a single layer of abrasives is deposited, resulting in sharp but thin cutting zones.

Finally, porosity constitutes the third fundamental element. Pores are voids within the wheel structure that serve three main functions: (i) to provide space for chip accommodation, (ii) to facilitate coolant access to the contact zone and (iii) to reduce friction and adhesion of the workpiece material. Porosity may occur naturally from the manufacturing process or be artificially induced by pore inducers; its role is crucial in thermal control, as it enables efficient fluid transport through the wheel. While vitrified and resin bonds allow for controlled porosity, metallic and galvanic bonds are typically dense [45–47].

Conventional vitrified grinding wheels are manufactured through a sequence of operations: (i) mixing of abrasives with bond materials, pore inducers and a small amount of organic binder, which provides plasticity and mechanical strength to the green body during shaping. (ii) Forming is usually carried out by pressing into the desired shape, followed by (iii) drying to remove residual moisture. During the subsequent (iv) sintering

cycle, the organic binder is removed in the initial heating stage and at higher temperature the bond consolidates, stabilizing the wheel structure [48–50]. By contrast, superabrasive wheels often adopt alternative processes such as brazing or electroplating to deposit a thin abrasive layer onto a metallic substrate, which ensures high cutting efficiency but at a higher cost [51–53].

The final microstructure (grain distribution, bond characteristics and porosity) directly governs the wheel's mechanical strength, wear resistance and cooling capability [54]. As such, the proper selection and design of grinding wheels remain critical to achieve efficiency and reliability in grinding operations.

2.1.2 Grinding Process

The grinding process is a precision machining technology widely employed to manufacture high added-value components, representing up to 20–25 % of the total machining cost [55,56]. As the final stage in the production chain, even small errors may compromise the workpiece, which demands high-accuracy machines and robust process control [57,58].

At the microscopic level, three distinct mechanisms occur along the contact length between wheel and workpiece [59–62]:

- Rubbing: at the entry zone, the undeformed chip thickness is insufficient for penetration. Only elastic deformation and friction take place and all energy input is converted into heat without contributing to material removal.
- Ploughing: as penetration increases, plastic deformation occurs, displacing material to the sides of the grain path. Although this mechanism does not generate chips, it is necessary for subsequent cutting. The energy consumed is largely dissipated as heat.
- Cutting: when shear stress exceeds the material strength, fracture occurs and chips are formed. The thickness at which this transition begins is defined as the critical chip thickness. Cutting is the only mechanism where energy is effectively transformed into material removal and maximizing its contribution is a central goal in grinding research.

These three mechanisms are schematically illustrated in Figure 2.1. Part (a) shows the interaction between abrasive grains and the workpiece along the contact length, including the resulting force components. Part (b) depicts the successive stages of rubbing, ploughing and cutting [61,63].

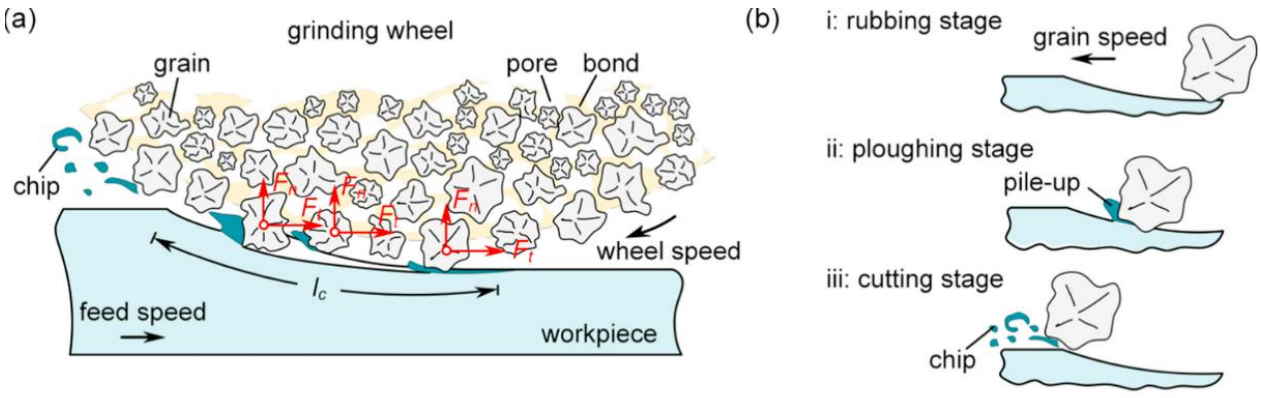


Figure 2.1 – Schematic representation of the grinding process: (a) interaction between abrasive grains and the workpiece, highlighting pores, bond and the main force components (F_t, F_n); (b) successive mechanisms of material removal: i) rubbing, ii) ploughing and iii) cutting stages [61,63].

Macroscopically, these interactions are reflected in two measurable force components: the tangential force (F_t), associated with chip formation and the normal force (F_n), related to grain penetration [64,65]. Due to the extremely small undeformed chip thickness, the specific grinding energy is several times higher than in conventional machining, making the process simultaneously effective and thermally challenging [63,65–67].

Grinding becomes particularly challenging when processing hardened steels, titanium alloys, nickel-based superalloys and carbides, nitrides and oxide ceramics; owing to their high hardness, toughness, stability, or brittleness, these materials tend to generate higher grinding forces, accelerate wheel wear and exhibit pronounced sensitivity to thermal damage [68,69].

More than three-quarters of the mechanical energy supplied to grinding is converted into heat at the abrasive–workpiece and abrasive–chip interfaces. Local temperatures can easily surpass 1000 °C under aggressive conditions, leading to tempering, phase transformations, residual stresses or even surface and subsurface cracking [12,70–72]. Controlling this heat is therefore one of the central concerns in grinding technology.

Besides material removal, the wheel itself undergoes progressive degradation. According to Marinescu *et al.* [54], the main wear mechanisms are:

- Abrasive wear: caused by the direct contact and relative motion between abrasive grains and the workpiece, leading to grain fracture or bond-grain interface weakening.
- Adhesive wear: common in metallic grinding, in which molten or softened workpiece material adheres to the wheel surface under high temperatures, altering local cutting conditions.

- Tribochemical wear: driven by chemical reactions at elevated temperatures, which modify material composition at the interface and accelerate wheel deterioration.

These mechanisms, together with the different wear modes acting on the wheel, highlight the challenges of heat control in grinding and justify the development of innovative strategies, such as wheel texturing, to improve efficiency and reliability.

2.2 Textured Grinding Wheels

Among the solutions proposed to overcome these limitations, textured grinding wheels have emerged as one of the most promising approaches. By incorporating grooves, slots or other patterns, these tools enhance coolant transport, facilitate chip removal and reduce grinding forces, making them especially effective for difficult-to-machine materials such as ceramic matrix composites [73], hard-brittle materials [74] and carbon fiber reinforced polymers [75]. Grooved wheels are applicable to a broader range of material removal operations. They not only enhance grinding performance relative to conventional wheels but also enable the controlled generation of structured surfaces [76].

The development of grooved wheels dates back to the twentieth century, with several patents describing slotted, textured or grooved wheels [77–79]. Academic research intensified in the 1970s, when helical grooves were produced using crushing roll dressing tools [80]. Since then, different methodologies have been proposed; traditional approaches such as crushing roll dressing and prefabricated grooves remain in use, but recent advances include laser machining, CNC-controlled single-point diamond dressing and additive manufacturing techniques such as Selective Laser Sintering (SLS).

According to Li *et al.* [81], textured wheels are characterized by the presence of specially designed active and passive zones on their working surface. The passive zones do not engage the workpiece but serve as reservoirs for cutting fluid and as additional chip storage spaces. By varying the pattern, geometry and scale of these textures, it is possible to improve chip evacuation, enhance cooling efficiency and reduce both grinding forces and surface damage [82].

The literature uses different terms for grooved wheels, such as intermittent, structured, segmented, textured or patterned grinding wheels. All describe tools with grooves or slots that create intermittent contact between the wheel and the workpiece [81].

2.2.1 Texturing Methods of Abrasive Grinding Wheels

A systematic review was conducted to identify the methods used to produce grooves in abrasive grinding wheels since 2010 and to determine the main advantages and limitations of each approach.

To obtain this information, an electronic search was performed in the ScienceDirect, Scopus and Web of Science databases up to July 2022, following the recommendations of the PRISMA Statement [83]. The search strategy considered studies involving textured abrasive grinding wheels that reported the grooving method and geometry. A broad set of keywords was applied, including "Textured abrasive tool", "Textured grinding wheel", "Grooved grinding wheel", "Segmented grinding wheel", "Patterned grinding wheel", "Structured grinding wheel", "Engineered grinding wheel", Texture AND "grinding wheel", Groove AND "grinding wheel" and Channel AND "grinding wheel". In addition, the authors' personal database was consulted to include other works not retrieved by the keyword search.

After removing duplicates, titles and abstracts were screened and decontextualized articles were excluded. When relevance could not be established from the abstract, the full text was retrieved. The following exclusion criteria were applied: (1) publications before 2010, (2) review articles, systematic reviews, meta-analyses, book chapters, conference papers, patents or reports, (3) studies not written in English, (4) studies not focused on tool texturing, (5) studies in which the grooving method was not clearly identified and (6) studies in which the textured tool was not a grinding wheel.

The database search, last updated on July 18, 2022, yielded 205 records from ScienceDirect, 486 from Scopus and 44 from Web of Science. An additional seven records were included from the authors' database. After removing 170 duplicates, 79 studies published before 2010, 175 works that were not research articles and 25 non-English studies, a total of 293 records were screened. Titles and abstracts were analyzed and 156 were excluded due to lack of relevance. Consequently, 137 articles were selected for full-text review. After further assessment, 57 studies were excluded based on criteria 4, 5 and 6, leaving 80 articles for evaluation in the present systematic review. The selection process is summarized in Figure 2.2.

Of the studies included in the review, 27 involved abrasive grinding wheels with machined grooves, 24 with engineered grooves, 18 with laser-produced grooves, 5 with grooves obtained by additive manufacturing (3D printed), 3 with abrasive waterjet grooves and 3 with segmented grooves. The distribution of works according to the grooving method and the year of publication is presented in Figure 2.3 and Figure 2.4, respectively.

From Figure 2.4, the number of publications on texturing methods for abrasive grinding wheels increased significantly between 2016 and 2019. Machined grooves accounted for the largest number of publications in this period. However, since 2019 there has been a clear shift toward less conventional methods such as laser processing, additive manufacturing and engineered grooves. In these latter cases, many of the publications report numerical simulations and analytical or mathematical models.

After this selection process, the reviewed studies were grouped by grooving method. The quantitative distribution is first presented, followed by a detailed description of each approach.

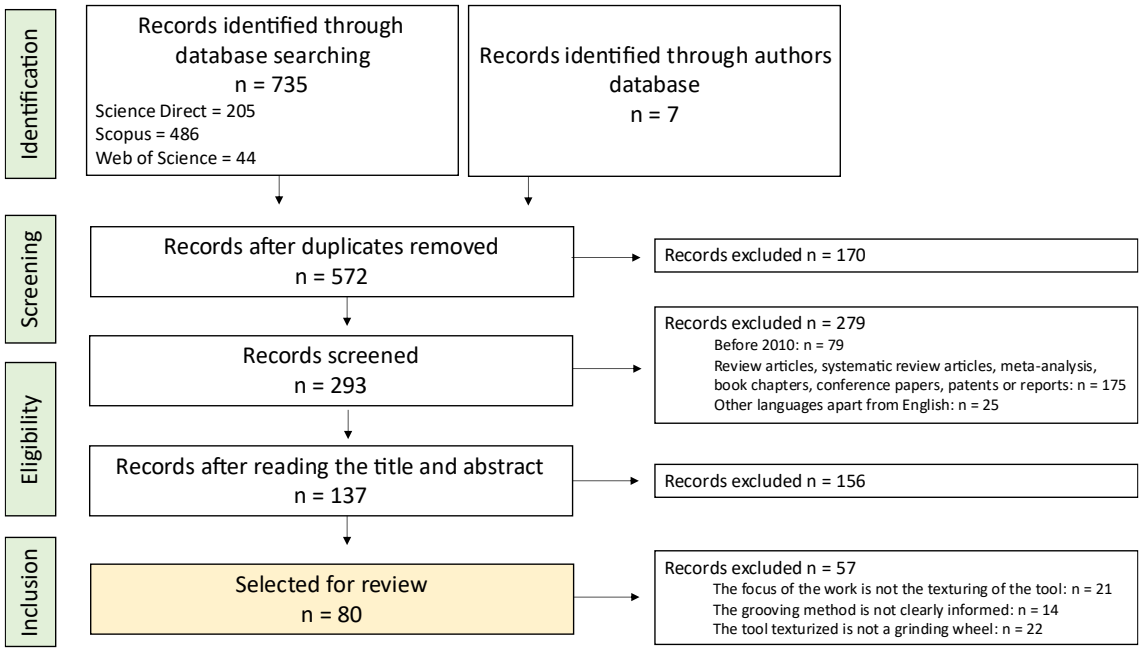


Figure 2.2 – PRISMA flow diagram of the study selection process.

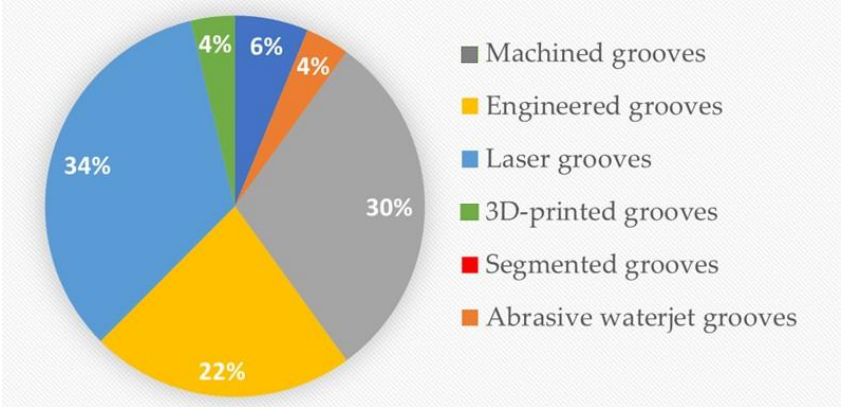


Figure 2.3 – Distribution of works by the processing method of the grooves.

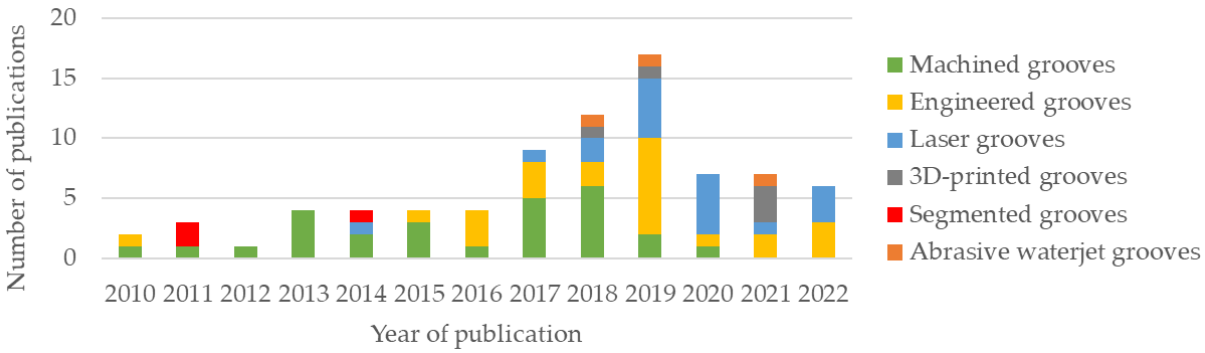


Figure 2.4 – Distributions of works by groove processing method.

Machined Grooves

Machined grooves are obtained by machining a conventional grinding wheel with another tool, such as a diamond disc, a milling cutter or single- or multi-point tools. The machining tool can be controlled manually, by an electromagnetic shaker or by a servomotor. In other cases, the machining tool is static and the grinding wheel movement is controlled.

The principle of the method is illustrated in Figure 2.5, where a single-point diamond dressing tool is used to generate a helical groove on the working surface of the grinding wheel, with groove depth denoted as a_g and groove width b_g [84].

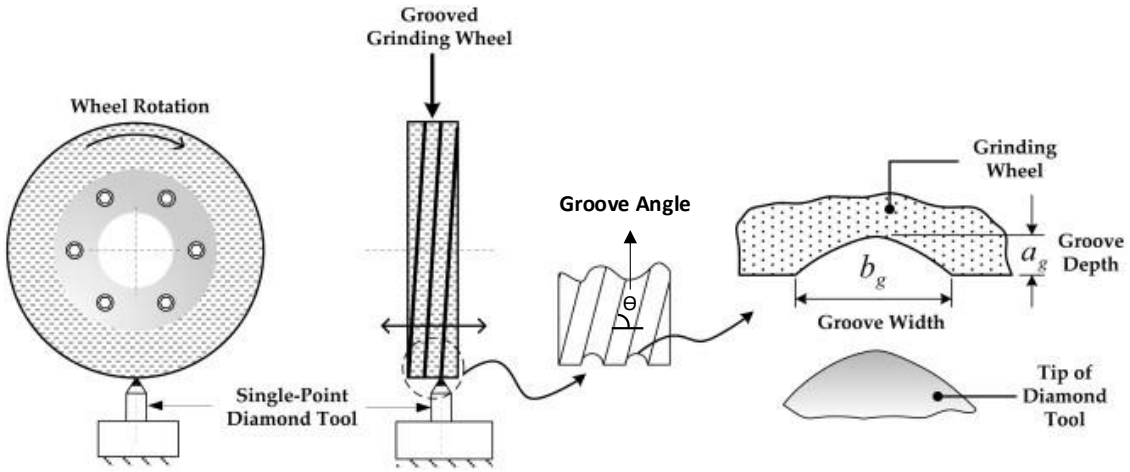


Figure 2.5 – Principle of machined grooves and groove geometry [84].

Table 2.1 summarizes the main focus of each publication on machined grooves, while Table 2.2 presents the groove geometries investigated and the type of tool employed for their production.

Table 2.1 – Summary of publications with machined grooves.

Author and year	Summary
Oliveira *et al.* (2010) [92]	Texturing method using an electro-mechanical exciter coupled to a dressing tool
Gavas *et al.* (2011) [93]	Influence of grooves and work material on surface roughness
Tawakoli *et al.* (2012) [94]	Dry and wet grinding with wheels of 25, 50 and 100 % active area
Aurich *et al.* (2013) [95]	Comparison of wheels with internal channels, with/without channels and external lubrication
Mohamed *et al.* (2013) [84]	Circumferential grooves with different active areas (50, 70 and 100 %) produced by single-point diamond tool
Nadolny (2013) [96]	Device for producing controlled macro- and micro-discontinuities
Silva *et al.* (2013) [97]	Dimensional evaluation of textures produced by Oliveira's method
Köklü *et al.* (2014) [98]	Effect of groove angle on surface quality and residual stress
Mohamed *et al.* (2014) [99]	System capable of grooving and re-grooving grinding wheels
Gavas *et al.* (2015) [100]	Influence of helically angled grooves on roughness and roundness
Denkena *et al.* (2015)a [101]	Introduction of a fly-cutting based structuring method
Denkena *et al.* (2015)b [102]	Patterning with diamond tools mounted on conventional dressing spindle
Wójcik *et al.* (2017) [103]	Effect of wheel grooves on roughness and residual stresses
Azarhoushang *et al.* (2017) [104]	Dry grinding with grooved wheels at 30, 60 and 75 % passive area
Caydas *et al.* (2017) [105]	Effect of helical grooves, workpiece speed and depth of cut on roughness
Liu *et al.* (2017) [106]	Analytical model of groove texture parameters
Silva *et al.* (2017) [85]	Evaluation of two types of grooved wheels for surface structuring
Mohamed *et al.* (2017) [91]	Use of circumferential grooves to generate parallel ridges on workpieces
Cao *et al.* (2018) [90]	Modeling and validation of grinding wheel texturing parameters

Table 2.1 – Summary of publications with machined grooves (cont.).

Author and year	Summary
Daneshi *et al.* (2018) [107]	Simulation of cylindrical plunge grinding with structured wheels
Silva *et al.* (2018) [88]	Development of a patterning system based on modal vibration analysis
Dewar *et al.* (2018) [108]	Comparison of grooved vs. non-grooved vitrified wheels
Forbrigger *et al.* (2018)a [89]	Robot-assisted grooving with kinematic error compensation
Forbrigger *et al.* (2018)b [109]	Helical grooves in profile wheels and general grooving factor calculation
Denkena *et al.* (2019) [86]	Study of wear behavior of CVD-D (Chemical Vapor Deposition Diamond) inserts in wheel patterning
Patel *et al.* (2019) [110]	Cylindrical plunge grinding with grooved vs. non-grooved wheels to study roughness vs. speed ratio
Riebel *et al.* (2020) [87]	Influence of groove depth and width on grinding performance

From Table 2.1, most studies on the machined groove method focus on evaluating the influence of groove parameters such as angle, size and geometry on grinding performance. In addition, some authors have proposed novel grooving strategies, either by employing different tools to generate the grooves [108,110], or by using dedicated software. Examples include the application of the Finite Element Method (FEM) to obtain the vibration mode shape of the GW during texturing [104] and the development of test geometries designed to compensate for kinematic errors [106]. It is also evident that the use of mathematical models has gained attention in recent years. These models have been applied, for example, to simulate groove profiles both on the grinding wheel and on the corresponding surface generated on the workpiece [101,102].

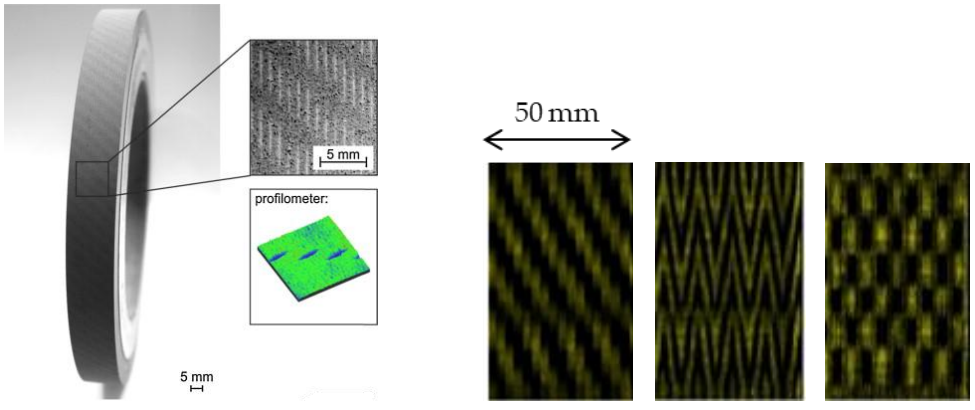
In general, grooves produced by mechanical methods exhibit simple geometries. As shown in Table 2.2 , the most common geometry is the helical type, followed by slits in the form of discontinuous lines. Zigzag and linear cross-shaped grooves, resembling a mesh, have also been reported. Although some authors described these geometries using different terms, this review grouped grooves according to geometric similarity rather than strictly following the terminology adopted in each publication. Representative examples of each geometry are illustrated in Figure 2.6. The reported groove width ranged from a maximum of 5 mm to a minimum of 0.0012 mm, while the depth varied between 5 mm and 0.002 mm.

Table 2.2 – Grooving tool and machined grooves geometries and dimensions.

Author and year	Grooving tool	Groove geometry			
		Form	Angle (deg)	Depth (mm)	Width (mm)
Oliveira *et al.* (2010) [92]	Single-Point	Helically, zigzag and cross linear	-	0.002–0.025	2
Gavas *et al.* (2011) [93]	Disc	Helically	90.52	3	5
Tawakoli *et al.* (2011) [94]	Disc	Helically	90	0.1	0.6
Aurich *et al.* (2013) [95]	Milling cutter	Slits	15	-	-
Mohamed *et al.* (2013) [84]	Single-Point	Helically	-	0.1	0.5–1.08
Nadolny (2013) [96]	Single-Point	Helically	-	0.5	1.7
Silva *et al.* (2013) [97]	Single-Point	Slits	-	0.005	1.5
Köklü (2014) [98]	Disc	Helically	15; 30; 45	3	2.6
Mohamed *et al.* (2014) [99]	Multiple-point	Helically		0.1–0.36	0.92– 1.60
Gavas *et al.* (2015) [100]	Disc	Helically	15; 30; 46	3	2.6
Denkena *et al.* (2015)a [101]	Multiple-point	Slits	-	0.020–0.2	0.2–0.5
Denkena *et al.* (2015)b [102]	Single-Point and Multiple-point	Slits	-	0.020–0.1	0.2–0.5
Wójcik *et al.* (2017) [103]	Disc	Helically	15	4	3
Azarhoushang *et al.* (2017) [104]	Disc	Helically	-	0.0058–0.0135	0.2640–0.353
Caydas *et al.* (2017) [105]	Disc	Helically	45	3	3
Liu *et al.* (2017) [106]	Single-Point	Helically	5.16	1.55	0.1

Table 2.2 – Grooving tool and machined grooves geometries and dimensions (cont.).

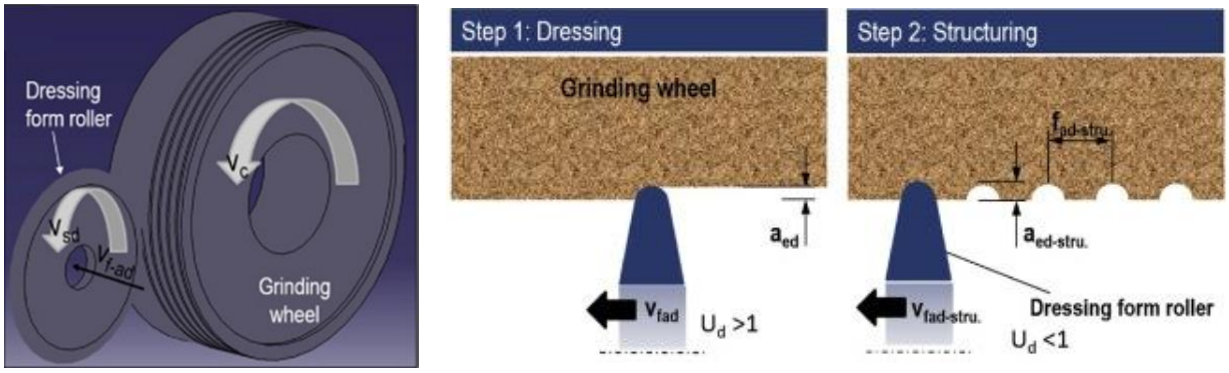
Author and year	Grooving tool	Groove geometry			
		Form	Angle (deg)	Depth (mm)	Width (mm)
Silva *et al.* (2017) [85]	Single-Point	Slits and zigzag	-	0.005	0.587–10.35
Mohamed *et al.* (2017) [91]	Single-Point	Helically	10 - 90	0.005–0.025	5
Cao *et al.* (2018) [90]	Multiple-point	Helically	-	0.02–0.05	0.12
Daneshi *et al.* (2018) [107]	Disc	Helically	-	0.0135	0.353
Silva *et al.* (2018) [88]	Disc	Slits	-	0.005	0.0012–0.006
Dewar *et al.* (2018) [108]	Single-Point	Helically	90	0.102	0.884
Forbrigger *et al.* (2018)a [89]	Single-Point	Helically	-	5	5
Forbrigger *et al.* (2018)b [109]	Single-Point	Helically	89.8	0.1–0.2	0.96–0.99
Denkena *et al.* (2019) [86]	CVD-D insert	Slits	-	-	0.156–0.488
Patel *et al.* (2019) [110]	Single-Point	Helically	-	0.102	1.15



a) b) c) d)

Figure 2.6 – Machined grooves in (a) slit form [101], (b) helical form, (c) zigzag form and (d) cross linear form [92].

Table 2.2 also shows that the most frequently used tools for grooving are single-point tools and cutting discs. All grooves produced with cutting discs present a helical geometry, except for the work of Silva *et al.* [88], who generated slit-shaped grooves on the grinding wheel surface. Figure 2.7a illustrates the structuring of a grinding wheel using a cutting disc (dressing form roller) [107]. The desired structures are created by setting specific dressing kinematic parameters, including dresser shape, dressing depth of cut (a_{ed}) and dressing feed (f_{ad}). As shown in Figure 2.7b, the wheel is first flattened under conventional dressing conditions (step 1). The target structure is then produced by dressing with an overlap ratio lower than one (Ud < 1) on the flattened surface (step 2).



a) b)

Figure 2.7 – Schematic of structuring the grinding wheel (a) flattening of the grinding wheel by common dressing which is followed by special conditioning to produce macro structures on the wheel surface (b) [107].

A cutting disc does not provide the accuracy and flexibility required for producing complex grooves. With a single-point diamond tool, it is possible to generate more detailed geometries such as zigzag patterns. Grooves produced with diamond tools, whether single- or multi-point, typically exhibit a conical profile determined by the tip of the grooving tool, as shown in Figure 2.5. However, to study groove width and depth independently, it is necessary to create grooves where width does not vary with depth. For this purpose, Riebel *et al.* [87] used a modified polycrystalline diamond tool to obtain a rectangular groove profile. These tools are composed of diamond grits embedded in a metallic matrix. The original tool had a cylindrical shape with a diameter of 3.2 mm, while the modified tool had the shape of a rectangular shank with a 1.7 mm edge used to groove the wheel. The deepest grooves reported in that study required more than 200 passes of the cutting tool, which meant that any synchronization error between the tool and the wheel would result in deviations in the final groove geometry [87].

In general, machining remains the most widely used method among researchers, primarily due to its low cost and versatility. However, when performed manually, groove quality is often difficult to control, which has motivated the development of automated processes. While automation improves consistency, it also increases the overall cost of the method. The main drawback of machining is the intensive wear of the grooving tool. Most published works focus on evaluating the influence of groove parameters such as angle, size and geometry on grinding performance. Despite being a simple and conventional method, recent studies have explored new strategies, including the use of software to compensate for kinematic errors and the application of mathematical models to enhance process understanding.

Engineered Grooves

On single-layer grinding wheels (electroplated grinding wheels), instead of removing grains from the surface, grooves can be created by arranging the abrasive grits in a predefined pattern [8]. Grinding wheels with ordered grain distribution are referred to as engineered wheels, where the groove depth corresponds to the height of the abrasive particles and the width to the spacing between each grain or agglomerate, as illustrated in Figure 2.8 [50].

Although these wheels demonstrate clear advantages in grinding performance, their fabrication is challenging when fine grains are used. In such cases, the abrasive particles must be positioned either manually or with templates, which makes the process highly dependent on particle size and significantly increases manufacturing complexity [51].

The main focus of each publication on engineered grinding wheels is summarized in Table 2.3 and the groove geometries investigated are presented in Table 2.4.

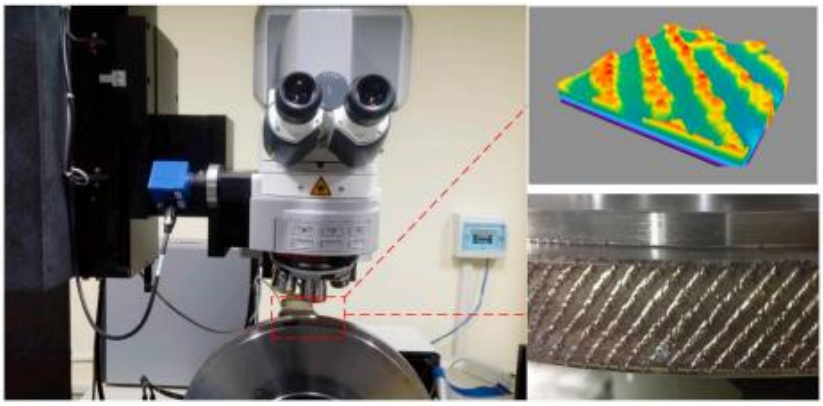


Figure 2.8 – Topography of a monolayer abrasive grinding wheel with an arrangement pattern [111].

Table 2.3 – Summary of publications with engineered grooves.

Author and year	Summary
Yuan *et al.* (2010) [115]	Electroplated wheel with controlled abrasive clusters tested on carbon/epoxy composites
Wang *et al.* (2015) [114]	Kinematic, elastic and plastic models of engineered wheels; simulation of surface topography
Yu *et al.* (2016)a [112]	Model of cutting point density using abrasive phyllotactic pattern
Yu *et al.* (2016)b [113]	Surface roughness model validated with phyllotactic vs. random grain
Yu *et al.* (2016)c [116]	Wear study comparing random vs. bio-inspired phyllotactic wheels
Zhang *et al.* (2017) [117]	Spiral fiber tool; fluid flow simulated and validated by cutting tests
Ding *et al.* (2017) [118]	Model of surface topology for single-layer CBN wheels; wear experiments conducted
Lyu *et al.* (2017) [119]	Mathematical model predicting grinding temperature
Yu *et al.* (2018) [120]	CFD study of grinding fluid behavior in a bionic grinding wheel
Zhang *et al.* (2018) [111]	Topography and kinematic model for undeformed chip thickness
Yu *et al.* (2019)a [121]	Optimization of grain arrangement to reduce grinding temperature
Yu *et al.* (2019)b [122]	Bionic phyllotaxis-inspired surface to reduce grinding energy
Yu *et al.* (2019)c [123]	Bionic phyllotaxis-inspired surface to reduce grinding forces
Zhang *et al.* (2019)a [124]	Integrated model for roughness and energy based on chip thickness distribution
Zhang *et al.* (2019)b [125]	Effects of removal rate, texture and dressing on chip thickness studied experimentally and numerically
Qiu *et al.* (2019) [126]	Resin-bonded wheel with 3D controllable grain arrangement
Zhu *et al.* (2019) [127]	Wear and self-sharpening behavior of helically arranged CBN wheels
Zhang *et al.* (2020) [128]	Patterned single-layer wheels; effects of grit spacing, size and angle in dry grinding
Peng *et al.* (2020) [129]	Internal coolant wheel with abrasive patterns;
Peng *et al.* (2021)a [130]	Internal coolant wheel; CFD analysis of curved channels and thermal field

Table 2.3 – Summary of publications with engineered grooves (cont.).

Author and year	Summary
Peng *et al.* (2021)b [131]	Bionic phyllotaxis cup wheel; CFD study of flow characteristics
Guo *et al.* (2022) [132]	Grinding mechanism and force model of engineered wheels with varied geometries
Wang *et al.* (2022) [133]	Simulation model predicting surface topography in superalloy grinding
Peng *et al.* (2022) [134]	Bowl-type internal cooling wheel with phyllotactic pattern optimized by CFD

Table 2.3 shows that the main objective of studies on engineered grooves is the development of mathematical models and simulations capable of describing the grinding process. These approaches allow a comprehensive analysis of the influence of various parameters, making it possible to investigate material removal mechanisms, grain density and grinding temperature [111–113]. By using simulations, the number of required experiments can be significantly reduced. In contrast, purely experimental methods provide results only at the end of grinding, such as the final surface topography, but cannot capture the material removal mechanisms during the process [114].

Engineered grooves are mainly investigated in wheels with a defined abrasive arrangement in a single layer. Research on wheels with three-dimensional controllable abrasive arrangements is less common. In the work of Qiu *et al.* [126], grinding wheels were designed with different 3D arrangements of abrasive particles and kinematic equations were used to calculate grinding trajectories and assess the effect of grain distribution on surface quality. A stereolithography apparatus based on additive manufacturing technology was developed to produce the wheels and the influence of abrasive distribution on trajectory uniformity was evaluated through experiments and simulations.

From Table 2.4, the most frequently studied geometry is the phyllotactic pattern. Phyllotaxis is an arrangement found in leaves, fruits and other plant structures [135]. Typical examples are shown in Figure 2.9 [120]. Although the phyllotactic theory has been known for more than a century, it has been revisited in recent years due to its potential technological applications. In nature, such arrangements help plants resist wind loads and facilitate the flow of wind and rain between leaves. The same principle is considered advantageous for grinding wheels, where ordered gaps between grains can improve coolant access and reduce forces. Consequently, most studies adopting this concept rely on simulations and mathematical modeling to define geometry accurately and quantify its potential benefits.

Table 2.4 – Engineered grooves geometries and dimensions.

Author and year	Groove geometry		
	Form	**Grain size (mesh)**	**Width (mm)**
Yuan *et al.* (2010) [115]	Phyllotaxis	-	1.7
Wang *et al.* (2015) [114]	Rectangular	80	0.98
Yu *et al.* (2016)a [112]	Phyllotaxis	-	0.29–0.39
Yu *et al.* (2016)b [113]	Phyllotaxis	70/80	0.87–1.21
Yu *et al.* (2016)c [116]	Phyllotaxis	70/80	0.87–1.21
Zhang *et al.* (2017) [117]	Helically	-	1.6–2.9
Ding *et al.* (2017) [118]	Helically	80/100	1.2
Lyu *et al.* (2017) [119]	Phyllotaxis	70/80	0.87–1.21
Yu *et al.* (2018) [120]	Phyllotaxis	-	0.88–1.21
Zhang *et al.* (2018) [111]	Helically	40/50	2.5
Yu *et al.* (2019)a [121]	Phyllotaxis	40/50	0.75–1.06
Yu *et al.* (2019)b [122]	Phyllotaxis	40/50	0.75–1.06
Yu *et al.* (2019)c [123]	Phyllotaxis	40/50	0.75–1.06
Zhang *et al.* (2019)a [124]	Helically	40/50	1.2–2.4
Zhang *et al.* (2019)b [125]	Helically	40/50	1.2–2.4
Qiu *et al.* (2019) [126]	Rectangular and circular	-	2.0–3
Zhu *et al.* (2019) [127]	Helically	80/100	1.2
Zhang *et al.* (2020) [128]	Rectangular	-	1.0–3
Peng *et al.* (2020) [129]	Helically and rectangular	80	1.5
Peng *et al.* (2021)a [130]	Helically	-	1
Peng *et al.* (2021)b [131]	Phyllotaxis	80	-
Guo *et al.* (2022) [132]	Helically	-	0.5
Wang *et al.* (2022) [133]	Helically	40/45	1.2
Peng *et al.* (2022) [134]	Phyllotaxis	80	-



a) b) c)

Figure 2.9 – Typical examples of phyllotactic pattern (a) keteleeria davidiana, (b) anthurium, (c) pinecone [120].

Abrasive wheels with an internal cooling system have been widely investigated in the last decade, as illustrated in Figure 2.10a [134]. Through internal channels, the coolant is delivered directly to the grinding zone, reducing fluid waste and minimizing the additional energy consumption caused by the air barrier [130]. To further enhance coolant flow at the wheel–workpiece interface, some authors have combined internal cooling channels with engineered grooves. For example, in Figure 2.10b [134] shows a wheel designed with a sunflower-inspired phyllotactic pattern applied to the abrasive ring.

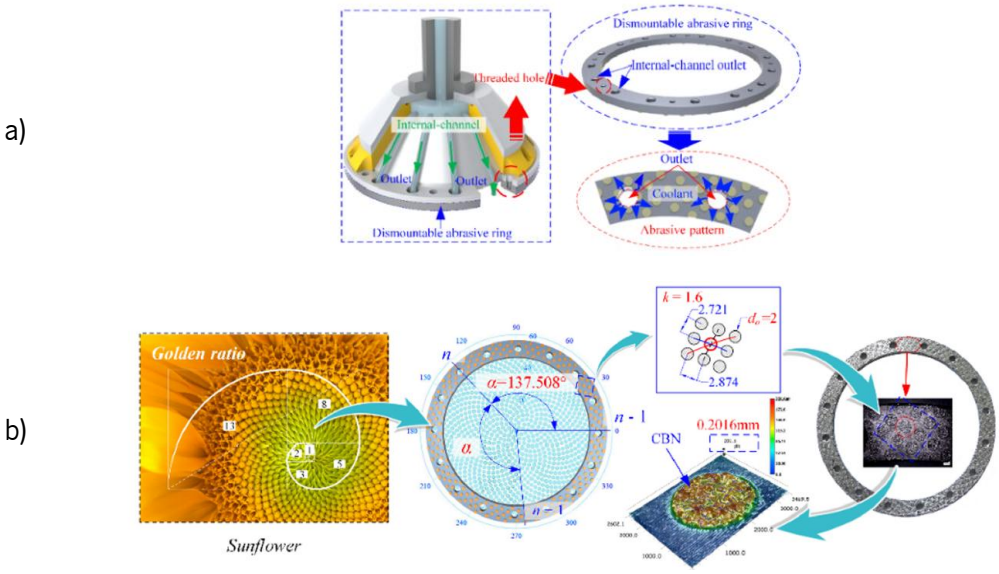


Figure 2.10 – (a) Structure of the internal-cooling grooved grinding wheel and (b) the abrasive ring with the phyllotaxy pattern of the abrasive [134].

Engineered grooves have been extensively studied since 2015, with particular emphasis on simulation and numerical modeling of abrasive particle arrangements aimed at optimizing groove geometries. Grinding wheels with three-dimensional controllable abrasive distributions represent a promising but still largely unexplored field, with only one publication reporting this approach to date. The main limitation of the method remains the long fabrication time, as the abrasive grains are often positioned individually.

Laser Grooves

Laser conditioning is an unconventional, non-contact method that can be applied to all types of abrasives and bonding systems [136]. In laser-based thermal methods, a high-energy density laser beam is directed onto the tool surface to remove material from selected regions by melting, heating, vaporization, plasma formation or ablation of abrasive grits and bond [137,138]. A typical experimental setup for laser structuring is shown in Figure 2.11 [139].

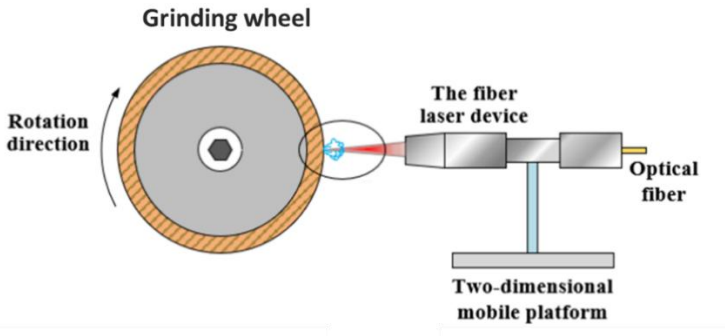
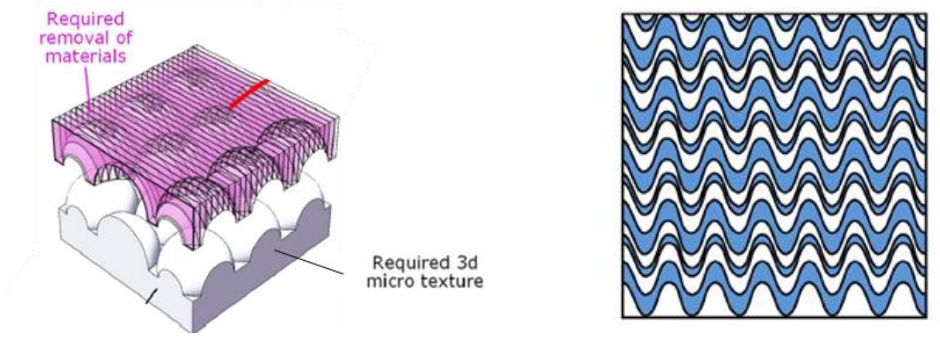


Figure 2.11 – Experimental setup for laser structuring [139].

The focus of each publication on laser grooves is summarized in Table 2.5, while the corresponding groove geometries and dimensions are presented in Table 2.6.

From Table 2.5, most publications on the laser method focus on evaluating the influence of groove parameters during grinding. The data presented in Table 2.6 complement this observation by showing the wide variety of geometries that can be produced. With the laser technique, both macro- and micro-textures can be generated, ranging from simple geometries such as helically shaped grooves to more complex forms such as wave patterns and hemispheres, as illustrated in Figure 2.12 [138,144].



a) b)

Figure 2.12 – Groove geometries produced by laser method with the shape of (a) hemispheres and (b) waves [138,144].

Table 2.5 – Summary of publications with laser grooves.

Author and year	Summary
Guo *et al.* (2014) [140]	Influence of laser parameters (power, focal shift, speed, passes) on micro-structured surfaces
Deng *et al.* (2017) [141]	Effect of groove angle and geometry on workpiece surface quality
Zhang *et al.* (2018) [142]	Evaluation of six groove geometries on grinding performance and wear
Guo *et al.* (2018) [143]	Effect of micro-grooves combined with grain refinement on CVD diamond wheels
Zhang *et al.* (2019)a [144]	Macro–micro patterns generated by laser; grinding force model developed and validated
Zhang *et al.* (2019)b [145]	Evaluation of five groove geometries; influence of process parameters on grinding forces
Wu *et al.* (2019) [146]	Laser grooves transferred onto surfaces of hard and brittle materials
Azarhoushang *et al.* (2019) [147]	Grinding of ceramic matrix composites using laser-structured vs. segmented wheels
Deng *et al.* (2019) [148]	Evaluation of groove geometry, structuring efficiency and grain exposure in coarse diamond wheels
Li *et al.* (2020)a [149]	Comparison of inclined vs. rectangular cross-section grooves in grinding
Li *et al.* (2020)b [150]	Effect of laser beam parameters on groove generation
Wu *et al.* (2020) [151]	Pulsed laser used to ablate microtextures directly on diamond grains
Zhang *et al.* (2020) [152]	Biomimetic fractal-branched wheel design based on leaf veins; tested against conventional wheels
Zhao *et al.* (2020) [153]	Computer-Aided Design / Computer-Aided Manufacturing (CAD/CAM)-assisted laser cladding for manufacturing textured CBN/CuSnTi wheels
Li *et al.* (2021) [138]	Effect of laser passes and scanning speed on groove geometry
Monier *et al.* (2022) [154]	Simulation of groove patterns; only one produced and tested
Hou *et al.* (2022) [155]	Ultrafast laser system developed to fabricate grooves with optimized scanning strategies
Geng *et al.* (2022) [156]	Complete conditioning chain (truing, dressing, texturing) of diamond wheels using a single laser source

Table 2.6 – Laser grooves geometries and dimensions.

Author and year	Groove Geometry			
	Form	**Angle (deg)**	**Depth (mm)**	**Width (mm)**
Guo *et al.* (2014) [140]	Helically	-	-	Max. 0.016
Deng *et al.* (2017) [141]	"V" and "W" shape	0, 30, 60 and 90	0.0382	0.0753
Zhang *et al.* (2018) [142]	Helically, cross linear, zigzag and "U" shape	0, 30, 45 and 90	0.85	1.2
Guo *et al.* (2018) [143]	Helically	-	0.008	Max. 0.006
Zhang *et al.* (2019)a [144]	Cross linear, waves and zig zag	30, 45 and 90	0.85	1.2
Zhang *et al.* (2019)b [145]	Helically, cross linear, zigzag and waves	0, 30 and 45	0.75	0.9
Wu *et al.* (2019) [146]	Helically	4.52	0.102	0.187
Azarhoushang *et al.* (2019) [147]	Slots (segmented grooves) and cross linear (laser grooves)	-	0.35	0.85
Deng *et al.* (2019) [148]	"V" and "W" shape	-	0.02–0.07	0.003–37
Li *et al.* (2020)a [149]	Helically	-	0.95 and 1	0.65
Li *et al.* (2020)b [150]	Helically, parallelogram, hexagonal, triangular and rectangular	60 and 90	0.3–1	0.8–1.8
Wu *et al.* (2020) [151]	Cross linear with/without holes	-	0.15–0.2	0.02–0.05
Zhang *et al.* (2020) [152]	Leaf vein	-	1	3
Zhao *et al.* (2020) [153]	Helically, zigzag and "U"	-	-	-
Li *et al.* (2021) [138]	In "V" and hemispheres	-	0.4–4	0.18–0.3
Monier *et al.* (2022) [154]	Slots	-	-	0.19–0.33
Hou *et al.* (2022) [155]	Lines with "U" shape	-	1	1
Geng *et al.* (2022) [156]	Helically and cross linear	-	0.08–0.25	0.2–0.35

Some studies provided a comprehensive analysis of groove parameters. Zhang *et al.* [142] produced six structured grinding wheels and carried out tests at different wheel speeds and depths of cut under constant feed rates to evaluate their influence on grinding performance. Grinding forces were compared and the effects of wheel speed, depth of cut and feed rate were analyzed. In addition, wheel wear and surface roughness were assessed under the different conditions. In another study, Zhang *et al.* [145] produced five different textures (Figure 2.13) and extended the analysis to include grinding temperatures, along with forces and roughness. Monier *et al.* [154] developed a simulation approach to represent textured wheels and corresponding structured surfaces under different operating conditions. Regular and irregular geometries were investigated by varying spacing, angle and segment dimensions, although grinding tests were conducted only for a single-slot geometry.

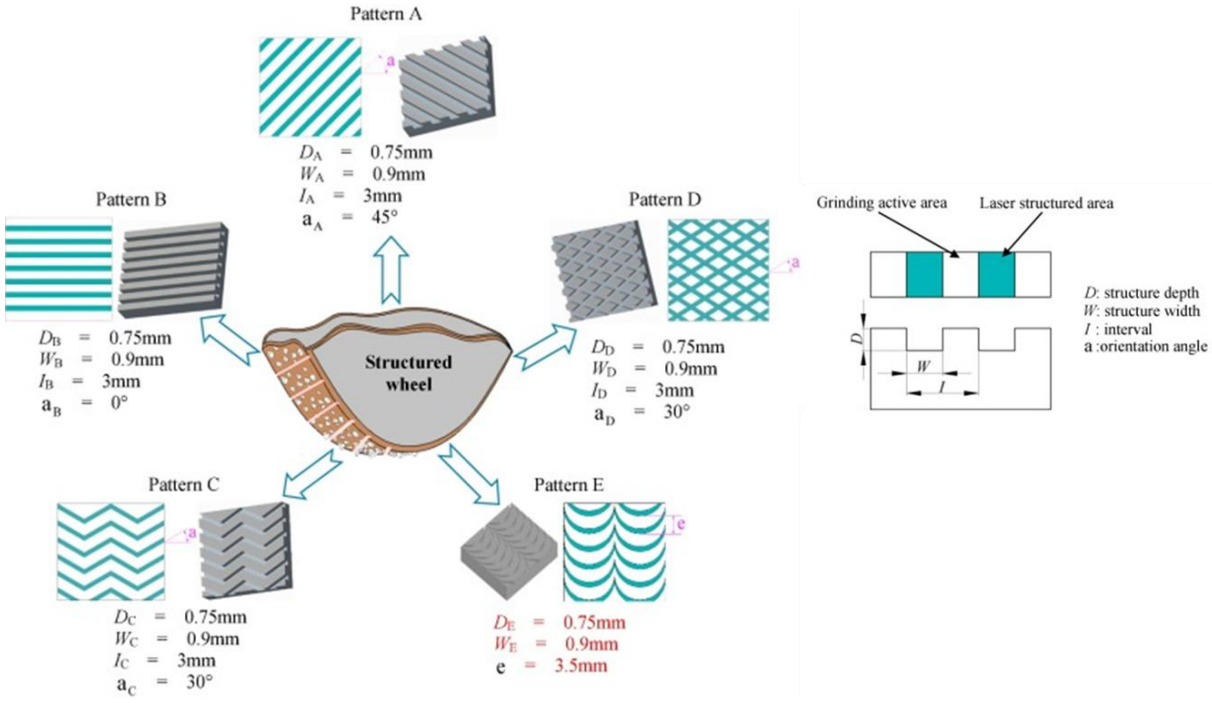


Figure 2.13 – Different laser groove patterns discussed by Zhang *et al.* [145].

More recently innovations have also been reported. Hou *et al.* [155] proposed an alternating laser scanning strategy with staggered forward and backward traces to reduce the incubation effect of adjacent scans and evaluated the ablation effects of an ultrafast laser on groove morphology. Geng *et al.* [156] integrated a nanosecond pulse laser into an ultra-precision machine tool to perform in-line conditioning of superabrasive wheels, including truing, dressing and texturing. An offset compensation method was introduced to account for focus-depth shifts and to generate accurate groove profiles.

Potential challenges remain, such as the adjustment of texturing parameters, high energy consumption and the risk of thermal damage [81]. To address these issues, Li *et al.* [150] investigated the effect of continuous-wave CO_2 laser parameters on the generation of five different textures in diamond abrasive tools. This study emphasized the importance of proper parameter selection and is particularly notable for employing a continuous-wave rather than a pulsed laser, as shown in Figure 2.14.

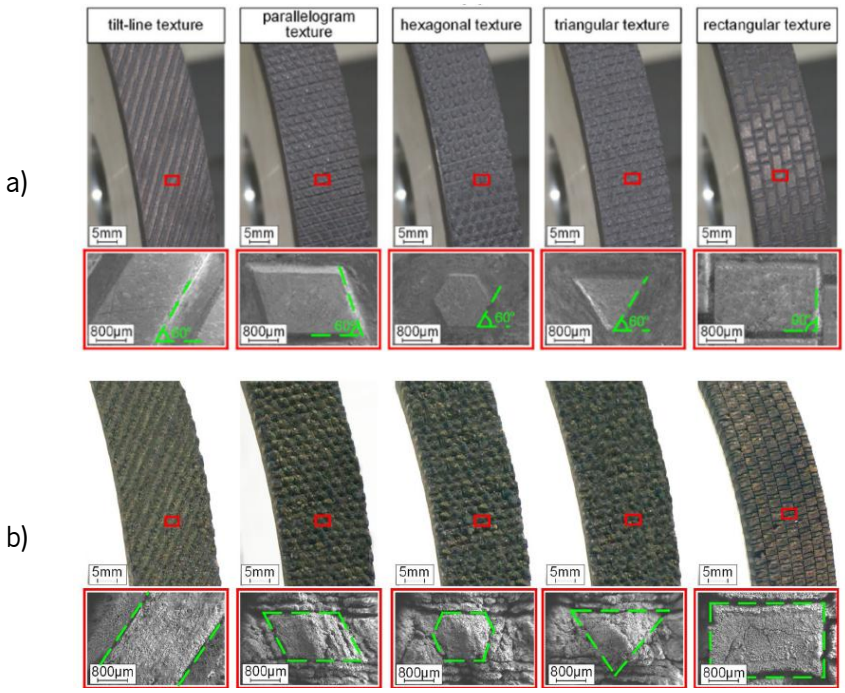


Figure 2.14 – Texture appearance obtained using (a) appropriate and (b) inappropriate parameters [150].

The main advantages of the laser method are the absence of tool wear, high repeatability and controllability, good precision and relatively short processing time. It also enables the production of microscale textures with complex geometries. However, its limitations include the need for fine adjustment of laser parameters, high energy consumption and elevated equipment and maintenance costs.

Additive manufacturing

The development of additive manufacturing technologies has introduced a novel approach for fabricating grinding wheels with complex porous structures. Except for the work of Qiu *et al.* [126], who produced a multi-layer engineered abrasive wheel, additive manufacturing is the only method that enables grooves to be integrated directly into the wheel volume during fabrication, eliminating the need to reapply textures after wear.

Textured grinding wheels produced by this method can be obtained through different techniques. Laser-assisted additive manufacturing uses a high-power laser beam to sinter or fuse material in successive layers, while Direct Ink Writing (DIW) is an extrusion-based, heat-free process in which a ceramic ink is deposited through a nozzle to form the desired structure [157]. Table 2.7 summarizes the studies conducted in this field and Table 2.8 details the groove geometries and the additive manufacturing techniques applied.

Table 2.7 – Summary of publications with 3D-printed grooves.

Author and year	Summary
Tian *et al.* (2018) [158]	Porous metal-bonded wheels fabricated by Selective Laser Melting (SLM)
Du *et al.* (2019) [159]	Resin-bond diamond wheels with internal cooling holes produced by SLS
Wang *et al.* (2021) [160]	Four wheels with different groove geometries fabricated by SLM; grinding performance evaluated
Li *et al.* (2021) [161]	Three wheels with different groove geometries fabricated by SLM; focus on design and modeling
Huang *et al.* (2021) [157]	Vitrified wheels with different groove geometries fabricated by DIW

Table 2.8 – 3D-printed method and geometry.

Author and year	Method	Groove geometry	
		Form	Width (mm)
Tian *et al.* (2018) [158]	SLM	Honeycomb and octahedron structure	-
Du *et al.* (2019) [159]	SLS	Holes	1.5 and 2.5
Wang *et al.* (2021) [160]	SLM	Triply periodic minimal surface (TPMS)	-
Li *et al.* (2021) [161]	SLM	TPMS	-
Huang *et al.* (2021) [157]	DIW	Triangle and lattice	4 and 6

The SLM principle adopted by several authors [158,160,161] is illustrated in Figure 2.15 [158] and examples of textured grinding wheels produced are shown in Figure 2.16 [158,161]. The SLM system consists of a powder delivery unit and a laser scanning unit. The laser beam selectively melts layers of AlSi10Mg alloy

powder according to the CAD model and the molten alloy solidifies around the diamond abrasive grains to form the bond of the grinding wheel. The process is carried out in an inert atmosphere and the wheel head is built on top of an aluminum substrate. After fabrication, the wheel head is separated from the substrate by wire electro-discharge machining.

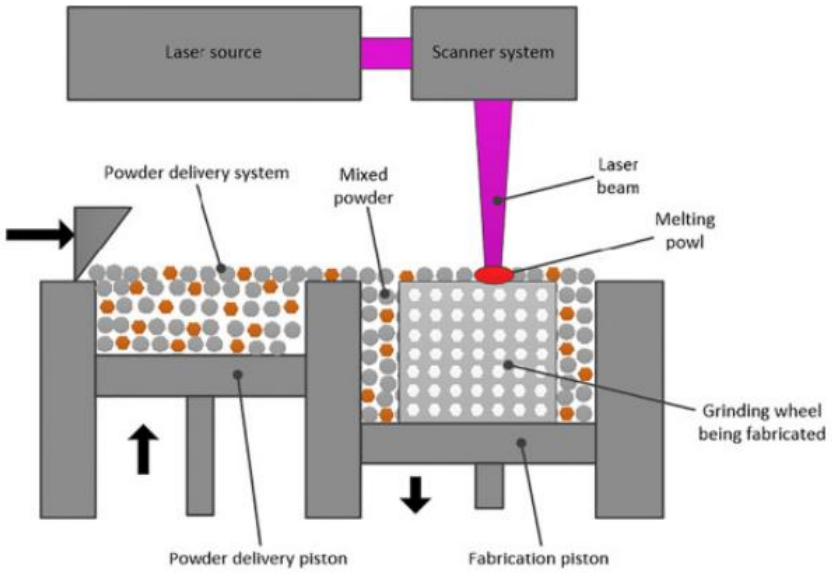


Figure 2.15 – Principle of the SLM process [158].

a)

b)

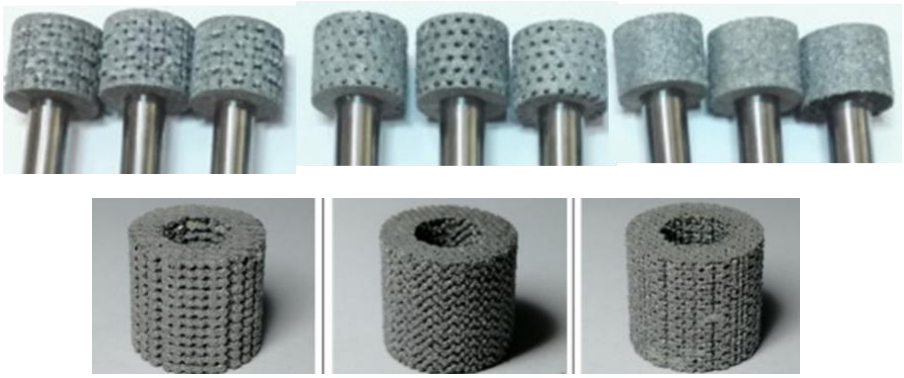


Figure 2.16 – Abrasive wheels structured by the SLM method by (a) Tian *et al.* [158] and (b) Li *et al.* [161].

The main limitation of the SLM method is the risk of diamond grain graphitization due to the high temperatures involved. In addition, because the laser melts the powder layer by layer, some inhomogeneity between the layers may occur [157].

The SLS method proposed by Du *et al.* [159] for manufacturing structured abrasive wheels is also based on a layer-by-layer process. In this case, the grooves are formed from nylon powder that is not scanned and

sintered. After SLS, the untreated nylon powder is removed, leaving the groove shape, as illustrated in Figure 2.17. The authors reported difficulties in producing internally connected holes with diameters smaller than 1.5 mm, since these features tended to clog and prevented the formation of continuous channels.



Figure 2.17 – Abrasive grinding wheel with internal cooling holes produced by SLS method [159].

The manufacturing method proposed by Huang *et al.* [157] and the resulting grinding wheels are shown in Figure 2.18. The DIW process begins with the preparation of a ceramic ink, obtained by dissolving xanthan gum in water and mixing it with vitrified bond powder (n68), polymethyl methacrylate (PMMA, used as pore former) and diamond powder (W10), as illustrated in Figure 2.18a-b. The ink is subsequently extruded using a direct ink writing machine (Figure 2.18c). After sintering in the box furnace and natural furnace cooling, the wheels were obtained as final samples (Figure 2.18d).

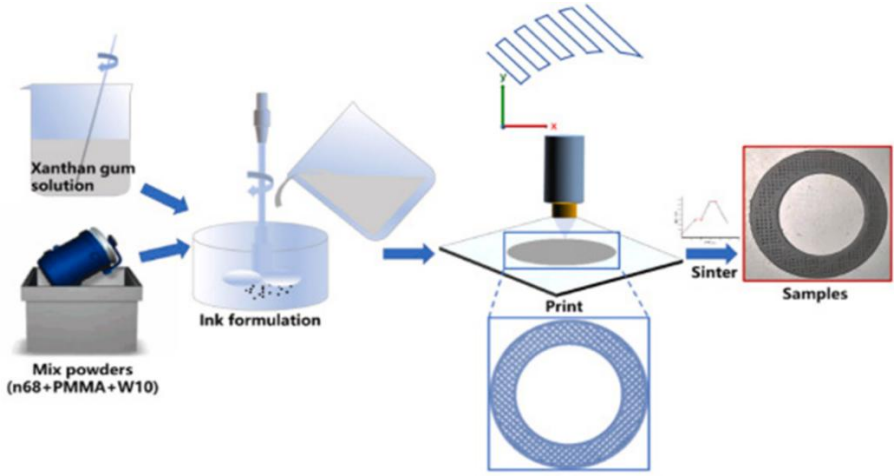


Figure 2.18 – Fabrication of the diamond grinding wheel by DIW [157].

Additive manufacturing offers versatile approaches for producing textured abrasive wheels. Although it requires significant time and resources, this method enables the fabrication of three-dimensional grooves and integrated structures, thereby eliminating the need for reconditioning after tool wear.

Segmented Grooves

Grinding wheels with segmented grooves are produced by incorporating segments into the manufacturing mold. The resulting grooves correspond to the geometry of the inserted segments. Once the grooves are completely worn, this method does not allow their regeneration. An example of a segmented grinding wheel is shown in Figure 2.19 [162]. Table 2.9 summarizes the main topics addressed in published studies on segmented wheels.



Figure 2.19 – A segmented grinding wheel [162].

Table 2.9 – Summary of work with segmented grooves.

Author and year	Summary
Tawakoli *et al.* (2011)a [163]	Segmented wheel designed, fabricated and tested; compared conventional vs. intermittent grinding
Tawakoli *et al.* (2011)b [162]	Feasibility of intermittent grinding with segmented wheels on ceramic matrix composites
Azarhoushang *et al.* (2014) [164]	Wear behavior of segmented vs. non-segmented diamond wheels in high-speed deep grinding of CFR (Carbon Fiber Reinforced) ceramics

From Table 2.9, the studies using this method compare different aspects of grinding performance between segmented and conventional wheels. All works employed the same groove geometry, illustrated in Figure 2.19, with an intermittent ratio of 0.5. However, the authors did not provide detailed information regarding the specific wheel manufacturing procedures used in each study.

Segmented grooves have demonstrated potential benefits in terms of reducing forces and improving grinding performance when compared with conventional wheels. However, the method is limited by the lack of flexibility in groove geometry, as well as by the impossibility of regenerating the structures once they are worn.

Abrasive Waterjet

Abrasive waterjet (AWJ) machining is considered a cold material removal process with high potential for efficient dressing of grinding wheels [165]. As illustrated schematically in Figure 2.20, a high-velocity abrasive waterjet is directed radially onto the grinding wheel surface from the nozzle at a controlled standoff distance [166]. Table 2.10 summarizes the studies conducted in this area and Table 2.11 presents the groove geometries investigated.

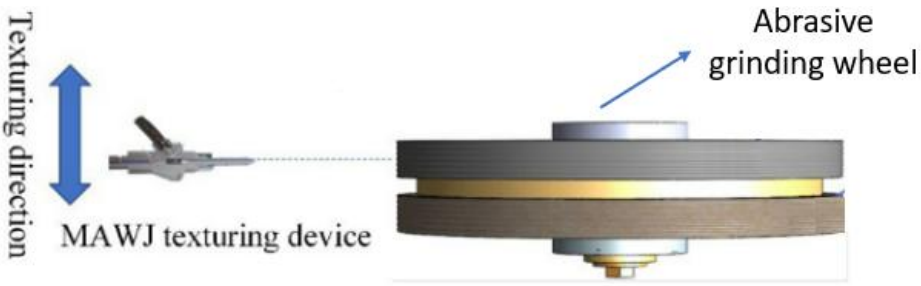


Figure 2.20 – Texturing procedure by Micro-abrasive water jet [166].

Table 2.10 – Summary of publications with grooves produced by AWJ.

Author and year	Summary
Li *et al.* (2018) [167]	Method proposed to design groove geometry based on target operating temperature
Zhang *et al.* (2019) [168]	Prediction of groove depth and width in metal-bonded wheels textured by AWJ
Zhang *et al.* (2021) [169]	Study of AWJ truing mechanisms and integrated rough–fine grinding process

The low dressing precision associated with AWJ micromachining remains a major limitation for its application in the manufacture of precision grooves on grinding wheels [169]. Consequently, the studies summarized in Table 2.10 focus on improving the accuracy of groove production. As shown in Table 2.11, the geometries

reported are relatively simple, although discontinuous angular grooves can also be produced, as illustrated in Figure 2.21 [167].

Table 2.11 – Geometries and dimensions of the grooves produced by AWJ.

Author and year	Groove geometry			
	Form	**Angle (deg)**	**Width (mm)**	**Depth (mm)**
Li *et al.* (2018) [167]	Helically, zigzag and "V"	31.4, 50.5 and 180	1.74 and 1.91	-
Zhang *et al.* (2019) [168]	Helically	90	0.9–1.1	0.6–1
Zhang *et al.* (2021) [169]	Helically	90	1.6	0.5

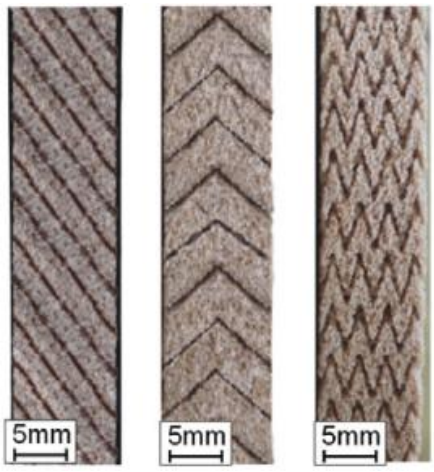


Figure 2.21 – Grooves produced by AWJ method [167].

2.2.2 Recent Advances in Texturing Methods (2022–2025)

In the period after 2022, several innovative approaches have been proposed for the texturing of grinding wheels, complementing the techniques previously reported. These contributions extend the possibilities of tool structuring, either by introducing new manufacturing technologies, by refining the control of traditional methods, or by incorporating concepts of smart and sustainable machining.

Laser texturing advanced considerably in recent years. Beyond the earlier focus on parametric evaluations, new studies have combined experimental validation with detailed modeling. Xie *et al.* [170] investigated CO_2 laser ablation on resin-bond diamond wheels, establishing correlations between laser parameters, ablation

morphology and grinding performance. More recently, Zhang *et al.* [53] applied pulsed laser texturing to brazed diamond wheels with ordered grains, introducing a methodology to assess abrasive grain protrusion consistency through global data acquisition and image processing. This study demonstrated that different laser-induced patterns (0°, 45°, square, rhombic and wave) influence not only grinding forces and surface quality but also the material removal mode in WC/Co, enabling a transition from brittle to ductile regimes under specific pattern conditions. Laser texturing has also been employed to produce bioinspired surface structures, with Wen *et al.* [27] fabricating feather-like grooves on bronze-bonded diamond wheels and Zhang *et al.* [26] introducing shark-fin inspired geometries on diamond wheels. These advances go beyond the pre-2022 literature, which primarily emphasized parameter optimization and simple surface morphologies and demonstrate how laser texturing can directly modulate grain exposure and wear mechanisms.

Additive manufacturing of grinding wheels has recently progressed from proof-of-concept demonstrations to systematic evaluations of bond composition, abrasive concentration and structural design. Barmouz *et al.* [171] fabricated hybrid resin–metal bond SiC grinding wheels using DLP, showing that optimized formulations improved tool life by up to 28 %, profile accuracy and surface finish by 44 %, while the integration of helical grooves reduced cutting forces by as much as 60 %. Wu *et al.* [172] developed diamond grinding wheels with linear cooling channels via dual-filament Fused Deposition Modelling (FDM), demonstrating that suitable diamond parameters enhanced grinding efficiency across brittle materials, with high-concentration coarse grains achieving the best balance between efficiency, self-sharpening and surface quality.

Abrasive water jet dressing has also progressed, with a recent study focusing on the analysis and optimization of AWJ parameters for texturing diamond wheels [173]. Compared with pre-2022 exploratory works, this contribution emphasizes higher precision and improved process stability, addressing one of the main limitations of AWJ as a texturing method.

Another important development is the emergence of self-adaptable or “smart” grinding wheels, exemplified by the sweating-type configuration proposed by Surendran and Sooraj [28]. In this concept, additive manufacturing is used to create an inner core with reservoirs and porous restrictors that release lubricant proportionally to the grinding temperature and wheel speed.

Taken together, these recent works highlight a clear trend towards greater control, functionality and adaptability in grinding wheel texturing. While studies up to 2022 demonstrated the feasibility and benefits of structured tools, the advances from 2022 onwards emphasize integration of Multiphysics modelling, hybrid material systems, parameter optimization and smart lubrication strategies. These developments indicate that

texturing methods are evolving from purely geometric modifications into multifunctional approaches that support intelligent, efficient and sustainable grinding.

2.2.3 General Assessment of Texturing Methods

The literature reports several approaches for producing grooves in abrasive wheels, each with specific advantages and limitations. Machined grooves are the most traditional option, valued for low cost and versatility, but limited by tool wear and relatively simple geometries. Engineered grooves in single-layer electroplated wheels enable ordered grain distributions and complex patterns, though their fabrication is slow and difficult to scale. Laser texturing offers precision, repeatability and flexibility, producing both micro- and macro-textures; recent works even show that pattern design can influence the material removal mode. However, equipment cost and risk of thermal damage remain persistent challenges. Additive manufacturing is unique in integrating internal channels and three-dimensional structures directly into the wheel, although it remains resource-intensive. Segmented wheels provide simple intermittent grinding solutions but cannot be regenerated once worn, while abrasive waterjet machining offers a cold, tool-free process, yet with low precision and limited use. Emerging concepts such as self-adaptable "sweating" wheels point to a new direction of intelligent lubrication control, responsive to process conditions.

Overall, texturing methods are evolving toward more complex geometries, hybrid materials and adaptive cooling strategies. Yet, the controlled fabrication of three-dimensional channel networks remains a major technological challenge, as most current solutions are still restricted to superficial grooves that require retexturing once worn.

2.3 Coolant Application in Surface Grinding

The application of grinding fluids is one of the most established strategies to control grinding temperatures and to preserve machining quality, thereby mitigating the risk of thermal damage and ensuring surface integrity. In addition to their cooling function, these fluids also provide lubrication, assist in chip removal and enhance surface finish, which directly influences both productivity and product quality. As a result, the method of delivering the fluid to the grinding zone has been recognized as a key factor for overall process efficiency [174,175].

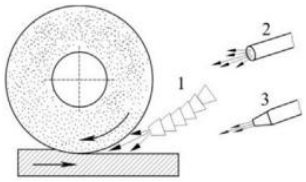
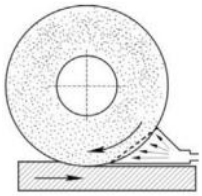
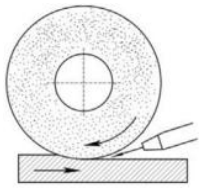
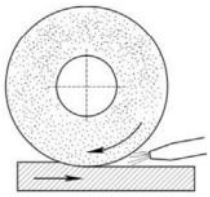
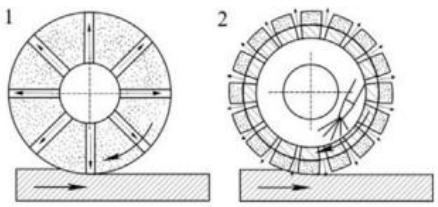
In most industrial applications, grinding fluids consist of oils or oil-based emulsions. While effective, these formulations present significant environmental and economic challenges [176]. Their life cycle typically involves chemical treatment, re-refining, biodegradation and in some cases incineration or purification for reuse. Each disposal or recovery route is associated with high operational costs and potential environmental burdens [177]. The global grinding fluids market reached a volume of 235.19 kilotons in 2022, with a market value projected to rise to USD 889.1 million by 2030, reflecting an annual growth rate of 3.7 % [178]. This highlights not only the scale of consumption but also the economic relevance of these fluids within modern manufacturing. In addition to cost implications, health and environmental concerns are increasingly evident: prolonged exposure may cause dermatological or allergic reactions in operators, while improper disposal can contaminate soil and water resources [179].

Given these drawbacks, a strong technological trend has emerged toward reducing the consumption of grinding fluids, aligning with concepts of green manufacturing, sustainable production and clean machining. In this context, a variety of alternative supply methods have been proposed, aiming to minimize flow rates while maintaining process stability. Table 2.12 summarizes the most representative coolant application strategies currently in use in surface grinding [31,43,179–184].

One possible approach to limit coolant consumption and reduce environmental impact is to enhance fluid penetration into the grinding zone through innovative delivery systems. Among the different concepts reported in the literature, particular attention is given here to the centrifugal grinding fluid provision by channels in the wheel body. This solution relies on the rotation of the wheel to assist fluid transport and direct it toward the active cutting zone. In what follows, the studies that have applied this internal cooling system are presented in chronological order.

The first reported attempt to implement this concept was the development of segmented grinding wheels with controlled radial coolant supply [183]. In this design (Figure 2.22a), a steel rim is fitted with multiple CBN abrasive segments and a pressurized chamber that forces coolant through radial holes between the segments. Assisted by centrifugal action, the fluid reaches the cutting edges directly, promoting localized cooling and cleaning. Grinding tests on AISI 4140 steel confirmed that this configuration reduced grinding forces and specific energy while maintaining lower flow rates. Moreover, the wheel preserved sharp cutting edges, enhanced chip evacuation and minimized clogging, resulting in improved surface integrity characterized by deeper compressive residual stresses and reduced thermally induced tensile stresses.

Table 2.12 – Examples of grinding fluid supply methods in surface grinding processes [31,43,179–184].

Method name	Construction scheme	Description	Typical flow rate
Flooding nozzles		Conventional flooding nozzles: 1 – Flexible segmented hose 2 – Tube 3 – Free jet nozzle	10–100 L/min
Shoe nozzle		Hydrodynamic provision of grinding fluid using nozzles in shape of shoe	5–30 L/min
Spot jet nozzle		Provision of grinding fluid using spot jet nozzle	5–15 L/min
Spray nozzle (MQL)		Provision of a minimal quantity of grinding fluid using spray nozzle	10–100 mL/h
Centrifugal grinding fluid provision by channels in the grinding wheel		Provision of grinding fluid by channels in the GW: 1 – Uniform grinding wheel 2 – GW with a metal body and abrasive segments	0.5–9 L/min

Another concept is the "*sandwich grinding wheel*" with centrifugal coolant provision (Figure 2.22b). The wheel consists of grinding rings separated by dividers containing outlet channels. Coolant is supplied through the

arbor and expelled outward by centrifugal force, precisely reaching the transition between rough and finish grinding regions. Experiments in internal cylindrical grinding of hardened 100Cr6 steel demonstrated that this design enabled a fivefold reduction in coolant flow, from 5.0 to 1.0 L/min, while maintaining grinding power and even improving surface roughness. The configuration also reduced wheel loading and facilitated chip evacuation, combining economic and ecological advantages [184].

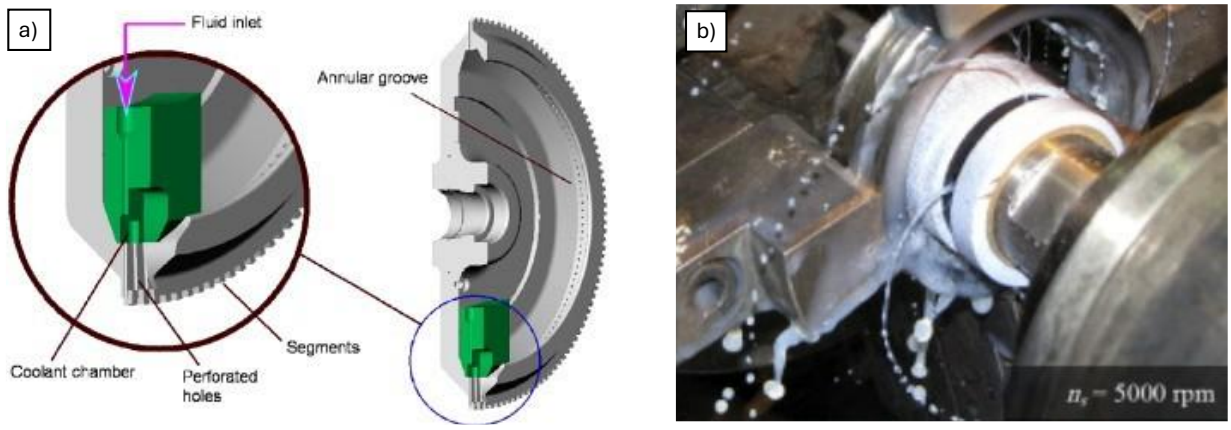


Figure 2.22 – (a) Segmented grinding wheel with controlled radial coolant supply [183]. (b) Sandwich grinding wheel with centrifugal coolant provision [184].

A more advanced concept was introduced by Sieniawski and Nadolny [31,32], known as the zonal centrifugal coolant provision system (Figure 2.23a). Here, the grinding wheel incorporates rows of radial channels formed during pressing by metallic wires, later withdrawn to create continuous holes [30]. Coolant supplied through the arbor is driven outward through the channels by centrifugal force. A movable limiter (Figure 2.23b) allows discharge to be confined to the wheel–workpiece contact region, enhancing efficiency. Grinding wheels with one, two and three layers of radial channels were tested (Figure 2.23c-e).

The results indicated that, in general, the three-layer configuration delivered the best performance, followed by the single-layer wheel and finally the two-layer design [31,32]. In the internal cooling flood mode (fluid discharged through all channels) the surface layer showed improved residual stress condition, grinding forces remained at a similar level and surface roughness slightly worsened, while providing the clear benefit of approximately 90 % reduction in coolant consumption. When the limiter was used to confine discharge to the contact zone, performance improved further, with more favorable residual stresses and tangential force decreases up to 28 %, while roughness remained at a comparable level to flood cooling, while maintaining roughness at a level comparable to conventional flood cooling, also with 90 % lower fluid demand.

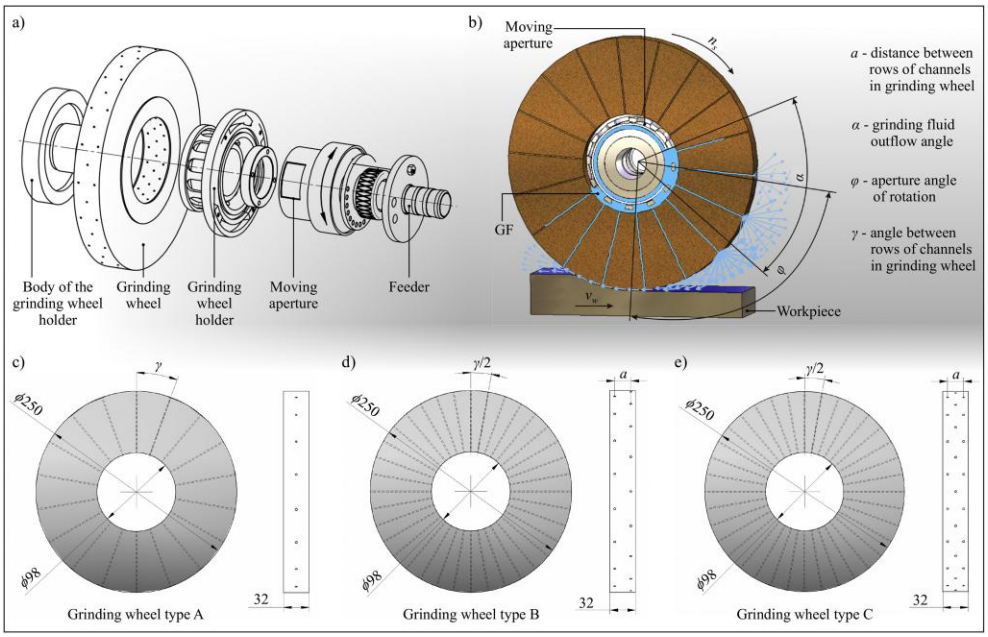


Figure 2.23 – (a) Grinding wheel with radial internal channels. (b) Movable limiter for zonal coolant delivery. (c) One-layer wheel. (d) Three-layer wheel [31].

More recently, Barmouz *et al.* [33] fabricated resin-bonded grinding wheels with internal cooling features using additive manufacturing (DLP). The channels, integrated during printing, included cylindrical and venturi geometries and in some cases additional surface slots (Figure 2.24c–d). Grinding experiments on aluminum alloy demonstrated that all structured wheels reduced grinding forces, improved chip evacuation and decreased tool wear compared to a reference. The venturi-channel design yielded the most pronounced improvements, with up to 45 % reduction in tangential forces and 70 % lower radial wear. Although the study highlighted the flexibility of additive manufacturing, Figure 2.24a–b also shows that the system still required external flood supply at relatively high flow rates (up to 45 L/min), preventing it from being classified as a fully internal lubrication method.

Peng *et al.* [182] proposed a directional internal coolant system for CBN wheels equipped with radial channels (Ø2 mm) and surface slot patterns (Figure 2.25). The design integrated a symmetric collector and flow-blocking ring to guide coolant from the arbor directly toward the grinding zone under centrifugal action. Different surface geometries were tested, including wheels without slots and with parallel, diagonal and V-shaped slot arrangements. The internal directional system reduced grinding temperature by up to 16.9 % at 5 L/min and by nearly 50 % when pressure increased from 0.2 to 0.8 MPa. Surface roughness decreased by up to 14.8 % at 7 L/min and nearly 38 % with higher pressure, while microhardness reductions of 6.1 % (9 L/min) to 16.7 % (higher pressure) were reported. Among the tested patterns, parallel slots provided the

greatest reduction in temperature (22.7 %) and microhardness (7.1 %), whereas diagonal slots were the most effective for lowering surface roughness.

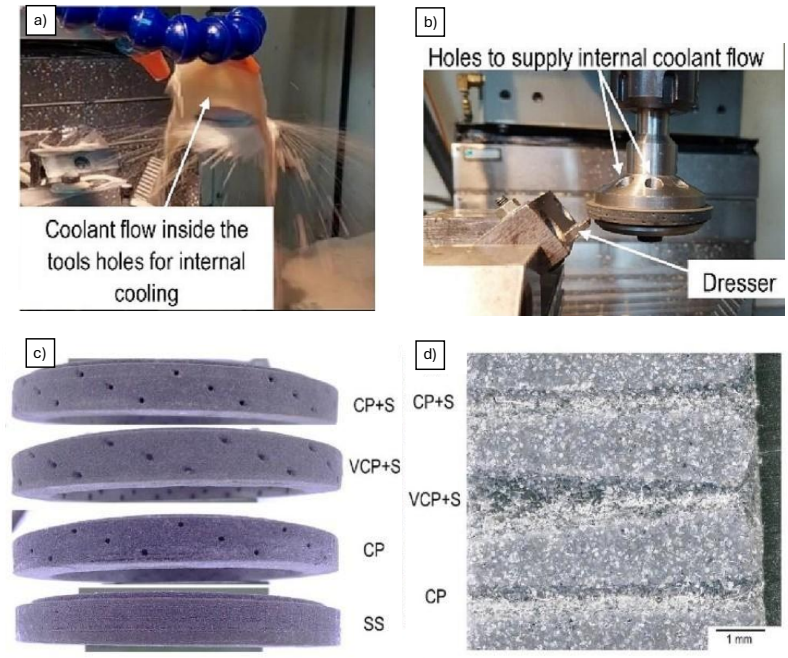


Figure 2.24 – Grinding wheels with internal cooling channels fabricated by additive manufacturing: (a) coolant supply through tool holder, (b) holes for internal flow and c-d) wheel designs (SS, CP, CP+S, VCP+S) [33].

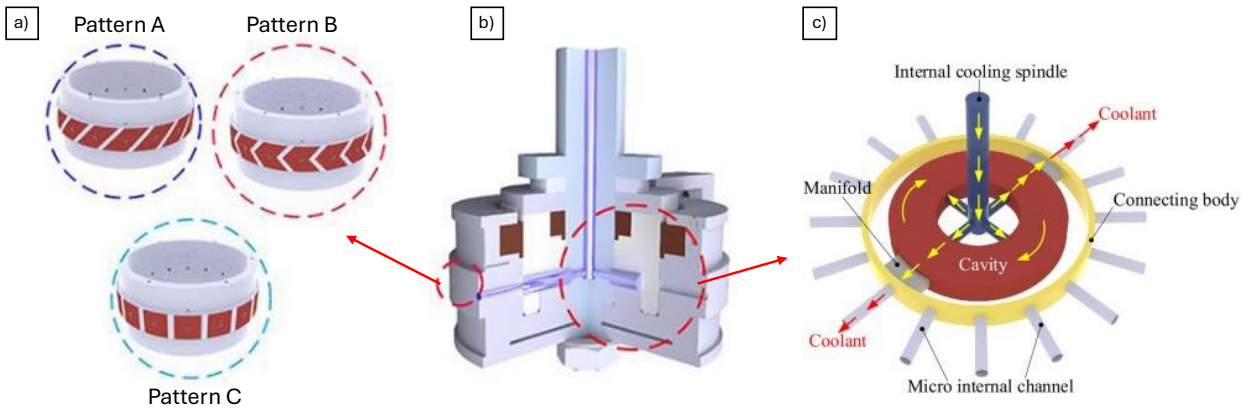


Figure 2.25 – Directional coolant supply system proposed by Peng *et al.* [182]: (a) tested wheel slot patterns, (b) schematic of the internal supply system and (c) detail of the coolant distribution through the manifold and micro-channels.

Table 2.13 summarizes the main grinding parameters and performance results reported in representative studies that applied internal channel concepts to enhance coolant delivery in surface grinding operations. In this table, V_s corresponds to the wheel speed, V_w corresponds to the workpiece feed and a_e corresponds to the depth of cut. It should be noted that Nadolny [184] investigated cylindrical grinding using the lateral

surface of the wheel. In this configuration, the kinematics differ substantially from those of surface grinding, resulting in significantly higher workpiece feed velocities (V_w). This explains the larger values presented in Table 2.13.

Table 2.13 – Representative studies on internally cooled grinding wheels in surface grinding, including main process parameters, channel designs and performance outcomes.

Author / Year	Wheel / Workpiece	Channel geometry	Grinding conditions	Flow rate	Main results
Nguyen & Zhang, 2009 [183]	CBN wheel, Ø 300 mm AISI 4140 steel	Radial 144 holes Ø 2 mm	$V_s = 23\ m/s;$ $V_w = 400\ mm/min;$ $a_e = 10 - 50\ \mu m$	4.8 L/min and 14.5 L/min (external)	↓ F_t up to 30 %; ↓ Specific energy 23.5 %; ↑ Surface roughness
Nadolny, 2015 [184]	Alumina wheel, Ø 35 mm 100Cr6 steel	Radial 4 channels Ø 1.0 mm	$V_s = 60\ m/s;$ $V_w = 45000\ mm/min;$ $a_e = 150\ \mu m$	1–2 L/min vs 5 L/min (external)	↓ Surface roughness ≈ 30 %; ↓ Grinding power 7–11 %
Sieniawski & Nadolny, 2016 [31,32]	Alumina wheel, Ø 250 mm CrV12 steel	Radial 1, 2 and 3 layers (18 channels per layer) Ø 2 mm;	$V_s = 30\ m/s;$ $V_w = 5000 - 20000\ mm/min;$ $a_e = 50\ \mu m$	0.5 L/min vs 5 L/min (external flood)	Internal flood: Improve residual stresses; similar F_t, ↓ Surface roughness. With limiter system: Improve residual stresses; ↓ F_t up to 28 %, Roughness unchanged, but with 90 % fluid saving
Barmouz *et al.*, 2023 [33]	SiC wheel, Ø 62 mm 7075 aluminum alloy	Cylindrical, CP+S, Venturi channels Ø 0.6 mm + slots	$V_s = 30\ m/s;$ $V_w = 600 - 6000\ mm/min;$ $a_e = 10 - 100\ \mu m$	45 L/min	↓ F_t up to 45 %; ↓ Wheel wear up to 70 %; ↓ Surface roughness up to 30 %
Peng *et al.*, 2025 [182]	CBN wheel, Ø 82 mm Inconel 718	Radial 16 channels Ø 2 mm Combined with textures	$V_s = 15\ m/s;$ $V_w = 800\ mm/min;$ $a_e = 20\ \mu m$	3–9 L/min	↓ Temperature up to 50 %; ↓ Surface roughness up to 38 %; ↓ Microhardness up to 16.7 %

As illustrated in Figure 2.26, the design of internal coolant systems has evolved toward increasingly complex geometries. Early approaches were restricted to simple radial holes, while more recent studies explored multi-layer arrangements, additive manufacturing of Venturi-shaped channels and surface slot textures. Despite these advances, most solutions remain limited either by manufacturing constraints or by continued reliance on external flooding.

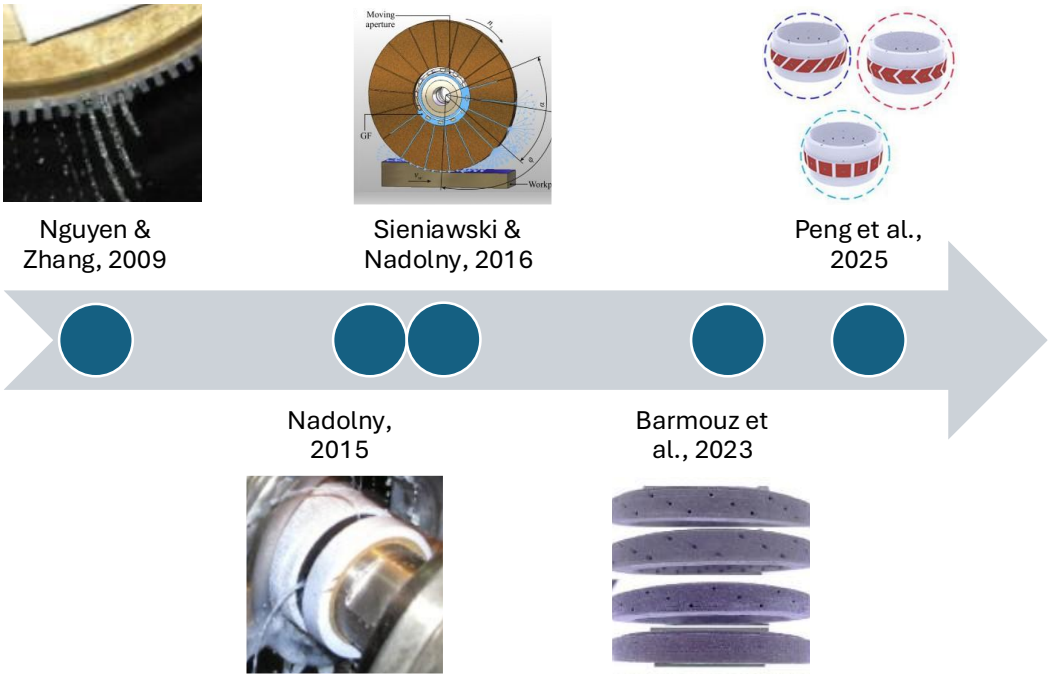


Figure 2.26 – Timeline of representative studies on grinding wheels with internal coolant supply [31–33,182–184].

Among the reviewed works, the zonal centrifugal system proposed by Sieniawski and Nadolny [31,32] stands out as the most effective in reducing coolant consumption, achieving savings of up to 90 % while maintaining grinding performance. This demonstrates that fluid reduction is feasible and represents a strategy worth further exploration.

Despite almost two decades of research, no approach has yet reconciled fluid efficiency, manufacturability and design flexibility in a single solution. This reinforces the central hypothesis of this thesis: that innovative manufacturing methods must be developed to embed complex internal channels directly into the wheel body, enabling both significant fluid reduction and improved grinding performance.

2.4 Fluid Flow Modeling in Grinding Wheels

Computational Fluid Dynamics (CFD) has progressively become an essential tool in grinding research due to the inherent complexity of fluid transport mechanisms in this process. The high rotational speeds of grinding wheels generate a boundary layer of air that strongly hinders coolant penetration, while the confined contact zone makes direct experimental observation extremely challenging. In this context, CFD provides a complementary approach to laboratory testing by enabling detailed predictions of fluid velocity, pressure and temperature fields under different operating and design conditions.

Early studies focused on simplified two-dimensional representations of external jet application, mainly to evaluate coolant penetration through the air barrier [185,186]. Subsequent developments introduced three-dimensional models, incorporating wheel rotation through *Multiple Reference Frame (MRF)* or sliding mesh techniques and employing turbulence models to capture flow instabilities [187–190]. More recently, CFD simulations have been coupled with experimental visualization and thermal measurements, which have improved model validation and strengthened confidence in numerical predictions [191,192].

The most significant advances are associated with structured wheels, where CFD has been applied to evaluate the performance of surface textures [120,123,193–199], internal channels for surface grinding [33,182,184] and internally cooled cup-type wheels for face grinding [130,134,200–208]. These studies demonstrate the potential of CFD not only as a predictive tool but also as a design-oriented methodology, guiding the development of new wheel geometries.

In the context of internally cooled wheels, different authors have employed CFD to support wheel design optimization. Although not employing *ANSYS® Fluent*, Nadolny [184] carried out CFD simulations using the FEM in *ANSYS* to estimate the coolant outflow velocity as a function of wheel speed, diameter and the number and size of channels in sandwich-type wheels for internal cylindrical grinding. This approach enabled the identification of the most effective configuration, which was subsequently validated experimentally. Barmouz *et al.* [33] used CFD to compare conventional cylindrical channels and Venturi-shaped channels in additively manufactured wheels, demonstrating that Venturi geometries increase jet velocity. More recently, Peng *et al.* [182] applied CFD to optimize the internal manifold and outlet positions of a directional cooling wheel, analyzing the effects of different coolant supply pressures on jet velocity, distribution uniformity and effective flow rate before proceeding to experimental tests. Table 2.14 summarizes the simulation setups, varied parameters and main outputs analyzed in these studies.

Table 2.14 – Summary of simulation setups, varied parameters and analyzed outputs in studies of internally cooled grinding wheels.

Author	Setup / Model	Parameters Varied	Outputs Analyzed
Nadolny [184]	*FEM (ANSYS 10)*, turbulence	Grinding speed (30–60 m/s), number and diameter of channels (1–3 mm)	Coolant outflow velocity
Barmouz *et al.* [33]	*ANSYS Fluent*, *k–ω SST*	Channel geometry (cylindrical vs. Venturi), wheel rotation	Outlet velocity field
Peng *et al.* [182]	*ANSYS Fluent*, transient *VOF*	Coolant pressure (0.1–0.8 MPa), manifold angle, slot geometry	Flow distribution (volume fraction of water) and jet pressure

The research on internally cooled cup-type wheels for face grinding has been more extensively explored through CFD simulations. The rotating domain models adopted in these studies are comparable to those required for the present work on internally channeled wheels, which makes them an important methodological reference. In general, CFD has been applied to study the flow behavior in terms of velocity, pressure and dispersion as affected by channel geometry, abrasive arrangement, flow rate and wheel speed. As summarized in Table 2.15, investigations have focused not only on the wheel body but also, in some cases, on the grinding zone flow, where the penetration of coolant into the contact region and its interaction with the abrasive grains and the workpiece, were analyzed.

Some of the more advanced models also coupled the CFD domain with *CFX* to simulate the temperature field and to evaluate the thermal response of the grinding zone. All models, however, were restricted to single-phase flow and did not consider multiphase formulations capable of describing the combined effects of coolant and air, which are highly relevant in grinding. Multiphase simulations have been more commonly applied to externally supplied fluid in textured wheels, whereas for internally cooled wheels the rotating inlet significantly increases the computational cost. Despite this limitation, accounting for multiphase flow remains a critical step toward more realistic predictions in future studies.

All models, however, were restricted to single-phase flow and did not consider multiphase formulations capable of describing the combined effects of coolant and air, which are highly relevant in grinding. Multiphase simulations have been more commonly applied to externally supplied fluid in textured wheels, whereas for internally cooled wheels the rotating inlet significantly increases the computational cost. Despite this limitation, accounting for multiphase flow remains a critical step toward more realistic predictions in future studies.

Table 2.15 – Summary of CFD simulations applied to internally cooled cup-type grinding wheels.

Author	Domain/Model	Parameters Varied	Outputs Analyzed
Peng *et al.* [206]	Wheel body/ Steady turbulent model	Channel diameter (1–3 mm); inlet pressure	Outlet velocity; velocity distribution
Peng *et al.* [130]	Wheel body and Grinding zone flow/ Adaptive *k–ε*; Wheel rotation: *MRF*;	Channel tangential angle (25°–45°) and diameter (1.6–2.4 mm); injection pressure; outlet location	Outlet velocity (max./area-avg); flow uniformity; grinding zone thermal field
Chen *et al.* [208]	Grinding zone flow	Outlet shape (circular vs. waist-shaped); wheel speed 1000–3000 rpm	Velocity distribution in grinding zone; coverage uniformity
Peng *et al.* [134]	Wheel body and Grinding zone flow/ rotation: *MRF*	Channel diameter (1–3 mm); wheel speed 1000–3000 rpm	Inter-channel uniformity; Outlet velocity; grinding zone flow field
Peng *et al.* [204]	Wheel body and Grinding zone flow/ Wheel rotation: *MRF* + *CFX*	Abrasive arrangement; wheel size (90 vs. 120 mm); grinding speed 5.76–17.28 m/s;	Velocity; effective flow rate; grinding zone temperature
Xiao *et al.* [200]	Wheel body and Grinding zone flow	Number of shaft holes; outlet position; abrasive patterns	Outlet velocity; flow-distribution; effective exit flow in grinding zone
Xiao *et al.* [203]	Wheel body and Grinding zone flow/ *RNG k–ε* + *CFX* (thermal field)	Flow channel type (linear vs. arc, Ø 1–2.4 mm); inlet pressure	Outlet velocity; flow distribution; matrix temperature;
Peng *et al.* [201]	Grinding zone flow/ Turbulent model + *CFX* (conjugate heat transfer)	Abrasive arrangement; abrasive-cluster diameter (1.3–1.8 mm); grinding speed 5.76–20.16 m/s;	Turbulent kinetic energy; effective flow rate; temperature distribution; coolant performance
Peng *et al.* [205]	Grinding zone flow/ *realizable k–ε* + *CFX* (conjugate heat transfer)	Abrasive arrangement; abrasive-cluster diameter (1.3–1.8 mm); grinding speed 5.76–20.16 m/s	Turbulent kinetic energy; coolant-utilization efficiency; temperature distribution
Zhao *et al.* [202]	Wheel body/ Transient Fluid–Structure; *k–ω SST*; Wheel rotation: rotating body	Wheel speed 1000–3000 rpm; Channel inclination (0 – 62°); Coolant type	Outlet velocity & flow distribution; grinding zone coverage; deformation response
Wang *et al.* [207]	Wheel body and Grinding zone flow	Cooling-hole position and diameter (1.5–2.5 mm); wheel speed 1000–5000 rpm	Outlet velocity & flow rate; velocity distribution in grinding zone; flushing uniformity

Among the studies summarized in Table 2.14 and Table 2.15, none has provided direct experimental validation of the simulations. The harsh and dynamic conditions of grinding make direct measurement extremely challenging. High wheel speeds generate strong air barriers and multiphase interactions between coolant, air and debris. Optical access is restricted, spray and reflections distort images, and the small size of internal channels further complicates direct measurements. As a result, most CFD studies in this field remain unvalidated, leaving uncertainty about their quantitative accuracy. High-speed imaging and particle tracking are well-established in other domains, such as biomedical engineering [209–211], where they are used to analyze blood flow and microfluidic transport, with high spatial and temporal resolution. Despite their proven capability, their application in grinding field is virtually unexplored due to the experimental difficulties described above and only a few recent works have begun to demonstrate that these techniques can be adapted to rotating systems with constrained optical access. This gap highlights an opportunity for their systematic adoption in grinding research, provided that suitable visualization strategies and transparent surrogate models are developed.

2.5 Summary and Discussions

Grinding is a process strongly influenced by thermal and tribological phenomena, where the efficiency of coolant application plays a decisive role. The literature shows that conventional external supply methods are limited by the air barrier generated by wheel rotation, resulting in poor fluid penetration into the contact zone and inefficient heat removal. Different strategies have been proposed to overcome these limitations, such as alternative cooling strategies, surface texturing and the introduction of internal channels.

Surface texturing techniques, including machined, engineered and laser grooves, have demonstrated improvements in fluid access and chip evacuation. However, their effectiveness is progressively reduced as the wheel wears and they are inherently restricted to surface modifications. In contrast, additive manufacturing has emerged as the only viable approach to create three-dimensional internal channels, providing greater flexibility in design and the possibility of continuous fluid supply throughout the entire tool life.

Studies on grinding wheels with internal cooling channels have reported substantial reductions in fluid consumption and significant improvements in thermal stability and grinding forces. Nevertheless, their

practical application remains limited by the complexity of fabrication and the lack of systematic design guidelines. In this context, CFD has been increasingly applied to analyze coolant transport in grinding, yet most works remain unvalidated due to the inherent experimental difficulties associated with high-speed rotating tools.

Overall, the literature highlights both the potential and the limitations of current cooling strategies. While internal channels fabricated by additive manufacturing represent a promising solution, further research is needed to establish reliable manufacturing methods, validate fluid flow predictions and systematically assess the influence of channel geometry on grinding performance. In parallel, the search for alternative and more cost-effective fabrication approaches, capable of enabling large-scale production without compromising cooling efficiency, has become increasingly relevant in recent years. These gaps form the basis for the investigation developed in the present thesis.

3. MATERIALS AND METHODS

This chapter describes the experimental methodology adopted to characterize the materials and evaluate the grinding performance of structured wheels with internal cooling channels. The first part presents the thermal and thermomechanical analyses performed on the polymeric precursors, binders and abrasive composites, which provided the basis for defining suitable processing and sintering conditions. The second part details the wear tests used to assess the tribological response of the fabricated wheels. Finally, the grinding experiments are described, including the machine setup, operating parameters and data acquisition methods employed to compare conventional and internally cooled wheels in terms of grinding forces, temperature variation and energy efficiency. Together, these methods establish the framework for the subsequent analysis of wheel behavior and cooling effectiveness.

3.1 Thermal and Thermomechanical Characterization

To characterize the thermal and thermomechanical behavior of the materials used in the fabrication of structured grinding wheels, a series of laboratory tests were carried out. These experiments provided the necessary information to evaluate the thermal transitions of the sacrificial polymer, the dimensional stability of the abrasive composites and the influence of processing parameters during mixing, pressing, drying and sintering.

The characterization of the channel precursor material was performed by simultaneous Differential Scanning Calorimetry and Thermogravimetric Analysis (DSC/TGA) [212,213] using the SDT2960 equipment from TA Instruments. The tests were conducted under an air atmosphere at a heating rate of 10 °C/min. In this work, Polylactic Acid (PLA) was selected as the sacrificial polymeric material, according to the criteria discussed in Chapter 4. Small PLA fragments were tested to identify the main thermal transitions and the decomposition window of the polymer, which are critical for defining the sintering cycle.

The Thermomechanical Analysis (TMA) [214] was employed to study the dimensional stability of the abrasive composites during heating. The tests were performed under an air atmosphere, with a constant preload of 0.01 N, applying different heating rates depending on the objective of each study. Cylindrical composite specimens with 6 mm diameter and 6 mm height were produced, with and without sacrificial PLA structure.

For the structured samples, a Y-shaped PLA insert with an arm section measuring 1 × 1 mm and a length of 2 mm was placed at the center of the mold before pressing, as illustrated in Figure 3.1. These specimens were used to evaluate the combined effects of the organic binder and the sacrificial polymer on the dimensional response during the thermal cycles.

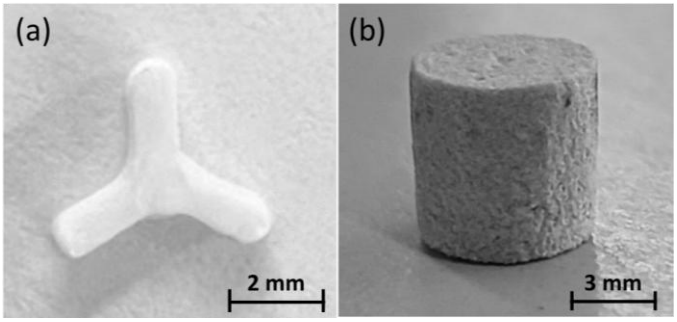


Figure 3.1 – (a) Y-shaped PLA insert used to generate internal features in the abrasive composite. (b) Vitrified composite specimen (Ø6 × 6 mm) containing the embedded PLA insert.

In addition, the influence of the binder formulation (polysaccharide) was investigated by TMA. Non-structured composites (without PLA) with different water contents in the polysaccharide solution were tested up to 80 °C to evaluate the binder response. Structured composites with Y-shaped PLA inserts were examined with different binder fractions (4.5, 7.5 and 10.5 wt. %) under a preload of 0.01 N and a heating rate of 4 °C/min, up to 650 °C, to assess the combined effect of the binder and sacrificial polymer during heating.

The hot pressing strategies were studied using a Dynamic Mechanical Analyzer (DMA) [213,215] in compression mode. Cylindrical samples with 6 mm diameter and 7 mm thickness, containing Y-shaped PLA inserts, were tested under a maximum load of 15 N and heated up to 60 °C. Different loading and unloading sequences (HP1 and HP2) were applied during heating and cooling to evaluate the effect of pressing conditions on the final geometry of the internal channels. In HP1, the load was applied before heating and maintained throughout the entire heating–cooling cycle, whereas in HP2 the load was also applied before heating but released before cooling, allowing the PLA insert to recover elastically while still above its glass transition temperature.

Finally, the drying step of the composites was evaluated through TMA, employing heating ramps of 0.1, 1.0 and 4.0 °C/min up to 75 °C, under a preload of 0.01 N. The objective was to investigate the influence of the drying rate on moisture removal from the organic binder and the effect on the structural integrity of the

green bodies prior to sintering. The experimental conditions of each test are summarized in Table 3.1**,** while the corresponding results are presented and discussed in Chapter 4.

Table 3.1 – Experimental conditions applied in the thermal and thermomechanical analyses.

Objective / Step	**Test (equipment)**	**Main conditions**	**Specimen**	**Details in Ch. 4**
PLA characterization	DSC/TGA (SDT2960)	Heating rate 10 °C/min; air atmosphere	PLA thin disc	Figure 4.3
Dimensional stability	TMA Q400	Heating rate 4 °C/min up to 950 °C; preload 0.01 N	Cylinders Ø 6 × 6 mm (with/without Y-PLA)	Figure 4.4
Binder plasticity (without PLA)	TMA Q400	Heating rate 4 °C/min up to 650 °C; preload 0.01 N	Cylinders Ø 6 × 6 mm;	Figure 4.5
Binder + PLA	TMA Q400	Heating rate 4 °C/min up to 650 °C; preload 0.01 N	Cylinders Ø 6 × 6 mm, Y-PLA;	Figure 4.6
Hot pressing strategies	DMA Q800 (compression)	Max. 60 °C; load 15 N; HP1 vs HP2	Cylinders Ø 6 × 7 mm, Y-PLA	Figure 4.8
Drying step	TMA Q400	Heating rates 0.1, 1.0, 4.0 °C/min up to 75 °C; preload 0.01 N	Cylinders Ø 6 × 6 mm, Y-PLA	Figure 4.10

3.2 Wear Tests

The wear behavior of both the reference and the structured vitrified grinding wheels was evaluated using a pin-on-disc configuration, schematically illustrated in Figure 3.2. The counterface consisted of an alumina pin with a 5 mm diameter, pressed against the rotating abrasive disc under a normal load of 20 N. The tests were performed at a sliding speed of 0.5 m/s (210 rpm), corresponding to a total sliding distance of 1800 m over a test duration of 60 min. A constant flow of distilled water at 6 mL/min was used as coolant fluid. Three discs were tested for each condition to ensure reproducibility. The experimental parameters are summarized in Table 3.2.

The wear rate of both the abrasive discs and the alumina counterface was measured by the gravimetric method, through weighing before and after testing using a precision balance. In addition to the wear rate, the

grinding ratio (G-ratio) was calculated as the ratio between the mass of material removed from the alumina pin and the mass loss of the grinding disc, providing a quantitative measure of tool efficiency under each condition.

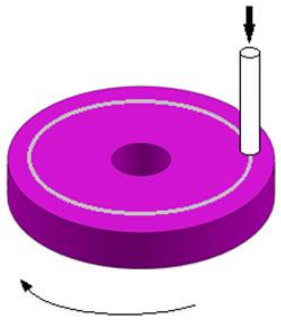


Figure 3.2 – Schematic representation of the pin-on-disc wear test configuration used for the abrasive grinding wheels.

Table 3.2 – Experimental conditions of the wear tests of the abrasive grinding wheels.

Parameters	Value	Units
Counterface (Alumina pin)	5	mm
Normal load applied	20	N
Sliding speed	0.5	m/s
Sliding distance	1800	m
Time	60	min

3.3 Scanning Electron Microscopy (SEM)

The morphology of the abrasive composites was examined by SEM [216] to evaluate the effect of the sacrificial PLA structures on the consolidation of the vitrified bond. Particular attention was given to the regions adjacent to the channels, where the continuity of the bond and the distribution of porosity were assessed. The analyses were performed using a NanoSEM – FEI Nova 200 (FEG/SEM) system. Samples were sectioned from the discs, mounted on aluminum stubs and coated with a thin conductive Au layer to prevent charging during observation. Both secondary electron (SE) and backscattered electron (BSE) modes were employed to capture microstructural features and contrast between abrasive grains, bond and pores.

3.4 Developed Internal Lubrication System

A custom grinding machine was projected and built specifically for this project to test structured wheels with internal channels (Figure 3.3a) [217]. Although designed as a dedicated prototype, the internal lubrication system can be easily adapted to conventional grinding machines by incorporating a similar wheel holder and fluid supply arrangement. The development of this system was essential because no commercial equipment currently exists that enables the delivery of coolant through internal channels embedded within the grinding wheel body.

In the implemented configuration, the coolant is introduced through a stationary inlet and guided along the rotating shaft until it reaches a specially adapted wheel holder equipped with radial outlet ports. These ports feed an internal chamber located between the shaft and the grinding wheel, which acts as a pressurized buffer reservoir. The chamber ensures a continuous and stable supply of fluid to the base of the channels. Once inside the wheel, the coolant is driven radially outward by centrifugal action, flowing through the channel network and exiting at the abrasive surface (Figure 3.3b-c), thereby reaching the grain–workpiece interface during grinding.

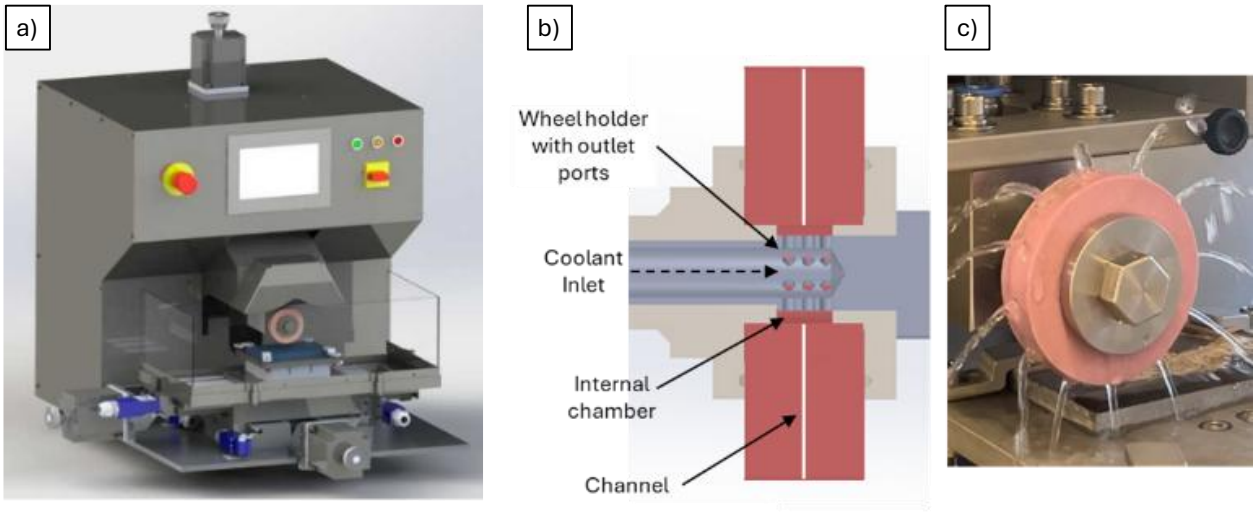


Figure 3.3 – Internal lubrication system: (a) Grinding machine (b) CAD model of the rotating shaft and wheel holder; (c) photograph of coolant exiting through the radial channels of the grinding wheel (wheel not rotating).

In addition to testing structured wheels with internal cooling, the machine was also designed to accommodate conventional grinding wheels operating with external flood lubrication. The test rig provides controlled movement along the X, Y and Z axes, enabling precise positioning of the workpiece and reproducible engagement with the wheel. Its main technical specifications are summarized in Table 3.3. The system

supports grinding wheels with diameters from 45 to 110 mm, spindle speeds up to 14000 rpm, table feed rates up to 500 mm/min and depth of cut of 10 µm. A three-component force dynamometer (TAS3F, HT Sensor Technology) was integrated to measure tangential and normal forces during operation, while additional instrumentation allowed the acquisition of temperature data inside the workpiece and fluid pressure. These features ensure that both structured and conventional lubrication strategies can be evaluated under comparable and realistic operating conditions.

Table 3.3 – Technical specifications of the custom grinding machine developed for testing structured wheels with internal channels.

	Features	**Details**
Grinding Wheel	Ø 45 - 110 mm	Accommodates various wheel sizes for different applications.
Workpiece	Up to 100 x 110 mm	Supports a range of workpiece sizes for versatility.
Rotational Speed	500 - 14000 rpm	Variable speeds to suit different machining requirements.
Feed Rate	Up to 500 mm/min	Allows control over the rate of material removal.
Depth of Cut	Minimum of 10 µm	Enables precision in material removal.
Coolant Flow Rate	Up to 4 L/min	Options for internal and external supply, providing flexibility in cooling methods.

3.5 Grinding Experimental Setup

Grinding tests were carried out under two lubrication strategies: conventional external flood cooling and internal cooling using structured wheels with radial channels. Figure 3.4 shows a schematic of both systems, indicating wheel rotation (V_s), workpiece feed (V_w), thermocouple position and load cell placement. In the external flooding system (Figure 3.4a), fluid was supplied through a directional nozzle with a 15 × 2 mm outlet positioned upstream of the contact zone. In the internal cooling system (Figure 3.4b), distilled water was introduced through the wheel center and transported outward by centrifugal action through the channel network.

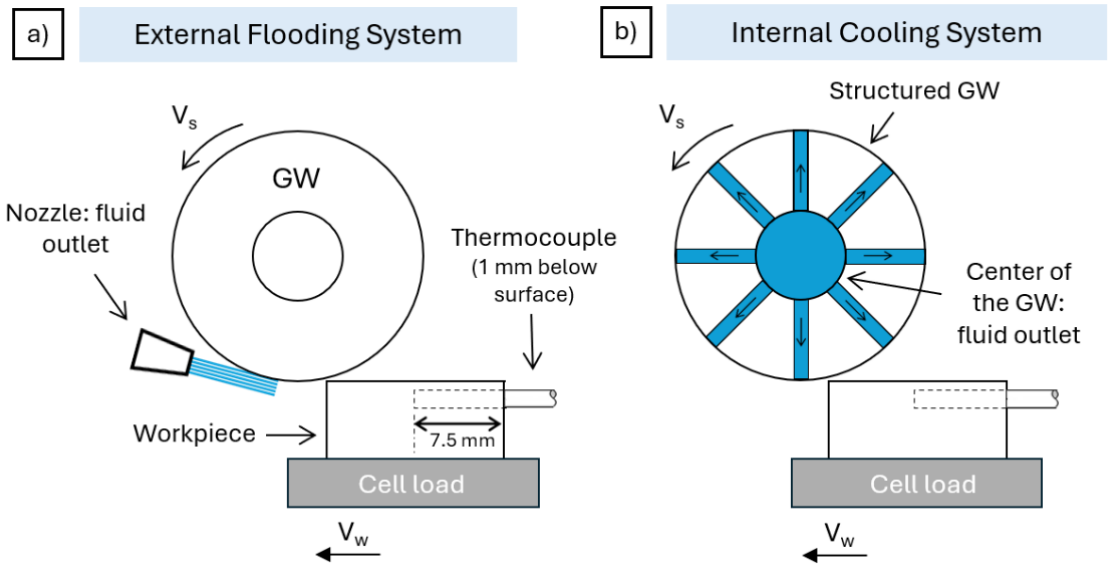


Figure 3.4 – Schematic representation of the lubrication systems: (a) external flood cooling, (b) internal cooling via radial channels. Directions of wheel rotation (V_s), workpiece feed (V_w), thermocouple location and load cell placement are indicated (schematic only, not to scale).

Temperature acquisition: A type K thermocouple, with a measurement accuracy of ±1.5 °C, was positioned 7.5 mm from the end of the grinding path and 1 mm below the workpiece surface. To enable this, the workpieces were previously drilled so that the thermocouple could be properly inserted and fixed in the desired position. Although subsurface, this configuration allowed a reliable estimation of the temperature close to the contact zone. Data was sampled at 5 Hz and the maximum temperature variation (ΔT) was considered for analysis. The thermocouple was calibrated before testing and reproducibility across repetitions confirmed the reliability of the data.

Force measurement: Tangential (F_t) and normal (F_n) forces were recorded with a three-component load cell (TAS3F, HT Sensor Technology), with a specified accuracy of ±0.3 %, placed beneath the workpiece holder. The specific grinding energy (Ec) was obtained according to Eq. (3.1):

$$Ec = \frac{F_t . V_s}{Q_w} \tag{3.1}$$

where F_t is the tangential grinding force (N), V_s is the cutting speed (m/s) and Q_w is the material removal rate (mm^3/s).

Experimental conditions: All tests were performed with a wheel speed of 5000 rpm ($V_s = 16.23\ m/s$), a feed rate of 100 mm/min and depths of cut $a_e = 10, 20, 50, 80, 100\ and\ 120\ \mu m$. The only exception

was the set of tests dedicated to studying the effect of channel inclination, in which depths were limited to values up to $a_e = 100\ \mu m$. The wheels were alumina-based, with vitrified bond and dimensions Ø 62 × 15 mm with an internal bore of Ø 21 mm. The workpieces were AISI 1045 steel blocks (80 × 15 × 10 mm) with a hardness of 198 HV.

Choice of coolant: Distilled water was used in both lubrication systems at a constant flow rate of 400 mL/min. The use of water without additives minimized contamination risks for the internal channels, ensured consistent fluid properties throughout the experiments and allowed isolating the influence of the cooling strategy itself.

Each condition was repeated three times and mean values were considered for analysis. Before testing, all wheels were balanced and run at 5000 rpm to verify dynamic stability. The grinding wheels were dressed before each test using a multi-point diamond tool to restore the active cutting surface, at a wheel speed of 1000 rpm, a feed rate of 100 mm/min and depth of cut $a_e = 30\ \mu m$. The complete set of parameters is summarized in Table 3.4.

Table 3.4 – Grinding parameters used in the tests for evaluating external and internal cooling systems.

Grinding process parameters	**Values**
Grinding wheel speed, $\boldsymbol{V_s}$	16.23 m/s (5000 rpm)
Workpiece feed rate, $\boldsymbol{V_w}$	100 (mm/min)
Depth of cut, $\mathbf{a_e}$	10, 20, 50, 80, 100, 120 (µm) (up to 100 µm for inclination tests)
Fluid flow rate	400 mL/min – distilled water
Grinding mode	Up Grinding
Grinding wheel abrasive	Alumina, vitrified (Ø 62 × 15 mm; bore Ø 21 mm)
Workpiece	AISI 1045 (80 × 15 × 10 mm); 198 HV

In addition to the schematic in Figure 3.4, Figure 3.5 shows a photograph of the experimental setup during operation with a grinding wheel. The main elements are: (a) grinding wheel (V_s: cutting speed), (b) workpiece (V_w: feed direction), (c) load cell beneath the workpiece holder and (d) thermocouple embedded 1 mm below

the workpiece surface. This configuration enabled the simultaneous acquisition of mechanical and thermal data under reproducible test conditions.

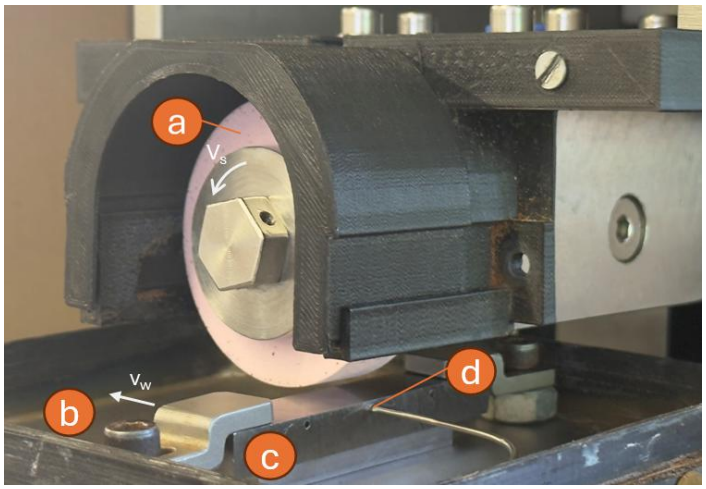


Figure 3.5 – Grinding experimental setup: (a) grinding wheel, (b) workpiece, (c) load cell, (d) thermocouple embedded below the workpiece surface.

4. MANUFACTURING OF STRUCTURED GRINDING WHEELS

This chapter presents the methodology and processing method developed for the manufacturing of structured vitrified grinding wheels with internal cooling channels. The content is largely based on two previously published works: "*A New Grinding Wheel Design with a 3D Internal Cooling Structure System*", published in the *Journal of Manufacturing and Materials Processing* [218] and "*Process Optimization of a Green Composite Containing a 3D Structure Produced via Additive Manufacturing*", published as a book chapter in the proceedings of the *2nd International Workshop on Additive Manufacturing and Sustainability (IWAM)* [219].

The chapter describes the optimization of each processing step, including binder formulation, pressing, drying and sintering, to accommodate sacrificial polymeric inserts. It concludes with the validation of the fabricated wheels, focusing on dimensional stability, microstructural integrity and wear performance, thereby consolidating the feasibility of the proposed approach.

4.1 New Grinding Wheel Design Methodology Concept

The concept of manufacturing vitrified grinding wheels with internal cooling channels emerged as a response to the limitations of conventional wheels in terms of coolant delivery. Traditional grinding wheels rely on an external fluid supply combined with random porosity in the vitrified matrix [54]. This porosity typically ranges from 30 to 45 % of the total wheel volume and consists of both open and closed pores. The open porosity, generally between 25 and 40 %, allows the penetration of coolant and the removal of chips, improving heat dissipation and maintaining the cutting efficiency of the wheel. Closed pores, usually between 5 and 15 %, are isolated within the matrix and have limited influence on fluid transport [43,54]. However, at high wheel speeds, the air barrier formed around the wheel surface significantly reduces coolant penetration, limiting its ability to reach the grinding zone [16]. This phenomenon often results in higher local temperatures, accelerated wheel wear and reduced process efficiency.

To address this challenge, a novel methodology was proposed in which sacrificial polymeric preforms, produced by additive manufacturing, are embedded into the abrasive mixture during pressing. During the

subsequent sintering stage, the polymer decomposes, leaving behind a controlled network of channels that directly guide the coolant flow towards the contact zone.

This design methodology combines the robustness of conventional vitrified wheel manufacturing with the versatility of additive manufacturing. The abrasive mixture remains composed of alumina grains, a vitrified bond precursor and a temporary binder, preserving the scalability and compatibility with the original industrial processing. The innovation resides mainly in the integration of 3D-printed inserts, with selected shape, design and size, which act as sacrificial templates to create well-defined internal channels, ensuring geometric stability and reducing defects during production.

The conceptual basis of the methodology can be summarized in three main requirements:

1. **Material compatibility.** The abrasive composite must withstand pressing and sintering, while the polymeric inserts must remain dimensionally stable during compaction and later decompose at a temperature below the softening point of the vitrified bond; for the insert, PLA fulfills this role, as it exhibits adequate stiffness at room temperature to resist pressing, yet fully decomposes between 300 and 450 °C, prior to mineral bond consolidation at approx. 620 °C.
2. **Geometrical adaptability.** The use of FDM enables the fabrication of inserts with customized shapes, diameters and distributions, allowing the design of optimized cooling paths. This flexibility contrasts with traditional pore formers, which yield random porosity with little control over geometry.
3. **Process continuity.** The proposed methodology integrates seamlessly into conventional vitrified wheel manufacturing, requiring two primary adaptations: (i) insertion of a polymeric preform into the mold before pressing and (ii) adoption of hot pressing, where controlled heating during compaction allows the PLA insert to soften gradually, reducing internal stresses and preventing cracks or distortions. The subsequent stages of mixing, drying and sintering follow the conventional process, complemented by secondary adjustments such as optimized binder content, a slower drying rate and a slightly modified heating ramp to ensure complete polymer burnout. Together, these refinements ensure process reliability and provide the structural stability required for the subsequent experimental validation.

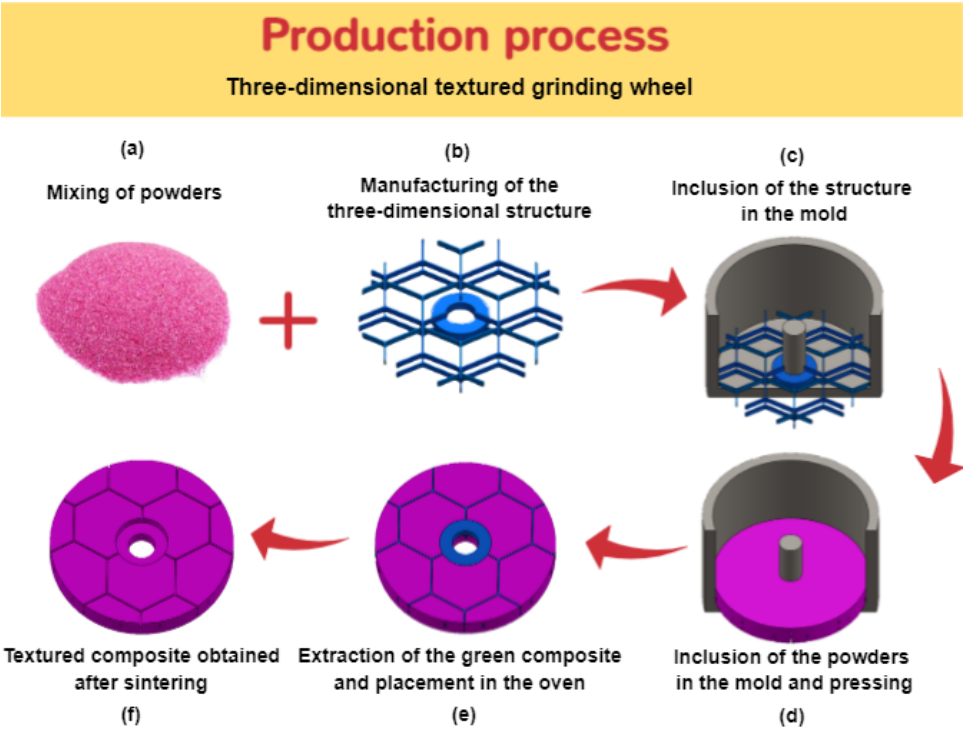


Figure 4.1 – Schematic representation of the new grinding wheel design methodology for the integration of internal cooling channels.

A schematic representation of the manufacturing concept is shown in Figure 4.1. The sequence illustrates the main steps: preparation of the abrasive mixture, fabrication of the sacrificial PLA preform, insertion into the mold, compaction of the composite and final sintering to obtain the structured grinding wheel with internal channels.

This concept forms the foundation for the next sections, where the processing conditions are optimized and validated through experimental studies. The methodology provides a scalable pathway for producing structured grinding wheels that combine conventional ceramic processing with additive manufacturing, linking established industrial practices to new design possibilities.

4.2 Printing Conditions

PLA was selected as the sacrificial material for the channel precursors not only due to its suitable thermal behavior, but also because of its practical and sustainable advantages. The PLA used in this work was a commercial filament supplied by DoWire (Portugal). PLA is a biodegradable and low-cost polymer, widely available for additive manufacturing [220,221]. It combines adequate stiffness at room temperature, which allows it to withstand pressing forces, with complete burnout during heating, ensuring the formation of clean

channels without ash entrapment. In addition, its ease of printing and dimensional accuracy make it well suited for fabricating complex preforms, while its mechanical properties are sufficient to maintain structural integrity during handling and compaction. These features justify the adoption of PLA as an effective and scalable solution for producing sacrificial inserts in structured grinding wheels.

To accommodate the high slenderness of the channels and to avoid the need for support structures, the polymeric inserts were printed in separate parts. The central section and the radial array of channels were fabricated independently and later assembled manually, ensuring uniformity of the channels while preventing deformation during printing. This strategy is illustrated in Figure 4.2, which shows the three printed components and their final assembly. The approach facilitated the fabrication of long, single-layer channels while maintaining geometrical accuracy and minimizing the risk of breakage during handling.

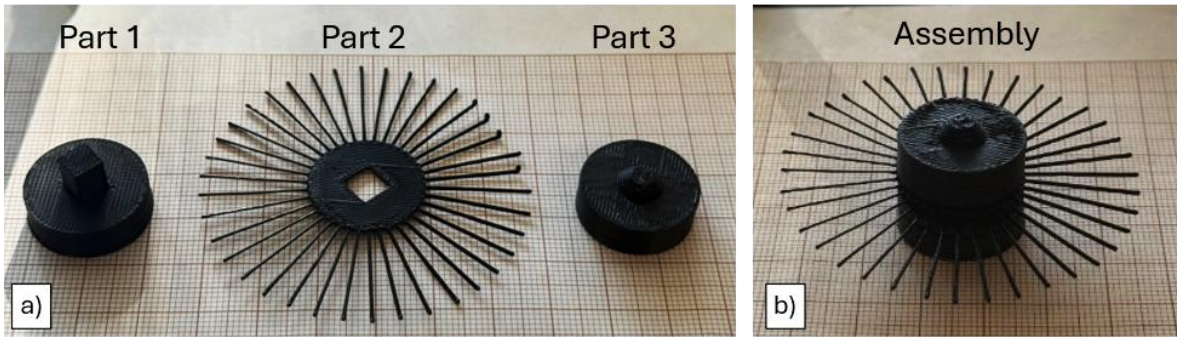


Figure 4.2 – Fabrication strategy of the PLA sacrificial inserts: (a) printed components comprising the base of the structure (Part 1), the single-layer channel array (Part 2) and the top section (Part 3); (b) final assembly forming the complete insert responsible for defining the internal channel geometry of the GW.

The fabrication of PLA sacrificial inserts through additive manufacturing was essential for generating the internal channel geometry of the structured grinding wheels with the required dimensional accuracy. For this purpose, FDM was employed using two different printers over the course of the work: Ultimaker 3 and Bambu A1. To compare geometric precision, printing parameters and fabrication time, a PLA insert containing ten channels with a nominal diameter of 1.7 mm was printed on both systems. The extrusion temperature was set to 220 °C in all tests. Several preliminary trials were performed by varying layer height and printing speed until optimal parameter sets were established, as presented in Table 4.1.

The dimensional analysis of the printed channels was performed by measuring their diameter along two perpendicular directions. For each direction, denoted D1 and D2, ten measurements were taken using a digital caliper. In this context, D1 corresponds to the channel width, while D2 represents the channel height aligned with the printing direction. The mean value and standard deviation were calculated separately for

both directions, allowing the determination of the average printed diameter. The ratio D1/D2 was also evaluated to quantify deviations from circularity introduced during the printing process. The relative deviation reported in Table 4.1 corresponds to the percentage difference between the average printed channel diameter and the nominal diameter defined in the CAD model.

Table 4.1 – Printing parameters and dimensional results for the PLA channel inserts produced with the Ultimaker 3 and Bambu A1.

Parameter	**Ultimaker 3**	**Bambu A1**			
Channel diameter - CAD (mm)	**Ø 1.7**	**Ø 1.7**	**Ø 1.5**	**Ø 1.0**	**Ø 0.6**
Initial layer height (mm)	0.15	0.3	0.3	0.2	0.2
Layer height (mm)	0.27	0.35	0.4	0.4	0.4
Initial layer speed (mm/s)	20	15	15	15	15
Other layer speed (mm/s)	40	25	25	25	10
Adhesion type	Raft	-	-	-	-
Printing time (min)	56	10.8	8	5.8	3.3
D1 (mm)	1.85 ± 0.05	1.73 ± 0.02	1.51 ± 0.02	1.01 ± 0.04	0.59 ± 0.03
D2 (mm)	1.81 ± 0.05	1.69 ± 0.02	1.50 ± 0.02	0.99 ± 0.02	0.58 ± 0.03
D1/D2	1.03	1.02	1.01	1.02	1.01
Printed channel diameter (mm)	1.83 ± 0.06	1.71 ± 0.03	1.51 ± 0.02	1.00 ± 0.03	0.58 ± 0.03
Relative deviation (%)	**7.6**	**0.4**	**0.4**	**0.1**	**2.7**

In contrast to the Ultimaker 3, the Bambu A1 is equipped with a flexible magnetic build plate, which enables printing directly on the surface without a raft. The flexibility of the plate facilitated removal of the single-layer channels without damage, reducing fabrication time and improving repeatability. For the same ten-channel geometry, the total printing time decreased from 56 minutes on the Ultimaker 3 to 10.8 minutes on the Bambu A1, representing a substantial improvement in process efficiency. The printed inserts also exhibited

higher dimensional accuracy, with deviations of only 0.4 % for the 1.7 mm channels. Based on these results, the Bambu A1 was selected for the fabrication of all sacrificial structures employed in this thesis.

Table 4.1 also summarizes the printing parameters and the dimensional analysis for all channel diameters used in this work, namely Ø 1.7, Ø 1.5, Ø 1.0 and Ø 0.6 mm. All geometries printed on the Bambu A1 showed low deviations relative to the nominal diameter and D1/D2 ratios close to 1, indicating minimal deviation from circularity and a good preservation of the intended channel geometry.

DSC/TGA Analysis of the PLA channel precursor

The thermal analysis of the PLA precursor is shown in Figure 4.3. The DSC curve highlights the characteristic transitions of PLA. A glass transition temperature (Tg) is observed at approximately 63 °C, where the polymer undergoes a reduction in stiffness. This is followed by an exothermic event at approximately 122 °C, corresponding to the crystallization temperature (Tc) and by an endothermic peak at 144 °C, which represents the melting point (Tm). These transitions are consistent with values reported in the literature [220–223] and provide a basis for defining the processing window during pressing, as the material softens significantly near Tg.

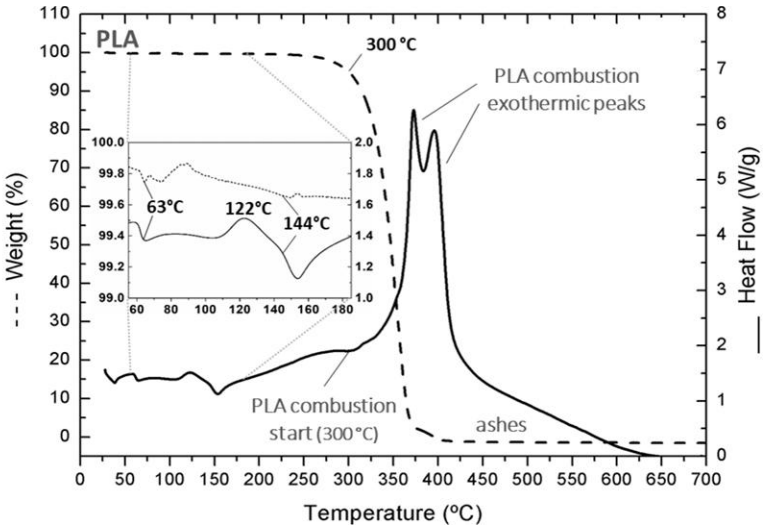


Figure 4.3 – DSC/TGA of the PLA precursor (10 °C/min, air atmosphere).

The TGA curve indicates that PLA is thermally stable up to approx. 300 °C, after which the decomposition occurs in two distinct stages, between 300 and 450 °C. The major mass loss in this interval corresponds to the complete burnout of the polymer, ensuring that no significant residues remain above this temperature.

Overall, these results confirm that PLA fulfills the requirements for its use as a sacrificial insert: it provides rigidity at room temperature, softens near Tg to accommodate low temperature hot pressing and decomposes entirely below the vitrified bond softening point (approx. 620 °C), leaving clean internal channels.

4.3 Optimization of Processing Conditions

To guide the optimization of the manufacturing process, we first assessed how the inclusion of sacrificial PLA affects the thermomechanical response of the abrasive composite during heating. The distinct mechanical behavior and thermal expansion of the PLA inserts compared to the abrasive composite make each processing step particularly sensitive to instability, especially during pressing and drying. The dimensional variation was continuously recorded by TMA during heating and cooling, enabling a direct comparison between reference composites and those containing PLA inserts. Although the TMA test does not reproduce the complete sintering cycle, it simulates the thermal exposure of the composite under controlled heating, allowing the identification of critical transitions and dimensional instabilities during drying and early sintering. The TMA results for composites with and without PLA are presented in Figure 4.4. The reference composite (without PLA) shows two characteristic features:

- a shrinkage between 30 and 100 °C, corresponding to moisture evaporation from the binder;
- a two-step contraction between 275 and 475 °C, associated with binder combustion.

When PLA is incorporated, additional features emerge:

- an expansion at Tg ≈ 63 °C, where the polymer softens and rapidly increases the dimensional change of the composite;
- a second expansion at Tm ≈ 144 °C, corresponding to polymer melting, which further amplifies the instability before decomposition.

Following these events, PLA decomposes between 300 and 450 °C, overlapping with binder burnout. This transformation occurs well below the vitrified bond softening range and therefore does not interfere with matrix consolidation, as previously confirmed by DSC/TGA analysis in Section 4.2. Together, these transformations significantly modify the dimensional stability of the composite and explain the greater tendency for crack formation when PLA is present. This evidence highlights the need to optimize the

subsequent processing steps (binder content, pressing strategy, drying rate and sintering cycle) to accommodate these transitions and ensure defect-free wheels.

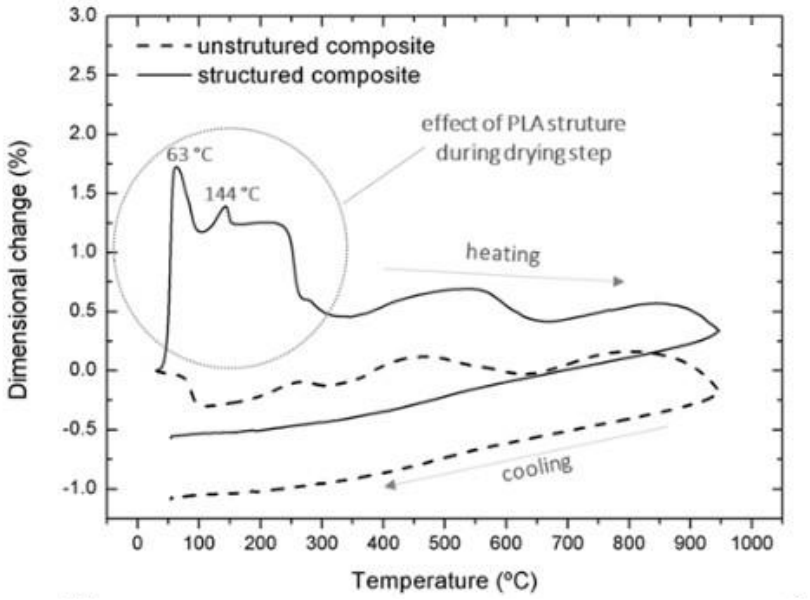


Figure 4.4 – Thermomechanical analysis (TMA) of abrasive composites with and without PLA structure (air atmosphere, heating rate 4 °C/min).

4.3.1 Formulation of the green composite

In the mixing stage of the abrasive composite, the formulation of the organic binder plays a decisive role in the plasticity of the green body and its ability to accommodate the PLA insert. Two parameters were investigated to ensure adequate plasticity and dimensional stability: (i) the water fraction in the polysaccharide solution and (ii) the total binder content in composites containing PLA to prevent excessive brittleness or over-plasticization during pressing.

Effect of water fraction (without PLA)

To isolate the influence of water content, preliminary tests were carried out on simple binder specimens composed only of polysaccharide and water. In this stage, different formulations of the polysaccharide solution were prepared with increasing water fractions. The underlying rationale was that higher water content would enhance plasticity, facilitating compaction and stress accommodation during pressing, although it could also compromise dimensional stability during heating. These formulations, designated W7, W20, W26 and W30, are summarized in Table 4.2 and were subsequently analyzed by TMA to assess their dimensional response upon heating.

Table 4.2 – Tested compositions for the study of plasticity in Ø 6 x 6 mm test specimens of organic binder (polysaccharide + water.

Binder sample	Polysaccharide powder (wt. %)	Water (wt. %)	Polysaccharide /Water ratio
W7	93.00	7.00	13.29
W20	80.30	19.70	4.08
W26	74.34	25.66	2.90
W30	70.00	30.00	2.33

The TMA of the formulations, shown in Figure 4.5, revealed that the dimensional response of the composites was strongly dependent on the water content of the polysaccharide solution. Samples with low water fraction, such as W7, showed reduced plasticity and limited capacity to accommodate dimensional changes during heating, which increases the risk of crack formation. As the water content increased, W20 and W26, the plasticity of the green body improved, although the best performance was observed for W30 sample, which presented the smoothest dimensional variation. This condition allowed the formation of a compact with sufficient mechanical resistance and extended plasticity, since the higher water retention facilitated particle rearrangement and stress accommodation. Such behavior ensures adequate mechanical strength of the green composite while reducing the likelihood of defects during drying and the early stages of sintering.

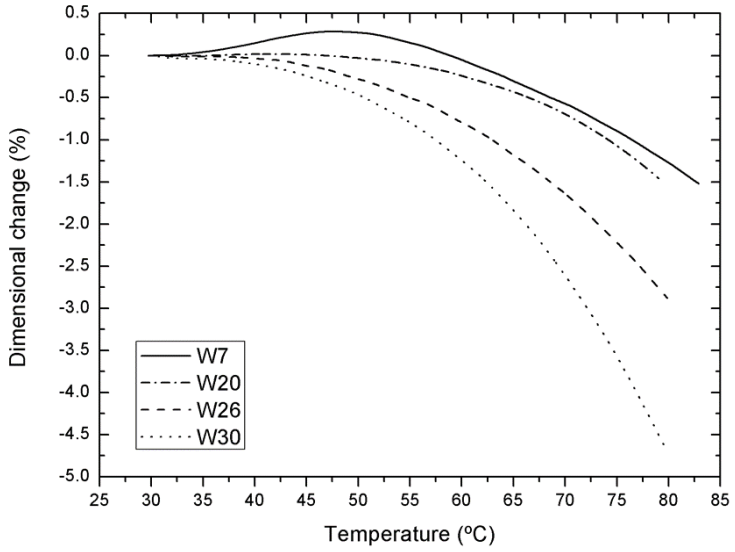


Figure 4.5 – Thermomechanical analysis (TMA) of polysaccharide solution samples with varying water contents (7, 20, 26 and 30, in wt %) under air atmosphere and heating rate of 4 °C/min.

Effect of binder content (with PLA)

To evaluate the influence of binder content in the presence of sacrificial structures, abrasive composites were produced with the W30 solution and different binder fractions (4.5, 7.5 and 10.5 wt. %). Each specimen incorporated a Y-shaped PLA insert, as previously illustrated in Figure 3.1, ensuring a representative geometry for the dimensional analysis. The corresponding compositions are listed in Table 4.3 and the TMA results are presented in Figure 4.6.

Table 4.3 – Study of plasticity in the cylindrical test specimen of green abrasive composite by varying the W30 organic binder content.

Abrasive composite	**Alumina (wt. %)**	**Vitrified powder (wt. %)**	**Organic binder (wt. %)**
B4.5	85.3	10.2	4.5
B7.5	82.6	9.9	7.5
B10.5	79.9	9.6	10.5

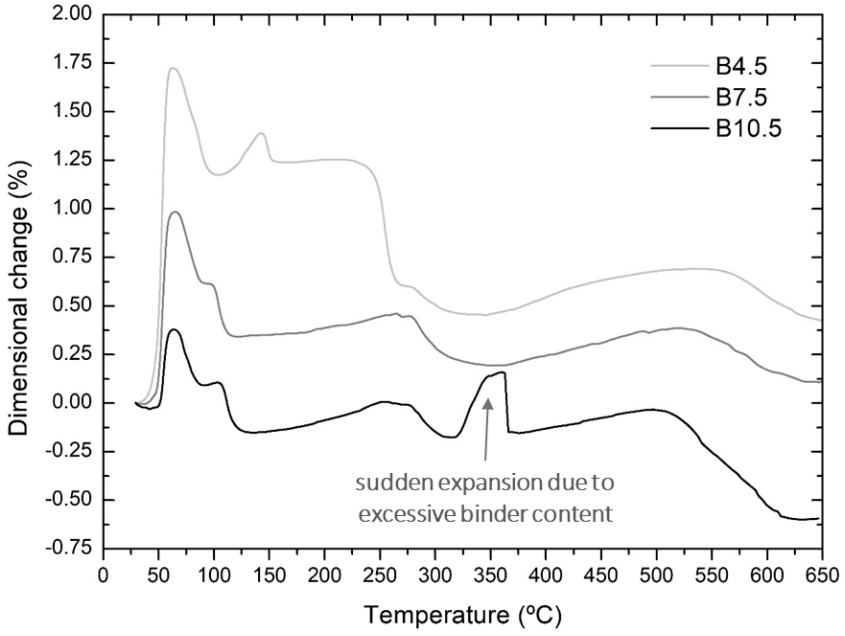


Figure 4.6 – Thermomechanical Analysis (TMA) of abrasive composites with included PLA structure, manufactured with W30 organic binder contents of 4.5 wt. %, 7.5 wt. % and 10.5 wt. % (4 °C/min, air atmosphere).

During the initial drying stage, at around 50–60 °C, the thermal expansion of the composites was found to be highly dependent on the binder content. Increasing the binder fraction from 4.5 to 7.5 wt. % reduced the dimensional change from approx. 1.7 % to approx. 1.0 %, indicating improved stability and a lower tendency for crack formation during drying. The formulation with 10.5 wt. % binder (B10.5) showed an even smaller dimensional change in this low-temperature interval, suggesting initially favorable plasticity. However, B10.5 proved unstable, exhibiting a sudden abnormal expansion near 350 °C, a phenomenon that was systematically reproduced across all test repetitions. This behavior is attributed to gas entrapment during PLA combustion, as the excessive binder content hindered normal gas release and led to localized swelling and instability in the composite.

These findings demonstrate that excessive binder content is detrimental for structured composites with PLA, as it disrupts polymer burnout and promotes dimensional instabilities. Therefore, the B10.5 formulation was discarded and the composition with 7.5 wt. % binder (B7.5) was selected as the best condition for subsequent analyses, offering a suitable balance between plasticity and dimensional stability.

4.3.2 Pressing Strategies

For grinding wheels with only superficial and simple channels, conventional uniaxial pressing was sufficient and no major defects were observed. However, as the channel geometry became more complex, cracks started to form near the PLA inserts. This behavior was attributed to the elastic recovery of the polymer after unloading, which compromised channel stability and highlighted the need for optimized pressing strategies.

To investigate this effect, the B7.5 formulation was used and compared under two hot-pressing strategies (HP1 and HP2). The corresponding specimen geometry and loading conditions are shown in Figure 4.7.

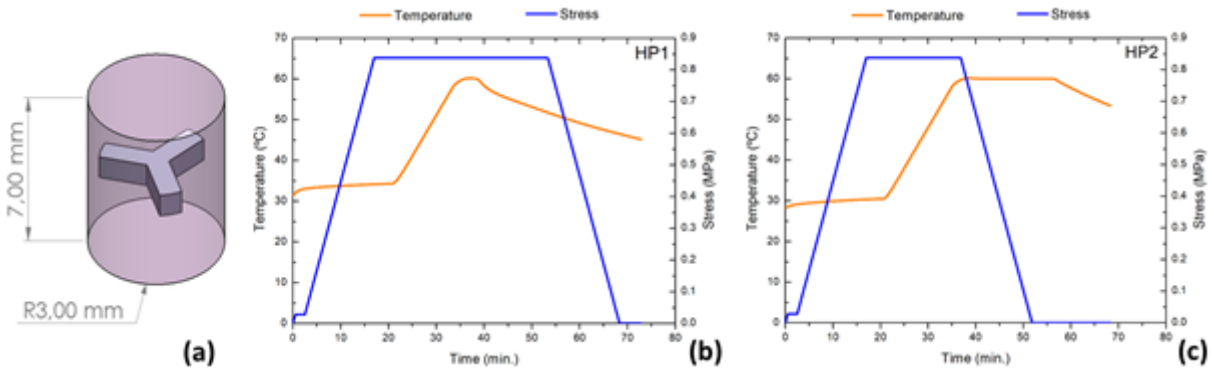


Figure 4.7 – Schematic representation of tested abrasive composite samples, featuring a PLA structure at the center (a). Temperature and stress profiles for the two hot-pressing strategies: HP1 (load maintained during cooling) and HP2 (load released before cooling) (b–c).

In HP1, the load was applied first and the temperature was then increased, with the load kept constant throughout the entire heating and cooling cycle. In HP2, the load was also applied before heating, but was released before cooling, allowing the PLA insert to recover elastically while still above its glass transition temperature (Tg ≈ 55–65 °C).

In Figure 4.8, a comparison between samples HP1 and HP2 reveals that the total deformation of sample HP1 (0.92 %) is more than double that of HP2 (0.44 %). The deformation component associated with the composite remains similar under both testing conditions. In contrast, the deformation component related to the PLA structure significantly influences the total deformation of the sample, showing a notably higher value in HP1 (0.65 %) compared to HP2 (0.23 %). This difference clearly affects the outcomes of the HP1 and HP2 processes. The total dimensional recovery after removing the load is greater in HP2, at 0.43 %, as the composite recovers without being restricted by the hardening of the PLA.

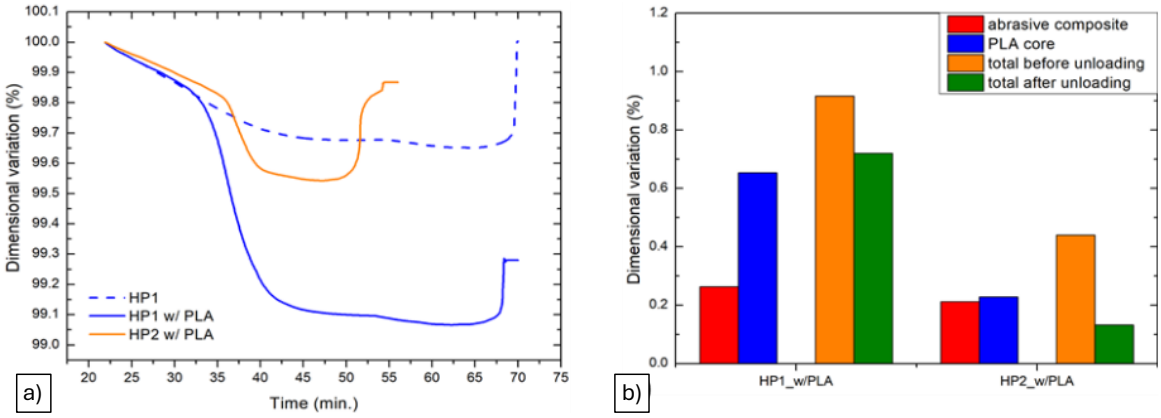


Figure 4.8 – (a) Dimensional variation of the abrasive composite with a PLA structure under HP1 and HP2 conditions, starting from the beginning of the thermal cycle and (b) dimensional variations of the composite and the PLA components, and the total deformation, before and after unloading and recovering.

During HP1, the PLA structure reaches its softening range while still subjected to the maximum load of 15 N. As the temperature subsequently decreases with the load still applied, the polymer begins to stiffen, restricting its ability to recover. As a result, the deformation in the PLA structure remains after the load is removed, with a measured permanent deformation of approximately 8 %, as indicated by the PLA structure thickness measurement results. Under these conditions, the geometry of the channels, formed by the burning of the structure during abrasive composite sintering, becomes compromised.

In contrast, with HP2, the load is removed while the composite is still at a temperature higher than the PLA glass transition temperature (Tg), allowing the PLA structure to remain at a more malleable state. In these conditions, the elastic recovery of the PLA structure is maximized and the plastic deformation is significantly

reduced to approximately 1 % (thickness measurements results). Consequently, the internal channels may retain their designed geometry, before sintering, ensuring the structural integrity and functionality of the structured abrasive composite.

In practice, this improvement is clearly observed in the manufactured wheels. Figure 4.9a shows the cracks that typically appeared around the channels when conventional uniaxial pressing was applied, compromising wheel integrity. After adopting the optimized HP2 strategy with the B7.5 composition, the cracks were eliminated, as illustrated in Figure 4.9b, confirming the effectiveness of the proposed approach.

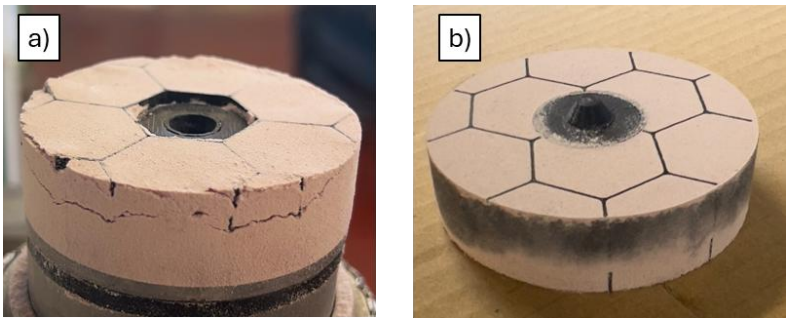


Figure 4.9 – Comparison between structured abrasive wheels after pressing: (a) cracks formed near the channels when conventional pressing was applied; (b) defect-free wheel produced using the optimized pressing strategy (HP2 with B7.5 composition).

When manufacturing even more complex wheels, with multi-layer PLA structures for internal lubrication (up to five layers), a new issue emerged: after pressing, the channels were no longer centered across the wheel thickness, but displaced to one side. To solve this, a two-stage pressing strategy was developed. The mold was filled with powders and PLA structures up to 30 mm in height, which was reduced to 15 mm after compaction. Instead of applying the full displacement unidirectionally, pressing was first applied from one side to compress 7.5 mm, corresponding to approximately 8–10 kN and then from the opposite side to complete the remaining 7.5 mm, requiring a higher load of 35–40 kN due to the increased densification of the composite. The second pressing stage, in which the composite experiences the highest load, was carried out under the HP2 cycle, allowing elastic recovery of the PLA and avoiding permanent deformation. This ensured that the PLA structures remained centered, preventing asymmetric channel positioning.

In summary, pressing strategies were optimized in two steps:

1. HP2 minimized permanent deformation of PLA and prevented cracks in the channel region.
2. Two-stage pressing ensured centered channels in multi-layer inserts, improving reproducibility and symmetry in wheel fabrication.

4.3.3 Drying Stage

After pressing, a drying stage is required to remove water from the binder and consolidate the green composite before sintering. The heating rate is a key parameter: if too high, it may cause abrupt dimensional changes and crack formation; if too low, it extends processing time but promotes more gradual and stable drying. To investigate this effect, structured composites with the B7.5 formulation and a Y-shaped PLA insert were analyzed at different heating rates (0.1, 1.0 and 4.0 °C/min). The dimensional variations are presented in Figure 4.10a–b.

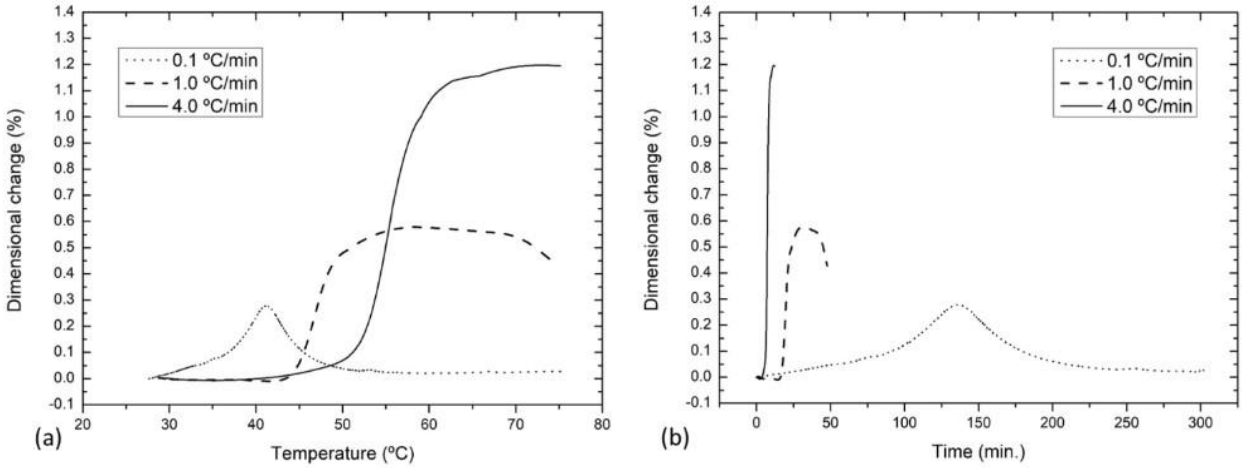


Figure 4.10 – Dimensional analysis (TMA) of B7.5 abrasive composite with incorporated PLA structure in green, as a function of heating rates (0.1, 1.0 and 4.0 °C/min): (a) temperature-dependent; (b) time-dependent.

The results confirmed that drying rate strongly affects dimensional stability. At the highest rate (4.0 °C/min), expansion was abrupt and reached values close to 1.2 %, creating conditions that favor crack formation in the green body. At 1.0 °C/min, the effect was attenuated but still visible, with noticeable local instabilities. At the lowest rate (0.1 °C/min), expansion was gradual and limited (below 0.3 %), substantially reducing the risk of cracking, although at the expense of significantly longer drying times.

In summary, although the slower ramp increases processing time, a heating rate of 0.1 °C/min was selected as the optimal drying condition, as it minimizes dimensional instabilities and prevents crack formation in composites containing PLA structures.

4.3.4 Sintering Stage

After drying, the organic binder hardens, increasing the stiffness and consistency of the green composite. The subsequent step is sintering, which consolidates the vitrified bond and finalizes the structure of the wheel.

In this work, sintering was performed at 950 °C for 240 minutes, i.e. the same maximum temperature typically used for conventional vitrified wheels, with the same bond precursor [48–50].

During the sintering step in air atmosphere, all organic components are first eliminated by combustion. In conventional composites, this includes the dried polysaccharide binder, whereas, in structured composites, the PLA inserts are also pyrolyzed, leaving behind a continuous network of hollow channels that define the internal lubrication network. The thermal cycle must therefore ensure complete burnout of organics before the vitrified bond precursor softens (glass softening, approx. 620 °C). As shown in the thermal analyses, both the PLA and the polysaccharide binder decompose fully below 500 °C, well before vitrification begins.

With these conditions established, no further modifications to the conventional sintering protocol were required. The optimized drying stage ensured defect-free green bodies and the adopted firing cycle successfully delivered complete burnout of organics together with stable consolidation of the vitrified bond. These adjustments ensured stable sintering without additional modifications.

4.4 Final Characterization of Produced Wheels

After defining the optimal processing method, it is essential to evaluate whether the manufactured grinding wheels effectively preserved the intended design and meet the requirements for practical application. This stage focuses on the dimensional control of the channel structures, verifying the geometric fidelity between the PLA precursor and the sintered wheel, as well as the overall reproducibility of the process. In addition, wear resistance tests were conducted to assess the mechanical performance of the structured composites in comparison with conventional wheels. Finally, a microstructural analysis by SEM was performed, providing detailed insight into the abrasive grains, vitrified bond and porosity distribution. Together, these analyses consolidate the validation of the developed methodology, confirming both the functional integrity and the durability of the structured grinding wheels.

4.4.1 Dimensional Control

Dimensional control was carried out to evaluate the geometric fidelity between the PLA precursors and the channels obtained after sintering. Two types of discs were produced: a reference disc without internal channels and a structured disc with a hexagonal network of channels distributed over three layers. Figure 4.11 shows these configurations, including the PLA structure used as a precursor, the structured disc after sintering and the corresponding cross-section where the channel network can be observed throughout the

wheel thickness. The PLA structure was initially printed with channels of approximately 0.50 mm in width and 4.50 mm in height. After sintering, these dimensions were well preserved, with average values of 0.52 ± 0.02 mm and 4.54 ± 0.12 mm, respectively.

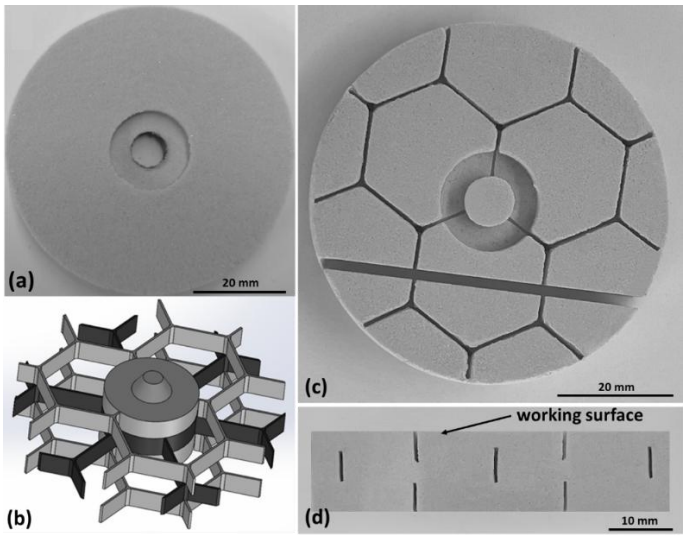


Figure 4.11 – (a) Unstructured reference disc. (b) Perspective view of the PLA structure. (c) Surface view of the hexagonal structured abrasive grinding wheel prototype. (d) Internal view of the grinding wheel, with the 3D internal cooling system.

Table 4.4 summarizes the main dimensional characteristics of the PLA precursor, the reference disc and the structured disc. The total cavity volume increased slightly (from 40.0 ± 2.8 % to 41.4 ± 3.0 %), while the active grinding surface decreased by only 3.9 %. These results demonstrate that the introduction of internal channels maintains dimensional fidelity relative to the precursor and does not significantly compromise the available cutting surface.

Table 4.4 – Dimensional characteristics of the PLA structure, the reference disc and the structured disc.

Characteristic	**CAD**	**Reference disc**	**Structured disc**
Outer diameter (mm)	–	62.3	62.3
Thickness (mm)	–	13.00 ± 0.19	13.00 ± 0.19
Channel width (mm)	0.50	–	0.52 ± 0.02
Channel height (mm)	4.50	–	4.54 ± 0.12
Porosity + channel volume (%)	–	40.00 ± 2.83	41.36 ± 2.96
Active grinding surface (%)	–	100.0	96.1 ± 0.2

4.4.2 Microstructural Analysis

The microstructural analysis was carried out by SEM to evaluate the integrity of the structured wheels after sintering. Figure 4.12 shows representative images of the structured disc, highlighting the distribution of abrasive grains, vitrified bond and pores. The cross-section of the channels confirmed that the decomposition of the PLA precursor was complete, leaving clean cavities with good geometric reproducibility and without evidence of residues or localized defects.

The abrasive grains were uniformly embedded in the vitrified matrix, with no signs of abnormal grain pull-out or bond disruption. The porosity distribution was homogeneous across the microstructure, confirming that the sacrificial PLA inserts did not interfere with composite consolidation. Near the channel walls, the bond phase remained continuous and well adhered to the abrasive particles, further demonstrating the structural stability of the regions adjacent to the cavities.

This analysis demonstrates that the proposed processing method allows the integration of internal channels without compromising the microstructural integrity of the wheel, ensuring both uniform bonding and a defect-free interface around the channels.

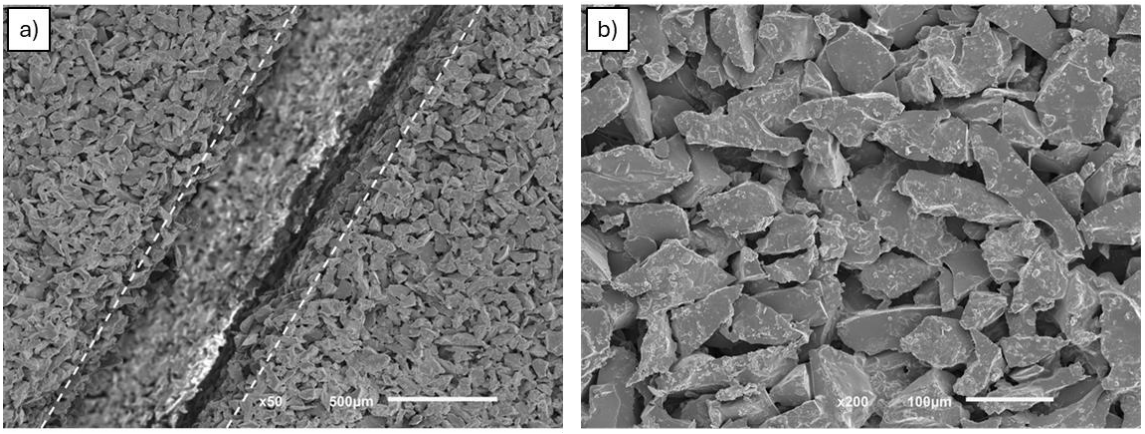


Figure 4.12 – SEM images of the structured grinding wheel after sintering: (a) cross-section of the channel region, showing a continuous vitrified bond around the cavity and absence of residues; (b) detail of the abrasive grains embedded in the vitrified matrix, with homogeneous porosity distribution.

4.4.3 Wear Tests

Wear resistance tests were performed to compare the performance of the structured wheel with that of the conventional reference. The results are shown in Figure 4.13.

The disc wear rate (Figure 4.13a) revealed a strong improvement with the structured configuration. The reference disc exhibited a mean wear rate of ≈2.0 $\times 10^{-5}$ g/m, whereas the structured wheel showed only

≈0.75 $\times 10^{5}$ g/m, corresponding to a reduction of approximately 62 %. This demonstrates the significant durability gain obtained with the presence of internal channels. For the alumina pins (Figure 4.13b), the structured wheel also performed better, reducing the wear rate from ≈0.6 $\times 10^{6}$ g/m in the reference condition to ≈0.5 $\times 10^{6}$ g/m.

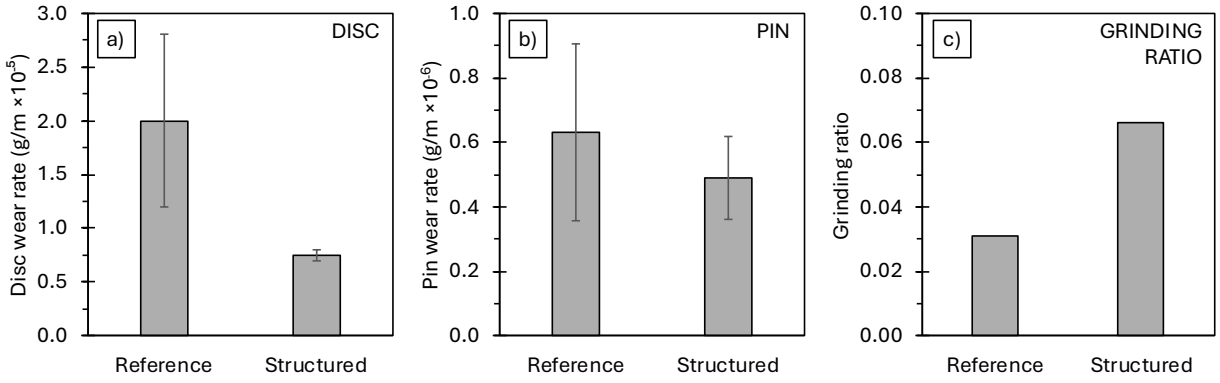


Figure 4.13 – Results of the wear tests: wear rate of the grinding discs (a) and the alumina pins (b); G-ratio for the reference and structured wheels (c).

The G-ratio (Figure 4.13c) more than doubled with the structured wheel, increasing from ≈0.03 in the reference to ≈0.065, which represents an improvement of approximately 117 %. This result confirms that the structured configuration not only reduces wear but also improves overall grinding efficiency. This improvement is most likely associated with tribological mechanisms provided by the channel network, including enhanced debris removal, increased chip accommodation space and reduced secondary abrasion on the counter body.

4.5 Summary and Conclusions

In this chapter, the manufacturing methodology for structured vitrified grinding wheels with internal channels was developed and optimized. Each processing step was examined to address the main challenges introduced by sacrificial PLA inserts, from binder formulation to pressing, drying and sintering steps. Thermal and thermomechanical analyses guided these adjustments, resulting in a robust processing method for defect-free composites. Beyond process optimization, the first validations confirmed dimensional fidelity, microstructural integrity and improved wear resistance of the structured wheels. The resulting set of optimal parameters is summarized in Table 4.5.

Table 4.5 – Optimal processing conditions established for the fabrication of structured abrasive composites with PLA inserts, including binder formulation, pressing, drying and sintering parameters.

Stage	Optimal condition	Key outcome
Binder formulation	W30 polysaccharide solution; 7.5 wt. % binder	Adequate plasticity and dimensional stability; minimized cracking risk
Pressing strategy	Hot pressing HP2; two-step pressing for multi-layer inserts	Reduced PLA deformation; elimination of cracks; centered channels
Drying	Heating ramp of 0.1 °C/min up to 75 °C	Gradual water removal; defect-free green bodies
Sintering	Conventional vitrified cycle up to 950 °C	Complete burnout of organics before vitrification; stable bond consolidation

The optimization of the processing method showed that binder formulation, pressing strategy, drying conditions and sintering cycle were all critical to accommodate sacrificial PLA inserts. The W30 solution with 7.5 wt. % binder ensured adequate plasticity and green strength, while hot pressing under HP2 minimized insert deformation and eliminated cracks. For multi-layer structures, a two-step pressing sequence was required to keep channels centered and slow drying at 0.1 °C/min prevented dimensional instabilities. Under these conditions, sintering could follow the conventional vitrified cycle at 950 °C, since both PLA and binder decomposed fully below 500 °C.

The fabricated wheels exhibited high dimensional fidelity, with deviations of only approx. 1 % in channel height and approx. 4 % in channel width relative to the PLA precursors. SEM analysis confirmed complete polymer burnout, a continuous vitrified bond around the channels and homogeneous porosity, while wear tests demonstrated approx. 62 % reduction in disc wear rate and a 117 % increase in grinding ratio compared to the reference.

Overall, the developed methodology provides a robust and reproducible method for producing vitrified wheels with internal channels, fully compatible with industrial processing. By integrating additive manufacturing of sacrificial preforms with optimized processing parameters, it was possible to fabricate defect-free wheels that preserved dimensional and microstructural integrity while achieving significantly improved wear performance. These advances establish a solid foundation for the experimental validation presented in the next chapter.

5. NUMERICAL MODELING OF COOLANT FLOW IN STRUCTURED GRINDING WHEELS

The performance of structured grinding wheels strongly depends on the ability of the internal channels to transport coolant efficiently to the grinding zone. Numerical modeling offers a powerful tool to analyze these flows, providing detailed insights into velocity fields, outlet distributions and the effect of channel geometry. However, given the complexity of multiphase and rotating flows, a careful definition of the computational domain, the mesh, physical models and the post-processing indicators is required to ensure that the results are both physically meaningful and experimentally verifiable.

This chapter presents the numerical framework developed to simulate coolant flow in structured grinding wheels and its experimental validation via high-speed imaging. Two complementary CFD setups were designed: Setup A, aimed at qualitatively visualizing external coolant dispersion and Setup B, focused on quantitatively predicting internal velocities and outlet profiles. Specific flow indicators were defined to interpret the coolant behavior and the predictions were validated through particle-tracking experiments performed on transparent resin wheel replicas.

The work presented in this chapter was disseminated through two publications in *Applied Thermal Engineering*: "*CFD analysis of multi-layer cooling channels in three-dimensionally structured grinding wheels"* [224] and "*Coolant Flow in Structured Grinding Wheels: CFD Validation via High-Speed Imaging and Particle Tracking" [225]*.

5.1 Modeling Strategy

The complexity of coolant transport in structured grinding wheels requires different modeling strategies depending on the physical phenomena of interest. A single numerical setup is not sufficient to capture simultaneously the global dispersion of fluid around the wheel, its interaction with the workpiece and the quantitative determination of outlet velocities inside the channels. To address this challenge, two complementary computational domains were developed in this thesis, each tailored to specific objectives.

Setup A was conceived as a multiphase model with a surrounding control volume, designed to reproduce the coexistence of air and water and to visualize coolant dispersion in the grinding environment. This configuration

enabled the analysis of how jets emerging from the internal channels mixed with the surrounding air and reached the workpiece surface, thus providing insight into the effectiveness of fluid delivery at the grinding interface. However, an inherent limitation of this approach is that the channel outlets are modeled as sliding interfaces in contact with the external air domain. As a result, post-processing planes cannot be positioned exactly at the channel exits, restricting the extraction of precise outlet velocity profiles. Setup A is therefore limited to qualitative visualization of fluid dispersion.

Setup B was developed to quantify coolant velocities inside the channels and at their outlets. This single-phase model employed a Relative Velocity Formulation under *MRF*, with the external air domain removed. By neglecting the air phase and isolating the pressure-driven component of the flow from the solid-body rotation, Setup B enabled robust predictions directly at the channel outlets. Post-processing indicators such as outlet velocity contours, streamline trajectories and cross-sectional velocity profiles provided clear outputs, allowing a detailed characterization of jet formation, near-wall losses and velocity uniformity. Crucially, these numerical predictions were validated experimentally through high-speed imaging and particle tracking. Both manual measurements and automatic processing with *TrackMate® plugin* (Fiji/ImageJ) confirmed the CFD predictions within approx. 16 % difference, reinforcing the physical consistency of Setup B.

Together, the two setups provide a comprehensive framework for analyzing coolant flow in structured grinding wheels. Setup A captures the external dispersion of the jets and their interaction with the air and the workpiece, while Setup B delivers quantitative velocity data within the wheel and channels. Applied in combination, they allow the complete description of the cooling process, bridging numerical predictions with experimental validation and establishing a robust methodology for future parametric studies. Moreover, the design of the internal channel system used in the experimental tests (Chapter 6 and 7) was defined based on the results obtained in the simulation phase.

5.2 Preliminary Modeling Choices

Before defining the full numerical setups, some preliminary modeling decisions had to be established to ensure physical consistency and comparability with experimental results. These choices included the definition of the velocity formulation, the appropriate turbulence treatment and the basic boundary conditions to be applied in each setup. Although these aspects may seem secondary, they strongly affect the interpretation of the results, especially in systems where rigid-body rotation, multiphase interactions and shear

instabilities coexist. This section therefore presents the rationale for these modeling decisions, establishing the foundation for the subsequent configuration of Setup A and Setup B.

5.2.1 Velocity Formulation

The correct choice of velocity formulation is critical for interpreting the coolant flow inside the wheel channels and at their outlets. As expressed in Eq. (5.1), the absolute velocity in a rotating system is the sum of the relative velocity and the rigid-body rotational component [226,227].

$$\vec{V}_{abs} = \vec{V}_{rel} + \vec{\Omega} \times \vec{\mathrm{r}} \tag{5.1}$$

where $\vec{V}_{abs}$ is the velocity in the stationary frame, $\vec{V}_{rel}$ is the velocity relative to the rotating wheel, $\vec{\Omega}$ is the angular velocity vector and $\vec{\mathrm{r}}$ is the position vector relative to the rotation axis.

When the absolute velocity formulation is used, the outlet velocity profiles include both the fluid motion induced by the pressure drop along the channel and the tangential velocity imposed by the wheel rotation $\left(\vec{\Omega} \times \vec{\mathrm{r}}\right)$. This superposition leads to artificially elevated outlet velocities, dominated by rigid-body rotation, which do not represent the actual transport capacity of the coolant through the channels. Furthermore, the resulting profiles show non-physical near-wall behavior, where velocity remains high instead of tending to zero.

In contrast, when the relative velocity formulation is applied, the rigid-body component is removed and the velocity field is evaluated in the rotating reference frame of the wheel. This ensures that the outlet profile reflects only the pressure-driven jet structure. In this case, the no-slip boundary condition is satisfied, as expressed in Eq. (5.2), where the relative velocity at the channel walls tends to zero:

$$\vec{V}_{rel} = 0 \qquad \textit{at the channel walls} \tag{5.2}$$

which ensures physically consistent predictions, with velocity smoothly decreasing to zero at the boundaries. As a result, the relative velocity field isolates the actual flow through the channels, enabling meaningful comparisons with experimental measurements after subtracting the rigid-body rotational component.

To illustrate the difference between the two formulations, Figure 5.1 shows velocity contours at the outlet cross-section of a representative channel, for simulations performed under identical conditions (1 Layer; 30 channels; Ø 1.6 mm; 5000 rpm; 800 mL/min). In the absolute formulation (Figure 5.1a), the velocity

magnitudes are artificially high and dominated by wheel rotation, while the near-wall velocities remain nonzero. In the relative formulation (Figure 5.1b), the outlet profile is physically consistent, with zero velocity at the walls and a clearly defined jet structure.

The relative velocity formulation is numerically more demanding, as it requires velocity transformations and finer near-wall resolution. For this reason, it was not used in the multiphase Setup A, whose objective is limited to qualitative visualization of coolant dispersion. In this case, the use of absolute velocity is sufficient to describe the global interaction between water and air, while the detailed evaluation of outlet profiles is carried out exclusively in Setup B.

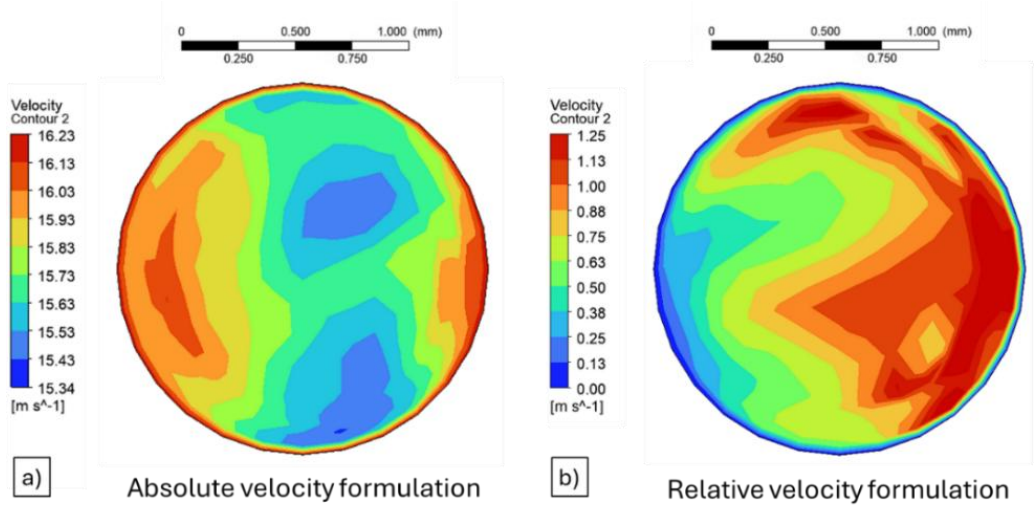


Figure 5.1 – Velocity profiles at the channel outlet with different formulations: (a) absolute velocity, dominated by wheel rotation; (b) relative velocity, showing a physically consistent jet with zero velocity at the walls. Simulation conditions: 5000 rpm, 800 mL/min.

This distinction ensures that each velocity formulation remains aligned with its intended purpose. Having clarified this fundamental aspect, the next step is to examine how turbulence is represented within the numerical model.

5.2.2 Turbulence Modeling

The choice of turbulence modeling is directly dependent on the Reynolds number of the internal channel flow, defined by Eq. (5.3) [228]:

$$\boldsymbol{Re = \frac{\rho U D}{\mu}} \tag{5.3}$$

where U is the mean velocity inside the channel, D the channel diameter (or hydraulic diameter for non-circular sections), ρ the fluid density and μ the dynamic viscosity of the fluid. According to classical criteria, laminar flow dominates for $Re < 2000$, transition occurs for $2000 < Re < 4000$ and turbulence is fully established above $Re > 4000$.

Based on the geometries tested experimentally, Reynolds numbers were calculated for the maximum flow rate of 800 mL/min. Table 5.1 presents representative cases, corresponding to the lowest, median and highest values obtained in Setup B.

Table 5.1 – Reynolds numbers for selected cases under a maximum flow rate of 800 mL/min (water at 20 °C, Setup B conditions, 0 rpm).

Case	**Channel configuration (diameter × number)**	U **(m/s)**	**Reynolds number**
Low	0.6 mm × 190 channels	0.25	149
Medium	1.6 mm × 30 channels	0.22	354
High	1.0 mm × 30 channels	0.57	566

These results demonstrate that, under the simulation conditions of Setup B, where the focus is the flow inside the channels, the regime remains fully laminar ($Re < 600$). Accordingly, a laminar model was adopted in this setup, which is physically consistent and avoids artificial diffusion associated with turbulence models at low Reynolds numbers. Furthermore, this choice ensures reliable comparison with experimental particle-tracking results, which also reflect laminar flow conditions.

As already mentioned, Setup A was designed to analyze the dispersion of coolant in the external environment, including the mixing of water jets with air and their impact on the workpiece surface. Although the flow inside the channels is laminar, once the jets emerge into the air domain, they are subjected to strong shear instabilities (e.g., *Kelvin–Helmholtz* mechanisms), which can rapidly promote transition and turbulence [199,229,230]. Widely employed for turbulent flows in industrial applications, including flow around solid surfaces and fluid jets, the *realizable* $k - \varepsilon$ two-equation model was the turbulence model was therefore selected [195,196]. The *realizable* version was chosen for its robustness in improving the accuracy of highly distorted flows, such as those occurring in the interaction between the coolant and the workpiece [190,192].

Another important consideration is that Setup A was conceived mainly for qualitative analysis. For this reason, some simulations were deliberately conducted with extrapolated flow rates above the experimental maximum, to better visualize dispersion and entrainment mechanisms in the external domain. Since higher flow rates proportionally increase the mean velocity, they also raise the Reynolds number, reinforcing the need for turbulence modeling in this setup.

Finally, even in the case of the optimization study focused on maximizing outlet velocity, the flow remained below the transition threshold. The highest mean velocity achieved was approximately 1.1 m/s (obtained in the high-rotation case at 5000 rpm), corresponding to a $Re \approx 1800$, which still falls within the laminar regime, albeit close to the transitional range. This confirms that, for all experimentally relevant cases, the internal flow remains laminar, whereas turbulence is mainly associated with the external mixing of jets.

In summary, turbulence modeling was selected according to the physical nature and objectives of each setup:

- **Setup A (multiphase external air domain):** *realizable* $k - \varepsilon$ turbulence model, justified by jet shear instabilities and by the use of extrapolated flow rates for qualitative visualization.
- **Setup B (single-phase internal domain):** laminar model, consistent with the Reynolds numbers.

With these preliminary modeling choices defined, the following section introduces Setup A, detailing its computational domain, mesh strategy and physical models.

5.3 Setup A: Multiphase Model with Control Volume

Setup A was designed to reproduce the coexistence of air and water in the grinding environment, with the objective of evaluating the coolant dispersion around the wheel and its interaction with the workpiece surface. Unlike simplified single-phase domains, this model incorporated a surrounding control volume of air, allowing the analysis of how the jets emerging from the internal channels mix with the surrounding medium and reach the contact zone.

5.3.1 Geometric Model and Computational Domain

The geometric model consists of a structured abrasive wheel with internal cooling channels, positioned above the workpiece. Coolant is supplied through the central axis of the wheel, distributed through the internal channels and reaches the vicinity of the grinding interface. To analyze how the fluid mixes with the

surrounding air and spreads across the workpiece, a control-volume box was created around the wheel [195,196,198]. This external air domain (control-volume box) represents the ambient atmosphere; its lateral and top boundaries were defined as openings to impose atmospheric pressure and allow natural outflow (Figure 5.2). The schematic also highlights the wheel rotation direction, which governs coolant dispersion over the workpiece surface.

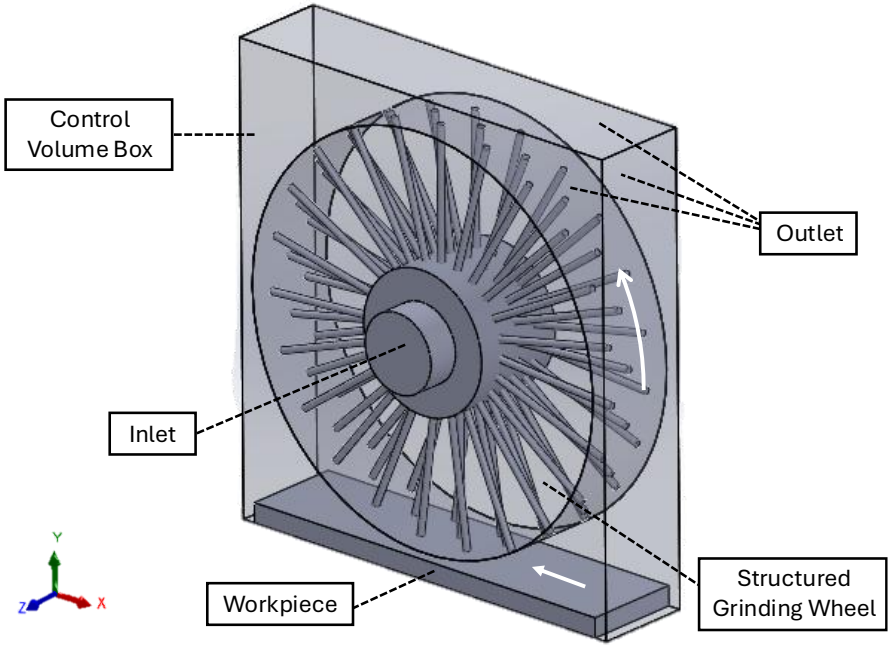


Figure 5.2 – Grinding wheel and fluid domain model.

The wheel has an outer diameter of 62 mm, a central bore of 21 mm and a width of 15 mm (Figure 5.3). It is mounted on a 12 mm diameter shaft, which simultaneously provides structural support and delivers coolant to the central bore. Before entering the internal channels, the central cavity of the wheel acts as a plenum chamber, temporarily accumulating the incoming flow and ensuring uniform distribution to the channel inlets. The wheel center aligns with the Z-axis, which was defined as the axis of rotation in the simulations.

A clearance of 1 mm was maintained between the wheel and the workpiece to facilitate mesh generation and ensure numerical stability, especially considering the complexity of the rotating multi-channel geometry. This modeling strategy is consistent with approaches used in previous CFD studies on grinding wheels [196]. It is important to note that the objective of this setup is to evaluate coolant transport and dispersion near the grinding zone, rather than to reproduce the mechanical interaction between abrasive grains and the workpiece.

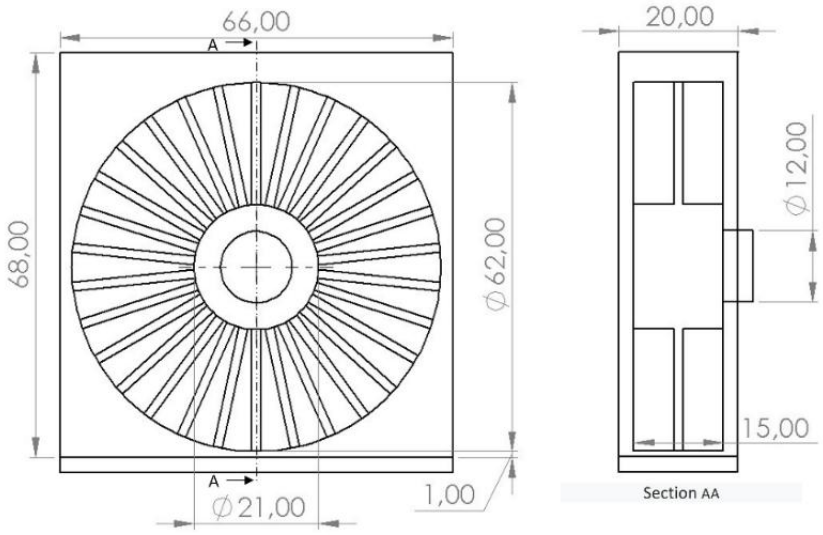


Figure 5.3 – Dimensional drawing of the structured grinding wheel used in simulations.

5.3.2 Mesh Generation and Independence Study

The computational domain was discretized using polyhedral elements, selected for their robustness in handling complex multi-channel geometries while ensuring stable numerical convergence. Local refinements were applied in the internal cooling channels, in the wheel center and in the 1 mm clearance above the workpiece, while coarser cells were adopted in the external control-volume box to limit the overall mesh size without affecting the solution in the regions of interest.

Mesh independence was verified through a convergence test using a wheel geometry with one channel layer (18 channels, 1.0 mm diameter, 90° inclination). The number of elements was progressively increased and the corresponding water mass flow rate across a monitoring surface located at the grinding zone was monitored as the convergence criterion.

As shown in Figure 5.4, the results stabilized for meshes containing approximately three million elements, indicating that further refinement would not significantly alter the outcome. Based on this, a mesh with about 3.3 million elements was adopted for all subsequent simulations. The typical element size was set to 0.1 mm in the cooling channels and in the grinding gap, 0.4 mm in the external control volume and 0.5 mm in the wheel center and at the fluid inlet region.

This configuration ensured an adequate balance between computational efficiency and physical fidelity, capturing the essential flow features in the channel outlets and in the contact region while keeping the simulation time within reasonable limits.

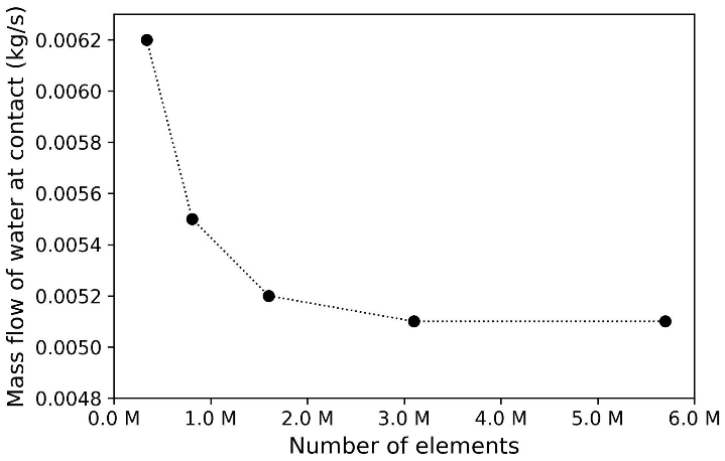


Figure 5.4 – Mesh convergence test results: relationship between the number of elements and the mass flow rate of water at the contact surface between the grinding wheel and the workpiece.

5.3.3 Physical Models

The abrasive wheel was modeled as a solid body without porosity and water was adopted as the cooling fluid. These simplifications avoided unnecessary complexity while keeping the focus on the coolant–workpiece interaction.

A multiphase approach was employed to represent the immiscible phases (air and water). The Volume of Fluid (VOF) model was chosen for its ability to capture the interface between phases, allowing a proper evaluation of the coolant reaching the workpiece surface [120,182,198]. The implicit time formulation was selected to enhance numerical stability and reduce processing time [191,231,232], while the dispersed phase option was activated to model water distributed in the continuous air phase [192]. The surface tension between air and water was set to 0.0728 N/m [187,233] and gravity was applied toward the workpiece.

As discussed, the absolute velocity formulation was used in this setup, since the objective was limited to qualitative visualization of coolant dispersion outside the wheel. Turbulence effects were modeled with the *realizable* $k - \varepsilon$ approach.

Wheel rotation was simulated using the *MRF* method, appropriate for steady-state analysis [234,235]. In this configuration, the wheel center was defined as the rotating region and the shaft and internal channel domains were assigned the same angular velocity. This approach was necessary because the coolant flows inside a geometry that is physically attached to the wheel: as the wheel spins, both the shaft and the channel walls move with the same angular velocity. Defining all these regions within the same rotating frame ensures that

the relative motion between fluid and solid boundaries is properly captured, while avoiding artificial shear effects that would appear if only the wheel center was assigned to rotation. Simulations were conducted with different wheel speeds and inlet flow rates, depending on the specific case under study.

Boundary conditions were defined as a mass-flow inlet at the wheel shaft, while the external boundaries of the control volume box were set as pressure outlets, allowing the coolant to leave the domain naturally at atmospheric pressure.

The Coupled algorithm was employed for simultaneous solution of pressure and velocity fields, with the Volume Fractions option activated [236]. A fixed global time step was used to guarantee numerical stability throughout the steady-state simulation [231]. Convergence was considered achieved when the residual criterion of 1×10^{-4} was satisfied and the mass-flow balance remained stable. The main setup configurations are summarized in Table 5.2.

Table 5.2 – Summary of simulation parameters used in Setup A.

Parameter	**Configuration**
Multiphase model	VOF: Implicit, Dispersed
Phase interaction	Surface tension air–water: 0.0728 N/m
Fluid properties [237]	Air – Density: 1.225 kg/m³; Viscosity: 1.79×10^{-5} kg/(m·s) Water – Density: 998.2 kg/m³; Viscosity: 1.00×10^{-3} kg/(m·s)
Velocity formulation	Absolute
Turbulence model	k-ε (2 eqn); realizable $k-\varepsilon$
Rotation method	*MRF*; wheel center, shaft and channels rotating together
Boundary conditions	Inlet: mass flow inlet at the shaft Outlet: pressure outlets, free flow to the environment
Wall treatment	No-slip
Numerical scheme	Coupled with Volume Fractions activated; second-order discretization
Gravity	Acting toward the workpiece
Convergence criteria	Residuals < 10^{-4} and stable mass-flow balance

5.3.4 Post-processing Indicators

The CFD simulations generated detailed three-dimensional flow fields, but interpreting these results requires specific indicators that provide a clearer view of how the coolant interacts with the grinding zone. Post-processing procedures were therefore defined to translate the raw simulation data into parameters that, although not strictly quantitative in all cases, are physically meaningful and related to the cooling performance of the wheel. The selected indicators include the water volume fraction, the mass-flow rate and the velocity field. Together, they allow a complementary analysis ranging from the qualitative visualization of coolant dispersion and coverage to a comparative assessment of how much fluid effectively reaches the contact zone. This section describes how each indicator was extracted in *ANSYS CFD-Post* and discusses its significance for evaluating different wheel geometries. As an example, results are presented for a grinding wheel with 30 radial channels of 1.5 mm diameter, distributed in three layers of 10 channels each (2000 rpm; 3 L/min). It should be noted that the use of extrapolated flow rates in Setup A does not aim at quantitative predictions. It should be noted that the use of extrapolated flow rates in Setup A was not intended to produce quantitative predictions, but rather to enhance jet visualization and highlight dispersion and entrainment mechanisms in the external domain.

Water Volume Fraction

The water volume fraction is a scalar variable that quantifies the proportion of water in a given computational cell, ranging from 0 (pure air) to 1 (pure water). In multiphase simulations with the VOF model, this parameter is essential to visualize the coolant distribution, identify preferential flow paths and evaluate how much water effectively reaches the grinding interface. Figure 5.5 illustrates different post-processing views of the water volume fraction field.

- Figure 5.5a shows the contour of water volume fraction across one of the channel layers. To obtain this plot, a plane coincident with the selected layer was created and the variable Volume Fraction of Water (Phase 2) was displayed as a contour map. This representation highlights the distribution of coolant inside and around the channels, evidencing how water is transported toward the external surface of the wheel.
- Figure 5.5b presents the contour of water volume fraction on the workpiece surface. In this case, a plane coincident with the surface of the workpiece was defined and the variable Volume Fraction of

Water was again plotted as a contour. This view provides a direct indication of how much coolant effectively reaches the contact zone and how it spreads across the width of the workpiece.

- Figure 5.5c brings a more quantitative perspective. A line was created along the grinding contact region, positioned at the workpiece surface where the wheel approaches the closest. The variable Volume Fraction of Water was then sampled along this line and the results were exported as an XY plot. In the horizontal axis (X), the Z-coordinate across the workpiece width is represented, while the vertical axis (Y) corresponds to the local water volume fraction. This profile allows evaluating the coolant coverage along the contact width and enables direct comparison across different wheel geometries.

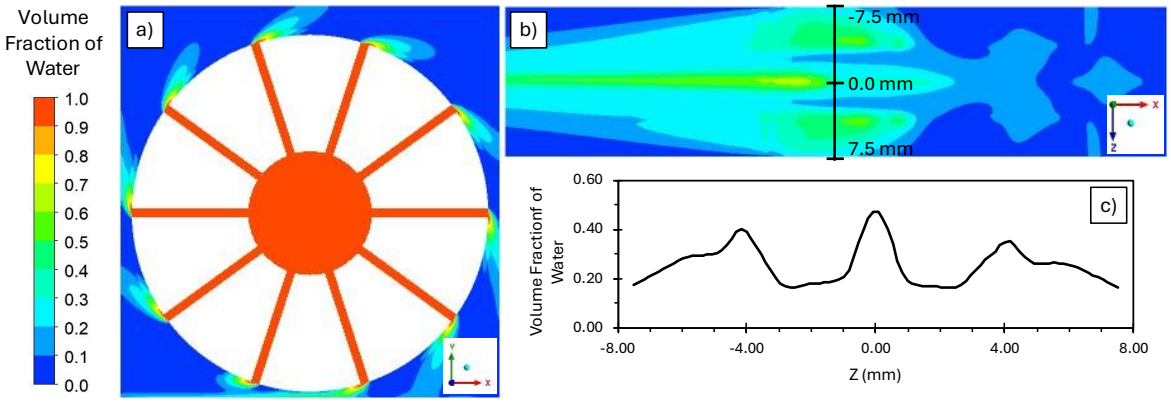


Figure 5.5 – Water volume fraction obtained for a grinding wheel with 30 radial channels of 1.5 mm diameter distributed in three layers (10 channels per layer): (a) contour on a plane crossing one of the channel layers; (b) contour on the workpiece surface; (c) water volume fraction profile extracted along the contact line on the workpiece surface.

Mass Flow Rate

The mass flow rate is a fundamental indicator of fluid transport, defined as the total mass of fluid crossing a given surface per unit time. In the context of grinding, it directly represents the quantity of coolant reaching the contact zone and, therefore, the potential to remove heat and reduce friction during the process. A higher mass flow rate into the grinding interface is associated with improved lubrication and cooling, while lower values indicate limited fluid penetration and a higher risk of thermal damage. For this reason, the mass flow rate was adopted as one of the primary quantitative parameters in the present analysis.

To evaluate this indicator numerically, a contact plane was created perpendicular to the grinding wheel axis and positioned at the contact region, where the wheel approaches the workpiece. The plane dimensions were

defined as 1 mm in height (representing the clearance between wheel and workpiece and 15 mm in width, corresponding to the wheel width). Once this plane was defined, the Calculator tool in *ANSYS CFD-Post* was used to integrate the variable Mass Flow Rate, selecting specifically the water phase so that only the coolant contribution was considered. The result corresponds to the effective mass of water crossing into the grinding zone, accounting simultaneously for the velocity field and the multiphase distribution. This provides a direct measure of how much coolant is actually delivered to the contact, enabling quantitative comparison across different wheel geometries and operating conditions and complementing the qualitative information extracted from the water volume fraction fields.

Velocity Field

The velocity field around the grinding wheel was also analyzed to visualize how the coolant disperses once it exits the channels and interacts with the surrounding air. Although Setup A was not designed to provide accurate values of the internal flow inside the channels, it offers useful qualitative information about the external jet behavior.

Two complementary representations were used for this purpose. In the first approach, Figure 5.6a, a contour plot of velocity magnitude was generated on planes surrounding the wheel, highlighting regions of higher jet momentum and showing how the coolant spreads over the wheel periphery and towards the workpiece surface. This was obtained in *ANSYS CFD-Post* by creating a plane around the wheel and selecting Velocity Magnitude as the contour variable, with a color scale extending from 0 to 8 m/s.

In the second approach, Figure 5.6b, velocity vectors were plotted in the same region to provide a clearer picture of the jet trajectories and recirculation zones induced by the wheel rotation. In *CFD-Post*, this was done by selecting Vector as the display type and using Velocity as the variable, adjusting the arrow scaling and color map to improve visualization. The same velocity scale used in the contour plot (0–8 m/s) was applied to the vectors, ensuring direct and consistent comparison between the two representations.

As illustrated in Figure 5.6, the contour plot (part a) highlights the external velocity distribution around the wheel, while the vector plot (part b) emphasizes the direction and deflection of the jets.

These indicators confirm that Setup A is suitable for analyzing external dispersion, but not for quantifying internal velocities. For this quantitative evaluation, a second configuration was required. Setup B therefore

focuses on the internal domain of the wheel and adopts a relative velocity formulation to predict outlet velocity profiles with higher accuracy.

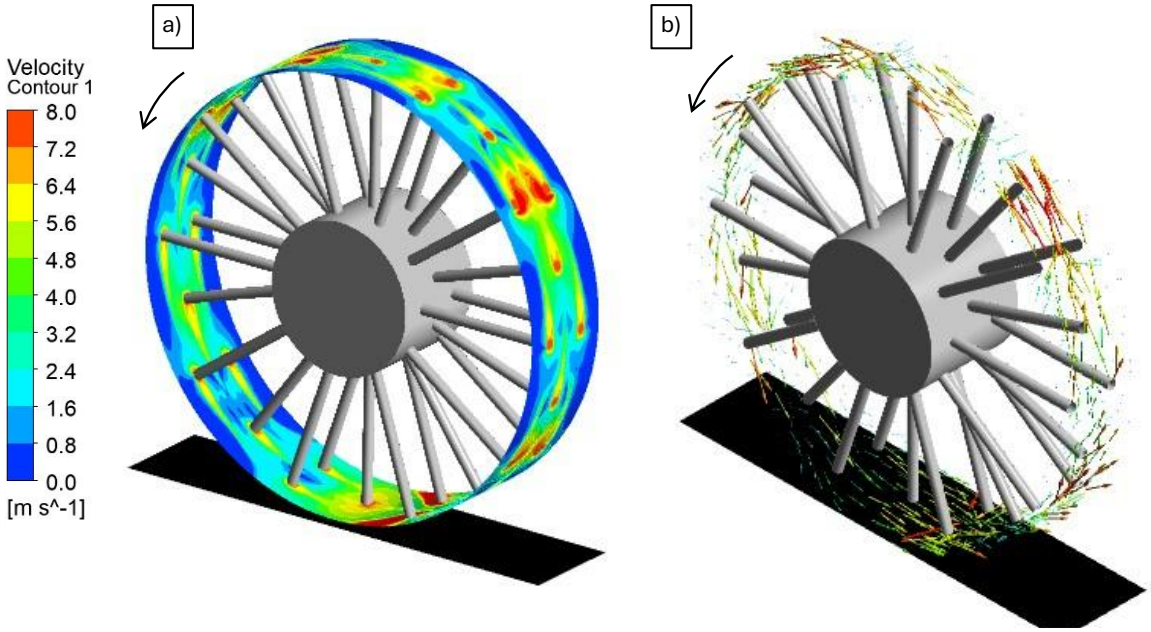


Figure 5.6 – Velocity field around the grinding wheel obtained from Setup A: (a) contour of velocity magnitude, (b) velocity vectors illustrating jet trajectories and recirculation. Both representations share the same velocity scale (0–8 m/s).

5.4 Setup B: Relative Velocity Model (Single-phase)

Setup B was developed to quantify coolant velocities inside the wheel channels and at their outlets. In contrast to Setup A, this setup restricted the computational domain to the shaft, the wheel center and the channels. By adopting a single-phase model with a relative velocity formulation under a rotating reference frame, this configuration isolated the pressure-driven component of the flow from the solid-body rotation. As a result, it enabled accurate prediction of outlet velocity profiles, providing the quantitative data necessary for validation against high-speed imaging experiments and for subsequent parametric studies of channel geometry.

5.4.1 Geometric Model and Computational Domain

In Setup B, the computational domain was restricted to the internal regions of the grinding wheel, comprising the shaft, the central plenum chamber and the cooling channels. In this configuration, the focus was exclusively on the internal flow and on the outlet conditions, ensuring higher geometric fidelity to the real system.

A key distinction is that the shaft was modeled in greater detail. While in Setup A the fluid inlet was simplified as a single chamber connected directly to the channel network, in Setup B, the coolant supply followed the actual distribution used in the experimental machine. As illustrated in Figure 5.7, the shaft outlet was represented by three rows of holes, with three ports each, equally spaced around the shaft circumference. This reproduced the real feeding pattern into the wheel center, providing a more accurate prediction of the pressure balance and the flow uniformity at the channel inlets.

The computational domain was divided into three main regions: the shaft, the wheel center and the cooling channels. The inlet boundary condition was defined at the shaft, while the channel outlets were defined as the outlet surfaces, as indicated in Figure 5.7. The wheel geometry was consistent with the experimental prototypes, with an outer diameter of 62 mm, a width of 15 mm, a central bore of 21 mm and a shaft diameter of 12 mm aligned with the axis of rotation.

This level of geometric detail ensured that the inlet distribution was accurately reproduced, which is critical for obtaining realistic velocity profiles at the channel outlets.

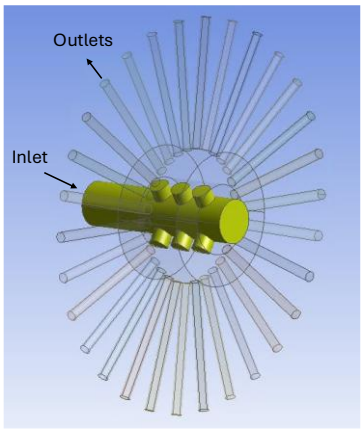


Figure 5.7 – Computational domain used in Setup B. The inlet was defined at the shaft and the channel outlets were set as outlet boundaries.

5.4.2 Mesh Generation and Independence Study

The computational domain of Setup B was discretized using a hybrid strategy, combining tetrahedral and structured hexahedral elements to balance accuracy and computational cost. The shaft was meshed with unstructured tetrahedral elements of 0.4 mm, while the wheel center was discretized with a multizone scheme using hexahedral elements of 0.28 mm and a face sizing of 0.18 mm. The cooling channels were also meshed with a multizone approach, adopting hexahedral elements of 0.18 mm to ensure accurate

resolution of the internal flow. Inflation layers were added to the channel walls, with a first layer thickness of 0.1 mm, six layers in total and a growth rate of 1.2, to capture velocity gradients close to the boundaries.

A finer discretization of the channels was essential in this setup, since the velocity profiles and outlet distributions were directly evaluated within these regions. Particular care was required when simulating wheel geometries with inclined channels, where adjacent channels are placed closer together. In such cases, *ANSYS Meshing* occasionally interpreted the proximity as solid contact between surfaces, generating artificial connections. These spurious links were manually removed to ensure channel continuity and numerical stability.

The mesh independence study was performed for a representative wheel geometry with one layer of 30 channels of 1.6 mm diameter (Figure 5.8a). The grid was progressively refined and the maximum outlet velocity in the channel aligned with gravity was monitored as the convergence criterion, since this is the primary indicator of performance in these simulations. As illustrated in Figure 5.8b, coarse meshes yielded significantly overestimated velocities, while results stabilized when the element count exceeded approximately 1.2 million. Beyond this threshold, the variation in outlet velocity was below 3 %, indicating mesh-independent predictions.

Based on these results, the final mesh adopted for all subsequent simulations contained approximately 1.2 million elements, corresponding to the configuration described above. This ensured reliable accuracy while keeping computational requirements at a reasonable level.

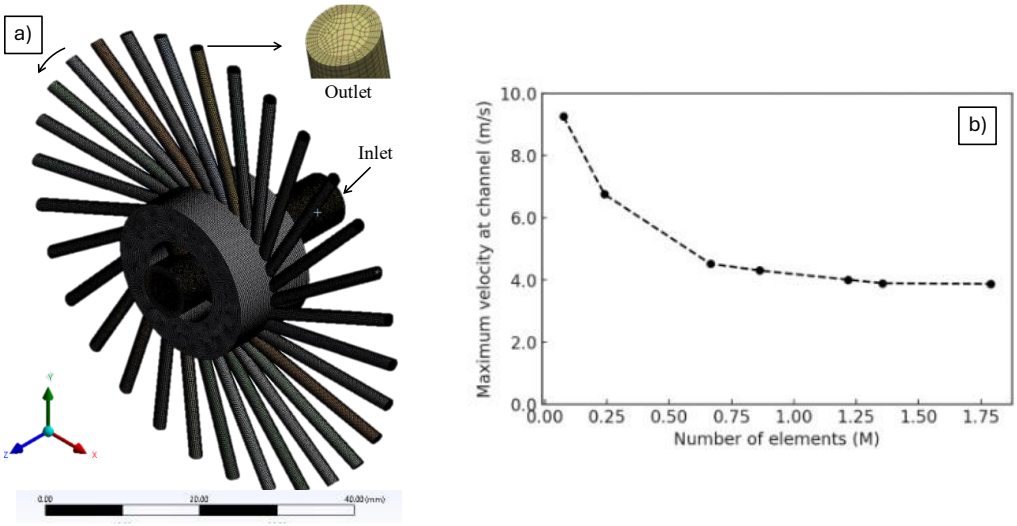


Figure 5.8 – Setup B: (a) computational mesh of the wheel; (b) convergence of maximum outlet velocity with increasing number of elements.

5.4.3 Physical Models

In Setup B, water was adopted as the working fluid, with constant physical properties at 20 °C. Gravity was enabled in the negative Y direction, aligned with the outlet channel used for mesh-independence monitoring. Since all tested geometries resulted in Reynolds numbers within the laminar regime, a laminar viscous model was applied. The velocity formulation was defined in the Relative Reference Frame, so that the rigid-body component of wheel rotation was removed from the flow field. This guaranteed that the outlet velocity profiles represented only the pressure-driven jet, with zero velocity at the channel walls. The wheel rotation was implemented using the *MRF* method: the wheel center was defined as the rotating region, while the shaft and channel domains were set to rotate consistently with this frame. The main physical and numerical configurations adopted in Setup B are summarized in Table 5.3.

Table 5.3 – Summary of simulation parameters used in Setup B.

Parameter	**Configuration**
Fluid properties	Water – Density: 998.2 kg/m³; Viscosity: 1.00×10^{-3} kg/(m·s)
Velocity formulation	Relative
Flow regime	Laminar
Rotation method	*MRF*; wheel center defined as rotating region; shaft and channels rotating consistently with this frame
Boundary conditions	Inlet: Mass flow inlet at the shaft Outlet: Pressure outlet at all channel exits, with prevention of reverse flow enabled
Wall treatment	No-slip
Numerical scheme	Coupled pressure–velocity; least-squares cell-based gradient evaluation; second-order discretization for pressure and momentum
Gravity	Enabled, aligned with channel outlet
Convergence criteria	Residuals < 10^{-4} and stable mass-flow balance

Boundary conditions included a mass flow inlet at the shaft and pressure outlet boundaries applied to all channel exits. The option *prevention of reverse flow* was enabled to suppress numerical instabilities at the

outlets, since local recirculation near the exit plane could otherwise generate artificial backflow and compromise convergence. All walls were treated as no-slip boundaries.

The solution was obtained with a coupled pressure–velocity scheme and second-order discretization for momentum and pressure equations. Convergence was assumed when scaled residuals reached 10^{-4} and the mass-flow balance remained stable.

With the numerical framework established, the next step was to define post-processing indicators capable of translating the raw CFD data into parameters directly related to coolant transport efficiency.

5.4.4 Post-processing Indicators

The CFD simulations of Setup B provided detailed velocity fields inside the wheel, but interpreting these results required specific indicators capable of quantifying the coolant transport through the channels. Post-processing procedures were therefore defined to translate the raw data into parameters directly related to the hydraulic efficiency of the wheel. The selected indicators include the outlet velocity distribution, the streamlines inside the channels and the cross-sectional velocity profiles. Together, they allow a comprehensive analysis of the coolant delivery process, from the visualization of flow paths to the quantitative assessment of velocity uniformity and wall-induced losses. This section describes how each indicator was extracted in *ANSYS CFD-Post*.

Outlet Velocity Distribution

The most relevant indicator in Setup B was the velocity distribution at the channel outlets, since this parameter reflects the effective transport capacity of the coolant. For this purpose, contour maps of velocity magnitude were generated at planes coincident with each channel outlet. An example is presented in Figure 5.9, corresponding to a wheel with 30 channels of 1.7 mm diameter in a single-layer configuration (5000 rpm; 400 mL/min). The contour clearly reveals regions of high velocity at the channel core and low-velocity zones near the walls.

To obtain these plots in *CFD-Post*, a plane was defined at the outlet cross-section of each channel and the variable Velocity Magnitude was selected as the contour field. In addition to visualization, quantitative values of the outlet velocity were extracted using the *Calculator* tool. For each outlet surface, the function *areaAve(Velocity)* was applied to compute the average velocity magnitude across the cross-section.

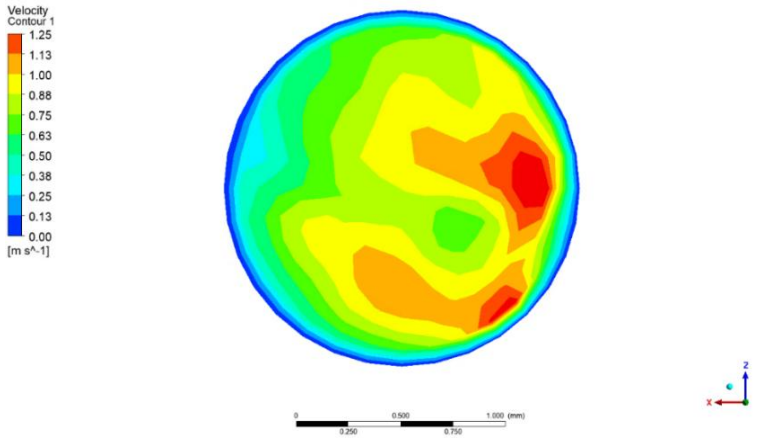


Figure 5.9 – Velocity contour at the outlet of a representative channel (diameter 1.7 mm, single-layer configuration with 30 channels).

Another post-processing metric derived from these contour maps was the quantification of low-velocity areas, particularly relevant when comparing different channel diameters. Regions in blue, typically close to the walls, correspond to zones where velocity is suppressed by viscous effects, representing effective hydraulic losses. To estimate the extent of these losses, the contour images were exported and analyzed in ImageJ®. By defining a threshold corresponding to the blue region of the color scale, By defining a threshold corresponding to the blue region of the color scale, the low-velocity region was defined as all pixels with velocity below 0.10 m/s, a value corresponding to approximately ten percent of the maximum outlet velocity in the analyzed cases and representative of the viscous-dominated zone near the walls. This threshold was chosen because it consistently isolated the shear-affected region across all geometries, allowing the area fraction of low-velocity zones to be calculated for each channel. This approach allowed the identification of geometries with reduced wall-dominated losses and improved effective outlet area.

Velocity Along the Channel Plane and Cross-sectional Profiles

To complement the outlet analysis, velocity contours were generated on a longitudinal plane aligned with the Z-axis, intersecting the channels along their full length. Although this is not a plane normal to the channel axis, it allows direct visualization of the velocity development over the entire channel extension, evidencing acceleration, wall effects and the onset of low-velocity regions. An example is presented in Figure 5.10, corresponding to a wheel with 30 channels of 1.5 mm diameter in a single-layer configuration (1000 rpm; 800 mL/min). The contour map shows the full channel length and the progressive formation of low-velocity boundary layers along the walls, while higher velocities remain concentrated near the core.

In *CFD-Post*, this was done by creating plane coincident with the global Z-axis, which produces a longitudinal section cutting through all channels. On this plane, the variable *Velocity Magnitude* was plotted as a contour map, with the same color scale applied for all cases to ensure comparability. This representation highlights how the velocity profile evolves from the plenum entrance to the outlet.

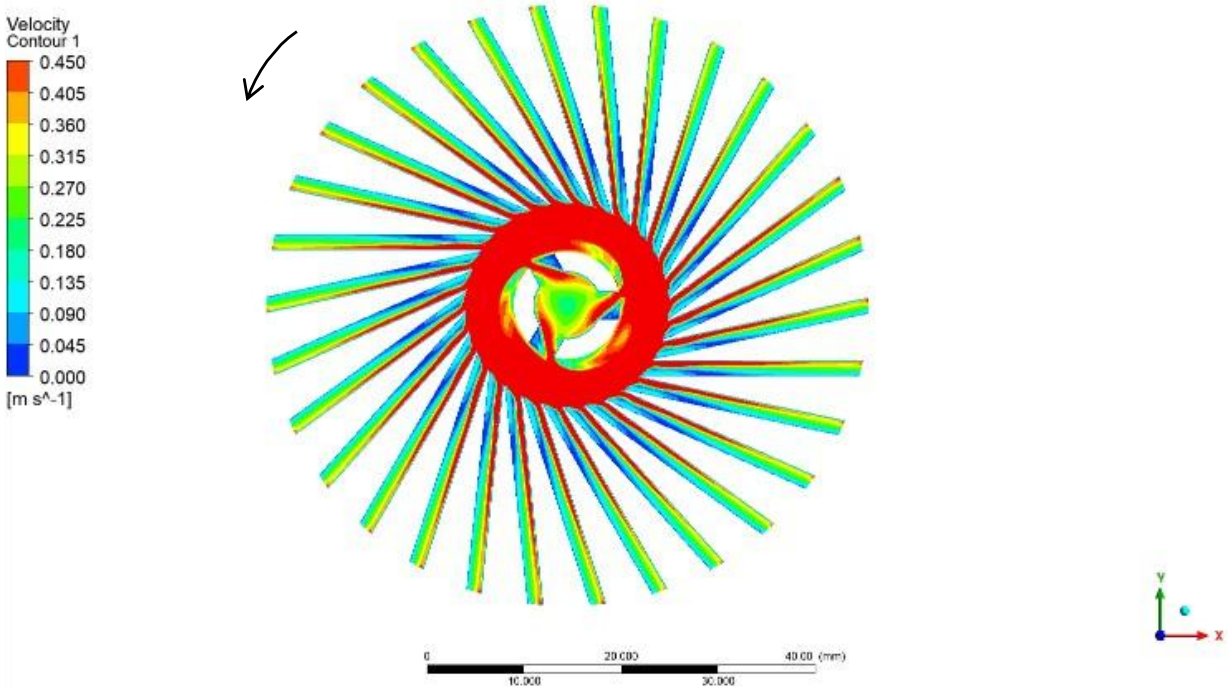


Figure 5.10 – Velocity contours across channel cross-sections of a structured wheel with 30 channels of 1.5 mm diameter in a single-layer configuration (1000 rpm; 800 mL/min).

Streamlines Inside the Channels

In addition to velocity contours, streamlines were used to visualize the fluid trajectories within the channels. This representation provides an intuitive understanding of how the coolant is guided from the wheel center to the outlets, highlighting possible recirculation zones or preferential flow paths. As illustrated in Figure 5.11, corresponding to a wheel with 30 inclined channels of 1.5 mm diameter in a single-layer configuration (250 rpm; 800 mL/min).

Streamlines are generated in *CFD-Post* by seeding particles at the shaft inlet and tracking them through the rotating domain. The color scale is set according to the velocity magnitude, enabling direct correlation between particle paths and local acceleration or deceleration zones.

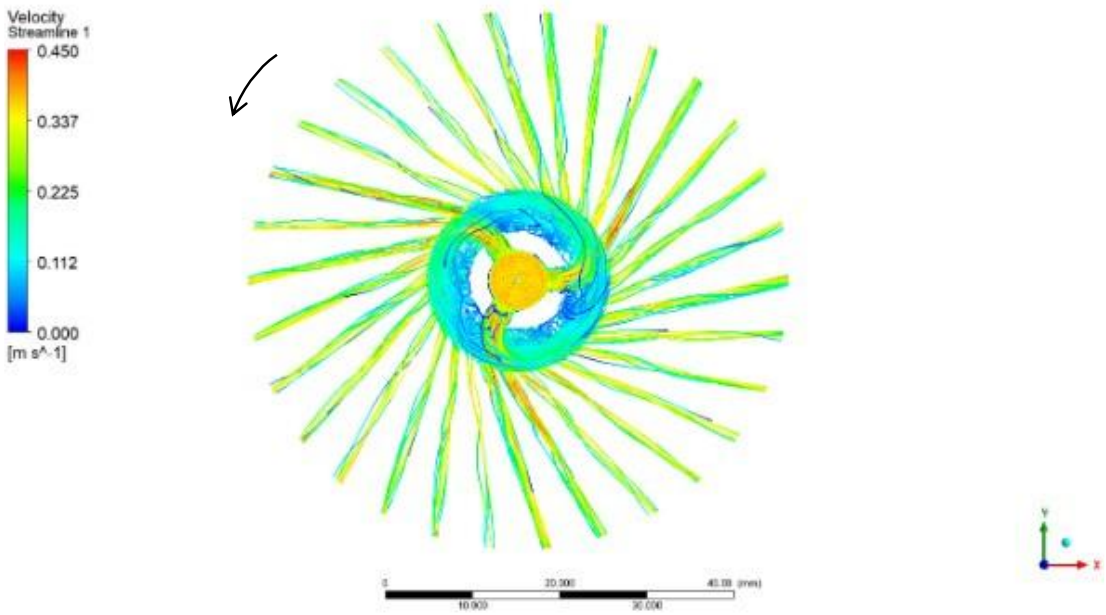


Figure 5.11 – Streamlines inside the channels of a structured wheel with 30 inclined channels of 1.5 mm diameter in a single-layer configuration (250 rpm; 800 mL/min).

5.5 Experimental Validation by High-speed Imaging

To complement the numerical results of Setup B, experimental flow visualization tests were performed using high-speed imaging. A transparent resin replica of the grinding wheel was fabricated to provide optical access to the internal channels, enabling direct observation of coolant trajectories under controlled conditions. This strategy preserved the channel geometry and overall dimensions of the vitrified prototypes while offering a reliable experimental counterpart to the CFD simulations.

The validation procedure combined four sequential stages: fabrication of the resin wheel, high-speed imaging setup, particle-tracking analysis using seeded tracer particles and quantitative comparison with CFD predictions. Together, these steps established a consistent framework to assess the accuracy of the numerical model and to verify its ability to predict the coolant transport inside the grinding wheel.

5.5.1 Fabrication of Transparent Resin Wheel

For flow visualization experiments, a transparent resin prototype of a structured grinding wheel was produced. The selected configuration corresponded to channels with positive inclination ($\theta = 12°$ in the wheel rotation direction, Figure 5.12e), consisting of 30 channels with a nominal diameter of 1.7 mm, a wheel with external diameter of 62 mm and an internal diameter of 21 mm. After curing, a slight shrinkage of the resin reduced

the actual channel diameter to 1.6 mm, a dimension that was later considered in the numerical model to ensure consistency between experiments and simulations. The final prototype is shown in Figure 5.12e.

The prototype was fabricated using a 3D printer (Anycubic Photon D2, Anycubic, Shenzhen, China) employing DLP technology and Anycubic Clean translucent photopolymer resin. Printing parameters were set to a layer height of 50 μm, an exposure time of 2.4 s per layer and 30 s for the base layers. The printing stage is illustrated in Figure 5.12a and the wheel immediately after printing is presented in Figure 5.12b.

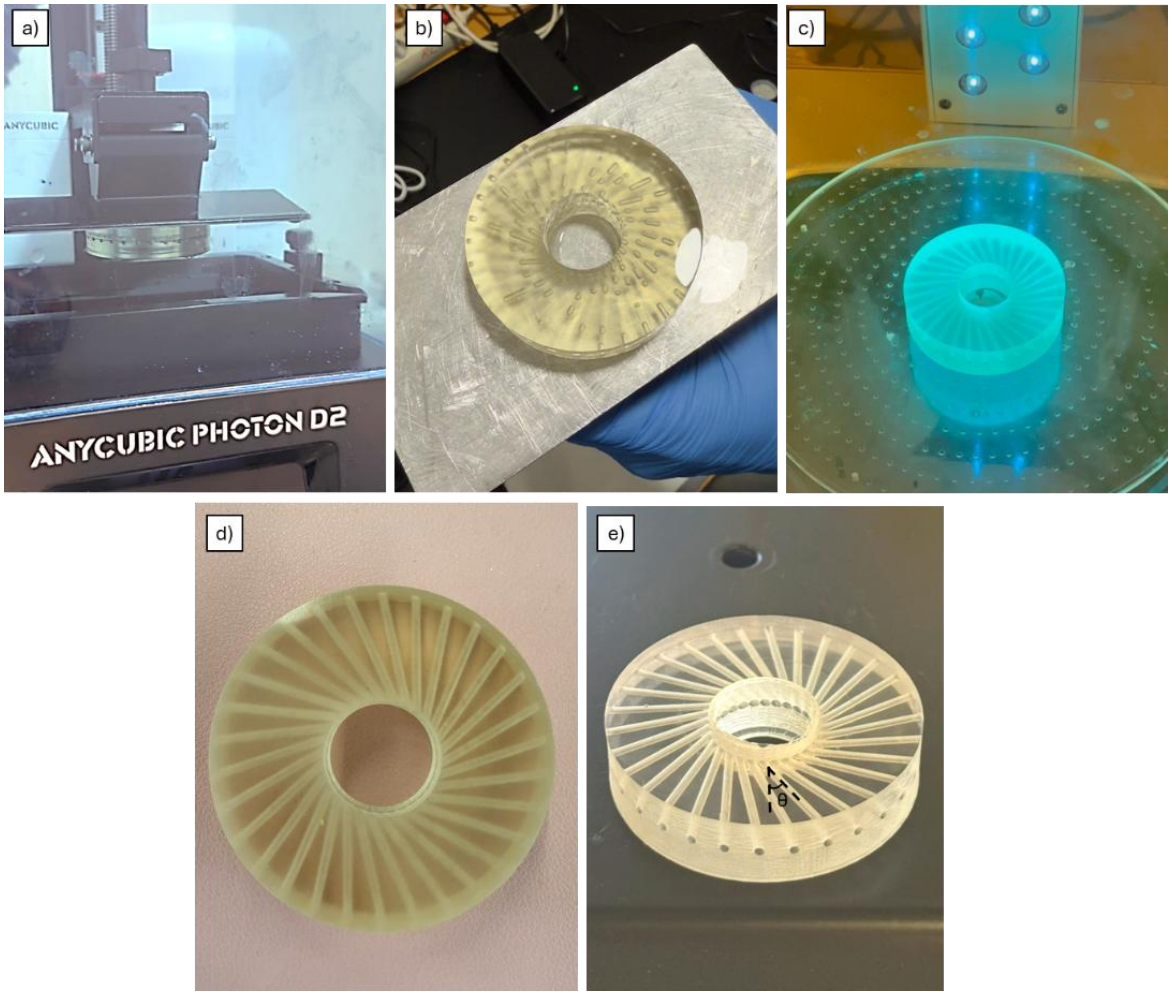


Figure 5.12 – Fabrication of the transparent resin grinding wheel: (a) printing on the Anycubic Photon D2 using DLP technology; (b) wheel immediately after printing; (c) post-curing under UV light; (d) prototype after curing; (e) final wheel after surface polishing, showing the positive inclination channels (θ = 12°).

After printing, the wheel was washed in isopropyl alcohol (≥ 95 % purity) for 5 min in an Anycubic Wash & Cure Plus unit under continuous agitation, followed by internal channel cleaning with compressed air and complete drying. Post-curing was then performed in the same unit under ultraviolet light (λ = 405 nm) for 6

min to ensure complete polymerization, improved mechanical strength and dimensional stability (Figure 5.12c-d).

Surface finishing was obtained by mechanical polishing in a bench-top metallographic polisher, starting with manual sanding using 2000-grit silicon carbide paper, followed by a two-stage polishing sequence on cloth-covered rotating discs with abrasive suspensions (diamond, 6 and 1 μm). Lubricant fluid was also applied during polishing. This procedure yielded a translucent surface, enabling clear optical access to the internal channels for flow visualization during the imaging experiments (Figure 5.12e).

5.5.2 High-speed Imaging Setup

The experimental setup was designed to capture the coolant trajectories inside the wheel channels using high-speed imaging. The transparent resin replica of the grinding wheel was mounted on the spindle of the surface grinding machine, allowing operation under controlled rotational speeds while enabling direct optical access to the internal flow.

Flow visualization was performed using a CMOS *Photron® Fastcam* SA5 high-speed camera, recording 512 × 512 pixel sequences at 6000 fps with an exposure time of 1/100000 s. The camera was positioned orthogonally to the wheel periphery, with the lens aligned to the central plane of the channels to minimize perspective distortion. Illumination was provided by a continuous halogen light source positioned in front of the wheel and a mirrored surface was placed behind the resin wheel to improve light uniformity and enhance particle visibility.

Plastic glitter particles (diameter = 0.40 mm) were dispersed in water and injected axially through the wheel spindle at a constant flow rate of 800 mL/min. This flow rate, higher than that used in the grinding tests (400 mL/min), was selected to improve visualization during high-speed recording.

The wheel was driven at a reduced rotational speed of 250 rpm, which facilitated the tracking of particle trajectories. The coolant reservoir containing the tracer particles was placed on a magnetic stirrer to promote uniform dispersion and prevent agglomeration.

The experimental setup used for these measurements is shown in Figure 5.13.

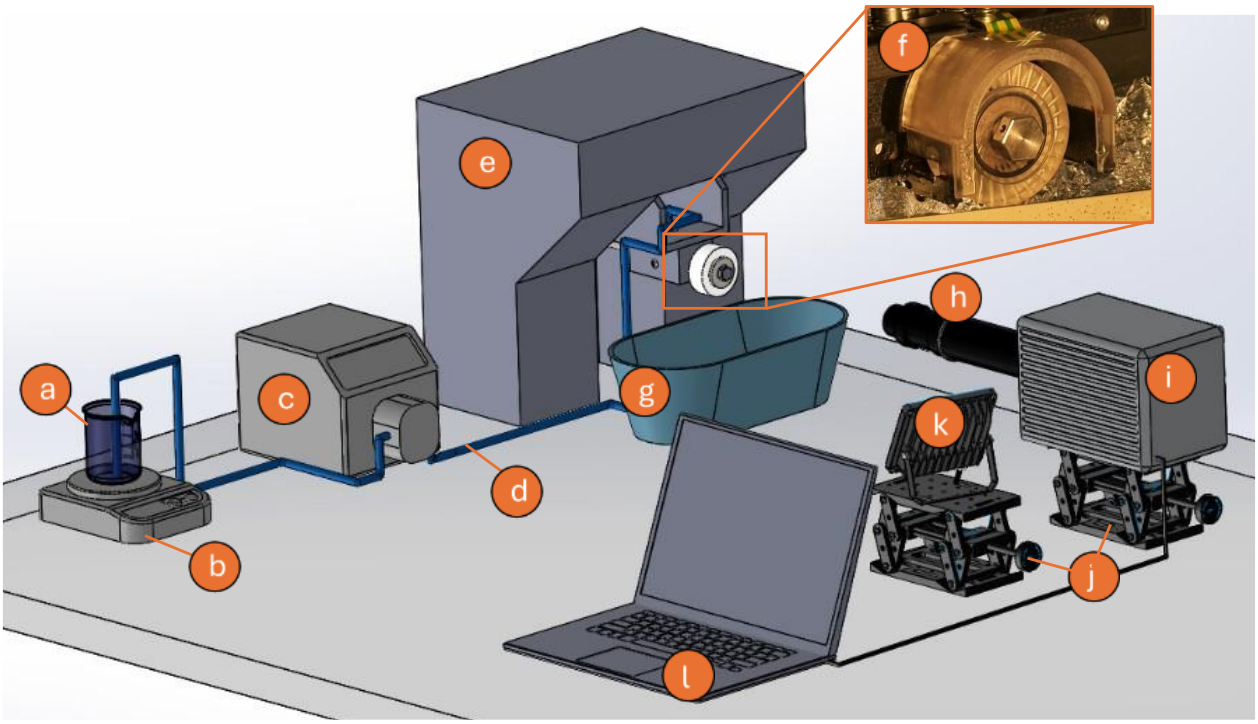


Figure 5.13 – Experimental setup for high-speed imaging: (a) coolant reservoir (supplied mass control), (b) magnetic stirrer, (c) coolant pump (flow control), (d) supply pipe, (e) surface grinding machine, (f) resin grinding wheel, (g) reservoir for water collection, (h) optical lenses, (i) high-speed camera, (j) triaxial translation stage, (k) illumination system and (l) computer for image acquisition and processing.

5.5.3 Particle Tracking Methodology

Two complementary methods were employed to extract quantitative velocity data from the high-speed recordings: manual tracking and automatic tracking using *ImageJ/TrackMate*. Both approaches required pre-processing of the video sequences to compensate for wheel rotation and to enhance particle contrast.

Manual Tracking

In the manual method, a reference particle (p_1) was identified in the first frame (time t_1) and tracked until it approached the channel exit, reaching position p_1' at time t_2 (Figure 5.14a and b). The corresponding images were corrected for wheel rotation, allowing the positions to be overlaid and aligned (Figure 5.14c). The linear distance between p_1 and p_1' (Δ_p) was measured in *ImageJ* [238] and the particle velocity (v_{p1}) was calculated by Eq. 5.4:

$$v_{p1} = \frac{\Delta_p}{(t_2 - t_1)} \tag{5.4}$$

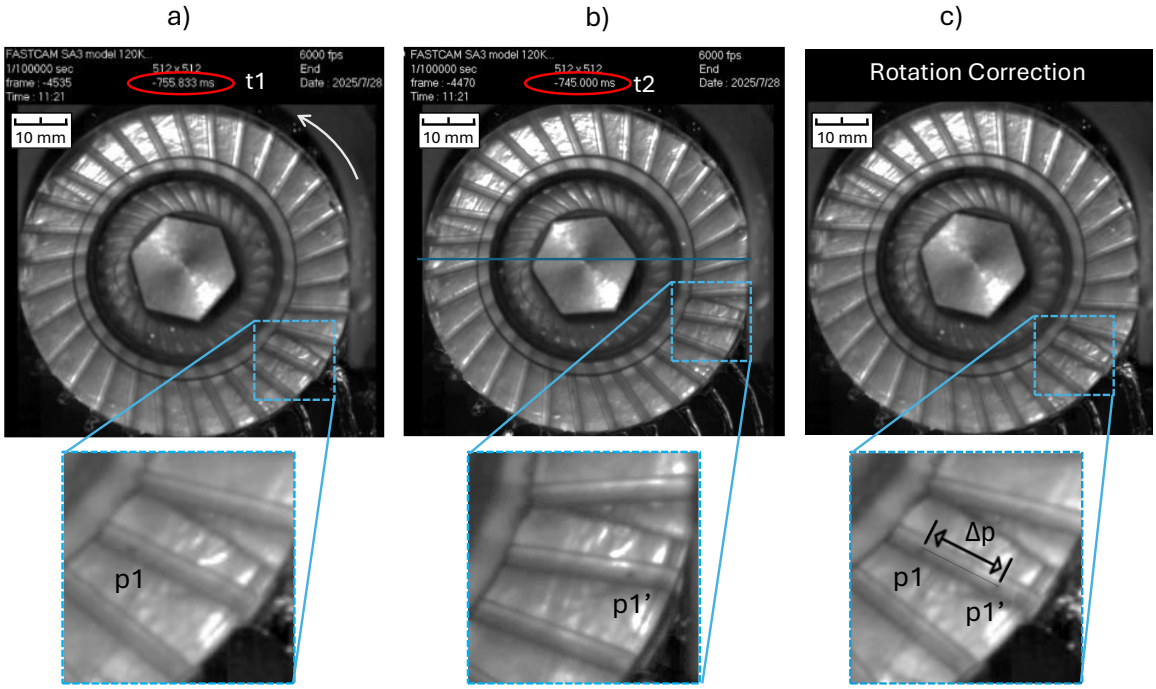


Figure 5.14 – Manual particle tracking method: (a) initial position of the reference particle (p_1) at time t_1; (b) final position (p_1') at time t_2; (c) rotation-corrected overlay of the two frames showing the measured displacement (Δp) used for velocity calculation.

This procedure was repeated for six particles located in different channels of the grinding wheel, ensuring that the validation reflected the general flow behavior rather than a single-channel condition.

Automatic Tracking with ImageJ/TrackMate

In the automatic method, raw images (923 frames; 512 × 512 px; Δt = 0.167 ms) were imported into *Fiji/ImageJ* 2 (ver. 1.54p) and rigidly aligned three consecutive times using *Linear Stack Alignment with SIFT* to eliminate rotation and micro-vibrations of the wheel. The contrast of each frame was normalized (*Enhance Contrast*, saturation = 0.4 percent) and a static background was computed by Median Z-projection and subtracted from the original stack (*Image Calculator* ▸ *Difference*), followed by Gaussian blur (σ = 1 px) to reduce high-frequency noise. The analysis was restricted to the outer ring, isolated by combining two circular selections (*ROI Manager* ▸ *XOR*) and clearing the outside region (*Clear Outside*).

Tracking was performed in *TrackMate* v7.14 [239] using the LoG detector (estimated diameter = 0.4 mm; threshold = 2; sub-pixel on) and the Simple LAP tracker (linking = 0.5 mm; gap-closing = 0.5 mm; frame-gap = 2). Tracks with a duration < 10 frames or displacement < 3.11 mm were discarded, resulting in 32 valid particle trajectories. Instantaneous velocities (2D distance/Δt) were exported in XML format, converted to

Microsoft® Excel and summarized as mean ± standard error for statistical analysis. The resulting trajectories were exported from *TrackMate* as an overlay image and imported into *ImageJ*. Each track was plotted as a line corresponding to the particle path, with the color scale representing the instantaneous velocity magnitude (blue = lowest, red = highest).

These visualizations provided a clear qualitative representation of the internal flow, although quantitative validation required comparison with CFD predictions, as presented in the following section.

5.5.4 Experimental Validation of CFD via Particle Velocity

Manual measurements were first performed on six individual particle trajectories to establish a baseline and serve as a reference for subsequent comparisons. Particle displacement was calculated from the linear distance travelled between two rotation-corrected frames, divided by the corresponding time interval. The resulting speeds ranged from 0.29 m/s to 0.56 m/s, with an average of 0.41 ± 0.11 m/s (Table 5.4).

Figure 5.15 compares the velocity field obtained by CFD simulation (a) with the particle trajectories extracted from high-speed videos using automatic tracking (b). Both approaches show a similar velocity range (0–0.6 m/s), reinforcing the agreement between the numerical predictions and the observed flow.

Table 5.4 – Manual measurements of particle displacement and speed obtained from the high-speed recordings.

Particle	Time (ms)	Displacement (mm)	Particle Speed (m/s)
P1	13.8	6.1	0.44
P2	13.8	7.7	0.56
P3	23.2	6.7	0.29
P4	25.3	8.0	0.31
P5	22.3	7.3	0.32
P6	13.8	7.1	0.51
	Average (m/s)		0.41 ± 0.11

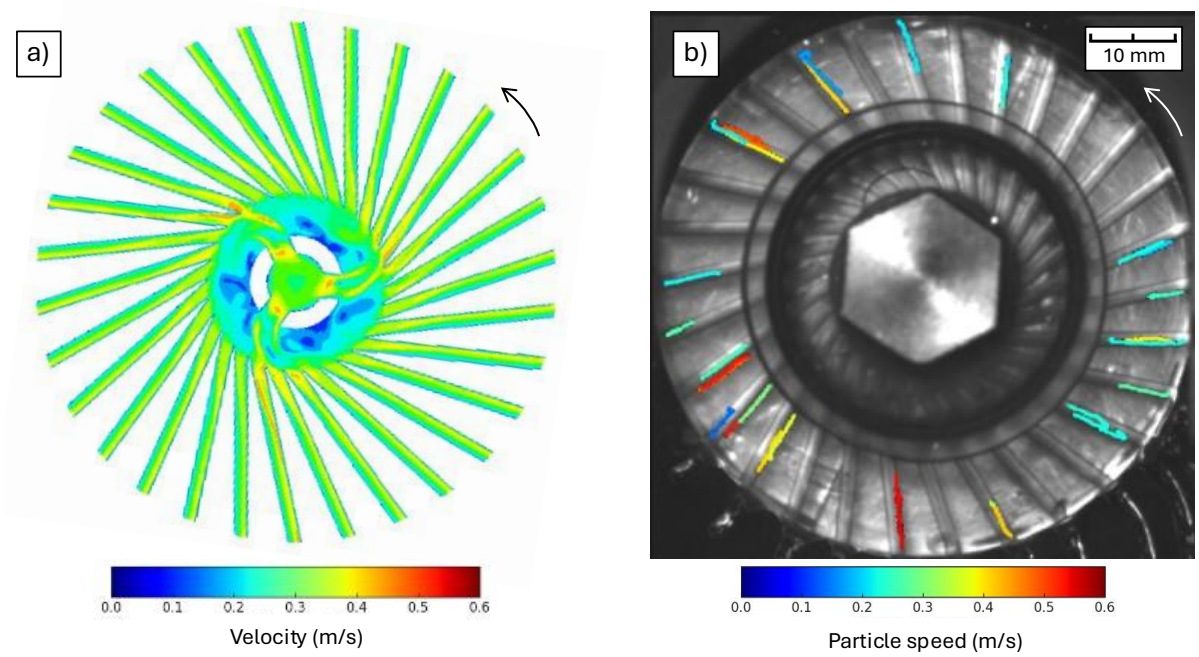


Figure 5.15 – (a) Fluid velocity field obtained by CFD simulation (positive inclination geometry, 250 rpm, 800 mL/min). (b) Particle trajectories tracked from high-speed videos using *TrackMate*. Colors represent local particle speed.

While the overall structure is consistent in both cases, the experimental trajectory occasionally show localized higher speeds. These deviations are attributed to transient accelerations of individual particles, optical distortions near the resin–air interface and occasional overlap between trajectories in successive frames, all of which may lead to momentary overestimation of speed. In addition, experimental particles are finite-size tracers (0.4 mm), which can experience slip and slight inertial effects, particularly in regions of curvature or flow redirection. A further source of variation is the non-uniform velocity distribution across the channel diameter, which naturally leads to different particle speeds depending on their position within the flow.

Nevertheless, the color distribution and trajectory alignment in both images indicate that the numerical model captures the main flow features inside the grinding wheel, supporting the validity of using the CFD outlet velocities as a quantitative reference for subsequent analyses.

To complement this qualitative agreement, the mean velocities obtained from each method were compared quantitatively. Figure 5.16 consolidates the results from the three evaluation methods: automatic tracking, manual measurements and CFD simulation.

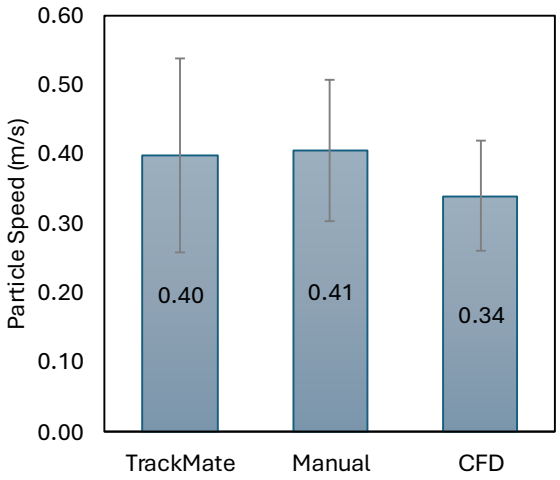


Figure 5.16 – Average particle speed obtained through automatic tracking (*TrackMate*), manual measurement and CFD simulation. Error bars represent the standard deviation.

For *TrackMate*, the value corresponds to the average speed of the 32 tracked particles, while in the CFD case, it represents the average velocity along reference lines placed in the channel cross-section at positions matching the particle-tracking region, ensuring direct comparability with the experimental results. The mean particle velocities from the experimental approaches are very close (0.40 m/s and 0.41 m/s), while the simulation yields a slightly lower value (0.34 m/s). Despite the ≈16 % difference, the three methods showed good agreement, validating the numerical model and demonstrating that the experimental particle-tracking method was effective for local flow characterization.

5.6 Summary and Conclusions

This chapter developed a CFD framework for analyzing coolant flow in structured grinding wheels and validated its predictions with high-speed imaging. Two complementary numerical setups were defined with distinct purposes. Setup A (multiphase model using absolute velocity formulation and an external air domain) was conceived to qualitatively visualize coolant dispersion and coverage around the wheel. Setup B (single-phase model using relative velocity formulation and restricted to the internal domain) focused on the internal hydraulics to quantify channel velocities and outlet profiles.

A key outcome of this chapter is that the two CFD setups are complementary, each addressing different aspects of coolant flow. Setup B, based on the relative velocity formulation, enabled physically consistent predictions of the pressure-driven flow inside the channels. Post-processing indicators such as outlet velocity distributions, streamline trajectories and cross-sectional contours provided a detailed description of coolant

acceleration, near-wall viscous losses and the uniformity of the emerging jets. Setup A, in contrast, extended the analysis to the external domain through a multiphase formulation, capturing the interaction between water and air. This enabled qualitative visualization of jet dispersion, air entrainment and the extent to which the coolant penetrates the grinding zone.

Applied together, the two approaches offer a complete picture of the cooling process in structured wheels: from internal transport in the rotating frame, through the formation and ejection of jets at the channel outlets, to their dispersion in the surrounding air and interaction with the air barrier created by wheel rotation. This integration of internal and external flow analysis ensures that the numerical framework can be used not only to optimize channel design but also to assess the overall cooling effectiveness of structured grinding wheels.

To validate the numerical results, high-speed imaging experiments were carried out using transparent resin wheels. Manual and automatic particle tracking provided quantitative velocity data at the channel outlets, showing good agreement with CFD predictions: manual and automatic tracking yielded mean velocities of 0.41 and 0.40 m/s, respectively, while CFD simulations predicted 0.34 m/s, with a difference of approx. 16 %. This agreement is within the expected range for laminar internal flows measured experimentally with finite-size tracers, confirming that the numerical approach captured the essential physics.

In conclusion:

- Use Setup A to study external dispersion and qualitative coverage.
- Use Setup B to obtain quantitative internal velocities and outlet profiles.
- The selected post-processing indicators (velocity contours, low-velocity area fraction, streamlines and cross-sectional profiles) captured the most relevant flow features.
- High-speed imaging validated the CFD predictions, confirming their reliability for analyzing structured grinding wheels.

Overall, the integration of CFD and high-speed imaging provided a robust and validated methodology for studying coolant flow in structured wheels. This framework forms the basis for the parametric studies presented in the next chapter, where the influence of channel diameter, inclination and number of layers is systematically investigated.

6. PARAMETRIC STUDIES ON CHANNEL GEOMETRY

This chapter presents the methodology adopted to evaluate the performance of internally cooled grinding wheels through a combination of experimental tests and CFD analysis. Initially, a screening study was carried out using the Taguchi method, which enabled the identification of the most influential factors on the distribution of coolant over the workpiece surface. Building on this first stage, a more detailed analysis was then conducted by separately addressing the geometric parameters of the cooling channels: starting with the number of layers, followed by the channel diameter and finally the channel inclination. This sequential approach ensured a comprehensive understanding of how design parameters affect coolant transport and grinding performance, under both numerical and experimental perspectives.

The work described in this chapter was disseminated in three journal articles:

CFD Analysis of Multi-Layer Cooling Channels in Three-Dimensionally Structured Grinding Wheels [224], published in *Applied Thermal Engineering*;

Coolant Flow in Structured Grinding Wheels: CFD Validation via High-Speed Imaging and Particle Tracking [225], published in *Applied Thermal Engineering*;

CFD and Experimental Investigation of Channel Diameter Effects in Structured Internally Cooled Grinding Wheels, currently under review in *Materials Today Communications*.

6.1 Screening by Taguchi-Grey Analysis

Although several simulation studies have investigated the geometric parameters of surface-textured grinding wheels, the use of internal cooling channels embedded within the wheel matrix remains a relatively new approach. However, the influence of internal geometry such as the number, arrangement, inclination and diameter of channels, on fluid flow and thermal performance has not yet been systematically evaluated.

In this study, a preliminary screening was conducted using CFD combined with statistical optimization based on the Taguchi–Grey relational method [240,241]. This approach provides an efficient way to explore a wide design space, highlighting the relative importance of each geometric parameter on coolant distribution and thermal behavior. Rather than aiming for definitive optimization, the objective here is to identify general trends. Examples include whether finer or larger channels promote better cooling, whether multi-layer

arrangements outperform single layers, or whether inclined channels offer advantages compared to straight ones.

The subsequent subchapters address experimental validation separately, while this section focuses exclusively on the statistical analysis of simulation results, providing guidance for selecting the most promising configurations to be further developed and tested.

6.1.1 Factor Selection

In this study, the L18 array was used because it is suitable for five factors, each with three levels, allowing for the evaluation of main effects with a minimal number of simulations. The selected variables and their levels are presented in Table 6.1. These factors were selected due to their potential influence on the transport and distribution of coolant during the grinding process, considering the geometric dimensions of the abrasive grinding wheels. Figure 6.1 illustrates some examples of the geometries used in the simulations, which aid in understanding the geometric parameters studied:

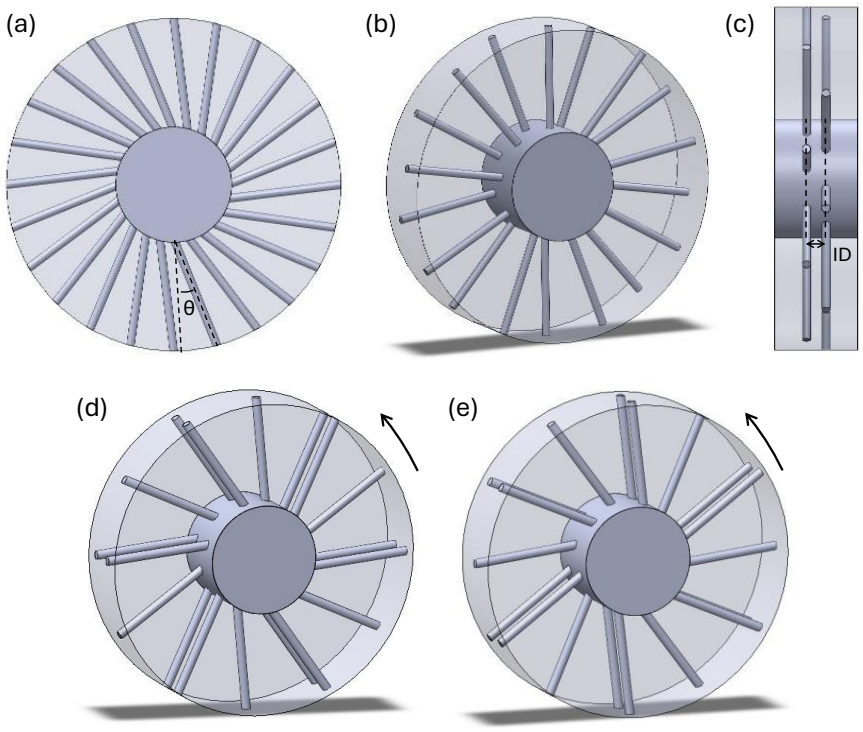


Figure 6.1 – Front view of a single-layer grinding wheel with channels inclined at an angle θ relative to the radial direction (a), structured grinding wheels with two layers of channels (b), side view showing the interlayer distance (ID) (c) and three-layer configurations in two scenarios: one channel in contact with the workpiece (d) and two channels in contact with the workpiece (e).

Table 6.1 – Factors and their levels, used in the Taguchi experimental design.

	Factors	Levels			
1	Number of Channel Layers	1	2	3	-
2	Number of Channels	18	24	30	-
3	Inclination - θ (deg)	0	7	12	-
4	Channel diameter (mm)	1	1.5	1.7	-
5	Interlayer Distance - ID (mm)	0	1	1.5	2

- **Number of Channel Layers:** The abrasive wheel can be configured with one (Figure 6.1a), two (Figure 6.1b-c), or three layers of channels (Figure 6.1d-e). For configurations with two layers, the channels are positioned alternately (Figure 6.1b). In the case of three layers, the two outer layers are aligned, while the middle layer is staggered (Figure 6.1d). This configuration results in a dynamic cooling process with two possible situations during operation depending on which channels intersect the workpiece surface: one where only one channel comes into contact with the workpiece (Figure 6.1d) and another where the two outer channels make simultaneous contact (Figure 6.1e). For the experiments with three layers, simulations were conducted for both scenarios and the average of the results was used to assess geometry cooling efficiency.
- **Number of Channels:** This is the total number of channels in the grinding wheel. A larger number of channels aims to enhance the homogeneity of fluid allocation over the workpiece. However, as the number of channels rises, the fluid volume per channel decreases, which can affect the internal velocity. Three levels were considered: 18, 24 and 30 channels. Figure 6.1a provides a 24-channel design example.
- **Channel Inclination (θ):** The channel inclination is defined as the angle between the channel axis and the radial direction of the wheel. When the angle is 0°, the channels are purely radial. Positive inclinations (e.g., +12°) tilt the channels forward in the sense of wheel rotation, guiding the fluid in a more tangential direction, which is expected to enhance coolant penetration at the contact zone.
- **Channel Diameter:** The diameter of the channel can directly influence the flow of fluid through the system. Larger diameters reduce resistance to flow, while smaller diameters increase fluid velocity and may enhance penetration at the contact interfaces. The analysis was conducted for three diameter levels: 1.0 mm, 1.5 mm and 1.7 mm.

- **Interlayer Distance (ID):** The ID controls the separation between channel layers within the grinding wheel, as illustrated in Figure 6.1c. Three levels were selected: 1.0, 1.5 and 2.0 mm. Larger gaps allow for a more uniform distribution of the fluid, while smaller distances concentrate channels in closer regions, potentially focusing the flow. In single-layer configurations, the ID was set to 0 in the orthogonal matrix.

The geometries assessed in this work were selected according to the Taguchi L18 orthogonal array to ensure an effective investigation of the main design factors while reducing computational effort. Table 6.2 lists the factor combinations and the corresponding simulations.

Table 6.2 – Geometry factor combinations used in the simulations according to the Taguchi experimental design (L18 array).

Geometry	Number of Layers	Number of Channels	Inclination (deg)	Channel Diameter (mm)	Interlayer Distance (mm)
1	1	18	0	1	0
2	1	24	7	1.5	0
3	1	30	12	1.7	0
4	2	18	0	1.5	2
5	2	24	7	1.7	1
6	2	30	12	1	1.5
7	3	18	7	1.7	1.5
8	3	24	12	1	2
9	3	30	0	1.5	1
10	1	18	7	1	0
11	1	24	12	1.5	0
12	1	30	0	1.7	0
13	2	18	12	1.7	1
14	2	24	0	1	1.5
15	2	30	7	1.5	2
16	3	18	12	1.5	1.5
17	3	24	0	1.7	2
18	3	30	7	1	1

6.1.2 Post-processing and Grey Relational Analysis

The simulations were performed using Setup A, as described in Section 5.3, with grinding wheel rotation set to 2000 rpm and a coolant flow rate of 3 L/min. In the post-processing conducted with *ANSYS*, two main responses were extracted: the mass flow rate at the contact plane and the water volume fraction along the contact line. These responses were selected because they directly represent the coolant delivery and distribution in the grinding zone.

The data were collected and then processed using Grey Relational Analysis. First, the responses were normalized according to the larger is better criterion, as defined in Eq. (6.1) [242]:

$$x_i' = \frac{x_i - \min(x_i)}{\max(x_i) - \min(x_i)} \tag{6.1}$$

After normalization, the Grey relational coefficient $\xi_i(k)$ was calculated for each response using Eq. (6.2):

$$\xi_i(k) = \frac{\Delta_{min} + \zeta.\Delta_{max}}{\Delta_i(k) + \zeta.\Delta_{max}} \tag{6.2}$$

where $\Delta_i(k)$ represents the absolute difference between the ideal normalized value (equal to 1) and the value of the i-th experiment for the k-th response. The distinguishing coefficient ζ was set to 0.5. Finally, the Grey relational grade γ_i was obtained by averaging the coefficients across the two considered responses, as presented in Eq. (6.3):

$$\gamma_i = \frac{1}{n}\sum_{k=1}^{n} \xi_i(k) \tag{6.3}$$

All calculations were implemented using Microsoft Excel based on the normalized output data obtained from the CFD simulations.

6.1.3 Results and Discussion

This section presents the results of the study in two parts: (i) optimization of cooling channel geometry using the Taguchi-Grey relational analysis and (ii) statistical evaluation of factor significance through ANOVA.

Grey Relational Analysis

Grey Relational Analysis was applied to evaluate system performance in terms of mass flow rate and water volume fraction, considering five geometric parameters: Number of Layers, Number of Channels, Inclination, Diameter and ID. Table 6.3 presents the Grey relational coefficients and γ values (Grey relational grade) for each experiment. Higher γ values indicate superior overall performance.

Table 6.3 – Grey relational coefficient and Grey grade values.

No.	Grey relational coefficient		γ	Order
	Mass Flow Rate	Water volume fraction		
1	0.345	0.333	0.339	18
2	0.558	0.658	0.608	8
3	0.777	1.000	0.889	**1**
4	0.548	0.411	0.479	13
5	0.744	0.548	0.646	6
6	0.459	0.404	0.432	15
7	0.738	0.356	0.547	10
8	0.590	0.458	0.524	12
9	0.817	0.386	0.602	9
10	0.333	0.351	0.342	17
11	0.548	0.677	0.612	7
12	0.678	0.829	0.754	**2**
13	0.626	0.451	0.538	11
14	0.452	0.381	0.417	16
15	0.899	0.608	0.753	**3**
16	0.922	0.381	0.652	5
17	1.000	0.473	0.737	4
18	0.552	0.364	0.458	14

Experiment 3 achieved the highest γ value (0.889), indicating that this configuration had the best performance among all tested parameter combinations. The geometry for this experiment consisted of one

layer, 30 channels, a 12° inclination, a 1.7 mm diameter and an ID of 0 mm. This result suggests that this combination of parameters yields performance closest to the normalized ideal values for mass flow rate and water volume fraction. However, other combinations, such as Experiments 15, 12 and 17, also demonstrated significant performance, with γ values of 0.753, 0.754 and 0.737, respectively.

While Experiment 3 showed the best individual performance, the Taguchi method was applied to determine the optimal levels for each geometric factor, optimizing the system in a more generalized manner, as shown in Table 6.4. The effects of geometric parameters on Grey relational grades are presented in Figure 6.2.

Table 6.4 – Main effects on Grey relation grades.

Level	Geometry Parameters				
	Number of Layers	**Number of Channels**	**Inclination**	**Channel Diameter**	**Interlayer Distance**
1	0.591	0.483	0.555	0.419	0.591
2	0.544	0.591	0.559	0.618	0.561
3	0.586	0.648	0.608	0.685	0.512
4	-	-	-	-	0.623
Delta	0.047	0.165	0.053	0.266	0.111
Order of effect	5	2	4	1	3

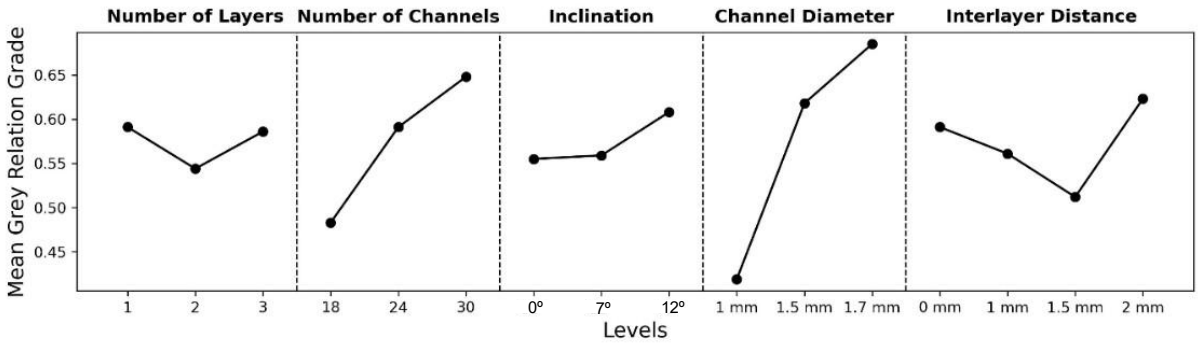


Figure 6.2 – Main effects plot for Mean Grey Relation Grade.

In Table 6.4, we observe that channel diameter and the number of channels have the greatest effect on the results, as indicated by the high delta values. The number of layers, however, appears less influential, showing

the least effect among the factors analyzed. This could be attributed to the fact that the number of layers influences performance more indirectly, primarily by affecting fluid distribution, which in turn impacts thermal control and chip removal capacity, factors that may not have been fully captured by the variables evaluated in the Grey Analysis.

As observed in Table 6.4 and Figure 6.2, the optimal levels of geometric parameters, which maximize the Grey relational grade, are: number of layers = 1, number of channels = 30, inclination = 12°, channel diameter = 1.7 mm and interlayer distance = 2.0 mm. However, when considering a single layer, the interlayer distance is no longer applicable. Thus, the optimized geometry corresponds to Experiment 3 in the Taguchi orthogonal table, which has already been tested, as it combines these factors without the need to assess interlayer distance.

ANOVA Analysis

The ANOVA analysis, Table 6.5, was established to determine the contribution of each geometric parameter to the Grey relational grade. The degrees of freedom (df) represent the number of independent values that can vary for each factor, while the sum of squares (sum_sq) quantifies the total variation associated with each parameter. The mean square (mean_sq) is obtained by dividing the sum of squares by the degrees of freedom, representing the average variability explained by each factor. The F-value compares the variability of each factor to the residual variability, where higher values indicate a stronger influence. Finally, the P-value assesses statistical significance, with values below 0.05 indicating that the factor has a statistically meaningful impact on the response rather than being a result of random variation [243].

Table 6.5 – Results of ANOVA on Grey relational grade.

	df	**sum_sq**	**mean_sq**	**F-value**	**P-value**	**Influence**
Number of Layers	2	0.0079	0.0040	0.8659	0.4613	2.1 %
Number of Channels	2	0.0841	0.0421	9.2069	0.0110	21.8 %
Inclination	2	0.0105	0.0052	1.1460	0.3711	2.7 %
Channel Diameter	2	0.2302	0.1151	25.1928	0.0006	59.7 %
Interlayer Distance	3	0.0212	0.0071	1.5464	0.2852	5.5 %
Residual	7	0.0320	0.0046			8.3 %

The ANOVA results confirm the Grey Relational Analysis findings, which identified channel diameter (59.7 %, P = 0.0006) and number of channels (21.8 %, P = 0.0110) as the most influential parameters for optimizing coolant flow patterns. Their statistical significance validates the observation that configurations with a larger channel diameter and more channels achieve superior mass flow rates and water volume fraction distribution. On the other hand, interlayer distance (5.5 %), inclination (2.7 %) and number of layers (2.1 %) had much lower contributions and were not statistically significant. This suggests a limited impact on cooling efficiency compared to channel diameter and number of channels. However, in a real grinding process, the contact between channels and the workpiece is dynamic, meaning that multi-layer configurations could still enhance fluid distribution over the complete grinding cycle. The staggered arrangement of multiple layers can promote a wider and more uniform distribution of the fluid, ensuring consistent cooling under intermittent contact conditions.

To further investigate this effect, the next stage of the study evaluates the optimized parameters (30 channels, 12° inclination, 1.7 mm diameter and 2 mm spacing) in one, two and three layer configurations. This provides a deeper understanding of the role of multiple layers in dynamic cooling fluid allocation and grinding efficiency.

6.2 Effect of Number of Layers

The number of channel layers is a relevant parameter because it directly affects how coolant is distributed across the wheel–workpiece contact. While the Taguchi–Grey analysis and ANOVA indicated that this factor had a relatively small statistical contribution compared to channel diameter and number of channels, its influence becomes more evident when considering the intermittent nature of the grinding process, in which multiple layers intermittently interact with the workpiece surface. To investigate this effect more accurately, dedicated dynamic CFD simulations were performed, focusing on the transient behavior of coolant delivery as different layers alternately come into contact. These numerical results are complemented by grinding tests, which provide practical evidence of how single, double and triple-layer wheels perform under real operating conditions. Together, the dynamic simulations and experimental data allow a clearer interpretation of the contribution of multi-layer configurations to fluid distribution and cooling efficiency.

6.2.1 Grinding Wheel Geometries

Three structured grinding wheels were manufactured with 30 channels of Ø 1.7 mm inclined at 12° in the wheel rotation direction, a configuration selected from the preliminary optimization study based on Taguchi–Grey relational analysis. The wheels differed only in the number of channel layers, namely one, two, or three, as illustrated in Figure 6.3. In all cases, the total outlet area of the channels at the wheel working surface was kept constant at approximately 68 mm², ensuring that the results reflect exclusively the effect of fluid distribution along the contact zone.



Figure 6.3 – Structured grinding wheels with internal channels inclined at 12°: (a) single-layer configuration, (b) two-layer configuration and (c) three-layer configuration.

6.2.2 Numerical Analysis

This section evaluates the fluid distribution across the workpiece for one-, two- and three-layer grinding wheel configurations. The analysis was carried out using Setup A, with a rotational speed of 2000 rpm and an inlet flow rate of 3 L/min. The analysis is performed dynamically over successive time steps to assess how the fluid spreads across the contact surface, influencing cooling efficiency, local flushing conditions and workpiece cooling. The objective is to understand how channel arrangement and motion impact the coverage and overall effectiveness of the cooling system.

For the single-layer configuration, the fluid distribution exhibits a well-defined central peak in water volume fraction along the contact line, as shown in Figure 6.4(a). This indicates that most of the fluid is concentrated in the central region (i.e. near the outlet flow channel), while the peripheral areas receive significantly less cooling fluid. Since only one or zero channels are active per cycle, there is minimal variation between time steps, meaning the fluid distribution remains relatively static over time (Figure 6.4 (c)).

As shown in Figure 6.4 (b), most of the fluid accumulates in the central plane and is diverted to the environment, which can lead to substantial fluid waste. While this configuration ensures effective fluid distribution in the center, it provides limited coverage across the width of the contact line. This restricted

lateral distribution may reduce the uniformity of local flushing conditions, increasing the likelihood that peripheral regions receive insufficient coolant. Such non-uniformity can contribute to higher local temperatures near the contact edges, highlighting the limitations of the single-layer design.

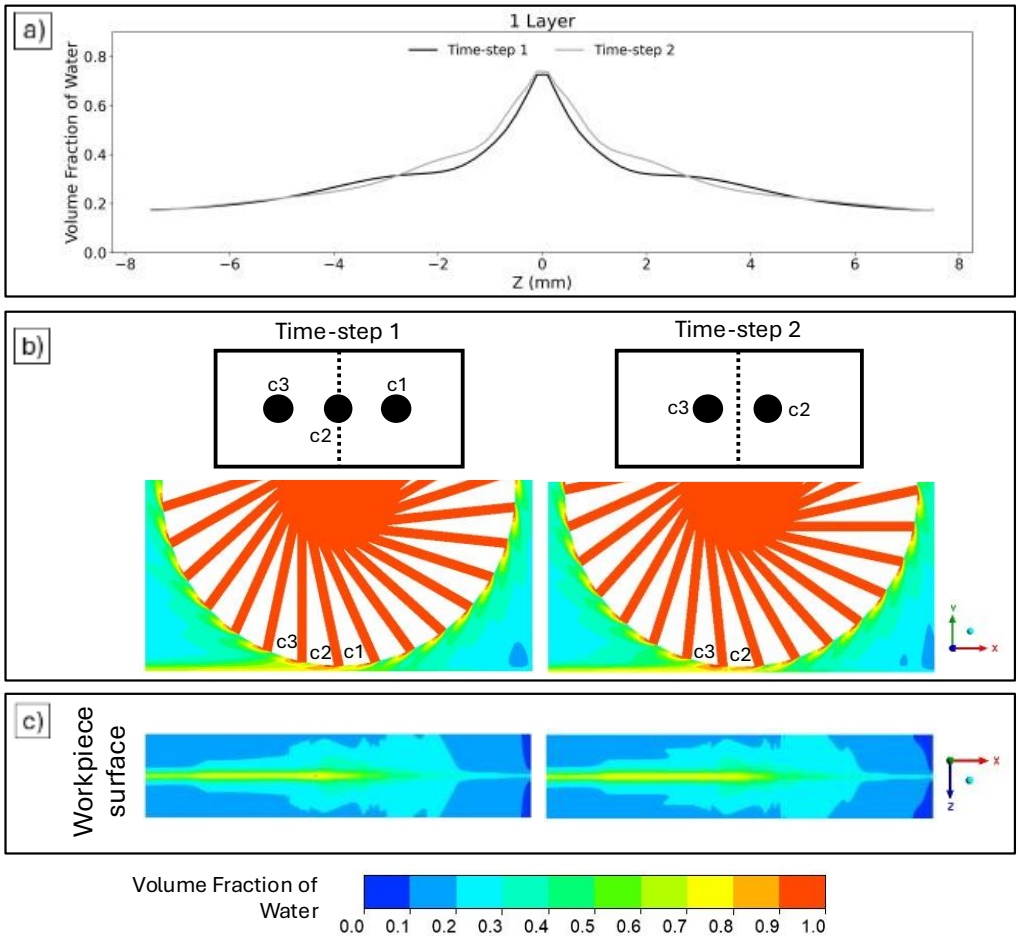


Figure 6.4 – Water volume fraction for the single-layer configuration over time: (a) along the contact line, (b) in each layer and (c) on the workpiece surface.

In the two-layer configuration, the alternating arrangement of channels results in a more dispersed coolant flow pattern across the contact line, as seen in Figure 6.5(a). The fluid is applied from different positions in successive time steps, leading to a cyclic pattern where the fluid peaks shift across the surface. Although this design improves lateral distribution compared to the single-layer wheel, fluid concentration at the center of the contact line remains relatively low.

At time-step 1, channel C2 is positioned at the contact line (Figure 6.5(b)), located in the second layer (Z = 1.85 mm). However, the peak water concentration occurs at Z ≈ -2.5 mm, indicating that the fluid reaching the workpiece mainly originates from channel C1 in the first layer, which has already passed the contact

point; this behavior is explained by the wheel rotation. This delayed arrival of fluid increases the effective coverage of the contact region, helping to reduce local heat accumulation and making the cooling distribution more uniform.

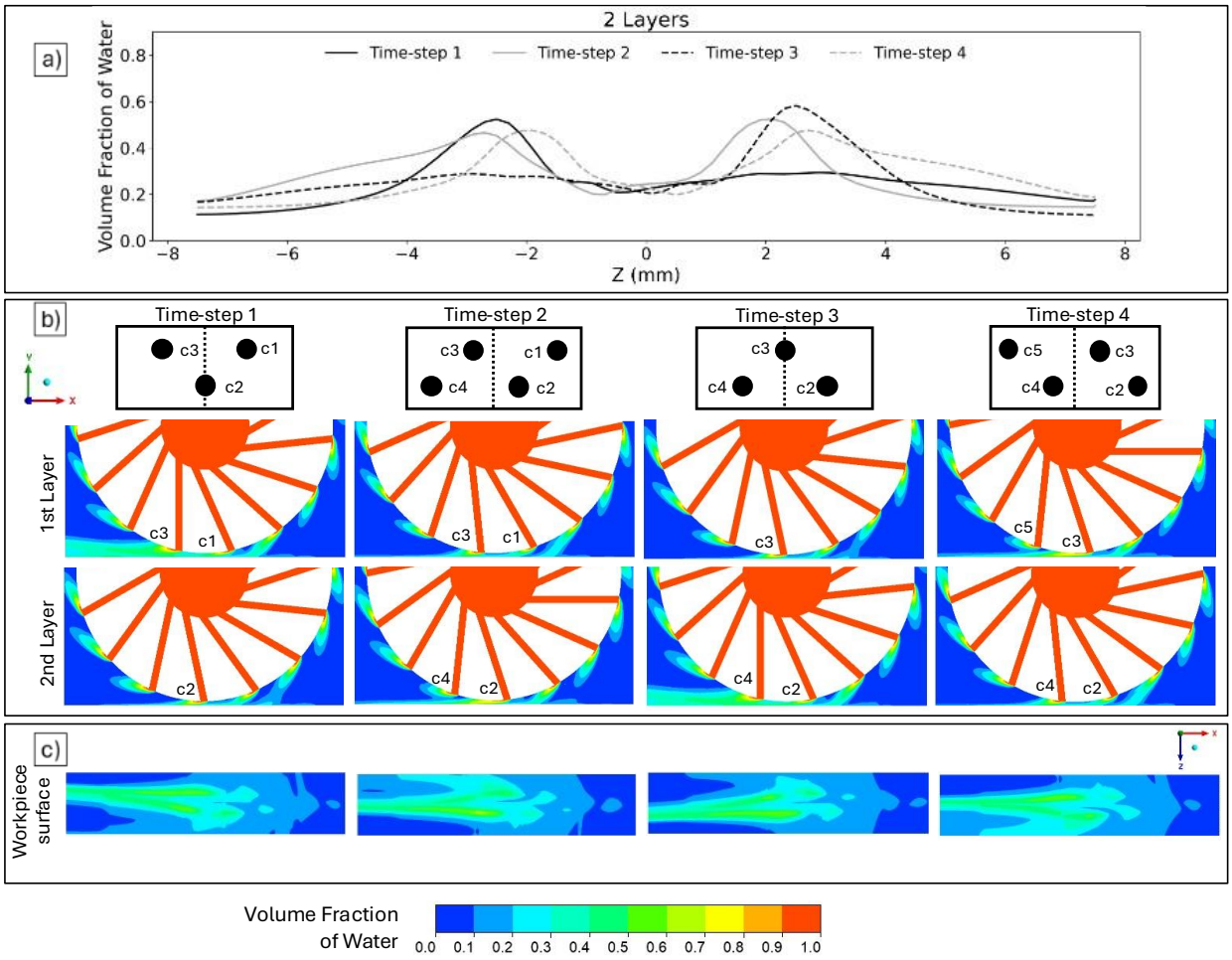


Figure 6.5 – Water volume fraction for the two-layer configuration over time: (a) along the contact line, (b) in each layer and (c) on the workpiece surface.

At time-step 2, C2 becomes the primary source of fluid in the contact zone, as shown by the peak at Z ≈ 2.0 mm in Figure 6.5(a). This alternating behavior repeats in time-steps 3 and 4, mirroring previous time steps as the wheel rotates. The central region of the contact line retains a relatively stable fluid presence, never dropping below 20 %, but it still exhibits lower overall intensity compared to surrounding areas (Figure 6.5(c)).

The three-layer configuration (Figure 6.6) introduces greater dynamism, with fluid application alternating effectively between time steps, in contrast to the two-layer case. A key observation is the cyclic flow movement along the contact line:

- At time step 1, the fluid concentration is higher at the sides, while the center is less cooled.
- At time step 2, the distribution shifts toward the center, reducing cooling at the sides.
- Time-step 3 redistributes the fluid again toward the sides, though with a different peak profile compared to step 1.
- Time-step 4 shows an asymmetric pattern, distinct from step 2, suggesting non-uniform yet continuous fluid movement.

This alternating pattern helps sustain cooling over time, avoiding dry spots and improving chip removal.

As in the previous configurations, a significant portion of the fluid reaching the contact line originates from channels that have already passed the contact point, due to the rotation of the grinding wheel. This effect is evident in Figure 6.6(a) and (b), where the peaks in fluid concentration correspond to channels positioned ahead of the contact zone.

Figure 6.6(b) also shows that the central layer releases the greatest amount of coolant, while the aligned lateral layers contribute to fluid replenishment and extend the coverage over the contact surface. This combined effect promotes a broader and more uniform distribution, improves the continuity of coolant delivery and reduces the intensity of unused jets diverted to the environment.

A comparative analysis of the three configurations confirms that the three-layer setup provides the most effective and dynamic coolant flow pattern along the contact line. The alternating channels create a continuous cyclic flow that helps maintain a more consistent fluid presence and supports debris removal and workpiece cooling. The two-layer configuration enhances fluid dispersion compared to the single-layer design, since the alternating channels spread the fluid more evenly across a broader area. However, as discussed previously, the two-layer configuration still exhibits zones of lower fluid concentration in the central region, where the contact line receives limited fluid supply, which may compromise local cooling performance. The single-layer configuration ensures stable but highly localized cooling, resulting in significant fluid waste and limited effectiveness at the edges of the contact.

These CFD results demonstrate clear differences in fluid behavior depending on the number of layers, highlighting the advantages of multi-layer configurations. Nevertheless, numerical analysis alone cannot capture the full complexity of the grinding process, especially regarding heat generation and removal. For this reason, experimental grinding tests are required to verify how these fluid-distribution patterns translate into

real cutting performance. The following section presents these experiments and evaluates how the different layer configurations behave under grinding operating conditions.

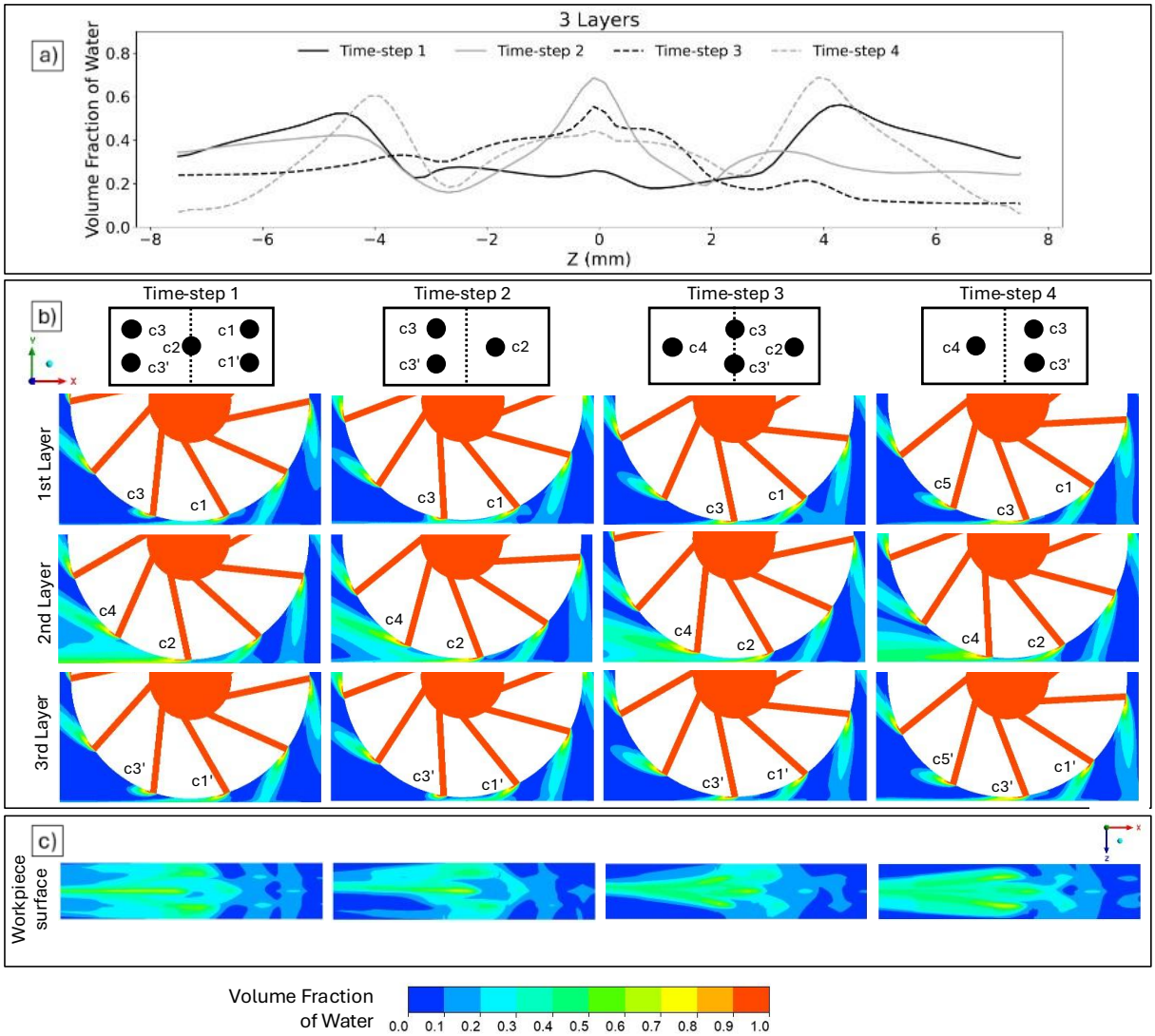


Figure 6.6 – Water volume fraction for the three-layer configuration over time: (a) along the contact line. (b) in each layer and (c) on the workpiece surface.

6.2.3 Grinding Performance

The grinding experiments were conducted to validate the CFD predictions and to quantify how the number of channel layers influences mechanical and thermal behavior under real cutting conditions. As outlined in Section 0, the tests were performed under a feed rate of 100 mm/min, a wheel speed of 5000 rpm, an inlet flow rate of 400 mL/min and depths of cut between 20 and 120 µm. Tangential and normal forces and

temperature variation (ΔT) were measured for the one-, two- and three-layer wheels to assess their combined tribological and cooling performance.

Cutting Forces

Figure 6.7 presents the tangential and normal forces as a function of depth of cut for the one-, two- and three-layer wheels. The forces increased linearly with depth in all cases, which is consistent with classical grinding mechanics, where larger cutting depths lead to proportionally higher chip thickness and grain engagement [43].

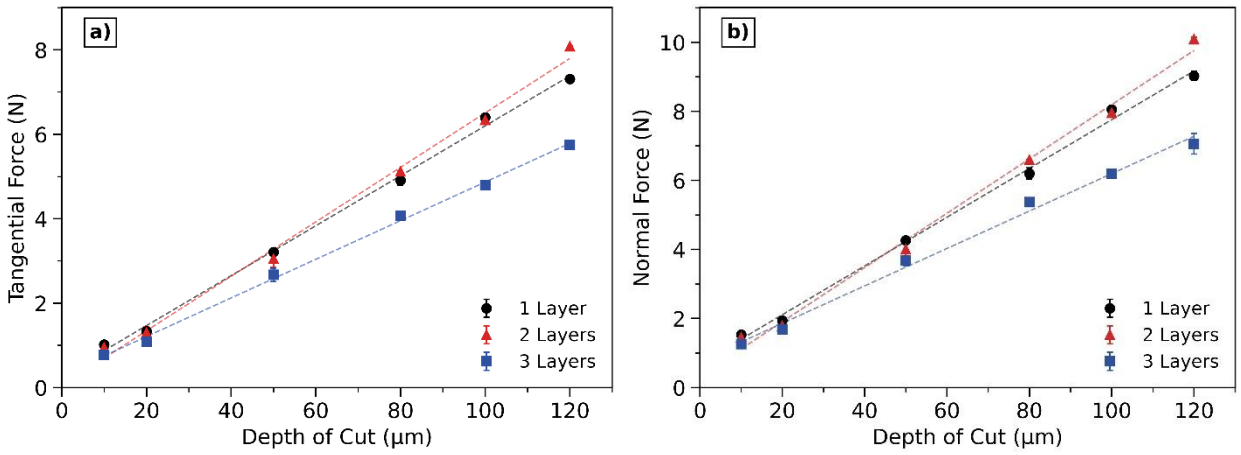


Figure 6.7 – Grinding forces as a function of depth of cut for wheels with one, two and three channel layers: (a) tangential force and (b) normal force.

The main distinction among the wheels concerns the performance of the three-layer configuration. Across all conditions, the three-layer wheel consistently showed lower F_t and F_n values, with reductions ranging from 17–25 % in tangential force compared with the single-layer wheel and from 12–29 % compared with the two-layer wheel. In contrast, the single- and two-layer configurations showed very similar force behavior. At shallow depths (10–20 µm) their forces differed by less than 3 %, indicating nearly identical performance. At larger depths, the single-layer wheel produced slightly lower forces than the two-layer configuration, although the difference remained modest.

Temperature Variation (ΔT)

Regarding temperature variation (ΔT), the results are shown in Figure 6.8. At 10 µm, the single-layer wheel exhibited almost twice the temperature of the two- and three-layer configurations (3.0 °C versus 1.5–1.6 °C,

corresponding to a reduction close to 50 %). From 20 µm onwards, the differences among the three wheels became evident earlier than in the force results: the three-layer wheel maintained the lowest ΔT (2.5 °C at 20 µm, which represents reductions of approximately 12 % relative to the two-layer wheel and 13 % relative to the single-layer wheel).

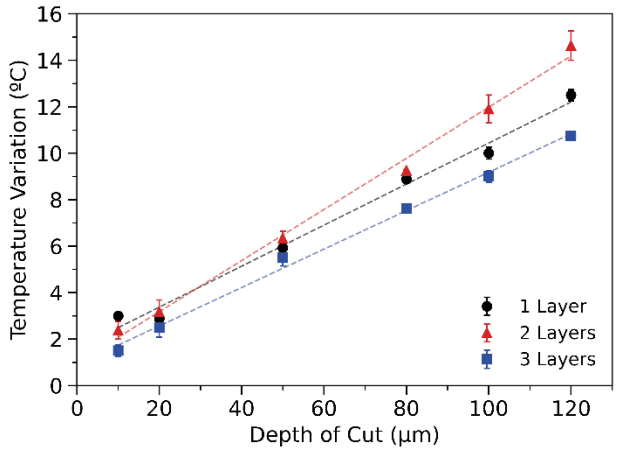


Figure 6.8 – Temperature variation (ΔT) as a function of depth of cut for grinding wheels with one, two and three channel layers.

At larger depths, the separation intensified. The three-layer wheel remaining the most effective (10.8 °C at 120 µm, a reduction of about 14 % compared with the single-layer and 26 % compared with the two-layer). The single-layer configuration presented intermediate behavior (12.5 °C at 120 µm), whereas the two-layer wheel consistently exhibited the highest ΔT values, reaching 14.6 °C at 120 µm.

Overall, the three-layer design ensured the most effective cooling across all cutting conditions, while the two-layer wheel showed the least favorable thermal performance, particularly under higher cutting depths.

This trend was also observed by Sieniawski *et al.* [32], who evaluated the effect of the number of channel layers on cutting forces. Their results showed that the three-layer configuration provided the best overall performance, followed by the single-layer and, finally, the two-layer wheel.

6.2.4 Concluding Remarks on Number of Layers

The combined CFD and grinding tests revealed distinct differences among the three wheel configurations:

- The single-layer wheel delivered a stable but highly localized fluid supply, leading to intermediate forces and ΔT values. Its performance was consistent, yet the coolant reached predominantly the central region of the contact line, with limited effectiveness at the edges.

- The two-layer wheel generated alternating fluid delivery between time steps, but the arrangement produced non-uniform replenishment in the central zone. Because this region is the most critical for heat dissipation, this irregular supply likely contributed to the higher forces and ΔT measured at larger depths of cut. As a result, it showed the highest forces and ΔT at higher depths of cut, becoming the least effective configuration overall, in agreement with the trend suggested by the Grey Relational Analysis.
- The three-layer wheel promoted the most uniform and continuous coolant distribution along the contact line, consistently achieving the lowest tangential and normal forces and the lowest ΔT, demonstrating superior cooling efficiency and grinding stability.

These results refine the conclusions from the Taguchi–Grey analysis and ANOVA, which initially suggested that the number of layers had only a minor statistical contribution. The combined CFD and experimental evidence demonstrates that, although its contribution is small in a static statistical sense, the dynamic interaction between layers plays a decisive role under realistic grinding conditions, improving both thermal and tribological performance.

6.3 Effect of Channel Diameter

In the preliminary screening study based on the Taguchi–Grey relational method, the channel diameter emerged as the most influential parameter on coolant transport efficiency. The ANOVA analysis confirmed its statistical significance, with a contribution of nearly 60 % to the Grey relational grade. The general trend observed was that larger channels promoted higher outlet velocities and improved coolant delivery, leading to superior performance.

To further investigate the practical implications of this parameter, a dedicated set of CFD simulations and grinding tests was conducted. Differently, from the Taguchi study, where the number of channels and outlet area varied simultaneously, the total outlet area was kept constant in the present analysis. By comparing wheels with 190 channels of 0.6 mm, 69 channels of 1.0 mm and 30 channels of 1.5 mm (all with approx. 54 mm^2 of outlet area), it was possible to isolate the specific influence of channel diameter on fluid distribution and grinding performance. This approach provides a more realistic evaluation of the design trade-offs, linking hydraulic behavior, near-wall losses and outlet uniformity with the actual grinding response, thereby complementing the statistical optimization with direct experimental validation.

6.3.1 Grinding Wheel Geometries

Figure 6.9 illustrates the three grinding wheel geometries evaluated in this study, highlighting the internal 3D structures produced in PLA and the corresponding sintered wheels. In this case, the designs differ by the channel diameter, while the inclination and the outlet area were kept constant.

All wheels were manufactured with identical external dimensions (62 mm in diameter, 15 mm in width and 21 mm in inner diameter). The total outlet area of the channels was maintained approximately constant at 54 mm^2, ensuring comparable conditions in terms of active grain exposure and nominal fluid input. This strategy allowed the effect of channel diameter to be isolated from other design factors, enabling a direct comparison of thermal and tribological performance.

The geometric specifications of the three configurations are summarized in Table 6.6.

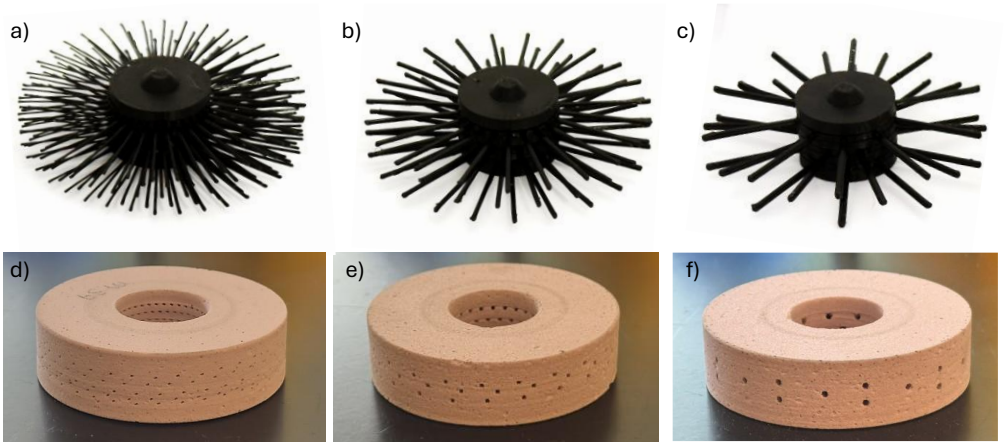


Figure 6.9 – Internal 3D structures, in PLA (a–c) and corresponding sintered grinding wheels (d–f) with different channel configurations: (a, d) 190 channels of ø 0.6 mm; (b, e) 69 channels of ø 1.0 mm; (c, f) 30 channels of ø 1.5 mm.

Table 6.6 – Geometric specifications of the structured grinding wheels evaluated in this study.

Grinding Wheel	Channel Diameter (mm)	Total Number of Channels	Channels per Layer	Number of Layers	Interlayer Distance (mm)	Total Outlet Area (mm^2)
GW_190_0.6	0.6	190	38	5	2.1	53.7
GW_69_1.0	1.0	69	23	3	3.5	54.2
GW_30_1.5	1.5	30	10	3	3.5	53.0

6.3.2 Numerical Analysis

The numerical results were divided into two complementary analyses. First, using Setup A, the flow distribution and velocity vectors on the wheel surface were examined under identical operating conditions of 5000 rpm and 400 mL/min. Then, with Setup B, simulations were performed to extract the outlet velocity profiles and identify regions of low hydraulic utilization using the same rotational speed and flow rate.

Figure 6.10 shows the velocity vectors on the external surface of the grinding wheel for the three geometries evaluated, covering both the channel outlets and the contact zone with the workpiece. The GW_190_0.6 configuration generates a high density of vectors distributed across the surface, indicating broad spatial coverage but with reduced jet momentum. This behavior reflects the limited capacity of narrow channels to sustain elevated outlet velocities. In contrast, the GW_30_1.5 wheel produces fewer but more intense jets, concentrated in localized regions, which increases the likelihood of areas receiving insufficient coolant. The GW_69_1.0 geometry exhibits an intermediate pattern, combining moderate jet intensity with more homogeneous coverage across the tool surface.

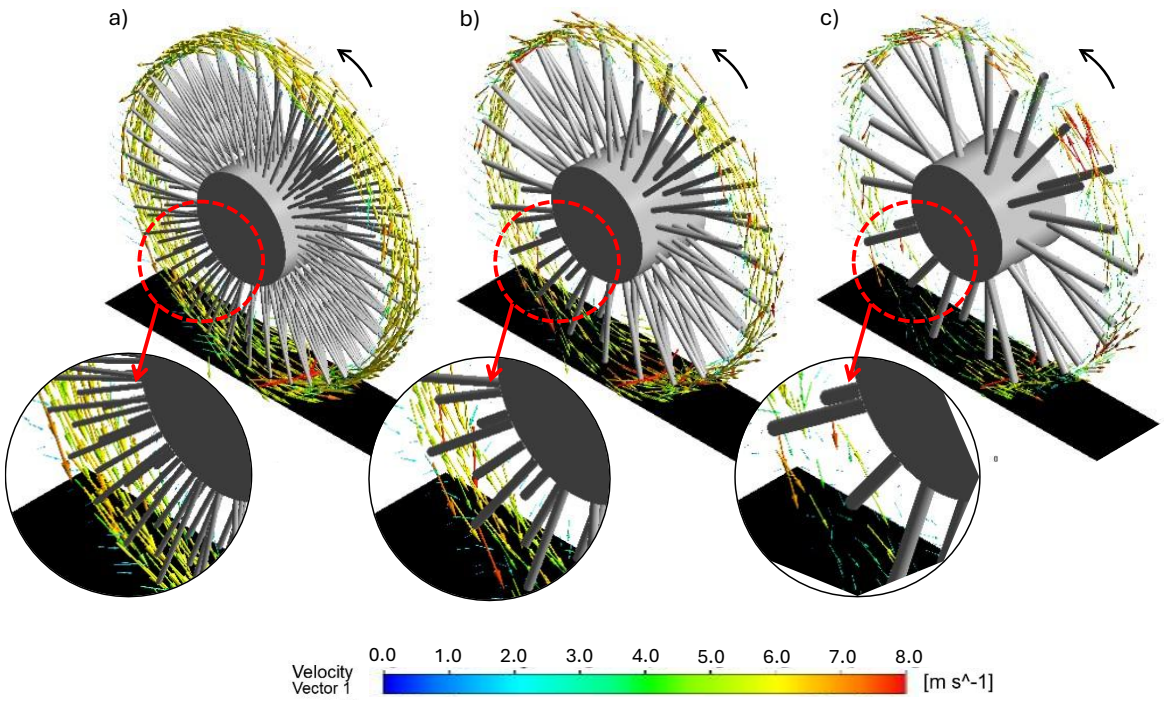


Figure 6.10 – Velocity vectors on the external surface of the grinding wheels and in the contact zone: (a) GW_190_0.6, (b) GW_69_1.0 and (c) GW_30_1.5.

To further investigate the local fluid performance at each channel outlet, velocity profiles were extracted using Setup B. The profiles were obtained from cross-sectional planes orthogonal to the channel exits. Based on these profiles, the areas with velocity below 0.1 m/s were quantified as indicators of reduced hydraulic efficiency. This threshold corresponds approximately to 10 % of the maximum outlet velocity across the evaluated geometries, consistently identifying the viscous-dominated near-wall region. This post-processing was performed in ImageJ, where the blue regions in the velocity contour maps were segmented. The fraction of this low-velocity area relative to the total channel cross-section was then calculated for each geometry and is presented in Table 6.7 together with the average outlet velocities and the corresponding outlet areas. Figure 6.11 shows the velocity contour maps at the outlet surface, where blue areas correspond to low flow and red areas to high flow.

Table 6.7 – Average outlet velocity and fraction of low-velocity regions (V < 0.1 m/s) for the three structured wheel configurations.

Grinding Wheel	Average velocity (m/s)	Total outlet area (mm²)	Area with V < 0.1 m/s	
			(mm²)	(%)
GW_190_0.6	0.45	53.7	10.2	19
GW_69_1.0	0.75	54.2	7.5	14
GW_30_1.5	0.80	53.0	3.8	7

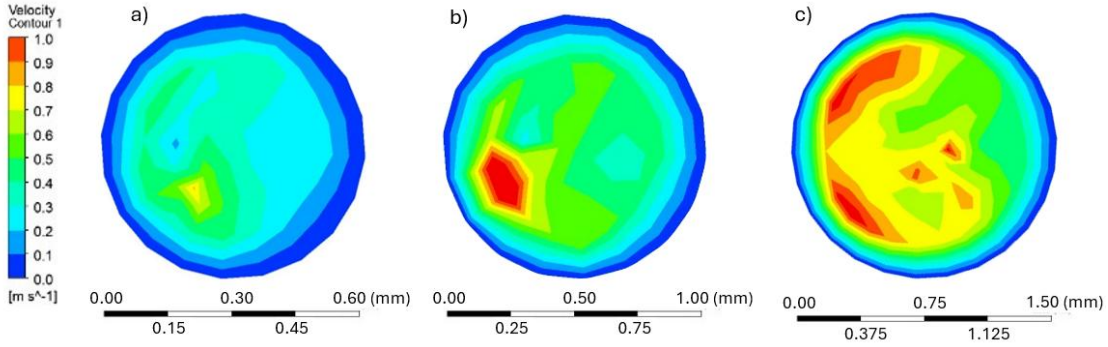


Figure 6.11 – Velocity contour maps at the outlet surface of the grinding wheels: (a) GW_190_0.6, (b) GW_69_1.0 and (c) GW_30_1.5.

The GW_190_0.6 configuration exhibited the lowest average outlet velocity (0.45 m/s) and the largest fraction of low-velocity regions (19 %). This behavior results from the high number of narrow channels, which increase pressure losses due to internal wall friction. As the channel diameter increases, these losses are

reduced, as evidenced by the higher outlet velocities measured in GW_69_1.0 (0.75 m/s) and GW_30_1.5 (0.80 m/s), which also showed smaller fractions of low-velocity areas (14 % and 7 %, respectively). However, the additional gain in average outlet velocity between the 1.0 mm and 1.5 mm configurations was relatively modest, indicating that the hydraulic response approaches a point where further increases in channel diameter yield diminishing improvements.

To provide a geometric interpretation of these differences, a Geometric Flow Index (GFI) was calculated by dividing the total channel volume by the corresponding internal wall area. This index expresses the balance between flow capacity and internal resistance. As shown in Figure 6.12, the percentage of low-velocity regions (V < 0.1 m/s) decreases linearly with increasing GFI, indicating a direct relationship between wall friction and energy losses. In contrast, the average outlet velocity increases with GFI, although the magnitude of this increase is more pronounced between the GW_190_0.6 and GW_69_1.0 configurations than between the GW_69_1.0 and GW_30_1.5 wheels.

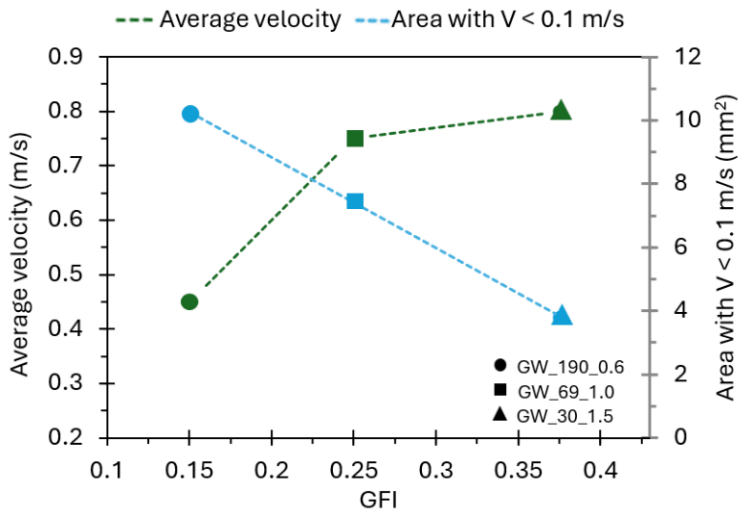


Figure 6.12 – Relationship between Geometric Flow Index (GFI), average outlet velocity and percentage of low-velocity area (V < 0.1 m/s) for the three grinding wheel configurations.

The distribution observed in GW_69_1.0 appears to balance surface coverage and velocity magnitude, generating moderately strong jets that are more evenly distributed across the wheel surface. Among the three configurations, this geometry provides an intermediate combination of jet intensity and coverage, representing a compromise between the broad, low-momentum flow of GW_190_0.6 and the concentrated high-velocity jets of GW_30_1.5. The following sections examine how this intermediate hydraulic behavior translates into differences in fluid delivery to the cutting zone.

6.3.3 Grinding Performance

Experimental tests were conducted on the structured wheels to validate numerical predictions and assess the effects of channel geometry on grinding forces, specific grinding energy and thermal behavior. As outlined in Section 0, the tests were performed under a feed rate of 100 mm/min, a wheel speed of 5000 rpm, an inlet flow rate of 400 mL/min and depths of cut between 20 and 120 µm.

Cutting Forces

Figure 6.13 shows the average values of the tangential (F_t) and normal (F_n) forces as a function of the depth of cut. Overall, the GW_69_1.0 configuration presented the lowest forces across the entire tested range, confirming the numerical indication that this geometry achieves a balanced hydraulic performance. Among the remaining geometries, GW_190_0.6 exhibited slightly lower forces than GW_30_1.5, although the differences remained small across all depths of cut.

At shallow depths (10 µm), GW_69_1.0 achieved a reduction of approximately 38 % in F_t compared with GW_30_1.5 and a reduction of about 26 % at 50 µm, demonstrating its superior ability to reduce cutting effort.

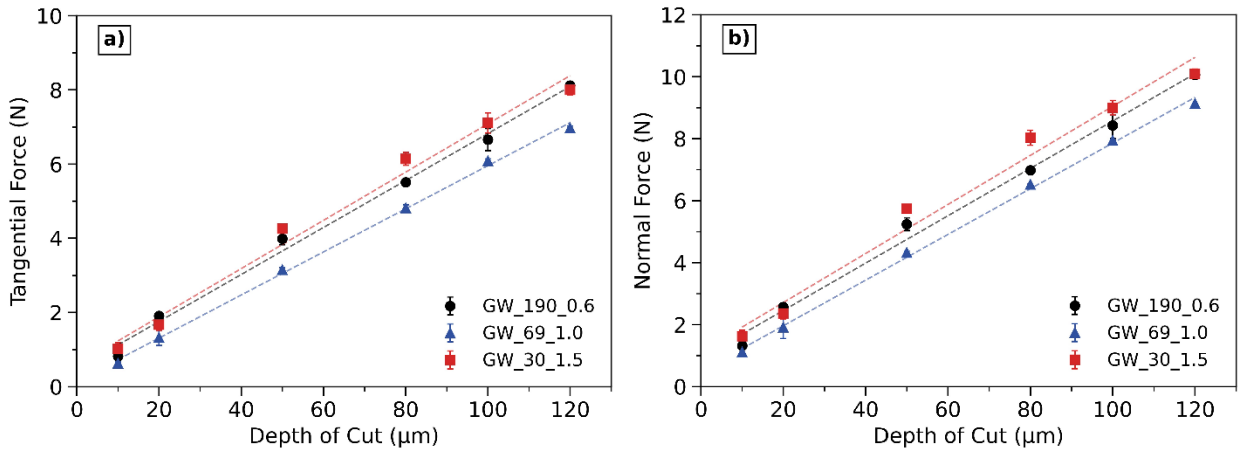


Figure 6.13 – Tangential (a) and normal (b) grinding forces as a function of depth of cut.

Specific Grinding Energy

Figure 6.14 shows the variation of specific cutting energy as a function of cutting depth. The GW_190_0.6 and GW_30_1.5 geometries presented the highest specific energy values at the shallowest depths (10–20 µm), with a tendency to progressively reduce from 50 µm onwards. This behavior indicates low energy

efficiency in the initial passes, possibly due to the predominance of surface plastic deformation mechanisms and friction without effective cutting. As the depth increases, grain penetration improves and the shear removal regime stabilizes, reducing energy consumption per volume removed.

In contrast, the GW_69_1.0 grinding wheel maintained low and more linear specific energy values throughout the analyzed range, suggesting a more favorable energetic response at the tested range of cutting. This difference highlights the influence of the channel's configuration on the lubrication dynamics and the cutting regime established in each case.

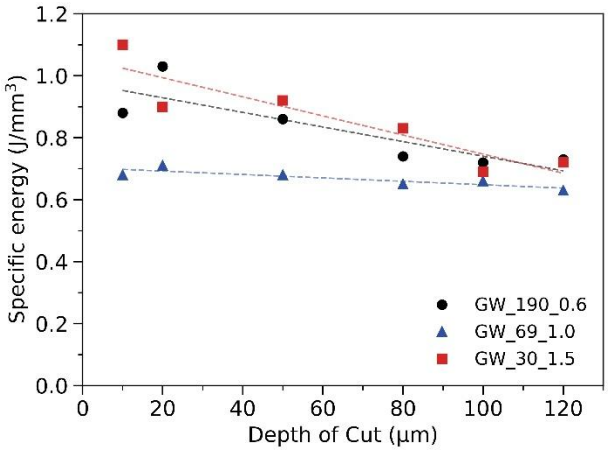


Figure 6.14 – Specific energy as a function of depth of cut.

The comparison among the three geometries indicates that, for GW_190_0.6 and GW_30_1.5, the initial behavior is dominated by a regime with a strong contribution of surface plastic deformation and friction, which results in high energy per removed volume at shallow depths [59–62]. This effect is associated with the combination of low outlet velocity in the Ø 0.6 mm configuration and limited surface coverage in the Ø 1.5 mm design, both of which restrict the effectiveness of internal lubrication during the early stages of the process.

On the other hand, the GW_69_1.0 configuration showed a more stable and energetically efficient response even at the smallest depths, indicating that material removal occurred predominantly by shear from the first passes. This performance suggests that the Ø 1.0 mm channels provided a more balanced lubrication condition in terms of velocity and surface coverage, enabling adequate grain penetration without requiring the cutting regime to be stabilized at larger depths.

Overall, the specific energy results reinforce that channel diameter influences both the initial tribological regime and the global energetic efficiency of the process. Among the three geometries evaluated, only the Ø 1.0 mm grinding wheel exhibited consistently efficient behavior across the entire range of cutting depths analyzed.

Temperature Variation (ΔT)

Figure 6.15 presents the maximum temperature variation (ΔT) in the workpiece as a function of cutting depth. The GW_190_0.6 configuration recorded the highest ΔT values under all conditions, while the GW_69_1.0 wheel showed the lowest average temperatures, with reductions of 40.9 % and 30.1 % at 50 µm and 100 µm, respectively, when compared to GW_190_0.6.

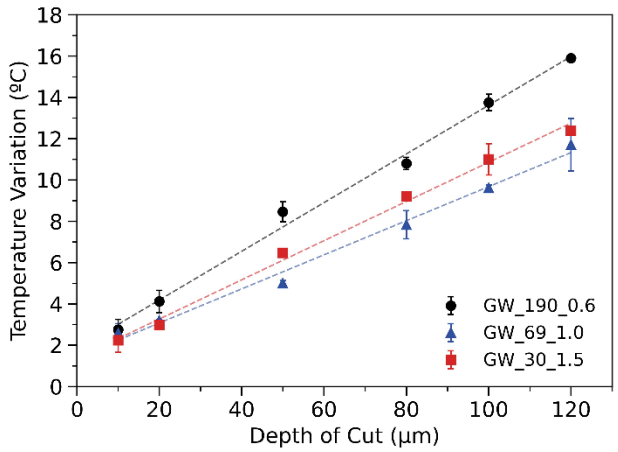


Figure 6.15 – Maximum temperature variation (ΔT) measured in the workpiece for different cutting depths.

This behavior reinforces the importance of fluid distribution and surface coverage in thermal dissipation during grinding. The lower ΔT observed in GW_69_1.0 indicates that this configuration was able to dissipate the additional heat more effectively than the likely due to a combination of sufficiently high outlet velocity and more homogeneous coolant distribution. This balance improves fluid access to the grinding zone, reducing thermal accumulation under higher grinding loads.

Overall, the experimental results demonstrated distinct performance patterns among the tested grinding wheel configurations. While each design presented advantages under specific conditions, the GW_69_1.0 configuration consistently delivered lower forces and temperature variation across all cutting depths. These findings suggest that geometric parameters, particularly channel diameter and distribution, play a critical role in defining the efficiency of internal lubrication.

6.3.4 Correlation Between CFD and Experimental Results

The comparative analysis between the CFD simulation results and the experimental data revealed clear relationships between the fluid behavior at the channel outlets and the grinding process performance.

The GW_190_0.6 configuration exhibited lower tangential and normal forces slightly than GW_30_1.5, despite its poorer performance in temperature control. This result is consistent with its broader and more homogeneous surface coverage, as predicted by the velocity-vector fields in Setup A. Even though this geometry produces lower outlet velocity, the increased number of jets distributes coolant more evenly, which helps attenuate local mechanical interaction peaks and reduces the intensity of micro-impacts between abrasive grains and the workpiece. In contrast, the concentrated and high-velocity jets in the GW_30_1.5 configuration favor localized heat removal but result in reduced lateral coverage and more intermittent lubrication, which can generate localized mechanical stresses at the abrasive grain–workpiece interface.

Regarding thermal behavior, the GW_30_1.5 configuration performed better at lower cutting depths (10–20 μm), likely due to the focused action of the more intense jets, promoting effective localized cooling. However, above 50 μm, its performance became inferior to that of GW_69_1.0. This change can be explained by the more limited surface coverage of the widely spaced channels, whose effectiveness decreases as the contact area increases, reducing the amount of coolant available across the full width of the grinding zone. As a result, local heat generation becomes more pronounced, making it difficult to maintain adequate cooling under more demanding cutting conditions.

Figure 6.16 shows the relationship between the outlet area fraction with velocity below 0.1 m/s and the experimental results for tangential force (a) and maximum temperature variation (b). As only three wheel geometries were evaluated, this comparison is intended as a qualitative assessment of the tendencies between the CFD parameter and the experimental behavior. Tangential force remains nearly unchanged as this variable increases, indicating that mechanical behavior is not strongly influenced by the low-velocity outlet area. In contrast, temperature exhibits an upward tendency, suggesting that thermal performance is more sensitive to the coolant velocity distribution at the outlet. This distinction supports the interpretation that fluid delivery with sufficient velocity is essential for effective heat removal at the contact zone, whereas force levels depend more closely on jet orientation, coverage and the resulting lubrication conditions.

At higher cutting depths, however, the behavior does not follow the same clear tendency observed at 10 μm. Grinding is a thermally complex process, and several mechanisms contribute simultaneously to heat

generation and removal. At low depths, such as 10 µm, the measured temperature in the workpiece follows closely the fraction of low-velocity outlet area, with smaller low-velocity regions resulting in lower ΔT. At 50 and 120 µm, the tendency becomes less clear, indicating that coolant velocity alone is not sufficient to ensure effective heat dissipation under more demanding conditions. Increased heat generation, a larger contact area and a higher chip volume all begin to play a more significant role, making the thermal response more complex as cutting depth increases. To better understand these interactions, a dedicated experimental program will be required, including temperature-profile measurements at multiple locations rather than relying solely on the maximum temperature value, as performed in the present study.

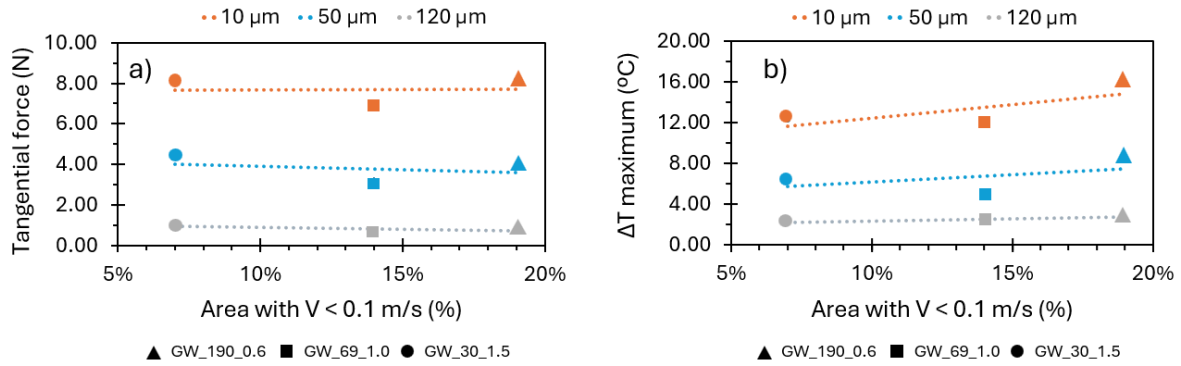


Figure 6.16 – Correlation between the outlet area with velocity below 0.1 m/s and experimental results: (a) tangential force; (b) maximum temperature variation (ΔT), for three cutting depths (10, 50 and 120 µm).

Figure 6.17 illustrates the correspondence between the simulated velocity distribution at the channel outlets and the flow patterns observed on the grinding wheels. To enhance visual identification of fluid dispersion, a coulorant was added to the distilled water used in the experimental setup.

The GW_190_0.6 configuration exhibits multiple visible outlet points with weaker yet well-distributed jets, matching the continuous and homogeneous pattern predicted by the simulation. This behavior is technically consistent with its low outlet velocity, but the large number of channels enhances overall coverage even when the jet momentum is limited.

The GW_69_1.0 configuration combines moderate jet intensity with a relatively uniform distribution, which aligns with its balanced hydraulic performance demonstrated previously. This connection is valid because its CFD results showed intermediate velocities with reduced low-velocity areas, consistent with smooth and visible flow spread.

In contrast, the GW_30_1.5 configuration concentrates the fluid output in fewer points, with intense jets that are less visible on the wheel surface, reflecting the lower surface coverage predicted in the simulation,

especially in the regions between channels. This interpretation is accurate: the large spacing between outlets reduces the number of visible wetting paths, even when jet velocity is high.

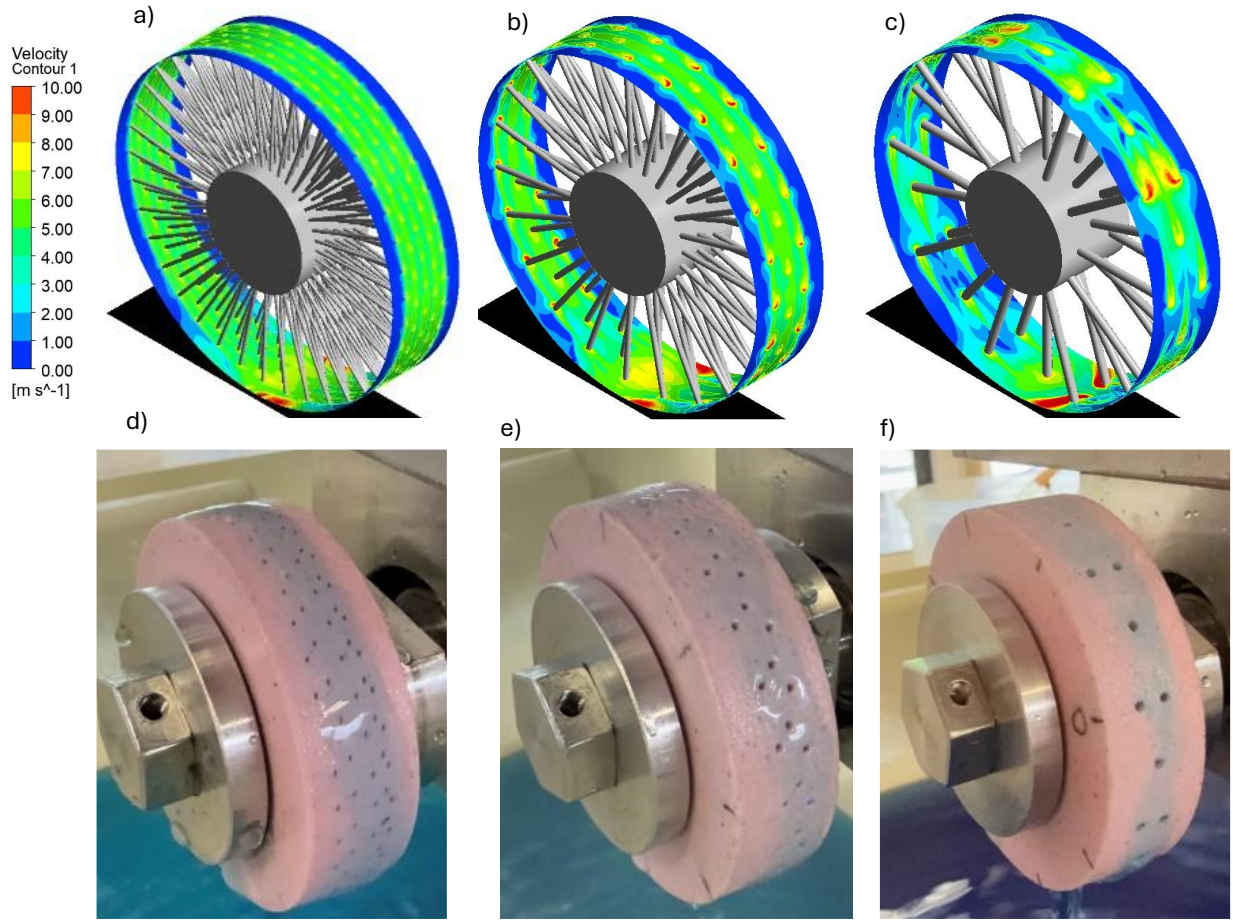


Figure 6.17 – Velocity distribution at the channel outlets obtained by CFD (a–c) and fluid ejection observed on the grinding wheel surface during operation (d–f): (a, d) GW_190_0.6; (b, e) GW_69_1.0; (c, f) GW_30_1.5.

This direct comparison between simulation and experimental observation not only reinforces the reliability of the adopted CFD modeling approach but also highlights its potential as a design support tool. The ability to predict both the distribution and behavior of fluid flow across different geometries significantly contributes to the development of structured grinding wheels with improved hydraulic and thermal performance.

6.3.5 Concluding Remarks on Channel Diameter

The combined CFD and grinding tests revealed clear differences between the three geometries evaluated:

- Narrow channels (0.6 mm, 190 units) generated broad surface coverage but suffered from excessive wall friction, leading to low outlet velocity and the highest ΔT in grinding tests.

- Wide channels (1.5 mm, 30 units) delivered higher outlet velocities but with poor coverage, which limited lubrication uniformity and slightly increased mechanical load, reflected in a higher specific grinding energy at intermediate depths of cut.
- Intermediate channels (1.0 mm, 69 units) provided the best overall balance, combining adequate velocity with distributed coverage. This configuration consistently achieved the lowest tangential and normal forces, the lowest specific energy and a reduction of approximately 40 percent in ΔT at 50 µm compared with the 0.6 mm configuration.

These results refine the conclusions drawn from the Taguchi analysis. While the statistical screening indicated that "the larger the diameter, the better," the detailed CFD and grinding validation demonstrate that the trend is not strictly monotonic but instead suggests the existence of an optimum range. The 1.0 mm configuration proved most effective, reconciling hydraulic efficiency with uniform fluid delivery and therefore represents a more robust design choice for structured grinding wheels.

6.4 Effect of Channel Inclination

In the Taguchi–Grey analysis, channel inclination was identified as statistically insignificant, with a contribution below 3 % to the Grey relational grade. At first glance, this result might suggest that inclination has no relevant effect on coolant delivery. However, it is important to note that the Taguchi study relied exclusively on CFD Setup A, which was limited to qualitative dispersion in the external domain and did not fully capture jet orientation, coherence, outlet velocity, or penetration into the grinding zone.

From a physical standpoint, channel inclination directly governs the direction and stability of the fluid jets emerging from the wheel. The angle between the channel axis and the centrifugal force vector defines whether the jet exits radially (favorable for penetration) or tangentially (more prone to dispersion). These aspects are critical for overcoming the air barrier, ensuring fluid entry into the grain–workpiece interface and ultimately influencing both tribological and thermal performance.

A dedicated study was carried out combining CFD outlet analysis, high-speed flow visualization and grinding tests. The objective was to clarify whether jet orientation impacts grinding performance under realistic operating conditions.

6.4.1 Grinding Wheel Geometries

Three internal channel configurations were designed to evaluate the effect of inclination, as illustrated in Figure 6.18: (a) positive inclination, with channels tilted at θ = 12° in the wheel rotation direction; (b) straight, with radially aligned channels (θ = 0°); and (c) negative inclination, with channels tilted at θ = 12° opposite to the rotation direction. All geometries consisted of 30 channels with a nominal diameter of 1.7 mm, an external diameter of 62 mm and an internal diameter of 21 mm.

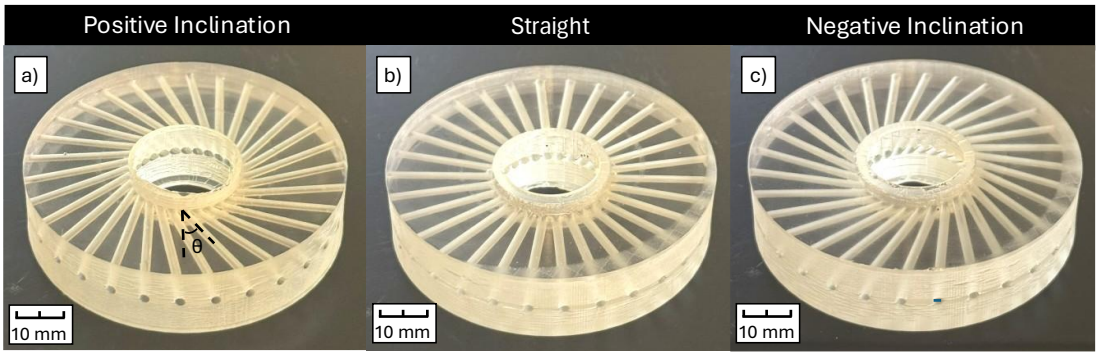


Figure 6.18 – Transparent resin prototypes of structured grinding wheels used for flow visualization and particle tracking: (a) positive inclination (θ = 12° in the rotation direction); (b) straight (θ = 0°); and (c) negative inclination (θ = 12° opposite to the rotation direction).

Transparent resin prototypes (Figure 6.18) were produced by additive manufacturing for flow visualization. The prototypes were fabricated using the same process employed for the wheel used in the particle tracking experiments, as described in Section 6.5.1. A single channel layer was adopted, which facilitated the observation and tracking of fluid motion, since the flow remained confined to one plane and avoided overlapping trajectories between layers. This simplified configuration was essential for achieving clear visualization of jet orientation and particle motion during high-speed imaging.

In contrast, vitrified grinding wheels with three channel layers, corresponding to the most favorable configuration identified in Section 6.2, were manufactured and tested in the grinding experiments. This ensured that the inclination analysis was performed under the most efficient internal cooling condition.

6.4.2 Numerical Analysis

All simulations were performed using Setup B, under a constant flow rate of 800 mL/min and varying rotational speeds, ensuring consistent comparison among the three inclination configurations. Figure 6.19 shows the evolution of the mean outlet fluid velocity as a function of the grinding wheel speed (V_s) for the

three internal channel inclination configurations: negative, straight and positive inclination. A monotonic increase in velocity is observed with increasing rotation, although with different gradients. At 5000 rpm, for instance, the mean velocity in the positive inclination channels (1.05 m/s) is approximately twice that of the negative inclination channels (0.51 m/s), highlighting the strong influence of channel geometry on hydraulic performance.

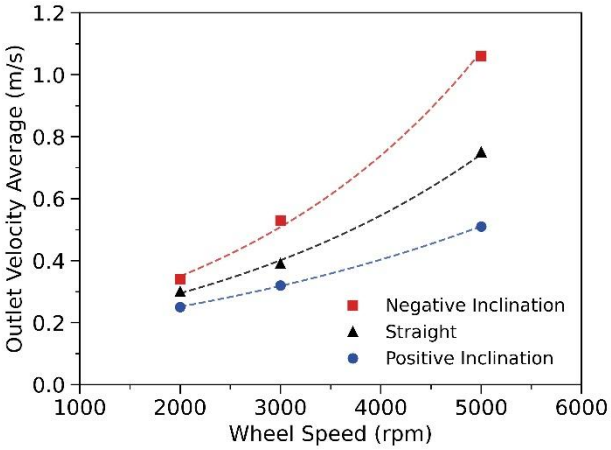


Figure 6.19 – Average outlet velocity as a function of wheel speed for three internal channel inclination geometries: negative, straight and positive.

The spatial distribution of velocity at the channel outlets further reinforces this effect. As shown in Figure 6.20 increasing the wheel speed benefits all geometries, but both the magnitude and uniformity of velocity distribution vary significantly. Some configurations concentrate higher velocities in small portions of the outlet cross-section, whereas others exhibit a more homogeneous pattern.

In the negative inclination case, even at high rotational speeds, the fluid exits remain confined to isolated and irregular regions within the outlet section, indicating a fragmented and hydraulically inefficient flow. The straight configuration presents a more coherent distribution: as the speed increases, the high-velocity band widens and becomes more evenly distributed across the outlet area, suggesting improved use of centrifugal field. The positive inclination case shows the most pronounced effect, at 2000 rpm, well defined high-velocity zones are already visible and at 5000 rpm the outlet cross-section is almost entirely occupied by a continuous, uniform high-velocity region. These results demonstrate not only the absolute increase in velocity with rotation, but also that the differences between geometries become more pronounced at higher speeds. At low speeds, certain sectors of comparable performance can still be observed among the three configurations; however, as V_s increases, the positive inclination channels stand out in both average velocity

and in the extent and uniformity of the high-velocity region. This reinforces the influence of inclination on the hydraulic efficiency of the grinding wheel.

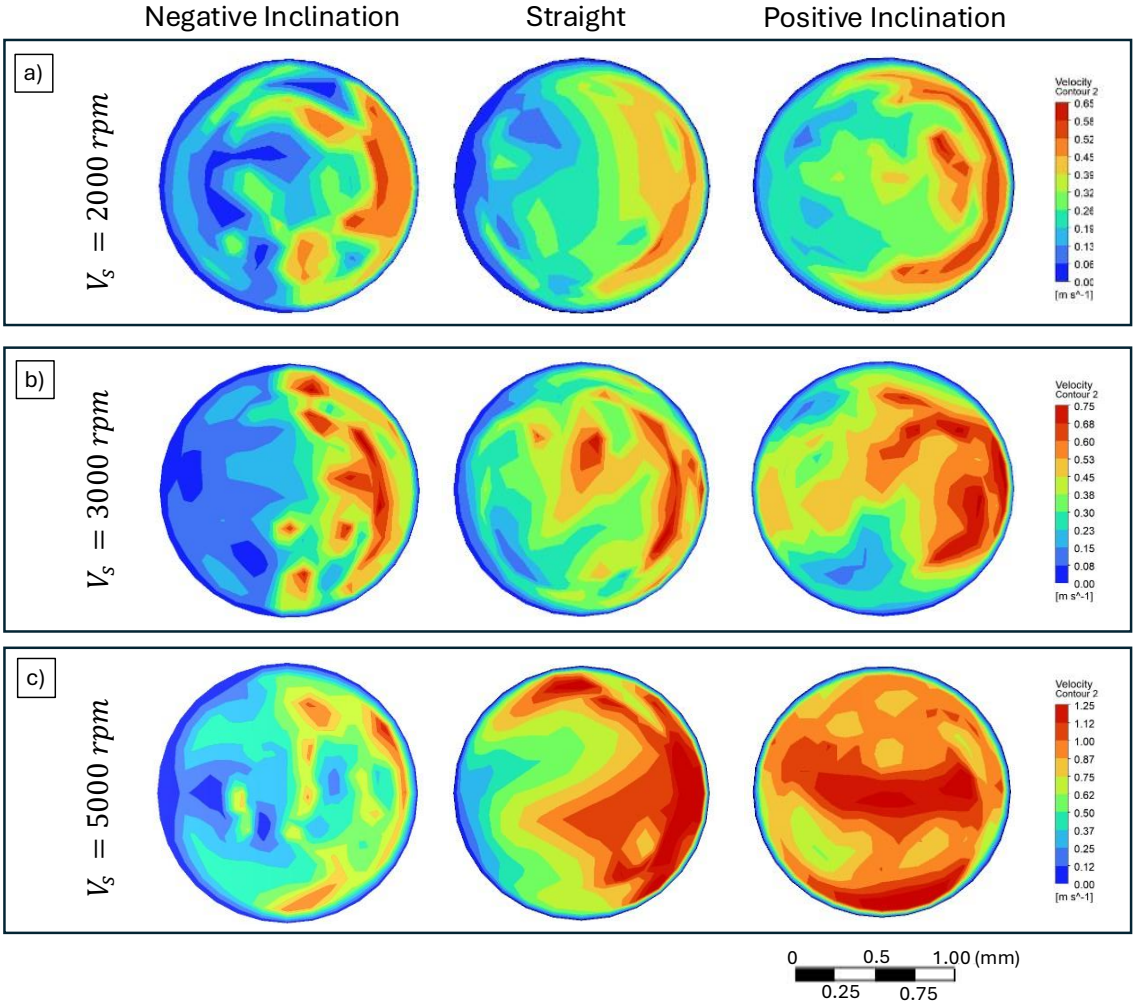


Figure 6.20 – Velocity contour maps at the channel outlets for grinding wheels with internal channels of negative inclination (left), straight (center) and positive inclination (right), at (a) 2000 rpm, (b) 3000 rpm and (c) 5000 rpm.

A detailed view of the transition between the wheel hub and the internal channels reveals the mechanisms behind the superior performance of the positive inclination geometry (Figure 6.21). The more favorable alignment between the channel axis and the direction of the centrifugal force promotes a smoother and more direct entry of the coolant into the channels. In contrast, in the straight and negative configurations the fluid trajectory appears less aligned with the channel axis, resulting in a more abrupt transition and increased sensitivity to flow deflection near the hub. This qualitative difference explains why the positive inclination geometry achieves superior outlet velocities, as the optimized vector orientation and smoother hydrodynamic transition act synergistically to enhance fluid transport efficiency.

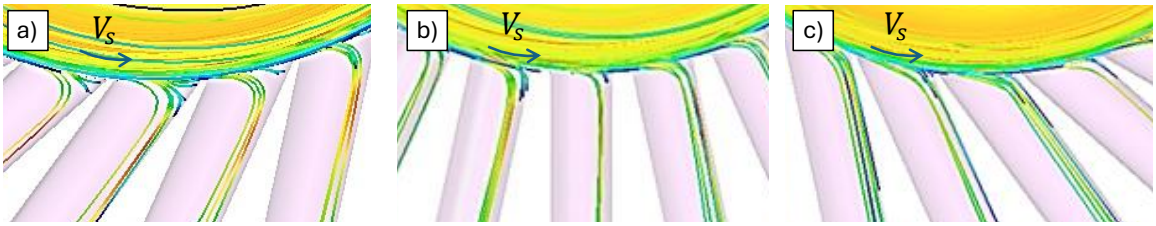


Figure 6.21 – Zoomed view of the streamline distribution at the transition between the wheel center and the channels, for three internal cooling channel geometries: (a) negative inclination, (b) straight and (c) positive inclination (5000 rpm).

6.4.3 Flow Visualization Using High-Speed Camera

High-speed imaging was used to capture the flow patterns for the three internal channel geometries tested at rotational speeds of 2000, 3000 and 5000 rpm and coolant flow of 800 mL/min (Figure 6.22). The captured images reveal critical information about the coherence and orientation of the fluid jets and how these characteristics evolve with increasing rotational speed. Notably, more coherent jets (i.e., without breakage or significant deviation) occur predominantly in the positive and straight geometries at higher speeds, a behavior consistent with the higher outlet velocities observed in CFD simulations. This is essential for efficient fluid application, as high-velocity coolant jets are required to overcome the air barrier generated by wheel rotation, increase local hydrodynamic pressure and promote effective penetration of the fluid into the contact zone [16].

In the negative inclination configuration, even at 5000 rpm, the jets remain thin, fragmented and prone to lateral dispersion. Several channels exhibit reduced flow, indicating both lower ejection velocity and greater tangential deviation. This pattern suggests that the unfavorable channel orientation, opposite to the centrifugal force vector, limits fluid acceleration along the channel and hinders efficient projection.

For the straight configuration, jet continuity visibly improves from 3000 rpm onwards, with well-defined streams over much of the outlet area at 5000 rpm. While performance is superior to the negative inclination, isolated regions with weaker or interrupted jets remain, which may compromise the uniformity of the fluid film on the workpiece and increase friction and tangential forces in zones temporarily lacking lubricant coverage [184].

The positive inclination configuration demonstrates the most cohesive and stable pattern among the three geometries. At 3000 rpm, thick, continuous and well-oriented jets are already visible; by 5000 rpm, the flow appears visually homogeneous in almost all channels, as highlighted by the magnified insets. This behavior fully agrees with CFD predictions, which showed both the highest mean outlet velocity and the largest uniform

high-velocity region for the positive geometry. The alignment of the channel axis with the centrifugal force vector enhances fluid acceleration and promotes a more radial, uniform ejection.

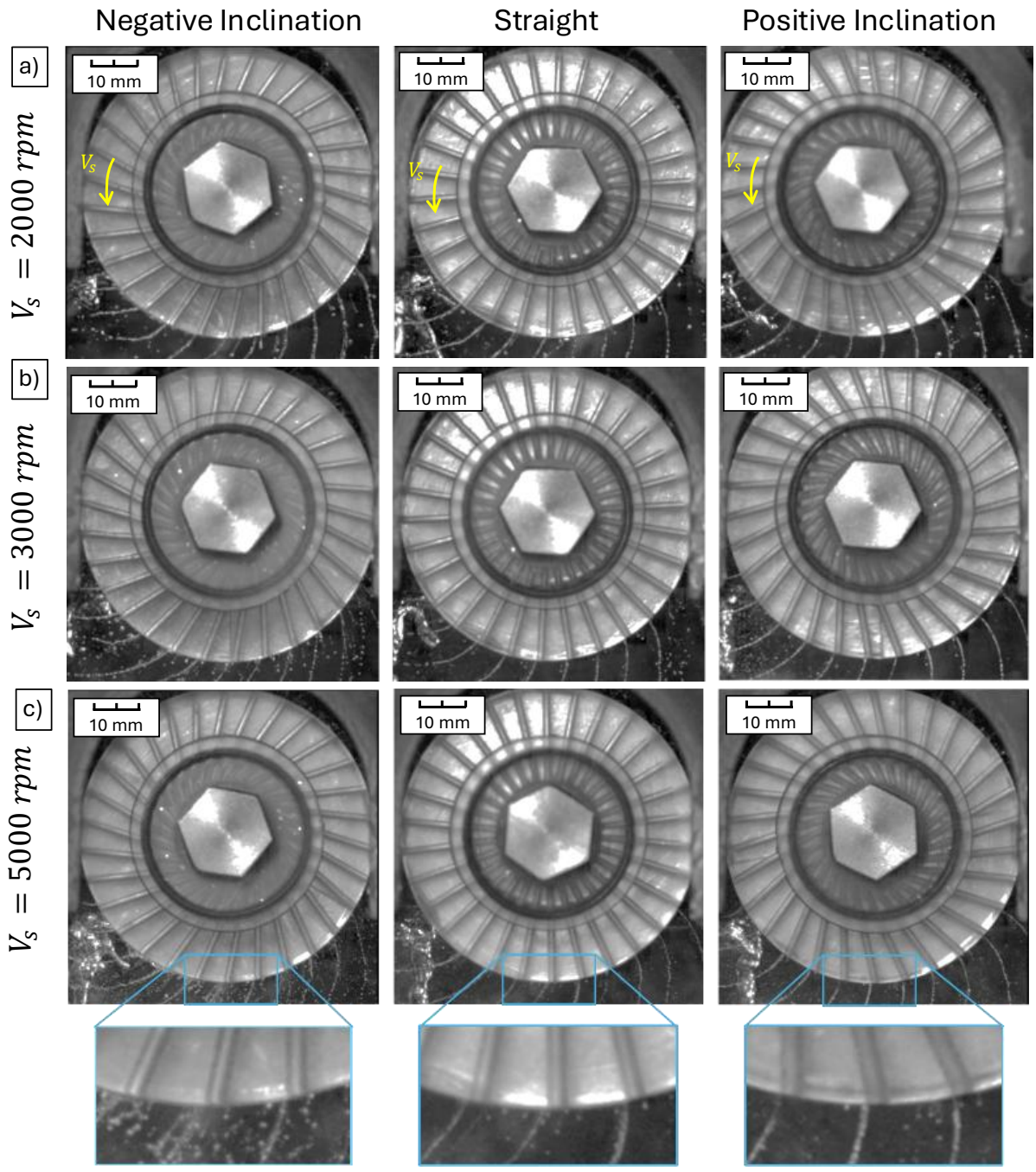


Figure 6.22 – High-speed images of fluid jets emerging from GW with three internal-channel geometries: negative (left column), straight (center) and positive inclination (right), at (a) 2000 rpm, (b) 3000 rpm and (c) 5000 rpm. Insets in (c) magnify the contact zone to highlight jet continuity at high rotation.

To quantify jet orientation, Figure 6.23 presents the average inclination angles measured for the jet emerging from the channel most aligned with gravity (i.e., the one directly facing the workpiece under actual grinding conditions) at 5000 rpm. Values were obtained from 25 distinct and non-consecutive frames and represent the mean inclination of the coolant jet relative to the perpendicular to the workpiece surface.

The positive inclination geometry produced the lowest average angle (≈ 6.7°), indicating an almost perpendicular ejection toward the workpiece surface. This condition is advantageous for grinding, as it directs the jet with greater intensity into the contact zone, facilitating deeper and more effective penetration. The straight geometry showed an intermediate angle (≈ 30.0°), reflecting functional but less efficient hydraulic performance, while the negative inclination produced significantly larger deviations (≈ 41.2°), resulting in more tangential jets, reduced coolant delivery to the active zone and increased lateral dispersion. Additionally, the negative inclination configuration exhibited the largest variability among frames (±5°), consistent with the fragmented and unstable jets observed in the high-speed recordings, whereas the straight and positive geometries showed lower deviations and more stable jet trajectories.

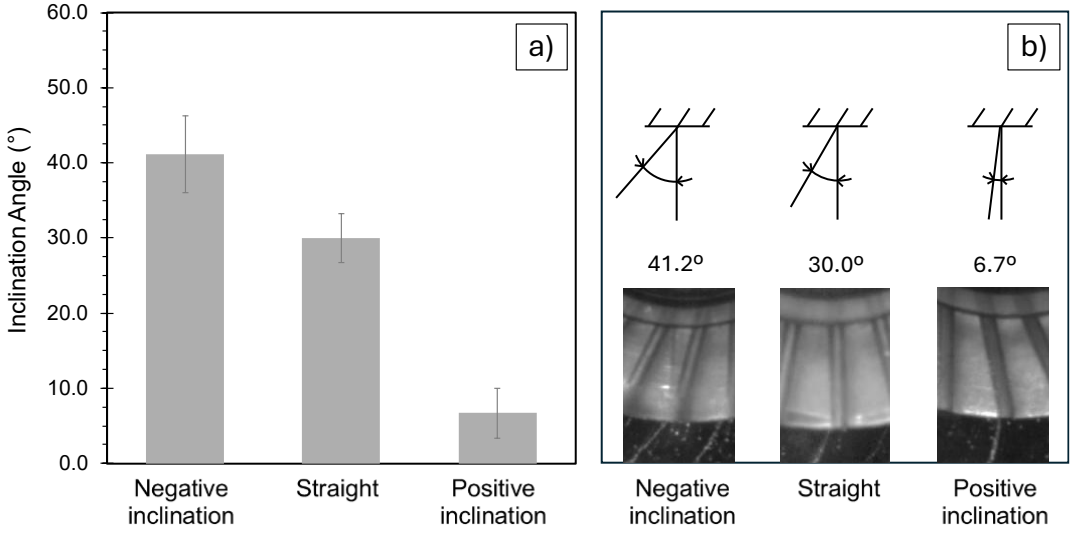


Figure 6.23 – (a) Average jet inclination angles at 5000 rpm for negative, straight and positive channels. (b) Schematics and high-speed images showing mean jet angles of 41.2°, 30.0° and 6.7°, respectively.

Overall, the high-speed camera recordings qualitatively confirm the CFD predictions, particularly regarding jet outlet velocity. While the simulations provided average values and velocity vector fields for different geometries and speeds, the images reveal the practical manifestations of these velocities: thicker, continuous and coherent jets appear only under the conditions where simulations predict higher flow intensity. This direct

correlation between numerically predicted velocity and the observed visual behavior reinforces the model's validity as a predictive tool for internal channel design. Minor discrepancies, such as intermittent jet fragmentation or slight lateral dispersion captured in the videos, correspond to transient free-surface effects and small-scale instabilities that are not represented in the steady-state single-phase model. Nevertheless, these differences do not alter the dominant trend. The good agreement between simulation and experiment in key parameters including jet intensity, direction and spatial coverage supports the practical use of CFD in developing more efficient internal lubrication solutions for grinding processes.

6.4.4 Grinding Performance

The grinding tests enabled a direct assessment of how channel inclination affects the thermal and mechanical behavior of the process. As outlined in Section 0, the tests were performed under a feed rate of 100 mm/min, a wheel speed of 5000 rpm, an inlet flow rate of 400 mL/min and depths of cut between 20 and 100 µm. Three geometries were evaluated: positive ($\theta = +12°$), straight ($\theta = 0°$) and negative ($\theta = -12°$). The analysis considered tangential and normal forces and maximum temperature variation (ΔT).

Cutting Forces

Figure 6.24a–b presents the tangential (F_t) and normal (F_n) forces as a function of depth of cut. The forces increased nearly linearly with depth, but clear differences were observed among the geometries. The positive inclination consistently achieved the lowest F_t values. At 10–20 µm, the reduction compared with negative inclination exceeded 50 %, evidencing a strong benefit in finishing conditions. At higher depths (80–100 µm), the relative difference decreased to approx. 39–37 %, although the positive geometry remained the best-performing configuration. When compared with the straight channels, regarded as the natural baseline design, the positive inclination also delivered clear advantages. For instance, at 50 µm, F_t was 4.26 N for straight channels and 2.67 N for the positive inclination, corresponding to a 34 % reduction, which confirms that aligning the channels with the rotation direction provides a measurable improvement in mechanical performance.

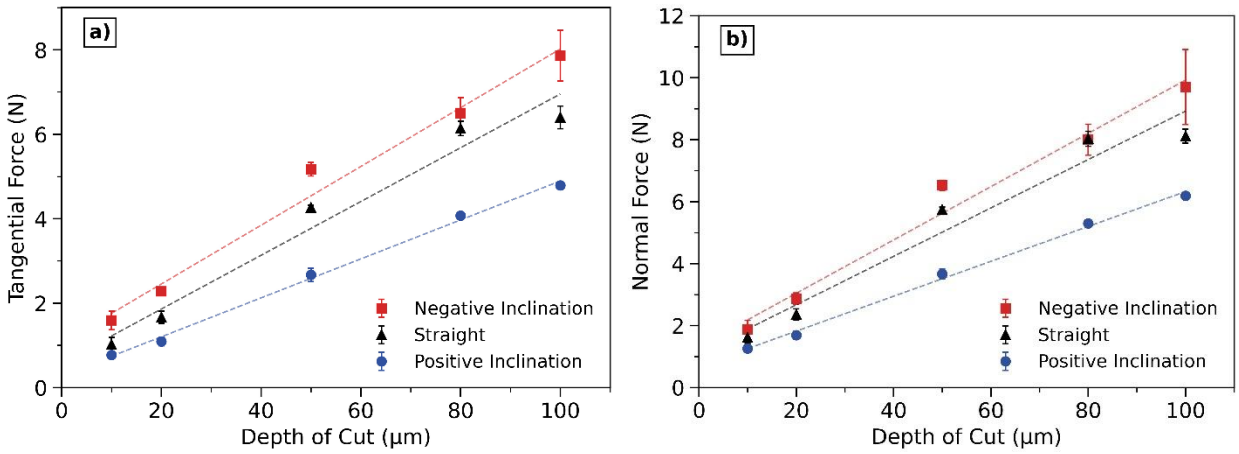


Figure 6.24 – Effect of channel inclination on grinding forces: (a) tangential force (F_t) and (b) normal force (F_n) as a function of depth of cut.

Temperature Variation (ΔT)

As shown in Figure 6.25, the maximum temperature variation increased with depth of cut for all channel inclinations, but the positive geometry consistently achieved the lowest values.

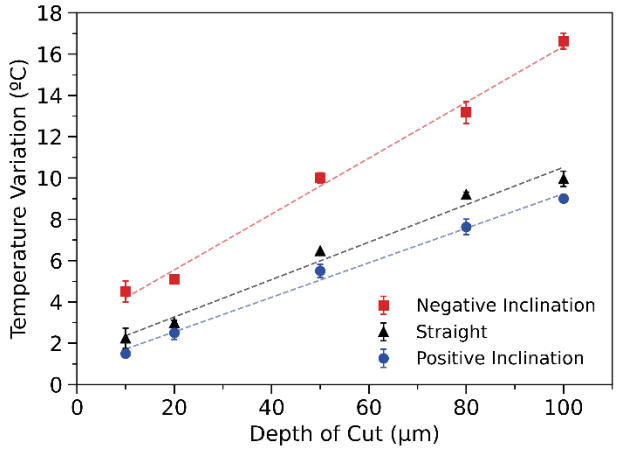


Figure 6.25 – Maximum temperature variation (ΔT) as a function of depth of cut for grinding wheels with positive, straight and negative channel inclination.

At 10 μm, the positive inclination reduced (ΔT) by 33 % compared with the straight configuration and by 67 % compared with the negative. At intermediate depths (50 μm), the reduction relative to straight channels was 15 % and 45 % relative to the negative inclination. At 100 μm, the advantage was maintained, with ΔT remaining around 10 % lower than the straight geometry and 46 % lower than the negative. The positive

inclination configuration presented the most efficient and stable thermal behavior, recording a maximum temperature variation of only 9 °C at a depth of cut of 100 μm.

6.4.5 Concluding Remarks on Channel Inclination

The combined CFD, flow visualization and grinding experiments demonstrated that channel inclination exerts a decisive influence on coolant delivery and grinding performance:

- Positive inclination ($\theta = +12°$) produced stable, radially oriented jets that penetrated effectively into the contact zone. This configuration consistently yielded the lowest tangential and normal forces and the greatest reduction in ΔT.
- Straight channels ($\theta = 0°$) provided intermediate behavior, with reasonably coherent jets and moderate improvements in grinding performance.
- Negative inclination ($\theta = -12°$) generated fragmented, tangential jets, which limited fluid entry into the cutting arc, resulting in higher mechanical loads and elevated ΔT.

An additional observation is that the effects of channel inclination were amplified at higher wheel speeds. At 5000 rpm, differences among the three configurations became markedly pronounced, whereas at lower speeds their behavior was more comparable. This helps explain why the Taguchi–Grey analysis did not identify inclination as a statistically significant factor: in that preliminary screening, simulations were conducted at 2000 rpm and based solely on external dispersion (Setup A), a condition that weakens the influence of jet orientation and reduces sensitivity to velocity-related differences. Under such simplified conditions, the contribution of inclination to the ANOVA became attenuated.

When evaluated under realistic operating conditions, combining higher rotational speeds, outlet-velocity analysis (Setup B) and experimental visualization, inclination proved to be a critical geometric parameter, strongly governing jet coherence, penetration and, consequently, the tribological and thermal stability of the grinding process.

Therefore, while inclination may appear secondary in simplified statistical analyses, it plays a substantial and practically significant role under operating regimes representative of industrial grinding, particularly at high rotational speeds where centrifugal effects enhance the hydrodynamic relevance of channel orientation.

6.5 General Discussion and Design Guidelines

The experimental and numerical results obtained in this chapter confirm that the three geometric parameters investigated, namely the number of layers, the channel diameter and the inclination, play distinct and complementary roles in governing fluid transport and grinding performance.

- Number of layers mainly controls the global distribution of coolant along the contact line. Increasing the number of layers enhances the uniformity of delivery, reducing both mechanical loads and thermal gradients. The three-layer configuration consistently outperformed the one- and two-layer wheels.
- Channel diameter and number of channels, under constant outlet area, define the hydraulic efficiency of the system. Very small channels (0.6 mm) promote wide coverage but suffer from excessive pressure losses, while large channels (1.5 mm) provide intense jets but poor global coverage. The intermediate solution (1.0 mm, 69 channels) achieved the most balanced performance.
- Inclination regulates the coherence and penetration of the coolant jet. Negative inclination (–12°) generated fragmented jets with poor penetration, whereas straight channels (0°) resulted in moderate performance. Positive inclination (+12°) consistently promoted stronger and more radial jets, improving both thermal and tribological stability.

In addition, the magnitudes and trends of grinding forces and temperatures reported in this chapter are consistent with previously published works [171,174,175,244], reinforcing the physical consistency of the present results and the validity of the adopted methodology.

Design Guidelines

Based on the integrated analysis, the following guidelines can be proposed for the design of internally cooled grinding wheels:

- A three-layer configuration ensures stable and uniform fluid distribution across the contact zone.
- Channels with 1.0 mm diameter (69 units, for an outlet area of approx. 54 mm^2) provide the best compromise between coverage and jet velocity, leading to lower cutting forces, reduced energy consumption and improved thermal control.

- A positive inclination of +12° in the direction of wheel rotation promotes coherent and radial jets that penetrate efficiently into the grinding zone, reducing ΔT and increasing process stability.

The combined numerical and experimental results indicate that the configuration with three layers, 69 channels of Ø1.0 mm and a +12° inclination presents the most favorable balance among the options evaluated in this work. While this specific combination was not tested as a complete integrated geometry, the individual effects of each parameter point consistently in the same direction: improved distribution of coolant along the contact width, enhanced hydraulic efficiency and better jet coherence and penetration.

Therefore, the simultaneous adoption of these three design choices is expected to provide enhanced overall performance, particularly in industrial grinding conditions that demand both effective cooling and stable tribological behavior. This recommendation is grounded in the mechanisms demonstrated throughout the chapter and offers a practical guideline for future wheel development.

7. GRINDING BEHAVIOR OF STRUCTURED GRINDING WHEELS

In the previous chapter, the manufacturing methodology for grinding wheels with internal channels was developed and optimized, ensuring dimensional fidelity, microstructural integrity and improved wear resistance. Having established the feasibility of this approach, the next step is to validate the functional performance of these wheels under laboratory simulated grinding conditions.

This chapter presents a comparative study between a conventional vitrified grinding wheel operating with external flood lubrication and a structured wheel designed for internal coolant delivery through embedded channels. The analysis focuses on key performance indicators, including grinding forces, specific energy and temperature variation (ΔT), to assess the effectiveness of the internal lubrication strategy.

The content of this chapter is based on the paper *"Performance of 3D-Structured Grinding Wheels with Multi-Layer Internal Cooling Channels"*, published in *Results in Engineering* [245]. The main objective is to demonstrate whether the integration of internal channels leads to measurable improvements in coolant utilization and to tangible gains in thermal and tribological behavior during grinding.

7.1 Wheel Configurations

For this study, two types of grinding wheels were produced: a conventional reference wheel without internal channels (Reference), designed for external flood cooling and a structured wheel with internal radial channels for coolant delivery (Structured). The structured wheel incorporated 30 channels of 1.7 mm diameter, distributed into three layers of 10 channels each and spaced 2 mm apart along the wheel width. The channels were manufactured with a forward inclination of $\theta = +12°$ relative to the radial direction, oriented in the sense of wheel rotation. This geometry was selected because it exhibited the best performance among the configurations evaluated in the previous chapter, particularly regarding jet coherence and coolant projection and was therefore adopted as the configuration of choice for the comparative grinding tests.

All wheels shared the same external dimensions, namely 62 mm outer diameter, 15 mm width and 21 mm bore. The development of the structured wheel, from the CAD design to the sacrificial PLA insert and the final vitrified component, is illustrated in Figure 7.1, while the corresponding dimensional characteristics are summarized in Figure 7.2.



Figure 7.1 – Development of the structured grinding wheel with internal cooling channels: (a) CAD model, (b) sacrificial PLA insert produced by additive manufacturing and (c) vitrified wheel after sintering.

a)

Parameter	Value
Number of Channels per layer	10.0
Number of layers	3.0
Channel Diameter (mm)	1.7
Total Outlet Area (mm²)	68.1
d1 (mm)	7.5
d2 (mm)	5.5
d3 (mm)	4.0
d4 (mm)	9.7
d5 (mm)	19.5

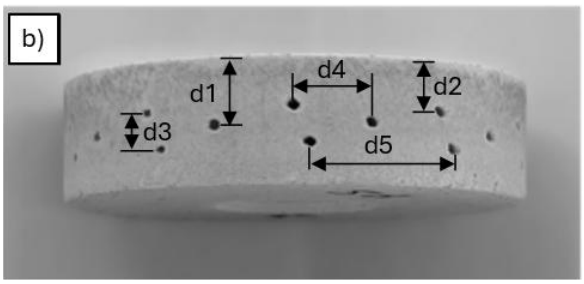


Figure 7.2 – Dimensional characteristics of the structured grinding wheel with internal cooling channels: (a) geometric parameters of the channel network and (b) dimensional references in the grinding wheel.

7.2 Grinding Stages and Thermal Segmentation

The concept of the three cutting stages in grinding was originally proposed by Malkin and Guo [61] and adapted here to structured wheels with internal cooling to describe the evolution of abrasive interaction between the grinding wheel and the workpiece over time. This approach, widely recognized in the literature, is used in the present work as the basis for thermal and force analysis.

Figure 7.3a presents a schematic representation of the three grinding stages, namely cut in, steady state and cut out, under conventional flood lubrication. In this case, fluid penetration into the contact zone can be hindered by the air barrier formed by the rotating wheel, leading to a delayed cooling effect and higher temperature gradients. Figure 7.3b illustrates the corresponding stages for structured wheels equipped with internal cooling channels. In this configuration, coolant is supplied directly to the contact zone through the internal channels, which conceptually provides more immediate fluid availability at cut in, continuous delivery

during steady-state and improved cooling conditions at cut out. The schematic highlights the expected differences in thermal distribution and contact dynamics between internal cooling and traditional external flooding.

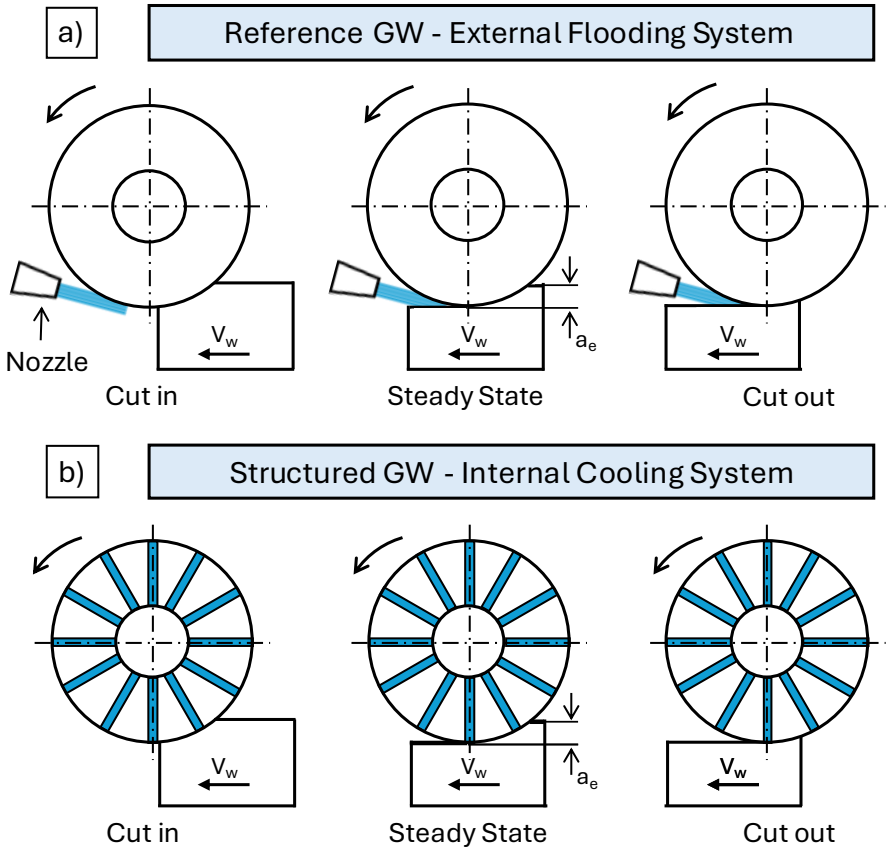


Figure 7.3 – Schematic representation of the three grinding stages (cut in, steady state and cut out) for a conventional flood lubrication system – Reference; (a) and a structured grinding wheel with internal cooling – Structured (b). Adapted from Malkin and Guo [61].

The experimental force signal corroborates this segmentation. Figure 7.4 depicts the tangential force (F_t) along the grinding path (example shown for $a_e = 120\ \mu m$), where the three stages are clearly distinguishable:

- Cut in (0–4 mm): the wheel enters the workpiece and F_t increases until the effective depth of cut is reached.
- Steady state (4–12.5 mm): material removal proceeds under stabilized force conditions.
- Cut out (12.5–15 mm): the contact area decreases and F_t drops as the wheel leaves the workpiece.

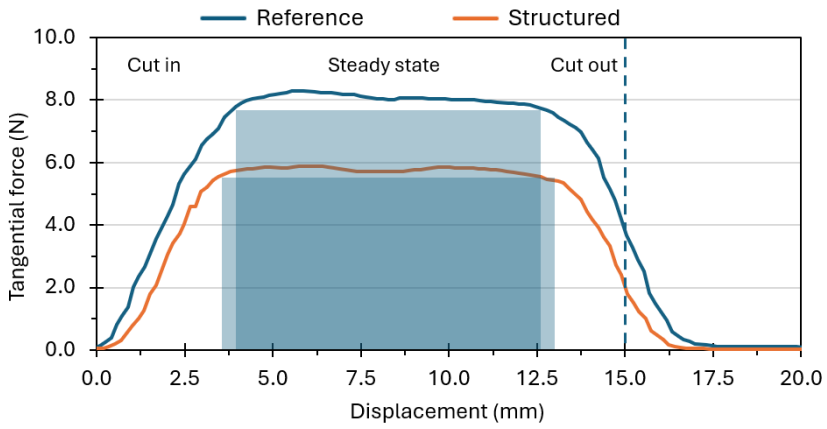


Figure 7.4 – Tangential force profile during the grinding operation for Reference and Structured wheels, with the three stages identified from the force signal.

Considering the same depth of cut (here $a_e = 120\ \mu m$ and comparing with the Reference, the Structured wheel reaches steady state earlier and at a lower force level (Figure 7.4), which is consistent with more immediate lubricant access to the grain–workpiece interface and with a reduced frictional contribution during the engagement phase. Furthermore, the average force value measured during the steady-state is visibly lower for the system with internal channels, highlighting the tribological benefits of direct fluid delivery to the cutting arc.

Beyond the force signals, the thermal response of the workpiece was analyzed to evaluate the effectiveness of fluid delivery during each grinding stage. Figure 7.5 presents the temperature profiles recorded by embedded thermocouples and the corresponding heating rates for two representative depths of cut: $a_e = 10\ \mu m$ (Figure 7.5a and b) and $a_e = 120\ \mu m$ (Figure 7.5c and d). The thermocouple was positioned 7.5 mm from the start of the grinding path and 1 mm below the workpiece surface, enabling the detection of subsurface heat propagation under both lubrication strategies.

From these data, three distinct thermal zones (Z1–Z3) were identified according to the variations in heating rate, allowing direct correlation with the classical cutting stages:

- Zone Z1 (0–5 mm): This initial region corresponds to the cut in stage of the grinding process. As the wheel approaches the thermocouple position (7.5 mm from the start of the grinding path), the observed temperature rise is mainly governed by lateral conduction within the workpiece rather than by local chip formation. At this stage, heat generation is still limited and far from the thermocouple

location. Consequently, no significant differences were detected between the Reference and the Structured wheels.

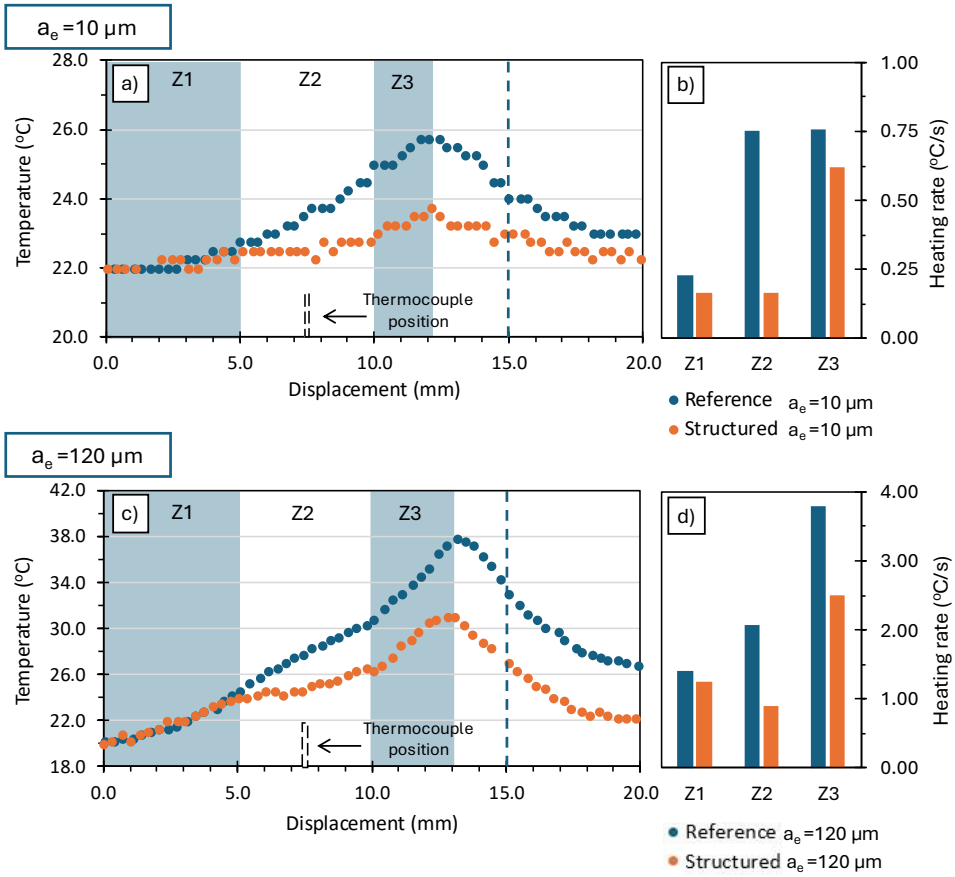


Figure 7.5 – Temperature profiles measured by thermocouple for cutting depths of 10 µm (a) and 120 µm (c) and corresponding heating rates (b, d), for both lubrication systems. The thermocouple was positioned 7.5 mm from the start of the grinding path, as shown in (a) and (c) and 1 mm below the surface.

- Zone Z2 (5 – 10 mm): Represents the thermal steady-state regime, in which the grinding wheel fully covers the thermocouple region. It is in this region that the most significant effect of internal cooling is observed: for $a_e = 10\ \mu m$, the heating rate was 78 % lower compared to the conventional system; for $a_e = 120\ \mu m$, the reduction was 52 %. This difference reflects the direct action of the cooling channels, which deliver the fluid directly to the cutting arc from the beginning of contact through to the exit.

  In the Reference, the fluid is delivered behind the active zone and its entry to the contact zone is partially hindered by the air layer generated by the wheel rotation, a phenomenon well described by Mihić *et al.* [29], who showed that this aerodynamic barrier reduces the effective fluid flow reaching

the abrasive interface. In the Structured, the channels overcome this limitation, transporting the fluid directly to the cutting zone, increasing the thermal efficiency of the process and reducing the heating rate of the workpiece.

- Zone Z3 (10 – ≈12.5 mm): corresponds to the peak-temperature region, which precedes the cut out phase. Although this interval is close to disengagement, its definition is based on the point of maximum measured temperature, because after this point the workpiece begins to cool down. In both lubrication systems, temperature rises sharply in Z3. However, the Structured still exhibited clear advantages: at $a_e = 10\ \mu m$, the heating rate in Z3 remained 18 % lower than in the Reference, while at $a_e = 120\ \mu m$ the reduction was 34 %.

The occurrence of the peak after the thermocouple position can be explained by two factors:

1. At the end of the grinding path, the reduced material volume beneath the active zone limits the workpiece's ability to conduct heat away, leading to localized accumulation.
2. Chip generation decreases progressively in the cut out stage, which reduces the contribution of chip removal as a heat-dissipation mechanism.

An additional observation is that, under mild conditions ($a_e = 10\ \mu m$), the temperature peak occurred slightly earlier than under severe conditions ($a_e = 120\ \mu m$). This shift is attributed to the lower heat generation at shallow cuts, which reduces cumulative thermal loading and brings the maximum closer to the beginning of the cut out.

Overall, the zone-based segmentation proved decisive for identifying where internal cooling exerts its greatest influence. While Z1 showed no distinction between systems, Z2 revealed the strongest improvements and Z3 confirmed that early stabilization of temperature is critical for reducing the final thermal peak. The Structured wheel demonstrated enhanced capacity to control heating throughout the grinding pass, minimizing thermal accumulation and ensuring a more stable process.

This combined framework, integrating classical cutting stages (Figure 7.3 and Figure 7.4) with thermal zones (Figure 7.5) provides a robust interpretation of how internal cooling modifies both force and temperature evolution in grinding.

7.3 Grinding Performance

The grinding tests were used to assess the mechanical and thermal response of the wheels operating with the internal cooling system (Structured) in comparison with the external cooling system (Reference). The evaluation considered the main performance indicators: tangential force (F_t), normal force (F_n), specific grinding energy (E_c) and temperature variation (ΔT).

7.3.1 Cutting Forces

Figure 7.6 presents the average tangential and normal forces recorded in the steady-state regime across different depths of cut. In all cases, the use of the Structured wheel led to a clear reduction in both force components when compared with the Reference. At $a_e = 10\ \mu m$, tangential force was reduced by 49.3 %, while normal force decreased by 37.6 %. Even at the highest depth of cut ($a_e = 120\ \mu m$), with decreases of 31.3 % in tangential force and 28.4 % in normal force. These results indicate that delivering coolant directly through internal channels effectively reduces rubbing and plowing contributions, thereby lowering the overall mechanical load during grinding [61].

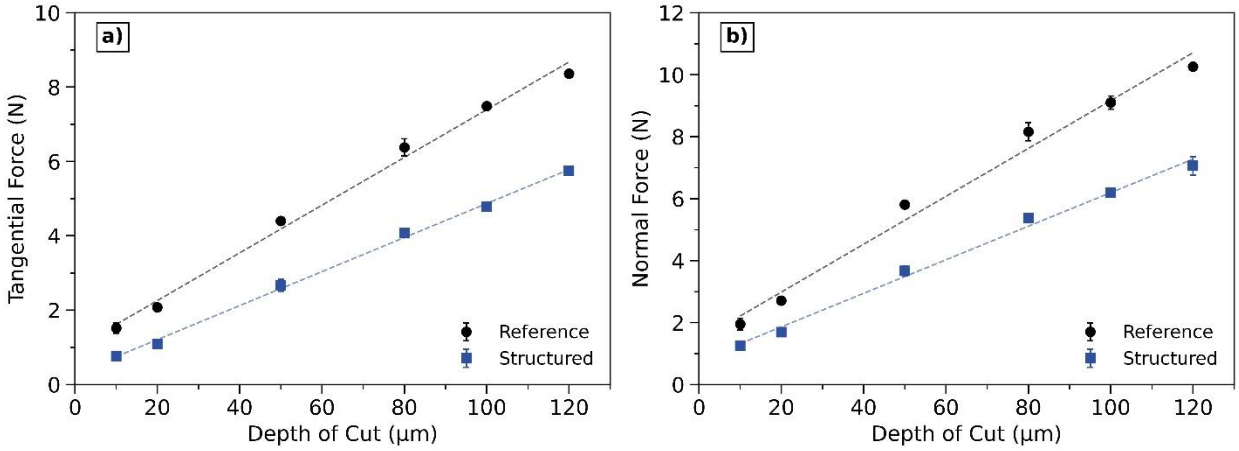


Figure 7.6 – Tangential (a) and normal (b) grinding forces as a function of depth of cut for grinding wheels operating with an External Cooling System and with an Internal Cooling System.

At shallow depths of cut, typically used in finishing operations, the relative advantage of the Structured was more pronounced, reflecting the higher sensitivity of light grinding to fluid availability at the grain–workpiece interface. As the depth of cut increased, the absolute forces rose for both lubrication systems and the relative reductions decreased, indicating that the expanded contact zone and increased thermal load partially limit the contribution of fluid penetration. Nevertheless, the Structured maintained a consistent reduction in both

tangential and normal forces across the full range of conditions, confirming its effectiveness under both mild and severe grinding regimes.

7.3.2 Specific Grinding Energy

Figure 7.7 shows the specific grinding energy (E_c) as a function of depth of cut. In all cases, the Structured wheel required significantly lower energy than the Reference, particularly in $a_e = 10 - 50\ \mu m$ µm range, where reductions of up to 50 % were observed. At very shallow depths ($a_e = 10\ \mu m$), however, E_c reached its highest value despite lower forces levels. This behavior is characteristic of light-cut grinding, in which plowing and elastic–plastic deformation dominates the interaction, increasing the energy required per unit volume of removed material. In addition, because E_c is defined relative to the removed volume, the extremely low material-removal rate at $a_e = 10\ \mu m$ amplifies the calculated energy, even when the tribological conditions are favorable [66].

As the depth of cut increased, grain engagement stabilized and the specific energy decreased accordingly, reflecting more efficient cutting action. At higher depths ($a_e = 80 - 120\ \mu m$), the difference between lubrication systems narrowed, indicating that the incremental benefit of internal cooling diminishes under severe conditions, though the system still retained a measurable advantage. Even in these conditions, however, the Structured wheel retained a consistent energetic advantage, showing that direct coolant delivery contributes positively to the overall efficiency of the grinding process.

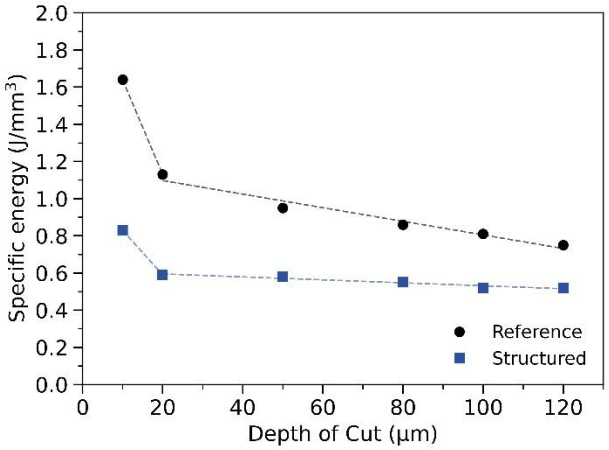


Figure 7.7 – Specific grinding energy as a function of depth of cut for wheels operating with an External Cooling System (Reference) and with an Internal Cooling System (Structured).

7.3.3 Temperature Variation (ΔT)

Figure 7.8 summarizes the maximum temperature variation measured by the thermocouple for both cooling systems. Across all depths of cut, the Reference exhibited the highest ΔT values, while the Structured consistently reduced thermal loading. The most significant improvements were observed at shallow depths, where fluid penetration is most effective: reductions of 58.6 % at $a_e = 10\ \mu m$ and 51.6 % at $a_e = 20\ \mu m$. Even under severe conditions ($a_e = 120\ \mu m$), ΔT was reduced by 35.4 % compared with the Reference.

A noteworthy result is that at $a_e = 120\ \mu m$, the Structured achieved a ΔT of approximately 10 °C, which is comparable to the ΔT measured for the Reference at only $a_e = 50\ \mu m$ (≈11 °C). In practical terms, this shows that the internally cooled wheel can operate at more than double the depth of cut while maintaining a similar thermal load on the workpiece.

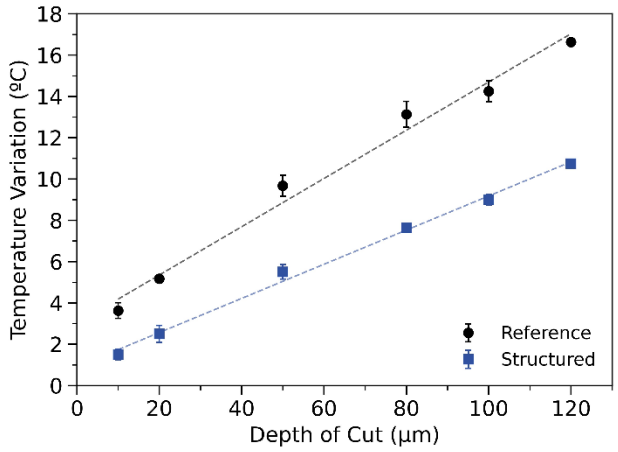


Figure 7.8 – Maximum temperature variation (ΔT) measured by thermocouple as a function of depth of cut for wheels operating with an External Cooling System (Reference) and with an Internal Cooling System (Structured).

7.4 Integrated Analysis

To consolidate the results presented in the previous sections, this part integrates the averaged indicators of grinding performance with the zone-based segmentation, allowing a comprehensive interpretation of the mechanical and thermal response under different cutting regimes. At shallow depths of cut (10–50 µm), representative of finishing operations, the internal cooling system achieved its most significant benefits. Tangential and normal forces were reduced by nearly half and specific grinding energy dropped by up to 50 %. Temperature variation also showed the strongest reductions in this range. The segmented thermal analysis (Figure 7.5 a–b) confirms these trends: in Zone Z2, when the thermocouple was fully covered by the wheel,

the heating rate under internal cooling was up to 78 % lower than with external flooding. This shows that direct fluid delivery promotes earlier stabilization of forces, suppresses plowing and limits heat accumulation, ensuring more stable and efficient conditions for precision grinding.

Under severe conditions (80–120 µm), associated with roughing or high-productivity grinding, the relative differences between systems became smaller, though internal cooling still preserved a measurable advantage. Both mechanical loads and ΔT increased with depth, causing the performance of the two systems to become partially closer. This occurs because, at higher depths of cut, heat generation and mechanical engagement dominate the process, reducing the relative contribution of coolant penetration. Even so, the internal cooling system consistently maintained lower forces and temperatures, demonstrating that its benefit persists under heavy-load conditions. The segmented thermal analysis (Figure 7.5c–d) again supports the integrated findings: in Zone Z3, where the maximum temperature occurs before disengagement, the heating rate with internal cooling remained up to 34 % lower than with external flooding.

Taken together, these results confirm the strong correlation between mechanical and thermal indicators. At shallow cuts, lower forces and lower ΔT are directly reflected in improved energy efficiency, which is critical for finishing operations. At higher cuts, despite the narrowing gap, internal cooling continues to reduce thermal load and mechanical stresses, enabling productivity gains without compromising process stability.

7.5 Summary and Conclusions

This chapter validated the functional performance of internally cooled grinding wheels compared with conventional external flooding. Across all tested conditions, internal cooling reduced forces, specific grinding energy and temperature variation, with the largest relative reductions occurring at shallow depths of cut. In this regime, representative of finishing operations, forces decreased by up to 50 %, specific energy by up to 50 % and temperature variation by up to 59 %. The segment-based analysis confirmed that these improvements are linked to earlier stabilization of forces at cut in and substantially lower heating rates in Zone Z2, ensuring thermal stability and surface protection in precision applications.

In practical terms, this makes internally cooled wheels particularly effective for finishing operations, where thermal control and dimensional accuracy are critical. At higher depths of cut, representative of roughing or high-productivity grinding, the relative differences between cooling systems narrowed, as thermal and mechanical loads increased for both configurations. Even so, internal cooling continued to reduce peak

gradients in Zone Z3, enabling deeper cuts without additional thermal risk. This dual capability allows both improved reliability in finishing and higher productivity in roughing, establishing internally cooled wheels as a versatile solution for industrial grinding.

8. CONCLUSIONS

8.1 Summary of the Main Contributions

In line with the objectives defined in Chapter 1 this thesis addressed the development, manufacturing and performance evaluation of internally cooled structured grinding wheels, combining experimental and numerical approaches to provide a comprehensive understanding of coolant transport and its influence on grinding performance. The main contributions of this research can be organized by following the technical progression of the work across the central chapters of the thesis.

In Chapter 4, an innovative manufacturing method for structured grinding wheels was established and validated. The process relied on polymeric inserts produced by additive manufacturing, which were subsequently eliminated during sintering to generate continuous internal channels. The method proved to be robust and reproducible, allowing the incorporation of three-dimensional geometries that are not feasible with conventional techniques. Dimensional characterization confirmed the accuracy of channel reproduction, while microstructural analysis showed that the removal of the inserts did not compromise the integrity of the vitrified matrix. From a practical point of view, this method enables the production of abrasive tools capable of maintaining active cooling channels throughout their service life, paving the way for industrial application of internally cooled wheels.

In Chapter 5, numerical modeling was employed to analyze flow phenomena that are not accessible through experiments alone. CFD simulation enabled the determination of fluid velocity inside the channels, jet spreading on the workpiece surface, interaction with the air barrier induced by wheel rotation and outlet profiles under different geometries. Validation was carried out through particle tracking and high-speed imaging, demonstrating that the models predicted outlet jet velocities with good accuracy. The average error of 16 % between CFD and experimental results supported the reliability of the methodology, establishing CFD as an effective design tool for predicting hydraulic performance prior to wheel fabrication.

In Chapter 6, the influence of channel geometry was investigated through a combination of CFD simulations, grinding tests and flow visualization with high-speed imaging. The results showed that multiple layers of channels ensure more stable and continuous fluid delivery, with the three-layer configuration consistently achieving the lowest forces and temperatures, while the two-layer arrangement proved the least effective.

Regarding channel diameter, performance was shown to depend on a balance between coverage and velocity: narrow channels offered broad coverage but suffered from frictional losses, wide channels provided high velocity but poor coverage and intermediate channels (1.0 mm) delivered the best overall performance, achieving the lowest forces, the lowest specific energy and a 40 % reduction in temperature compared relative to the 0.6 mm configuration.

Channel inclination was also demonstrated to be a decisive factor under realistic operating conditions. Positive inclination generated stable, radially oriented jets that penetrated effectively into the contact zone, yielding the best tribological and thermal performance. Straight channels showed intermediate behavior, whereas negative inclination led to fragmented jets, poor penetration and higher loads.

In Chapter 7, grinding experiments provided direct evidence of the benefits of internal cooling compared with conventional lubrication. The structured wheels reduced tangential and normal forces, decreased the specific grinding energy and contributed to more stable thermal conditions during cutting. Quantitatively, internal cooling consistently reduced grinding forces by up to 50 %, specific energy by up to 50 % and temperature variation by up to 59 %. The most pronounced improvements were obtained at shallow depths of cut, which is consistent with the higher sensitivity of finishing operations to fluid availability and thermal control.

Taken together, the results obtained in Chapters 4 to 7 demonstrate that the optimal design of structured grinding wheels should favor multiple channel layers, intermediate diameters and positive inclination. These conclusions reflect the consistent trends observed across manufacturing validation, CFD predictions and experimental grinding performance. By combining manufacturing feasibility, validated CFD models and systematic grinding tests, the thesis provides robust design guidelines and a solid experimental and numerical foundation for the development of efficient and sustainable internally cooled grinding wheels.

8.2 Future Work

The results presented in this thesis open several opportunities for further research that can expand and consolidate the concept of internally cooled structured grinding wheels. One relevant direction is the exploration of new channel geometries beyond the cylindrical designs studied here. Bio-inspired architectures and Venturi-shaped channels may promote local acceleration of the coolant, improve jet coherence and penetration into the contact arc and ultimately enhance both thermal control and tribological stability.

Another important aspect concerns the extension of the operating conditions evaluated. The present work focused on a reference steel and a limited set of grinding parameters, but future studies should examine a wider range of workpiece materials, feed rates, depths of cut and coolant types. Such investigations would provide a broader understanding of the robustness of internally cooled wheels and their adaptability to diverse industrial scenarios.

The integration of internal cooling with engineered surface textures on the wheel periphery also emerges as a promising path. Hybrid wheels could simultaneously benefit from improved fluid delivery from within and from enhanced chip evacuation at the surface, potentially amplifying the tribological and thermal advantages demonstrated in this work.

In addition, future studies should also address the quality of the ground surface, since surface roughness, integrity and residual stress are decisive indicators of process performance and industrial applicability. A systematic evaluation of these aspects would provide further insight into the practical benefits of internally cooled grinding wheels. A deeper investigation of wheel wear mechanisms, including grain fracture, bond weakening and wheel loading, would further clarify the long-term behavior of structured wheels and support the development of predictive wear models.

Finally, the development of a selective coolant delivery system could further reduce fluid consumption. By restricting flow to the downward sector of the rotating wheel, ensuring that only the channels directed toward the grinding zone are supplied, the system would concentrate coolant where it is most effective. Such an approach would avoid unnecessary discharge through non-contributing channels and could be realized through sectorized manifolds, rotating distributors or passive valve mechanisms synchronized with wheel rotation. Combining this selective supply with optimized channel architecture and realistic coolant formulations may lead to a new generation of more efficient and sustainable grinding systems.

8.3 Publications

Peer-Reviewed Journal Articles

1. **S. Costa**, P. Capela, M. Sousa, A. Hassui, J. Ribeiro, M. Pereira, D. Soares, CFD and Experimental Investigation of Channel Diameter Effects in Structured Internally Cooled Grinding Wheels, *In review.*

2. **S. Costa**, P. Capela, A. Hassui, J. Ribeiro, M. Pereira, D. Soares, Performance of 3D-structured grinding wheels with multi-layer internal cooling channels, *Results in Engineering* 28 (2025) 107881. https://doi.org/10.1016/j.rineng.2025.107881.

3. **S. Costa**, A. Souza, L. Neves, J. Ribeiro, M. Pereira, D. Soares, Coolant flow in structured grinding wheels: CFD validation via high-speed imaging and particle tracking, *Applied Thermal Engineering* 281 (2025) 128689. https://doi.org/10.1016/j.applthermaleng.2025.128689.

4. **S. Costa**, P. Capela, A. Hassui, J. Ribeiro, M. Pereira, D. Soares, CFD analysis of multi-layer cooling channels in three-dimensionally structured grinding wheels, *Applied Thermal Engineering* 279 (2025) 127633. https://doi.org/10.1016/j.applthermaleng.2025.127633.

5. **S. Costa**, P. Capela, M.S. Souza, J.R. Gomes, L. Carvalho, M. Pereira, D. Soares, A New Grinding Wheel Design with a 3D Internal Cooling Structure System, *Journal of Manufacturing and Materials Processing* 8 (2024) 159. https://doi.org/10.3390/jmmp8040159.

6. P. Capela, **S. Costa**, M.S. Souza, S. Carvalho, M. Pereira, L. Carvalho, J.R. Gomes, D. Soares, Wear behavior of a new composite formulation, with TEOS addition, for abrasive vitrified grinding wheels, *Wear* 512–513 (2023) 204524. https://doi.org/10.1016/J.WEAR.2022.204524.

7. **S. Costa**, M. Pereira, J. Ribeiro, D. Soares, Texturing Methods of Abrasive Grinding Wheels: A Systematic Review, *Materials* 15 (2022) 8044. https://doi.org/10.3390/ma15228044.

8. P. Capela, S.F. Carvalho, **S. Costa**, S. Souza, M. Pereira, L. Carvalho, J.R. Gomes, D. Soares, Wear Behavior of Grinding Wheels with Superficial Cooling Channels, *ASME International Mechanical Engineering Congress and Exposition, American Society of Mechanical Engineers* (2021) 85574. https://doi.org/10.1115/IMECE2021-72319.

Book Chapters

1. **S. Costa**, P. Capela, M. André, A. Monteiro, M. Pereira, J. Ribeiro, D. Soares, Optimization of a Green Composite Containing a 3D Structure Produced via Additive Manufacturing. *2nd International Workshop on Additive Manufacturing and Sustainability*, Instituto Politécnico de Bragança, 2025: pp. 11–14.
2. **S. Costa**, P. Araújo, P. Capela, J. Gomes, J. Ribeiro, M. Pereira, D. Soares, Design of an experimental grinding machine for testing abrasive wheels with a 3D internal cooling channels structure. *Lubricants, Tribology and Condition Monitoring: LUBMAT-IBERTRIB 2024 Conference Program and Proceedings*, Tekniker, San Sebastian, 2024: pp. 271–272.
3. P. Capela, **S. Costa**, M. Souza, S. Carvalho, M. Pereira, J. Gomes, D. Soares, Effect of grooves and their geometry on the wear behavior of structured grinding wheels. *Book of Abstracts of 11th Iberian Conference on Tribology*, Instituto Politécnico de Setúbal, 2022: pp. 101–102.
4. **S. Costa**, F. Marques, M. Pereira, J. Ribeiro, D. Soares, Control of the dimensional variation adjusting the thermal drying cycle of abrasive composites with incorporated PLA. *1st International Congress on Additive Manufacturing (Book of Abstracts) - IWAM 22*, Instituto Politécnico de Bragança, 2022: pp. 35–38.
5. **S. Costa**, P. Capela, M. Pereira, J. Ribeiro, D. Soares, Dimensional Variations in Drying of Composite Components for Abrasive Wheels. *Materials Proceedings* 8 (2022) 137. https://doi.org/10.3390/MATERPROC2022008137.

National and International Conferences

1. P. Capela, **S. Costa**, M. Correia, L. Carvalho, M. Pereira, J. Teixeira, D. Soares, Effect of Porosity in Grinding Wheels with Internal Cooling Channels on Grinding Process Efficiency. *International Mechanical Engineering Congress and Exposition (IMECE2025)*, Memphis, United States of America, November 16 – 20, 2025.

2. **S. Costa**, P. Capela, J. Ribeiro, M. Pereira, D. Soares, Effect of Lubrication Channel Inclination on Grinding Forces in 3D Structured Grinding Wheels. *XIII Iberian Conference on Tribology and XIII Iberian Vacuum Conference (IBERTRIVA 2025)*, Coimbra, Portugal, June 17 – 18, 2025.

3. P. Capela, **S. Costa**, M. Correia, L. Carvalho, M. Pereira, J.C. Teixeira, D. Soares, Effect of Internal Cooling Channel Diameter on the Thermal and Mechanical Performance of Grinding Wheels. *XIII Iberian Conference on Tribology and XIII Iberian Vacuum Conference (IBERTRIVA 2025)*, Coimbra, Portugal, June 17 – 18, 2025.

4. P. Capela, **S. Costa**, J. Gomes, J. Ribeiro, M. Pereira, D. Soares, Experimental and CFD Simulation Analysis of 3D Cooling Channels to Improve the Performance of Grinding Wheels. *25th International Conference on Wear of Materials (WOM 2025)*, Sitges, Spain, April 13 – 17, 2025.

5. **S. Costa**, P. Capela, J. Ribeiro, M. Pereira, D. Soares, Effect of Coolant Flow Rate and Depth of Cut on Grinding Temperature Using Structured Grinding Wheel. *25th International Conference on Wear of Materials (WOM 2025)*, Sitges, Spain, April 13 – 17, 2025.

6. **S. Costa**, P. Capela, M. André, A. Monteiro, M. Pereira, J. Ribeiro, D. Soares, Process Optimization of a Green Composite Containing a 3D Structure Produced via Additive Manufacturing. *2nd International Workshop on Additive Manufacturing and Sustainability (IWAM 24)*, Instituto Politécnico de Bragança, Bragança, Portugal, October 4, 2024.

7. **S. Costa**, P. Araújo, P. Capela, J. Gomes, J. Ribeiro, M. Pereira, D. Soares, Design of an Experimental Grinding Machine for Testing Abrasive Wheels with a 3D Internal Cooling Channels Structure. *Lubricants, Tribology and Condition Monitoring (LubMat-IberTrib 2024),* San Sebastian, Spain, June 18 – 20, 2024.

8. **S. Costa**, M. Pereira, J. Ribeiro, D. Soares, Simulation based Optimization of Fluid Distribution for Enhanced Grinding Performance. *4th International Brazilian Conference on Tribology (TriboBR 2023)*, Vitória, Brazil, November 26 – 30, 2023.

9. P. Capela, **S. Costa**, M. Souza, S. Carvalho, M. Pereira, J. Gomes, D. Soares, Effect of Grooves and their Geometry on the Wear Behavior of Structured Grinding Wheels. *11th Iberian Conference on Tribology (IberTrib 2022)*, Setúbal, Portugal, October 6 – 7, 2022.

10. **S. Costa**, P. Capela, M.S. Souza, S. Carvalho, M. Pereira, L. Carvalho, J. Gomes, D. Soares, Effect of Distance between Grooves on the Wear of Structured Grinding Wheels. *7th World Tribology Congress (WTC 2021)*, Lyon, France, September 5 – 10, 2022.

11. **S. Costa**, F. Marques, M. Pereira, J. Ribeiro, D. Soares, Control of the Dimensional Variation Adjusting the Thermal Drying Cycle of Abrasive Composites with Incorporated PLA. *1st International Congress on Additive Manufacturing (IWAM 22)*, Bragança, Portugal, September 30, 2022.

12. **S. Costa**, P. Capela, M. Pereira, J. Ribeiro, D. Soares, Dimensional Variations in Drying of Composite Components for Abrasive Wheels. *Materials 2022*, Marinha Grande, Portugal, April 10 – 13, 2022.

13. P. Capela, S.F. Carvalho, **S. Costa**, S. Souza, M. Pereira, L. Carvalho, J.R. Gomes, D. Soares, Wear Behavior of Grinding Wheels With Superficial Cooling Channels. *International Mechanical Engineering Congress and Exposition (IMECE2021)*, Virtual Conference, November 1 – 5, 2021.

REFERENCES

[1] W. Le Zhu, A. Beaucamp, Compliant grinding and polishing: A review, Int J Mach Tools Manuf 158 (2020) 103634. https://doi.org/10.1016/j.ijmachtools.2020.103634.

[2] W. Lyu, T. Wang, R. Hou, J. Liu, Going green and profitable: The impact of smart manufacturing on Chinese enterprises, Comput Ind Eng 181 (2023) 109324. https://doi.org/10.1016/j.cie.2023.109324.

[3] H. Huang, X. Li, D. Mu, B.R. Lawn, Science and art of ductile grinding of brittle solids, Int J Mach Tools Manuf 161 (2021) 103675. https://doi.org/10.1016/j.ijmachtools.2020.103675.

[4] Y. Li, G. Li, Z. Wang, W. Zhu, A form-grinding wheel optimization method for helical gears based on a PSO-SVM model, Precis Eng 88 (2024) 664–673. https://doi.org/10.1016/j.precisioneng.2024.04.007.

[5] M. Li, Q. Li, X. Pan, Z. Zhang, M. Li, S. Xu, Z. Wang, Y. Zhou, L. Ma, T. Yu, J. Zhao, Progress and prospects in cutting of particle reinforced metal matrix composites, Compos Struct 372 (2025) 119598. https://doi.org/10.1016/j.compstruct.2025.119598.

[6] M. Kumar, A. Kumar, H.N.S. Yadav, A. Alok, M. Das, Abrasive based finishing method applied on biomedical implants: A review, Mater Today Proc 47 (2021) 3985–3992. https://doi.org/10.1016/j.matpr.2021.04.137.

[7] N. Qian, W. Ding, J. Xu, Challenges and solutions for high-efficiency-sustainable grinding of aero-engine hot-end components, Chin J Aeronaut 38 (2025) 103536. https://doi.org/10.1016/j.cja.2025.103536.

[8] J. Jia, Q. Zhang, W. Yang, H. Yao, G. Wu, H. Zhao, J. Zhu, K. Li, B. Guo, J. Qin, Analysis and optimization of microchannel array precision grinding processes with micro-structured micro-grinding tool, Chin J Aeronaut 38 (2025) 103261. https://doi.org/10.1016/j.cja.2024.09.037.

[9] N. Ding, S. Jiang, J. Duan, S.K. Singh, S.R. Dutta, D.K. Madhukar, V. Tonkonogyi, A. Yakimov, L. Bovnegra, M. Yang, M. Kong, C. Li, Y. Long, Y. Zhang, S. Sharma, R. Li, T. Gao, M. Liu, X. Cui, X. Wang, X. Ma, Y. Yang, Temperature field model in surface grinding: a comparative assessment, Int J Extrem Manuf 5 (2023) 042011. https://doi.org/10.1088/2631-7990/acf4d4.

[10] Z. Li, W. Ding, L. Shen, X. Xi, Y. Fu, Comparative investigation on high-speed grinding of TiCp/Ti–6Al–4V particulate reinforced titanium matrix composites with single-layer electroplated and brazed CBN wheels, Chin J Aeronaut 29 (2016) 1414–1424. https://doi.org/10.1016/j.cja.2016.01.005.

[11] C. Mao, Z. Zhou, J. Zhang, X. Huang, D. Gu, An experimental investigation of affected layers formed in grinding of AISI 52100 steel, Int J Adv Manuf Technol 54 (2011) 515–523. https://doi.org/10.1007/s00170-010-2965-z.

[12] P. Zhao, B. Lin, J. Zhou, B. Lv, J. Li, J. Zhang, L. Wang, T. Sui, Review of grinding temperature theory and measurement for the needs of the times: Promoting the development of advanced manufacturing, J Mater Process Technol 337 (2025) 118744. https://doi.org/10.1016/j.jmatprotec.2025.118744.

[13] K. Jayakumar, Effect of grinding parameters and coolants on grindability of Ti grade 9 alloy, Mater Today Proc (2024). https://doi.org/10.1016/j.matpr.2024.04.030.

[14] M. Hadad, B. Sadeghi, Minimum quantity lubrication-MQL turning of AISI 4140 steel alloy, J Clean Prod 54 (2013) 332–343. https://doi.org/10.1016/j.jclepro.2013.05.011.

[15] A. Basem, M. Naji, H.A. Al-Asadi, M. Sediq Safi, G. Daminova, M. Alhadrawi, M.J. Alfaker, S. Islam, Small-quantity cooling lubrication in creep-feed grinding: Surface quality and residual stress analysis, Results Eng 22 (2024) 102348. https://doi.org/10.1016/j.rineng.2024.102348.

[16] E. Brinksmeier, C. Heinzel, M. Wittmann, Friction, cooling and lubrication in grinding, CIRP Annals 48 (1999) 581–598. https://doi.org/10.1016/s0007-8506(07)63236-3.

[17] H. Tschätsch, A. Reichelt, Cutting fluids (coolants and lubricants), in: Applied Machining Technology, Springer, Berlin, Heidelberg, 2009: pp. 349–352. https://doi.org/10.1007/978-3-642-01007-1_21.

[18] B.S. Linke, Sustainability concerns in the life cycle of bonded grinding tools, CIRP J Manuf Sci Technol 7 (2014) 258–263. https://doi.org/10.1016/j.cirpj.2014.05.002.

[19] Y. Zhang, L. Li, X. Cui, Q. An, P. Xu, W. Wang, D. Jia, M. Liu, Y.S. Dambatta, C. LI, Lubricant activity enhanced technologies for sustainable machining: Mechanisms and processability, Chin J Aeronaut 38 (2025) 103203. https://doi.org/10.1016/j.cja.2024.08.034.

[20] X. Luo, S. Wu, D. Wang, Y. Yun, Q. An, C. Li, Sustainable development of cutting fluids: The comprehensive review of vegetable oil, J Clean Prod 473 (2024) 143544. https://doi.org/10.1016/j.jclepro.2024.143544.

[21] A. Elsheikh, A.B.M. Ali, A. Saba, H. Faqeha, A.A. Alsaati, A.M. Maghfuri, W. Abd-Elaziem, A.A. El Ashmawy, N. Ma, A review on sustainable machining: Technological advancements, health and safety considerations, and related environmental impacts, Results Eng 24 (2024) 103042. https://doi.org/10.1016/j.rineng.2024.103042.

[22] J. Ma, E. Cui, B. Zha, G. Zheng, K. Li, X. Cheng, L. Gu, Experimental assessment of cryogenic LN2 enhanced GNPs-Cu/ZrO2 multiphase composite nano-fluids MQL in the turning of GH4169, Mater Today Commun 48 (2025) 113321. https://doi.org/10.1016/j.mtcomm.2025.113321.

[23] M. Danish, M.K. Gupta, S. Rubaiee, A. Ahmed, M.E. Korkmaz, Influence of hybrid Cryo-MQL lubri-cooling strategy on the machining and tribological characteristics of Inconel 718, Tribol Int 163 (2021) 107178. https://doi.org/10.1016/j.triboint.2021.107178.

[24] E. Benedicto, D. Carou, E.M. Rubio, Technical, economic and environmental review of the lubrication/cooling systems used in machining processes, Procedia Eng 184 (2017) 99–116. https://doi.org/10.1016/j.proeng.2017.04.075.

[25] A.M. Khan, S. Anwar, M. Jamil, M.M. Nasr, M.K. Gupta, M. Saleh, S. Ahmad, M. Mia, Energy, environmental, economic, and technological analysis of Al-GnP Nanofluid- and cryogenic LN2-assisted sustainable machining of Ti-6Al-4V alloy, Metals (Basel) 11 (2021) 88. https://doi.org/10.3390/met11010088.

[26] X. Zhang, Z. Zhou, D. Wen, Z. Shi, X. Chen, X. Tang, W. Rong, T. He, Grinding performance of MgF2 ceramics using biomimetic shark fin grinding wheels with different structure parameters, Ceram Int 50 (2024) 40943–40954. https://doi.org/10.1016/j.ceramint.2024.07.407.

[27] D. Wen, L. Wan, X. Zhang, T. He, Z. Chen, A.M.M. Ibrahim, Wear characteristics of diamond grinding wheels with biomimetic structures in grinding silicon carbide ceramics, Mater Today Commun 44 (2025) 112071. https://doi.org/10.1016/j.mtcomm.2025.112071.

[28] S.B. Thekkoot Surendran, V.S. Sooraj, Sweating type surface grinding wheels for self-adaptable lubricant delivery governed by cutting temperature and speed, J Manuf Process 134 (2025) 915–931. https://doi.org/10.1016/j.jmapro.2024.12.081.

[29] S.D. Mihić, S. Cioc, I.D. Marinescu, M.C. Weismiller, Detailed study of fluid flow and heat transfer in the abrasive grinding contact using computational fluid dynamics methods, J Manuf Sci Eng 135 (2013) 041002. https://doi.org/10.1115/1.4023719.

[30] T. Karpiński, J. Sieniawski, Cylindrical grinding wheel and a mold for its preparation, 203295, 2005.

[31] J. Sieniawski, K. Nadolny, The effect upon grinding fluid demand and workpiece quality when an innovative zonal centrifugal provision method is implemented in the surface grinding of steel CrV12, J Clean Prod 113 (2016) 960–972. https://doi.org/10.1016/j.jclepro.2015.11.017.

[32] J. Sieniawski, K. Nadolny, Experimental study into the grinding force in surface grinding of steel CrV12 utilizing a zonal centrifugal coolant provision system, Proc Inst Mech Eng B J Eng Manuf 232 (2016) 394–403. https://doi.org/10.1177/0954405416645256.

[33] M. Barmouz, B. Azarhoushang, A. Zahedi, F. Rabiei, F. Steinhäuser, Progress in grinding performance by additive manufacturing of grinding wheels integrated with internal venturi cooling channels and surface slots, J Manuf Process 99 (2023) 485–500. https://doi.org/10.1016/j.jmapro.2023.05.078.

[34] S. Costa, M. Pereira, J. Ribeiro, D. Soares, Texturing methods of abrasive grinding wheels: A systematic review, Materials 15 (2022) 8044. https://doi.org/10.3390/ma15228044.

[35] W.B. Rowe, Principles of modern grinding technology, 2nd ed., Butterworth-Heinemann, Oxford, 2013.

[36] R. Cai, W.B. Rowe, Assessment of vitrified CBN wheels for precision grinding, Int J Mach Tools Manuf 44 (2004) 1391–1402. https://doi.org/10.1016/j.ijmachtools.2004.04.004.

[37] J.H. Liu, Z.J. Pei, G.R. Fisher, Grinding wheels for manufacturing of silicon wafers: A literature review, Int J Mach Tools Manuf 47 (2007) 1–13. https://doi.org/10.1016/j.ijmachtools.2006.02.003.

[38] N. V. Baidakova, T.N. Orlova, Influence of abrasive grain geometrical characteristics on the grinding quality, Procedia Eng 206 (2017) 194–199. https://doi.org/10.1016/j.proeng.2017.10.459.

[39] S. Bhowmik, R. Naik, Selection of abrasive materials for manufacturing grinding wheels, Mater Today Proc 5 (2018) 2860–2864. https://doi.org/10.1016/j.matpr.2018.01.077.

[40] B. Huang, C. Li, Y. Zhang, W. Ding, M. Yang, Y. Yang, H. Zhai, X. Xu, D. Wang, S. Debnath, M. Jamil, H.N. Li, H.M. Ali, M.K. Gupta, Z. Said, Advances in fabrication of ceramic corundum abrasives based on sol–gel process, Chin J Aeronaut 34 (2021) 1–17. https://doi.org/10.1016/j.cja.2020.07.004.

[41] Y. Ran, J. Sun, R. Kang, Z. Dong, Y. Bao, Towards understanding the machining process in grinding of ceramic matrix composites: A review, Compos B Eng 284 (2024) 111657. https://doi.org/10.1016/j.compositesb.2024.111657.

[42] B. Chen, Q. Li, M. Amin, S. Yuan, Impact of central abrasive grain absence on micro-hole helical grinding, Chin J Aeronaut 38 (2025) 103433. https://doi.org/10.1016/j.cja.2025.103433.

[43] S. Malkin, C. Guo, Grinding technology: theory and application of machining with abrasives, 2nd ed., Industrial Press Inc., New York, 2008.

[44] S. Malkin, N.H. Cook, The wear of grinding wheels: part 1 — attritious wear, J Eng Ind 93 (1971) 1120–1128. https://doi.org/10.1115/1.3428051.

[45] C. Tian, X. Li, H. Li, G. Guo, L. Wang, Y. Rong, The effect of porosity on the mechanical property of metal-bonded diamond grinding wheel fabricated by selective laser melting (SLM), Mater Sci Eng A 743 (2019) 697–706. https://doi.org/10.1016/j.msea.2018.11.138.

[46] B. Zhao, A.K. Gain, W. Ding, L. Zhang, X. Li, Y. Fu, A review on metallic porous materials: pore formation, mechanical properties, and their applications, Int J Adv Manuf Technol 95 (2018) 2641–2659. https://doi.org/10.1007/s00170-017-1415-6.

[47] C. Tian, Y. Wan, X. Li, Y. Rong, Pore morphology design and grinding performance evaluation of porous grinding wheel made by additive manufacturing, J Manuf Process 79 (2022) 1–10. https://doi.org/10.1016/j.jmapro.2022.04.024.

[48] P. Capela, L. Faria, C. Junior, L. Carvalho, A. Guedes, M. Pereira, D. Soares, Study and optimization of the drying process of a ceramic abrasive composite, Int J Appl Ceram Technol 13 (2016) 308–315. https://doi.org/10.1111/ijac.12455.

[49] P. Capela, S.F. Carvalho, A. Guedes, M. Pereira, L. Carvalho, J. Correia, D. Soares, J.R. Gomes, Effect of sintering temperature on mechanical and wear behaviour of a ceramic composite, Tribol Int 120 (2018) 502–509. https://doi.org/10.1016/j.triboint.2017.12.009.

[50] P. Capela, S. Costa, M.S. Souza, S. Carvalho, M. Pereira, L. Carvalho, J.R. Gomes, D. Soares, Wear behavior of a new composite formulation, with TEOS addition, for abrasive vitrified grinding wheels, Wear 512–513 (2023) 204524. https://doi.org/10.1016/j.wear.2022.204524.

[51] Q. Li, A. Kubota, M. Murai, K. Kawamura, Ultra-precision truncation of coarse-grained electroplated diamond grinding wheels using triboelectrically excited nitrogen, Diam Relat Mater 159 (2025) 112815. https://doi.org/10.1016/j.diamond.2025.112815.

[52] B. Kirsch, Quantitative analysis of the wear of electroplated cBN grinding wheels when grinding AISI 4140, Wear 578–579 (2025) 206227. https://doi.org/10.1016/j.wear.2025.206227.

[53] Z. Zhang, Q. Zhang, Q. Wang, W. Wang, J. Xu, Pulsed laser texturing of brazed diamond grinding wheels with orderly arranged abrasive grains and their grinding performance on WC/Co composites, J Mater Process Technol 344 (2025) 119022. https://doi.org/10.1016/j.jmatprotec.2025.119022.

[54] I.D. Marinescu, M.P. Hitchiner, E. Uhlmann, W.B. Rowe, I. Inasaki, Handbook of machining with grinding wheels, 2nd ed., CRC Press, Boca Raton, 2016. https://doi.org/10.1201/b19462.

[55] W.B. Rowe, Grinding technology-theory and applications of machining with abrasives, Tribol Int 23 (1990) 443. https://doi.org/10.1016/0301-679x(90)90061-s.

[56] F. Hashimoto, H. Yamaguchi, P. Krajnik, K. Wegener, R. Chaudhari, H.W. Hoffmeister, F. Kuster, Abrasive fine-finishing technology, CIRP Annals 65 (2016) 597–620. https://doi.org/10.1016/j.cirp.2016.06.003.

[57] A. Bazan, A. Kawalec, T. Rydzak, P. Kubik, Variation of grain height characteristics of electroplated cBN grinding-wheel active surfaces associated with their wear, Metals (Basel) 10 (2020) 1479. https://doi.org/10.3390/met10111479.

[58] M. Gołąbczak, R. Święcik, A. Gołąbczak, D. Kaczmarek, R. Dębkowski, B. Tomczyk, Electrodischarge methods of shaping the cutting ability of superhard grinding wheels, Materials 14 (2021) 6773. https://doi.org/10.3390/ma14226773.

[59] X. Chen, W.B. Rowe, Analysis and simulation of the grinding process. Part I: Generation of the grinding wheel surface, Int J Mach Tools Manuf 36 (1996) 871–882. https://doi.org/10.1016/0890-6955(96)00116-2.

[60] B. Denkena, J. Köhler, J. Kästner, Chip formation in grinding: An experimental study, Prod Eng 6 (2012) 107–115. https://doi.org/10.1007/S11740-011-0360-8.

[61] S. Malkin, C. Guo, Thermal analysis of grinding, CIRP Annals 56 (2007) 760–782. https://doi.org/10.1016/j.cirp.2007.10.005.

[62] E. Brinksmeier, A. Giwerzew, Chip formation mechanisms in grinding at low speeds, CIRP Annals 52 (2003) 253–258. https://doi.org/10.1016/s0007-8506(07)60578-2.

[63] H.N. Li, T.B. Yu, Z.X. Wang, L. Da Zhu, W.S. Wang, Detailed modeling of cutting forces in grinding process considering variable stages of grain-workpiece micro interactions, Int J Mech Sci 126 (2017) 319–339. https://doi.org/10.1016/j.ijmecsci.2016.11.016.

[64] L. Li, Y. Zhang, X. Cui, Z. Said, S. Sharma, M. Liu, T. Gao, Z. Zhou, X. Wang, C. Li, Mechanical behavior and modeling of grinding force: A comparative analysis, J Manuf Process 102 (2023) 921–954. https://doi.org/10.1016/j.jmapro.2023.07.074.

[65] C. Wei, C. He, G. Chen, Y. Sun, C. Ren, Material removal mechanism and corresponding models in the grinding process: A critical review, J Manuf Process 103 (2023) 354–392. https://doi.org/10.1016/j.jmapro.2023.08.045.

[66] M. Barmouz, F. Steinhäuser, B. Azarhoushang, Green grinding of ultra-high molecular weight polyethylene using glass fiber reinforced highly porous 3D-printed metal bond grinding wheel, Results Mater 26 (2025) 100696. https://doi.org/10.1016/j.rinma.2025.100696.

[67] S. Liu, Y. Tian, B. Liu, G. Zhang, J. Han, H. Yun, Modeling and simulation of temperature field in high-shear and low-pressure grinding with liquid-body-armor-like grinding wheel, J Manuf Process 124 (2024) 1080–1091. https://doi.org/10.1016/j.jmapro.2024.07.023.

[68] R.A. Laghari, M. Jamil, A.A. Laghari, A.M. Khan, Material characteristics and machinability of metal matrix composite materials: A critical review on recent advances and future perspectives, Measurement 242 (2025) 115839. https://doi.org/10.1016/j.measurement.2024.115839.

[69] K. Zeng, X. Wu, F. Jiang, J. Shen, L. Zhu, L. Li, A comprehensive review on the cutting and abrasive machining of cemented carbide materials, J Manuf Process 108 (2023) 335–358. https://doi.org/10.1016/j.jmapro.2023.10.042.

[70] W.B. Rowe, Temperatures in grinding-a review, J Manuf Sci Eng 139 (2017) 121001. https://doi.org/10.1115/1.4036638.

[71] I. Pombo, J.A. Sánchez, E. Martin, L. Godino, J. Álvarez, Accurate measurement of temperatures in industrial grinding operations with steep gradients, Sensors 24 (2024) 1741. https://doi.org/10.3390/S24061741.

[72] Y. Luo, W. Liao, W. Tang, X. Wang, C. Mao, M. Zhang, K. Tang, W. Wang, B. Cheng, A. Razzak, Theoretical and experimental analysis of temperature distribution in variable-depth reciprocating grinding process, J Manuf Process 151 (2025) 89–102. https://doi.org/10.1016/j.jmapro.2025.07.014.

[73] Q. An, J. Chen, W. Ming, M. Chen, Machining of SiC ceramic matrix composites: A review, Chinese J Aeronaut 34 (2021) 540–567. https://doi.org/10.1016/j.cja.2020.08.001.

[74] C. Li, X. Li, S. Huang, L. Li, F. Zhang, Ultra-precision grinding of Gd3Ga5O12 crystals with graphene oxide coolant: Material deformation mechanism and performance evaluation, J Manuf Process 61 (2021) 417–427. https://doi.org/10.1016/j.jmapro.2020.11.037.

[75] T. Gao, C. Li, M. Yang, Y. Zhang, D. Jia, W. Ding, S. Debnath, T. Yu, Z. Said, J. Wang, Mechanics analysis and predictive force models for the single-diamond grain grinding of carbon fiber reinforced polymers using CNT nano-lubricant, J Mater Process Technol 290 (2021) 116976. https://doi.org/10.1016/j.jmatprotec.2020.116976.

[76] E. Brinksmeier, B. Karpuschewski, J. Yan, L. Schönemann, Manufacturing of multiscale structured surfaces, CIRP Annals 69 (2020) 717–739. https://doi.org/10.1016/j.cirp.2020.06.001.

[77] A. Scrivener, Means for shaping the operative surfaces of grinding wheels, 2135202, 1938.

[78] H.E. Sherk, Slotted abrasive wheel, 2049874, 1936.

[79] W.T. deGraaff, Grinding wheel having dead end grooves and method for grinding therewith, 5611724A, 1995.

[80] K. Nakayama, J. Takagi, T. Abe, Grinding wheel with helical grooves-an attempt to improve the grinding performance, CIRP Annals 25 (1977) 133–138.

[81] H.N. Li, D. Axinte, Textured grinding wheels: A review, Int J Mach Tools Manuf 109 (2016) 8–35. https://doi.org/10.1016/j.ijmachtools.2016.07.001.

[82] G. Zhang, X. Deng, D. Liu, T. Song, A nano-MQL grinding of single-crystal nickel-base superalloy using a textured grinding wheel, Int J Adv Manuf Technol 121 (2022) 2787–2801. https://doi.org/10.1007/s00170-022-09431-6.

[83] M.J. Page, J.E. McKenzie, P.M. Bossuyt, I. Boutron, T.C. Hoffmann, C.D. Mulrow, L. Shamseer, J.M. Tetzlaff, E.A. Akl, S.E. Brennan, R. Chou, J. Glanville, J.M. Grimshaw, A. Hróbjartsson, M.M. Lalu, T. Li, E.W. Loder, E. Mayo-Wilson, S. McDonald, L.A. McGuinness, L.A. Stewart, J. Thomas, A.C. Tricco, V.A. Welch, P. Whiting, D. Moher, The PRISMA 2020 statement: An updated guideline for reporting systematic reviews, Int J Surg 88 (2021) 105906. https://doi.org/10.1016/j.ijsu.2021.105906.

[84] A.M.O. Mohamed, R. Bauer, A. Warkentin, Application of shallow circumferential grooved wheels to creep-feed grinding, J Mater Process Technol 213 (2013) 700–706. https://doi.org/10.1016/j.jmatprotec.2012.11.029.

[85] E.J. Silva, B. Kirsch, A.C. Bottene, A. Simon, J.C. Aurich, J.F.G. Oliveira, Manufacturing of structured surfaces via grinding, J Mater Process Technol 243 (2017) 170–183. https://doi.org/10.1016/j.jmatprotec.2016.12.009.

[86] B. Denkena, T. Grove, T. Gartzke, Wear mechanisms of CVD diamond tools for patterning vitrified corundum grinding wheels, Wear 436–437 (2019) 203007. https://doi.org/10.1016/j.wear.2019.203007.

[87] A. Riebel, R. Bauer, A. Warkentin, Investigation into the effect of wheel groove depth and width on grinding performance in creep-feed grinding, Int J Adv Manuf Technol 106 (2020) 4401–4409. https://doi.org/10.1007/s00170-020-04933-7.

[88] E.J. da Silva, G.P. Marcos, G.S. Venter, A.C. Bottene, J.F.G. de Oliveira, C.A. Rodrigues, Development of a patterning system for vitrified CBN wheels based on modal analysis, CIRP Ann Manuf Technol 67 (2018) 341–344. https://doi.org/10.1016/j.cirp.2018.04.076.

[89] C. Forbrigger, R. Bauer, A. Warkentin, Improving the accuracy of a profile grinding wheel grooving robot attachment for a CNC grinding machine, Int J Adv Manuf Technol 98 (2018) 3205–3216. https://doi.org/10.1007/s00170-018-2406-y.

[90] H. Cao, X. Chen, H. Li, Dressing strategy and grinding control for cylindrical microstructural surface, Int J Adv Manuf Technol 99 (2018) 707–727. https://doi.org/10.1007/s00170-018-2466-z.

[91] A.L.M.O. Mohamed, A. Warkentin, R. Bauer, Prediction of workpiece surface texture using circumferentially grooved grinding wheels, Int J Adv Manuf Technol 89 (2017) 1149–1160. https://doi.org/10.1007/s00170-016-9126-y.

[92] J.F.G. Oliveira, A.C. Bottene, T.V. França, A novel dressing technique for texturing of ground surfaces, CIRP Annals 59 (2010) 361–364. https://doi.org/10.1016/j.cirp.2010.03.119.

[93] M. Gavas, I. Karacan, E. Kaya, A novel method to improve surface quality in cylindrical grinding, Exp Tech 35 (2011) 26–32. https://doi.org/10.1111/j.1747-1567.2009.00575.x.

[94] T. Tawakoli, D.H. Lee, A. Rasifard, Dry plunge cylindrical grinding utilising structured grinding wheel, Int J Mechatron Manuf Syst 5 (2012) 154–164. https://doi.org/10.1504/ijmms.2012.046523.

[95] J.C. Aurich, B. Kirsch, Improved coolant supply through slotted grinding wheel, CIRP Ann Manuf Technol 62 (2013) 363–366. https://doi.org/10.1016/j.cirp.2013.03.071.

[96] K. Nadolny, Micro-discontinuities of the grinding wheel and their effects on its durability during internal cylindrical grinding, Mach Sci Technol 17 (2013) 74–92. https://doi.org/10.1080/10910344.2012.747900.

[97] E.J. Da Silva, J.F.G. De Oliveira, B.B. Salles, R.S. Cardoso, V.R.A. Reis, Strategies for production of parts textured by grinding using patterned wheels, CIRP Annals 62 (2013) 355–358. https://doi.org/10.1016/j.cirp.2013.03.123.

[98] U. Köklü, Grinding with helically grooved wheels, Proc Inst Mech Eng E: J Process Mech Eng 228 (2012) 33–42. https://doi.org/10.1177/0954408912470775.

[99] A.M.O. Mohamed, R. Bauer, A. Warkentin, A novel method for grooving and re-grooving aluminum oxide grinding wheels, Int J Adv Manuf Technol 73 (2014) 715–725. https://doi.org/10.1007/s00170-014-5880-x.

[100] M. Gavas, M. Kỳna, U. Köklü, Effects of various helically angled grinding wheels on the surface roughness and roundness in grinding cylindrical surfaces, Mater Technol 49 (2015) 865–870. https://doi.org/10.17222/mit.2014.065.

[101] B. Denkena, T. Grove, T. Göttsching, Grinding with patterned grinding wheels, CIRP J Manuf Sci Technol 8 (2015) 12–21. https://doi.org/10.1016/j.cirpj.2014.10.005.

[102] B. Denkena, T. Grove, T. Göttsching, E.J. da Silva, R.T. Coelho, R. Filleti, Enhanced grinding performance by means of patterned grinding wheels, Int J Adv Manuf Technol 77 (2015) 1935–1941. https://doi.org/10.1007/s00170-014-6579-8.

[103] R. Wójcik, K. Nadolny, The effect of the grinding wheel modification on the state of the workpiece surface layer after internal cylindrical grinding of steel C45, Proc Inst Mech Eng E: J. Process Mech Eng 231 (2016) 1162–1173. https://doi.org/10.1177/0954408916656887.

[104] B. Azarhoushang, A. Daneshi, D.H. Lee, Evaluation of thermal damages and residual stresses in dry grinding by structured wheels, J Clean Prod 142 (2017) 1922–1930. https://doi.org/10.1016/j.jclepro.2016.11.091.

[105] U. Çaydas, M. Çelk, Genetic algorithm-based optimization for surface roughness in cylindrically grinding process using helically grooved wheels, Surf Rev Lett 24 (2017). https://doi.org/10.1142/s0218625x18500312.

[106] Y. Liu, S. Gong, J. Li, J. Cao, Effects of dressed wheel topography on patterned surface textures and grinding force, Int. J. Adv. Manuf. Technol. 93 (2017) 1751–1760. https://doi.org/10.1007/s00170-017-0647-9.

[107] A. Daneshi, K. Müller, B. Azarhoushang, Cylindrical plunge grinding of twist free surfaces by structured wheels, Precis Eng 51 (2018) 481–489. https://doi.org/10.1016/j.precisioneng.2017.10.003.

[108] S. Dewar, R. Bauer, A. Warkentin, Application of high-angle helical-grooved vitrified wheels to cylindrical plunge grinding, Int J Adv Manuf Technol 96 (2018) 2443–2453. https://doi.org/10.1007/s00170-018-1801-8.

[109] C. Forbrigger, A. Warkentin, R. Bauer, Improving the performance of profile grinding wheels with helical grooves, Int J Adv Manuf Technol 97 (2018) 2331–2340. https://doi.org/10.1007/s00170-018-2098-3.

[110] A. Patel, R.J. Bauer, A. Warkentin, Investigation of the effect of speed ratio on workpiece surface topography and grinding power in cylindrical plunge grinding using grooved and non-grooved grinding wheels, Int J Adv Manuf Technol 105 (2019) 2977–2987. https://doi.org/10.1007/s00170-019-04406-6.

[111] Y. Zhang, C. Fang, G. Huang, X. Xu, Modeling and simulation of the distribution of undeformed chip thicknesses in surface grinding, Int J Mach Tools Manuf 127 (2018) 14–27. https://doi.org/10.1016/j.ijmachtools.2018.01.002.

[112] H. Yu, J. Wang, Y. Lu, Modeling and analysis of dynamic cutting points density of the grinding wheel with an abrasive phyllotactic pattern, Int J Adv Manuf Technol 86 (2016) 1933–1943. https://doi.org/10.1007/s00170-015-8262-0.

[113] H. Yu, J. Wang, Y. Lu, Simulation of grinding surface roughness using the grinding wheel with an abrasive phyllotactic pattern, Int J Adv Manuf Technol 84 (2016) 861–871. https://doi.org/10.1007/s00170-015-7722-x.

[114] S. Wang, C. Li, D. Jia, Y. Zhang, Q. Zhang, Modelling and simulation of the surface topography generation with engineered grinding wheel, Int J Comput Mater Sci Surf Eng 6 (2015) 111–129. https://doi.org/10.1504/ijcmsse.2015.071647.

[115] H.P. Yuan, H. Gao, Y.D. Liang, Fabrication of a new-type electroplated wheel with controlled abrasive cluster and its application in dry grinding of CFRP, Int J Abras Technol 3 (2010) 299–315. https://doi.org/10.1504/ijat.2010.036963.

[116] H. Yu, Y. Lu, J. Wang, Study on wear of the grinding wheel with an abrasive phyllotactic pattern, Wear 358–359 (2016) 89–96. https://doi.org/10.1016/j.wear.2016.04.007.

[117] M. Zhang, Y. Tan, F. Zhou, C. Mao, Z. Xie, C. Li, Analysis of flow field in cutting zone for spiral orderly distributed fiber tool, Int J Adv Manuf Technol 92 (2017) 4345–4354. https://doi.org/10.1007/s00170-017-0471-2.

[118] W. Ding, C. Dai, T. Yu, J. Xu, Y. Fu, Grinding performance of textured monolayer CBN wheels: Undeformed chip thickness nonuniformity modeling and ground surface topography prediction, Int J Mach Tools Manuf 122 (2017) 66–80. https://doi.org/10.1016/j.ijmachtools.2017.05.006.

[119] Y. Lyu, H. Yu, J. Wang, C. Chen, L. Xiang, Study on the grinding temperature of the grinding wheel with an abrasive phyllotactic pattern, Int J Adv Manuf Technol 91 (2017) 895–906. https://doi.org/10.1007/s00170-016-9811-x.

[120] H. Yu, Y. Lyu, J. Wang, X. Wang, A biomimetic engineered grinding wheel inspired by phyllotaxis theory, J Mater Process Technol 251 (2018) 267–281. https://doi.org/10.1016/j.jmatprotec.2017.08.041.

[121] H. Yu, Y. Lyu, J. Wang, Experimental investigation on grinding temperature of Ti–6Al–4 V using biomimetic engineered grinding wheel, Int J of Precis Eng and Manuf 6 (2019) 163–173. https://doi.org/10.1007/S40684-019-00050-3.

[122] H. Yu, Y. Lyu, J. Wang, Green manufacturing with a bionic surface structured grinding wheel-specific energy analysis, Int J Adv Manuf Technol 104 (2019) 2999–3005. https://doi.org/10.1007/s00170-019-04159-2.

[123] H. Yu, W. Zhang, Y. Lyu, J. Wang, Research on grinding forces of a bionic engineered grinding wheel, J Manuf Process 48 (2019) 185–190. https://doi.org/10.1016/j.jmapro.2019.10.031.

[124] Y. Zhang, X. Xu, Influence of surface topography evolution of grinding wheel on the optimal material removal rate in grinding process of cemented carbide, Int J Refract Metals Hard Mater 80 (2019) 130–143. https://doi.org/10.1016/j.ijrmhm.2019.01.009.

[125] Y. Zhang, C. Fang, G. Huang, C. Cui, X. Xu, Numerical and experimental studies on the grinding of cemented carbide with textured monolayer diamond wheels, Int J Refract Metals Hard Mater 84 (2019) 105022. https://doi.org/10.1016/j.ijrmhm.2019.105022.

[126] Y. Qiu, H. Huang, Research on the fabrication and grinding performance of 3-dimensional controllable abrasive arrangement wheels, Int J Adv Manuf Technol 104 (2019) 1839–1853. https://doi.org/10.1007/s00170-019-03900-1.

[127] Y. Zhu, W. Ding, Z. Rao, Z. Zhao, Self-sharpening ability of monolayer brazed polycrystalline CBN grinding wheel during high-speed grinding, Ceram Int 45 (2019) 24078–24089. https://doi.org/10.1016/j.ceramint.2019.08.115.

[128] F.-L. Zhang, M.-C. Li, J. Wang, H.-P. Huang, C.-Y. Wang, Y.-M. Zhou, Effect of arraying parameters on dry grinding performance of patterned monolayer brazed CBN wheel, Int J Adv Manuf Technol 107 (2020) 2081–2089. https://doi.org/10.1007/s00170-020-05176-2.

[129] R. Peng, K. Liu, J. Tong, X. Tang, Performance of the internal-cooling grooved grinding wheel with patterned abrasives, Int J Adv Manuf Technol 106 (2020) 1633–1644. https://doi.org/10.1007/s00170-019-04694-y.

[130] R. Peng, J. Tong, X. Tang, X. Huang, K. Liu, Application of a pressurized internal cooling method in grinding inconel 718: Modeling-simulation and testing-validation, Int J Mech Sci 189 (2021) 105985. https://doi.org/10.1016/j.ijmecsci.2020.105985.

[131] R. Peng, Y. Luo, B. Liu, J. Tong, L. Zhao, Application of bionic phyllotaxis in internal cooling cup wheel: modeling-simulation and experimental verification, Int J Adv Manuf Technol 114 (2021) 3803–3822. https://doi.org/10.1007/s00170-021-07097-0.

[132] Z. Guo, J. Cheng, J. Wu, X. Zhang, B. Liu, Modeling and experimental study on the grinding performance of precision diamond grinding tool with defined texture, Int J Adv Manuf Technol (2022). https://doi.org/10.1007/s00170-021-08372-w.

[133] W. Wang, Q. Zhang, C. Chu, Z. Zhang, J. Xu, Simulation and experimental study of the ground surface topography of GH4169 by grains arrayed brazed diamond wheels, Int J Adv Manuf Technol 118 (2022) 303–317. https://doi.org/10.1007/s00170-021-07963-x.

[134] R. Peng, L. Zhao, J. Tong, M. Chen, M. Zhou, A. Li, Design and evaluation of an internal-cooling grooved grinding wheel, J Manuf Process 73 (2022) 1–16. https://doi.org/10.1016/j.jmapro.2021.10.061.

[135] C.W. Wardlaw, Phyllotaxis and organogenesis in ferns, Nature 164 (1949) 167–169. https://doi.org/10.1038/164167a0.

[136] B. Azarhoushang, A. Zahedi, Laser conditioning and structuring of grinding tools – a review, Adv Manuf 5 (2017) 35–49. https://doi.org/10.1007/s40436-016-0167-0.

[137] U. Shankar, N.R. Babu, A Model for predicting the geometry of crater on grinding wheel surface ablated with a single pulsed laser, Procedia Manuf 26 (2018) 509–520. https://doi.org/10.1016/j.promfg.2018.07.060.

[138] H.N. Li, Y.J. Zhao, S. Cao, H. Chen, C. Wu, H. Qi, X. Sun, H. Wang, C. Li, G. Liu, Controllable generation of 3D textured abrasive tools via multiple-pass laser ablation, J Mater Process Technol 295 (2021) 117149. https://doi.org/10.1016/j.jmatprotec.2021.117149.

[139] S. Cai, W. Liu, J. Song, K. Deng, Y. Tang, Research and progress on truing and sharpening process of diamond abrasive grinding tools, Appl Sci 12 (2022) 4683. https://doi.org/10.3390/app12094683.

[140] B. Guo, Q. Zhao, X. Yu, Surface micro-structuring of coarse-grained diamond wheels by nanosecond pulsed laser for improving grinding performance, Int J Precis Eng 15 (2014) 2025–2030. https://doi.org/10.1007/s12541-014-0559-7.

[141] H. Deng, J. He, A study of the grinding performance of laser micro-structured coarse-grained diamond grinding wheels, Int J Adv Manuf Technol 93 (2017) 1989–1997. https://doi.org/10.1007/s00170-017-0639-9.

[142] X.H. Zhang, Z.X. Kang, S. Li, Q.P. Wu, Z.C. Zhang, Experimental investigations on the impact of different laser macro-structured diamond grinding wheels on alumina ceramic, Int J Adv Manuf Technol 96 (2018) 1959–1969. https://doi.org/10.1007/s00170-018-1644-3.

[143] B. Guo, M. Wu, Q. Zhao, H. Liu, J. Zhang, Improvement of precision grinding performance of CVD diamond wheels by micro-structured surfaces, Ceram Int 44 (2018) 17333–17339. https://doi.org/10.1016/j.ceramint.2018.06.197.

[144] X. Zhang, Z. Kang, S. Li, Z. Shi, D. Wen, J. Jiang, Z. Zhang, Grinding force modelling for ductile-brittle transition in laser macro-micro-structured grinding of zirconia ceramics, Ceram Int 45 (2019) 18487–18500. https://doi.org/10.1016/j.ceramint.2019.06.067.

[145] X. Zhang, Z. Zhang, Z. Deng, S. Li, Q. Wu, Z. Kang, Precision grinding of silicon nitride ceramic with laser macro-structured diamond wheels, Opt Laser Technol 109 (2019) 418–428. https://doi.org/10.1016/j.optlastec.2018.08.021.

[146] M. Wu, B. Guo, Q. Zhao, J. Zhang, X. Fang, P. He, High efficiency precision grinding of micro-structured SiC surface using laser micro-structured coarse-grain diamond grinding wheel, Int J Precis Eng 6 (2019) 577–586. https://doi.org/10.1007/s40684-019-00058-9.

[147] B. Azarhoushang, M. Kadivar, R. Bösinger, S. Shamray, A. Zahedi, A. Daneshi, High-speed high-efficient grinding of CMCs with structured grinding wheels, Int J Abras Technol 9 (2019) 1–15. https://doi.org/10.1504/ijat.2019.097964.

[148] H. Deng, Z. Xu, L. Wang, P. Zhu, Laser micro-structuring of a coarse-grained diamond grinding wheel, Int J Adv Manuf Technol 101 (2019) 2947–2954. https://doi.org/10.1007/s00170-018-3101-8.

[149] C. Li, Z.J. Shi, X.H. Zhang, Z.Y. Shi, S. Li, R.Y. Jiang, Z.R. Wang, Z.C. Zhang, An investigation on grinding mechanism of alumina ceramic using a grooved grinding wheel with inclined cross section, Int J Adv Manuf Technol 111 (2020) 2391–2399. https://doi.org/10.1007/s00170-020-06250-5.

[150] H.N. Li, K.G. Xie, B. Wu, W.Q. Zhu, Generation of textured diamond abrasive tools by continuous-wave CO2 laser: Laser parameter effects and optimisation, J Mater Process Technol 275 (2020) 116279. https://doi.org/10.1016/j.jmatprotec.2019.116279.

[151] S. Wu, F. Zhang, Y. Ni, F. Chen, Z. Yan, Grinding of alumina ceramic with microtextured brazed diamond end grinding wheels, Ceram Int 46 (2020) 19767–19784. https://doi.org/10.1016/j.ceramint.2020.05.009.

[152] X. Zhang, Z. Wang, Z. Shi, Z. Shi, R. Jiang, Z. Kang, Improved grinding performance of zirconia ceramic using an innovative biomimetic fractal-branched grinding wheel inspired by leaf vein, Ceram Int 46 (2020) 22954–22963. https://doi.org/10.1016/j.ceramint.2020.06.070.

[153] X. Zhao, T. Yu, C. Jia, S. Lu, L. Chen, W. Wang, Study on textured CBN grinding wheel by laser cladding, Int J Adv Manuf Technol 106 (2020) 865–876. https://doi.org/10.1007/s00170-019-04240-w.

[154] A. Monier, B. Guo, Q. Zhao, T.S. Mahmoud, Modeling and simulation of the advanced structured surfaces machined by specially patterned grinding wheels via the structuring grinding process, Int J Adv Manuf Technol 119 (2022) 3321–3342. https://doi.org/10.1007/s00170-021-08296-5.

[155] Z. Hou, Z. Yao, Y. Sun, H. Shen, Grooving profile control for structured grinding wheels with picosecond pulsed laser, Int J Adv Manuf Technol 119 (2022) 5851–5862. https://doi.org/10.1007/s00170-022-08655-w.

[156] Z. Geng, Z. Tong, G. Huang, W. Zhong, C. Cui, X. Xu, X. Jiang, Micro-grooving of brittle materials using textured diamond grinding wheels shaped by an integrated nanosecond laser system, Int J Adv Manuf Technol 119 (2022) 5389–5399. https://doi.org/10.1007/s00170-022-08695-2.

[157] J. Huang, J. Lu, Y. Wang, Z. Ma, Fabrication of porous structure vitrified bond diamond grinding wheel via direct ink writing, Ceram Int 47 (2021) 34050–34058. https://doi.org/10.1016/j.ceramint.2021.08.314.

[158] C. Tian, X. Li, S. Zhang, G. Guo, L. Wang, Y. Rong, Study on design and performance of metal-bonded diamond grinding wheels fabricated by selective laser melting (SLM), Mater Des 156 (2018) 52–61. https://doi.org/10.1016/j.matdes.2018.06.029.

[159] Z.-J. Du, F.-L. Zhang, Q.-S. Xu, Y.-J. Huang, M.-C. Li, H.-P. Huang, C.-Y. Wang, Y.-M. Zhou, H.-Q. Tang, Selective laser sintering and grinding performance of resin bond diamond grinding wheels with arrayed internal cooling holes, Ceram Int 45 (2019) 20873–20881. https://doi.org/10.1016/j.ceramint.2019.07.076.

[160] C. Wang, D. Wang, C. Tian, L. Wang, Y. Rong, X. Li, Grinding performance evaluation of 3D-printed porous metal-bonded grinding wheel in BK7 glass grinding, Int J Adv Manuf Technol 117 (2021) 1445–1457. https://doi.org/10.1007/s00170-021-07819-4.

[161] X. Li, C. Wang, C. Tian, S. Fu, Y. Rong, L. Wang, Digital design and performance evaluation of porous metal-bonded grinding wheels based on minimal surface and 3D printing, Mater Des 203 (2021) 109556. https://doi.org/10.1016/j.matdes.2021.109556.

[162] T. Tawakoli, B. Azarhoushang, Intermittent grinding of ceramic matrix composites (CMCs) utilizing a developed segmented wheel, Int J Mach Tools Manuf 51 (2011) 112–119. https://doi.org/10.1016/j.ijmachtools.2010.11.002.

[163] T. Tawakoli, B. Azarhoushang, Theoretical and experimental investigation of intermittent grinding of SiC with a segmented grinding wheel, Int J Abras Technol 4 (2011) 90–99. https://doi.org/10.1504/ijat.2011.039005.

[164] B. Azarhoushang, Wear of non-segmented and segmented diamond wheels in high-speed deep grinding of carbon fibre-reinforced ceramics, Int J Adv Manuf Technol 74 (2014) 1293–1302. https://doi.org/10.1007/s00170-014-6082-2.

[165] J. Wang, Abrasive waterjet machining of engineering materials, Trans Tech Publications, Zurich, 2003.

[166] F. Su, Z. Zhang, P. Yao, H. Yu, H. Xing, M. Ge, Y. Zhao, Fabrication of cylindrical microlens array on RB-SiC moulds by precision grinding with MAWJ-Textured diamond Wheels, Appl Sci 12 (2022) 6893. https://doi.org/10.3390/app12146893.

[167] H.N. Li, D. Axinte, On the inverse design of discontinuous abrasive surface to lower friction-induced temperature in grinding: An example of engineered abrasive tools, Int J Mach Tools Manuf 132 (2018) 50–63. https://doi.org/10.1016/j.ijmachtools.2018.04.006.

[168] Z. Zhang, P. Yao, C. Huang, J. Wang, D. Xue, W. Deng, Z. Zhang, Investigation and modeling of microgrooves generated on diamond grinding wheel by abrasive waterjet based on Box–Behnken experimental design, Int J Adv Manuf Technol 100 (2019) 321–332. https://doi.org/10.1007/s00170-018-2749-4.

[169] Z. Zhang, P. Yao, J. Wang, X. Bao, Z. Ye, C. Huang, H. Zhu, B. Zou, H. Liu, The mechanisms of high-efficiency grinding for micro/meso-structural arrays on ceramic moulds through an innovative wheel truing technology, Ceram Int 47 (2021) 27624–27638. https://doi.org/10.1016/j.ceramint.2021.06.187.

[170] K.G. Xie, A.G.A. Rushworth, H. Chen, J. Li, On the modelling and experimental study of CO2 laser ablation on resin-bond diamond grinding wheels: Understanding the effect of processing parameters on the time-dependent temperature field, J Manuf Process 124 (2024) 1471–1484. https://doi.org/10.1016/j.jmapro.2024.07.007.

[171] M. Barmouz, B. Azarhoushang, Additive manufacturing of hybrid bond grinding wheels via digital light processing: Performance enhancement through composition alteration and groove incorporation, Results Eng 27 (2025) 105808. https://doi.org/10.1016/j.rineng.2025.105808.

[172] J. Wu, Q. Zhang, Y. Li, S. Zhang, X. Kong, L. Rong, Y. Xiao, H. Li, Z. Ding, Diamond parameter design and assessment of a novel 3D printed diamond grinding wheel with linear cooling channels, Diam Relat Mater 150 (2024) 111760. https://doi.org/10.1016/j.diamond.2024.111760.

[173] S. Zhang, Z. Zhang, H. Xing, G. Hao, X. Liang, Analysis and optimization of abrasive waterjet dressing parameters for surface texturing of diamond grinding wheels, Diam Relat Mater 149 (2024) 111661. https://doi.org/10.1016/j.diamond.2024.111661.

[174] S. Majumdar, P. Das, S. Kumar, D. Roy, S. Chakraborty, Evaluation of cutting fluid application in surface grinding, Measurement 169 (2021) 108464. https://doi.org/10.1016/j.measurement.2020.108464.

[175] S.K.T. Vanan, E.U. Olugu, C.K. Ang, S.A. Lawal, O.C. Aja, Evaluation of surface grinding of AISI 304 stainless steel using dry and compressed air cooling techniques, SN Appl Sci 3 (2021) 389. https://doi.org/10.1007/s42452-021-04395-w.

[176] M. Dogra, V.S. Sharma, J.S. Dureja, S.S. Gill, Environment-friendly technological advancements to enhance the sustainability in surface grinding- A review, J Clean Prod 197 (2018) 218–231. https://doi.org/10.1016/j.jclepro.2018.05.280.

[177] K.K. Gajrani, D. Ram, M.R. Sankar, Biodegradation and hard machining performance comparison of eco-friendly cutting fluid and mineral oil using flood cooling and minimum quantity cutting fluid techniques, J Clean Prod 165 (2017) 1420–1435. https://doi.org/10.1016/j.jclepro.2017.07.217.

[178] Grinding fluids market size, share & analysis report 2030, KBV Research (n.d.). https://www.kbvresearch.com/grinding-fluids-market/ (accessed September 20, 2025).

[179] S. Debnath, M.M. Reddy, Q.S. Yi, Environmental friendly cutting fluids and cooling techniques in machining: a review, J Clean Prod 83 (2014) 33–47. https://doi.org/10.1016/j.jclepro.2014.07.071.

[180] S.M. Alimuzzaman, M.P. Jahan, C.S. Rakurty, N. Rangasamy, J. Ma, Cutting fluids in metal AM: A review of sustainability and efficiency, J Manuf Process 106 (2023) 51–87. https://doi.org/10.1016/j.jmapro.2023.09.075.

[181] M. Iruj, S. Yaqoob, J.A. Ghani, H. Jaber, N. Saibani, M. Alkhedher, State-of-the-art hybrid lubrication (Cryo-MQL) supply systems, performance evaluation, and optimization studies in various machining processes, Results Eng 22 (2024) 102090. https://doi.org/10.1016/j.rineng.2024.102090.

[182] R. Peng, W. Yan, L. Zhao, M. Chen, X. Xiao, Design and performance evaluation of a directional internal-cooling grooved grinding wheel with optimized coolant supply structure, J Manuf Process 141 (2025) 155–168. https://doi.org/10.1016/j.jmapro.2025.02.059.

[183] T. Nguyen, L.C. Zhang, Performance of a new segmented grinding wheel system, Int J Mach Tools Manuf 49 (2009) 291–296. https://doi.org/10.1016/j.ijmachtools.2008.10.015.

[184] K. Nadolny, Small-dimensional sandwich grinding wheels with a centrifugal coolant provision system for traverse internal cylindrical grinding of steel 100Cr6, J Clean Prod 93 (2015) 354–363. https://doi.org/10.1016/j.jclepro.2015.01.046.

[185] S. Ebbrell, N.H. Woolley, Y.D. Tridimas, D.R. Allanson, W.B. Rowe, The effects of cutting fluid application methods on the grinding process, Int J Mach Tools Manuf 40 (2000) 209–223. https://doi.org/10.1016/s0890-6955(99)00060-7.

[186] R. Alberdi, J.A. Sanchez, I. Pombo, N. Ortega, B. Izquierdo, S. Plaza, D. Barrenetxea, Strategies for optimal use of fluids in grinding, Int J Mach Tools Manuf 51 (2011) 491–499. https://doi.org/10.1016/j.ijmachtools.2011.02.007.

[187] C. Baumgart, J.J. Radziwill, F. Kuster, K. Wegener, A study of the interaction between coolant jet nozzle flow and the airflow around a grinding wheel in cylindrical grinding, Procedia CIRP 58 (2017) 517–522. https://doi.org/10.1016/j.procir.2017.03.261.

[188] K. Nadolny, S. Kieraś, New approach for cooling and lubrication in dry machining on the example of internal cylindrical grinding of bearing rings, Sustain Mater Technol 24 (2020) e00166. https://doi.org/10.1016/j.susmat.2020.E00166.

[189] C. Heinzel, B. Kirsch, D. Meyer, J. Webster, Interactions of grinding tool and supplied fluid, CIRP Ann Manuf Technol 69 (2020) 624–645. https://doi.org/10.1016/j.cirp.2020.05.001.

[190] S. Majumdar, S. Mandal, I. Biswas, D. Roy, S. Chakraborty, Modelling of air boundary layer around the grinding wheel, Int J Model Simul 40 (2020) 104–113. https://doi.org/10.1080/02286203.2018.1562013.

[191] J. Kundrák, A.P. Markopoulos, N.E. Karkalos, Numerical simulation of grinding with realistic representation of grinding wheel and workpiece movements: A finite volumes study, Procedia CIRP 58 (2017) 275–280. https://doi.org/10.1016/j.procir.2017.03.192.

[192] A. Gupta, P. Swami, A.S.S. Balan, P. Kuppan, R. Oyyaravelu, Numerical modeling and heat transfer analysis of minimum quantity lubrication grinding of Inconel 751, Mater Today Proc 5 (2018) 13358–13366. https://doi.org/10.1016/j.matpr.2018.02.328.

[193] Z. Chen, X. Zhang, D. Wen, S. Li, X. Wang, L. Gan, X. Rong, Improved grinding performance of SiC using an innovative bionic vein-like structured grinding wheel optimized by hydrodynamics, J Manuf Process 101 (2023) 195–207. https://doi.org/10.1016/j.jmapro.2023.06.010.

[194] C. Tian, Y. Wan, X. Li, Y. Rong, Permeability design and assessment of the additively manufactured metal-bonded diamond grinding wheel based on TPMS structures, Int J Refract Metals Hard Mater 114 (2023) 106237. https://doi.org/10.1016/j.ijrmhm.2023.106237.

[195] S.B. Thekkoot Surendran, V.S. Sooraj, Enhancing useful flow of cutting fluid and thermal performance in surface grinding via segmented wheel, Mater Today Proc 90 (2023) 208–213. https://doi.org/10.1016/j.matpr.2023.06.090.

[196] H. Yu, W. Zhang, S. Zhang, J. Zhang, Z. Han, Optimization of hydrodynamic properties of structured grinding wheels based on combinatorial bionics, Tribol Int 173 (2022) 107651. https://doi.org/10.1016/j.triboint.2022.107651.

[197] Z. Wang, J. Li, Q. Liu, L. Chen, J. Lv, T. Yu, J. Zhao, No-impact trajectory design and fabrication of surface structured CBN grinding wheel by laser cladding remelting method, Opt Laser Technol 181 (2025) 111956. https://doi.org/10.1016/j.optlastec.2024.111956.

[198] H. Yu, K. Sun, W. Ren, J. Zhang, Z. Han, Synergistic improvement of grinding fluid utilization and workpiece surface quality using combinatorial bionic structured grinding wheels, J Manuf Process 130 (2024) 102–117. https://doi.org/10.1016/j.jmapro.2024.08.046.

[199] M. Hong, G. Huang, H. Fan, L. Wu, W. Li, Y. Xu, X. Xu, W. Zeng, Investigation of additive-manufactured spiral textured grinding wheel (TGW) for grinding of zirconia ceramics, Ceram Int 51 (2025) 35448–35462. https://doi.org/10.1016/j.ceramint.2025.05.266.

[200] X. Xiao, Y. Jin, M. Chen, R. Peng, H. Tang, J. Gao, An internal cooling grinding wheel: From design to application, Chin J Aeronaut 36 (2023) 465–482. https://doi.org/10.1016/j.cja.2023.02.024.

[201] R. Peng, Q. Yang, L. Zhao, M. Chen, Evaluation of the feasibility and machining performance of internal cooling grinding Inconel 718 superalloy, J Manuf Process 108 (2023) 551–564. https://doi.org/10.1016/j.jmapro.2023.11.011.

[202] L. Zhao, R. Peng, J. Gao, Y. Li, X. Tang, X. Chen, Z. Tan, Synergistic nanofluids-porous self-lubricating internal cooling wheel for superalloy grinding, Int J Mech Sci 302 (2025) 110576. https://doi.org/10.1016/j.ijmecsci.2025.110576.

[203] X. Xiao, B. Li, R. Peng, X. Hao, X. Huang, Y. Li, L. Zhao, M. Chen, J. Gao, Analysis of the material removal and heat transfer during internal cooling grinding of GH4169, J Mater Process Technol 322 (2023) 118199. https://doi.org/10.1016/ j.jmaprotec.2023.118199.

[204] R. Peng, L. Zhao, X. Tang, X. Xiao, J. Gao, Heat transfer performance assessment of abrasive phyllotaxy arrangement in internal cooling grinding, Int J Heat Mass Transf 197 (2022) 123317. https://doi.org/10.1016/j.ijheatmasstransfer.2022.123317.

[205] R. Peng, R. Wang, J. Gao, L. Zhao, X. Huang, J. Yao, Improve the grinding performance of Inconel 718 superalloys by using an internal cooling wheel with a phyllotaxy of abrasive arrangement, Int J Adv Manuf Technol 135 (2024) 2517–2537. https://doi.org/10.1007/s00170-024-14625-1.

[206] R. Peng, X. Huang, X. Tang, R. Chen, Y. Hu, Performance of a pressurized internal-cooling slotted grinding wheel system, Int J Adv Manuf Technol 94 (2018) 2239–2254. https://doi.org/10.1007/s00170-017-1014-6.

[207] Z. Wang, Z. Sun, Y. Huang, T. Yu, J. Zhao, Design and preparation of a self-inhaling internal cooling crinding wheel with a leaf order arrangement structure, Appl Sci 15 (2025) 44. https://doi.org/10.3390/app15010044.

[208] M. Chen, R. Peng, A. Li, X. Xiao, L. Zhao, Assessment of surface structure optimization in internal cooling grinding, Int J Adv Manuf Technol 123 (2022) 2139–2155. https://doi.org/10.1007/s00170-022-10304-1.

[209] Y. Saffar, M. Kulka, D.S. Nobes, R. Sabbagh, Simultaneous circulating tumor cells (CTCs) tracking and flow field characterization through integrated single camera imaging in a micro-hydrocyclone, Chem Eng J 520 (2025) 165681. https://doi.org/10.1016/j.cej.2025.165681.

[210] S. Salavatidezfouli, S. Barzegar, A. Sheidani, A. Hajisharifi, M. Girfoglio, G. Stabile, G. Rozza, Effect of particle aspect ratio in targeted drug delivery in abdominal aortic aneurysm, Eur J Mech B Fluids 106 (2024) 181–196. https://doi.org/10.1016/j.euromechflu.2024.04.009.

[211] E.J. Carboni, B.H. Bognet, G.M. Bouchillon, A.L. Kadilak, L.M. Shor, M.D. Ward, A.W.K. Ma, Direct Tracking of Particles and Quantification of Margination in Blood Flow, Biophys J 111 (2016) 1487–1495. https://doi.org/10.1016/j.bpj.2016.08.026.

[212] E. Freire, Differential scanning calorimetry, in: Methods Mol Biol, 1st ed., Humana Press, Clifton, 1995: pp. 191–218. https://doi.org/10.1385/0-89603-301-5:191.

[213] B. Lothenbach, P. Durdziński, K. De Weerdt, Thermogravimetric analysis, in: A Practical Guide to Microstructural Analysis of Cementitious Materials, 1st ed., CRC Press, Boca Raton, 2018: pp. 196–231. https://doi.org/10.1201/b19074-5.

[214] J. James, Thermomechanical analysis and its applications, in: Thermal and Rheological Measurement Techniques for Nanomaterials Characterization, 1st ed., Elsevier, Moolamattom, 2017: pp. 159–171. https://doi.org/10.1016/b978-0-323-46139-9.00007-4.

[215] R.P. Chartoff, J.D. Menczel, S.H. Dillman, Dynamic mechanical analysis (DMA), in: Thermal Analysis of Polymers: Fundamentals and Applications, 1st ed., Wiley, Hoboken, 2009: pp. 387–495. https://doi.org/10.1002/9780470423837.ch5.

[216] A. Ul-Hamid, A Beginners' Guide to Scanning Electron Microscopy, 1st ed., Springer, Cham, 2018. https://doi.org/10.1007/978-3-319-98482-7.

[217] S. Costa, P. Araújo, P. Capela, J. Gomes, J. Ribeiro, M. Pereira, D. Soares, Design of an experimental grinding machine for testing abrasive wheels with a 3D internal cooling channels structure, in: Lubricants, Tribology and Condition Monitoring: LUBMAT-IBERTRIB 2024 Conference Program and Proceedings, 1st ed., Tekniker, San Sebastian, 2024: pp. 271–272.

[218] S. Costa, P. Capela, M.S. Souza, J.R. Gomes, L. Carvalho, M. Pereira, D. Soares, A new grinding wheel design with a 3D internal cooling structure system, J Manuf Mater Process 8 (2024) 159. https://doi.org/10.3390/jmmp8040159.

[219] S. Costa, P. Capela, M. André, A. Monteiro, M. Pereira, J. Ribeiro, D. Soares, Optimization of a green composite containing a 3D structure produced via additive manufacturing, in: 2nd International Workshop on Additive Manufacturing and Sustainability, 1st ed., Instituto Politécnico de Bragança, Bragança, 2025: pp. 11–14.

[220] S. Farah, D.G. Anderson, R. Langer, Physical and mechanical properties of PLA, and their functions in widespread applications — A comprehensive review, Adv Drug Deliv Rev 107 (2016) 367–392. https://doi.org/10.1016/j.addr.2016.06.012.

[221] M.A. Ruz-Cruz, P.J. Herrera-Franco, E.A. Flores-Johnson, M.V. Moreno-Chulim, L.M. Galera-Manzano, A. Valadez-González, Thermal and mechanical properties of PLA-based multiscale cellulosic biocomposites, J Mater Res Technol 18 (2022) 485–495. https://doi.org/10.1016/j.jmrt.2022.02.072.

[222] R. Prathipa, C. Sivakumar, B. Shanmugasundaram, Biodegradable polymers for sustainable packaging applications, Int. J. Mech. Eng. Technol 9 (2018) 293–303.

[223] M. Schneider, C. Günter, A. Taubert, Co-deposition of a hydrogel calcium phosphate hybrid layer on 3D printed poly(lactic acid) scaffolds via dip coating: towards automated biomaterials fabrication, Polymers (Basel) 10 (2018) 275. https://doi.org/10.3390/polym10030275.

[224] S. Costa, P. Capela, A. Hassui, J. Ribeiro, M. Pereira, D. Soares, CFD analysis of multi-layer cooling channels in three-dimensionally structured grinding wheels, Appl Therm Eng 279 (2025) 127633. https://doi.org/10.1016/j.applthermaleng.2025.127633.

[225] S. Costa, A. Souza, L. Neves, J. Ribeiro, M. Pereira, D. Soares, Coolant flow in structured grinding wheels: CFD validation via high-speed imaging and particle tracking, Appl Therm Eng 281 (2025) 128689. https://doi.org/10.1016/ j.applthermaleng.2025.128689.

[226] H.K. Versteeg, W. Malalasekera, An introduction to computational fluid dynamics the finite volume method, 2nd ed., Pearson Education India, Essex, 2007.

[227] G.K. Batchelor, An introduction to fluid dynamics, Cambridge University Press, 2000.

[228] P.J. LaNasa, E.L. Upp, Basic Flow Measurement Laws, in: Fluid Flow Measurement, 3rd ed., Elsevier, Boston, 2014: pp. 19–29. https://doi.org/10.1016/b978-0-12-409524-3.00002-2.

[229] S.B. Pope, Turbulent Flows, 1st ed., Cambridge University Press, Cambridge, 2000. https://doi.org/10.1017/cbo9780511840531.

[230] J.C. Lasheras, E.J. Hopfinger, Liquid jet instability and atomization in a coaxial gas stream, Annu Rev Fluid Mech 32 (2000) 275–308. https://doi.org/10.1146/annurev.fluid.32.1.275.

[231] M. Saeedipour, S. Vincent, J.L. Estivalezes, Toward a fully resolved volume of fluid simulation of the phase inversion problem, Acta Mech 232 (2021) 2695–2714. https://doi.org/10.1007/s00707-021-02972-z.

[232] J. Chen, Y. Fu, N. Qian, C.Y. Ching, D. Ewing, Q. He, A study on thermal performance of revolving heat pipe grinding wheel, Appl Therm Eng 182 (2021) 116065. https://doi.org/10.1016/j.applthermaleng.2020.116065.

[233] S. Mirjalili, A. Mani, A conservative second order phase field model for simulation of N-phase flows, J Comput Phys 498 (2024) 112657. https://doi.org/10.1016/j.jcp.2023.112657.

[234] M. Rasouli, S.M. Mousavi, H. Azargoshasb, O. Jamialahmadi, Y. Ajabshirchi, CFD simulation of fluid flow in a novel prototype radial mixed plug-flow reactor, J Ind Eng Chem 64 (2018) 124–133. https://doi.org/10.1016/j.jiec.2018.03.008.

[235] A. Reid, R. Rossi, C. Cottini, A. Benassi, CFD simulation of a Rushton turbine stirred-tank using open-source software with critical evaluation of MRF-based rotation modeling, Meccanica 60 (2025) 1613–1637. https://doi.org/10.1007/s11012-024-01824-z.

[236] W.K. Meng, C. hao Yu, J. Li, R. dong An, Numerical simulation of gas-liquid two-phase flow impacting fixed structure by CLSVOF/IB method based on OpenFOAM, J Hydrodyn 33 (2021) 1176–1189. https://doi.org/10.1007/s42241-021-0100-2.

[237] F.M. White, Fluid Mechanics 7th Edition in SI units, 7th ed., McGraw-Hill Education, New York, 2016.

[238] C.A. Schneider, W.S. Rasband, K.W. Eliceiri, NIH Image to ImageJ: 25 years of image analysis, Nat Methods 9 (2012) 671–675. https://doi.org/10.1038/nmeth.2089.

[239] D. Ershov, M.-S. Phan, J.W. Pylvänäinen, S.U. Rigaud, L. Le Blanc, A. Charles-Orszag, J.R.W. Conway, R.F. Laine, N.H. Roy, D. Bonazzi, G. Duménil, G. Jacquemet, J.-Y. Tinevez, TrackMate 7: integrating state-of-the-art segmentation algorithms into tracking pipelines, Nat Methods 19 (2022) 829–832. https://doi.org/10.1038/s41592-022-01507-1.

[240] A.S. Sobh, E.M. Sayed, A.F. Barakat, R.N. Elshaerr, Turning parameters optimization for TC21 Ti-alloy using Taguchi technique, Beni-Suef Univ J Basic Appl Sci 12 (2023) 1–11. https://doi.org/10.1186/s43088-023-00356-x.

[241] M.W. Hisam, A.A. Dar, M.O. Elrasheed, M.S. Khan, R. Gera, I. Azad, The versatility of the taguchi method: Optimizing experiments across diverse disciplines, J Stat Theory Appl (2024) 365–389. https://doi.org/10.1007/s44199-024-00093-9.

[242] S. Chakraborty, H.N. Datta, S. Chakraborty, Grey relational analysis-based optimization of machining processes: a comprehensive review, Process Integr Optim Sustain 7 (2023) 609–639. https://doi.org/10.1007/s41660-023-00311-4.

[243] D.C. Montgomery, Design and analysis of experiments, 10th ed., John Wiley & Sons, Hoboken, 2020.

[244] P. Morsch, J. Kühn, R. Werner, H. Anlauf, D.U. Geier, T. Becker, H. Nirschl, Influence of the filter cloth and nozzles type on the in-situ cleaning procedure of filter presses, Chem Eng Sci 226 (2020) 115889. https://doi.org/10.1016/j.ces.2020.115889.

[245] S. Costa, P. Capela, A. Hassui, J. Ribeiro, M. Pereira, D. Soares, Performance of 3D-structured grinding wheels with multi-layer internal cooling channels, Results Eng 28 (2025) 107881. https://doi.org/10.1016/j.rineng.2025.107881.